FOSSIL ENERGY

DOE/BC/15311-8
(OSTI ID: 786051)

HEAVY AND THERMAL OIL RECOVERY PRODUCTION MECHANISMS

SUPRI TR-127
August 2001

By:
Anthony R. Kovscek
William E. Brigham
Louis M. Castanier

Date Published: October 2001

Work Performed Under Contract No. DE-FC26-00BC15311

Stanford University
Stanford, California

National Energy Technology Laboratory
National Petroleum Technology Office
U.S. DEPARTMENT OF ENERGY
Tulsa, Oklahoma

DOE/BC/15311-8
Distribution Category UC-122

Heavy and Thermal Oil Recovery Production Mechanisms

SUPRI TR—127

By
Anthony R. Kovscek
William E. Brigham
Louis M. Castanier

October 2001

Work Performed Under DE-FC26-00BC15311

Prepared for
U.S. Department of Energy
Assistant Secretary for Fossil Energy

Tom Reid, Project Manager
National Petroleum Technology Office
P.O. Box 3628
Tulsa, OK 74101

Prepared by
Stanford University
Department of Petroleum Engineering
Green Earth Sciences Bldg., Room 080B
367 Panama Street
Stanford, CA 94305-2220

TABLE OF CONTENTS

Acknowledgements

This work was prepared with the support of the U.S. Department of Energy, under Award No. DE-FC26-00BC15311 These contributions are gratefully acknowledged. However, any opinions, findings, conclusions, or recommendations expressed herein are those of the authors and do not necessarily reflect the views of the DOE.

We acknowledge contributions from the Stanford University Petroleum Research Institute (SUPRI-A) Industrial Affiliates:

Aera Energy LLC
Chevron Oil Company
ExxonMobil
Petroleos de Venezuela, S.A.-Intevep
Phillips Petroleum
Shell International Exploration and Production
Texaco
Totalfina Elf

Research Program 2000-03
Stanford University Petroleum Research Institute (SUPRI-A)

Tony Kovscek

Introduction

The Stanford University Petroleum Research Institute (SUPRI-A) studies oil recovery mechanisms relevant to thermal and heavy oil production as well as thermal and conventional recovery from low permeability and fractured porous media. Our scope of work is relevant across near-, mid-, and long-term time frames. The primary functions of the group are to conduct industry leading research, provide research and engineering services to affiliated companies, and educate and train students for careers in industry.

In August of 2000, we received funding from the U.S. Department of Energy (DOE) to support partially our efforts from 2000 to 2003. The DOE support is contingent upon the SUPRI-A program maintaining an active dialogue with oil industry companies and upon cost-sharing a major portion of research expenses. This document details the proposed technical program until the year 2003. The program spans a spectrum of topics and is divided into five categories: (i) multiphase flow and rock properties, (ii) hot fluid injection, (iii) primary heavy-oil production, (iv) reservoir definition, and (v) in-situ combustion. Directions are outlined briefly in each area below.

Multiphase Flow and Rock Properties

Application of enhanced oil recovery processes and simulation of these processes demands understanding the physics of displacement and accurate representation of constitutive relations such as relative permeability and capillary pressure. A common thread running through the experimental portion of this work is the use of the SUPRI X-ray computed tomography (CT) scanner to image oil, water, and gas saturation distributions. Thus, we obtain the position and shapes of displacement fronts in porous media. The CT equipment developed at Stanford is unique in that it allows both multi-energy scans for imaging of three phases and vertical or horizontal positioning.

Imbibition. Water imbibition is fundamental to both steamdrive and waterflood performance in fractured and unfractured rocks. Steam injection is accompanied by condensation and flow of the resulting hot water away from the injector. Imbibition studies are naturally divided into experiments that probe behavior in the matrix, flow in fractures, and matrix/fracture interactions. To advance the art of analysis of imbibition experiments, we propose an unconventional mode of collecting CT data. In a conventional experiment, X-ray CT data is taken in slices normal to the central (i.e., long) axis of the core or sand pack. Figure 1 illustrates a cell for one-dimensional imbibition where it is possible to examine the entire length of a core with a single CT scan. Thus, the cross-section of the coreholder and the water jacket shown schematically in Fig. 1 represents the scanned volume. In addition to providing temperature control, the shape of the water jacket and the large mass density of water will minimize imaging problems. A variant of this set up can be used to examine multidimensional imbibition and coupled matrix/fracture flow.

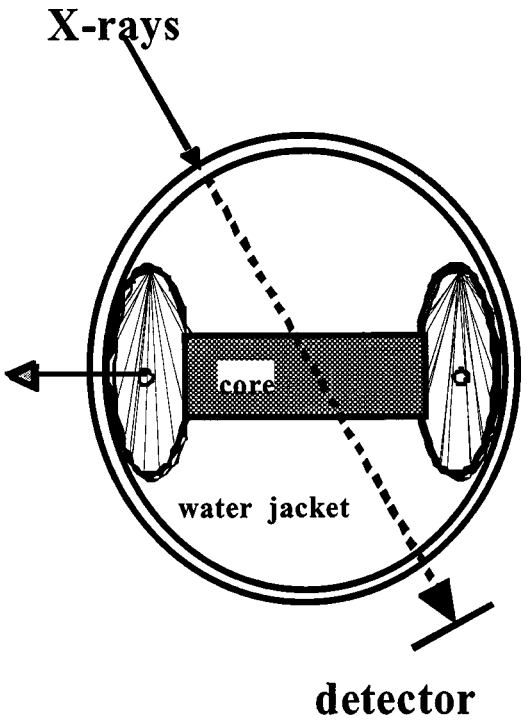

Figure 1: Imbibition cell for CT scanner application.

We intend to apply this newly designed imbibition cell to study spontaneous imbibition of water into oil-containing and air containing porous media for cocurrent and countercurrent imbibition. Experiments are being conducted under flow and initial fluid saturation conditions that are relevant to the field and also under quasi-static conditions. Ideally, reservoir rock samples with varying wettability will be characterized with respect to pore size, shape and frequency; then rock from the same or a similar sample will be subjected to imbibition/displacement tests. This work is necessary to further develop our understanding of oil/water location given different dynamic and quasi-static conditions. Once a sufficient base of spontaneous imbibition data is collected, we will develop a semi-analytical technique for obtaining relative permeability and capillary pressure for water-gas systems and perhaps the more complicated oil-water system as well as improved correlations for imbibition performance.

Matrix to fracture interactions of porous media are much studied, but not well understood. In companion work, we study imbibition and oil production mechanisms to better understand matrix/fracture transport in fractured porous media. We use both the CT scanner with cores of prescribed fracture geometry and etched-silicon micromodels that allow direct visualization of flow processes under a microscope. Micromodels will be redesigned so that both countercurrent and cocurrent imbibition can be visualized. Hence, we will observe directly oil production from the matrix into the fracture and water imbibition into the matrix. Water flow rate through the fracture will also be varied to simulate fractures that are nearer or farther from a well. Companion experiments with similar matrix-fracture geometry will be conducted and monitored in the CT scanner. An imbibition cell will be constructed for multidimensional systems with well characterized fractures. Cubic sandstone cores that are roughly 5 cm along a side will be used in a scanning geometry similar to Fig. 1. Fracture apertures will be set by metallic shims of precise thickness. Fracture aperture and fluid flow rate in fractures will be variable. We will examine how fluid flow rate in fractures affects displacement patterns and recovery. When complete, we will have a much clearer understanding of how capillary and viscous forces interact to affect matrix to fracture fluid transfer. This will lead to more accurate formulations for the corresponding terms used in reservoir simulation.

Temperature and Relative Permeability. There are apparent effects of temperature on relative permeability during steam or hot fluid flow (c.f. Akin et al 1999 for a review). It has been demonstrated through both experiments and reservoir simulation that in heavy oils viscous fingering of warm oil at low to moderate temperature posed a problem for interpretation of such experiments using standard techniques such as the Johnson-Bosler-Nauman (JBN) method (Akin et al. 1999). As a logical successor to this work, we propose to determine whether viscous fingering effects are present in systems at high temperature and to develop interpretation methods for such dynamic displacement data.

Mobility Control of Steam. The SUPRI program continues to study mobility control of gases, such as steam, using surfactants. Past work has centered on understanding foam generation mechanisms, experimentally observing foam in heterogeneous porous media, and pilot testing of the foam process. Mechanistic modeling and models appropriate for field-scale simulation of the foam process are necessary to bring these disparate topics together.

Our thrust in this area will be two-fold. First, efforts will be directed toward understanding and modeling foam generation and stability at low surfactant concentrations. Foam displacement experiments will be conducted at a variety of surfactant concentrations in homogeneous one-dimensional sandpacks. Modeling and interpretation of the experiments will follow. Second, we will expand our mechanistic model to foam processes in heterogeneous porous media (Kovscek et al, 1997). Specifically, we will begin with the mechanistic description of aqueous foam behavior in one-dimensional media and conduct a thorough analysis of how the physically-based foam-simulation parameters scale with permeability and rock type. The two major components of the population balance model to consider are bubble size and gas mobility. Bubble size is determined by the interplay of foam generation and coalscence forces which are described by rate expressions. Thus, by considering individually the mathematical expressions and rate constants describing foam generation and coalescence, we will elucidate how bubble size changes among different permeability regions. Next, we will ascertain the manner in which gas-phase mobility shifts as permeability is increased or decreased for a constant bubble size.

Once this scaling analysis is complete, it will be tested by incorporating permeability sensitive foam simulation parameters into a multidimensional population balance model. Our previous experiments (Bertin et al 1999) can then be simulated and the match between experiments and the new theory observed. This work will establish the conditions of permeability contrast and surfactant concentration where foam diverts effectively gas from high- to low-permeability zones.

Hot-Fluid Injection

Steam injection is the most common form of enhanced oil recovery (Moridis 1998). Heat in the form of steam is commonly injected into reservoirs containing heavy (c.f., (Prats 1982)) and medium (c.f. (Olsen et al. 1993; Kovscek et al. 1997b)) gravity oils to reduce oil viscosity, cause volumetric expansion of oil, and thereby improve production. There are two primary thrusts to our effort in this area. The first is nonconventional wells for thermal oil recovery and the second is steamdrive in fractured, low permeability porous media.

Nonconventional Wells. Horizontal wells have been used in steamdrive operations in place of traditional rows of vertical producers or injectors. The motivation here is that a single horizontal well can be cheaper and more productive than a row of vertical wells (Joshi 1991). The drainage pattern around a horizontal production well can also be substantially better than around a row of vertical producers. Oil is captured in a dipping reservoir that would otherwise flow past vertical wells. Steam assisted gravity drainage (SAGD) (Butler 1997) lies on the less conventional side of horizontal well applications. The objective of SAGD is to use gravity forces to their maximum extent, while minimizing the role of viscosity in heavy-oil production, through optimal spacing of horizontal producers and injectors.

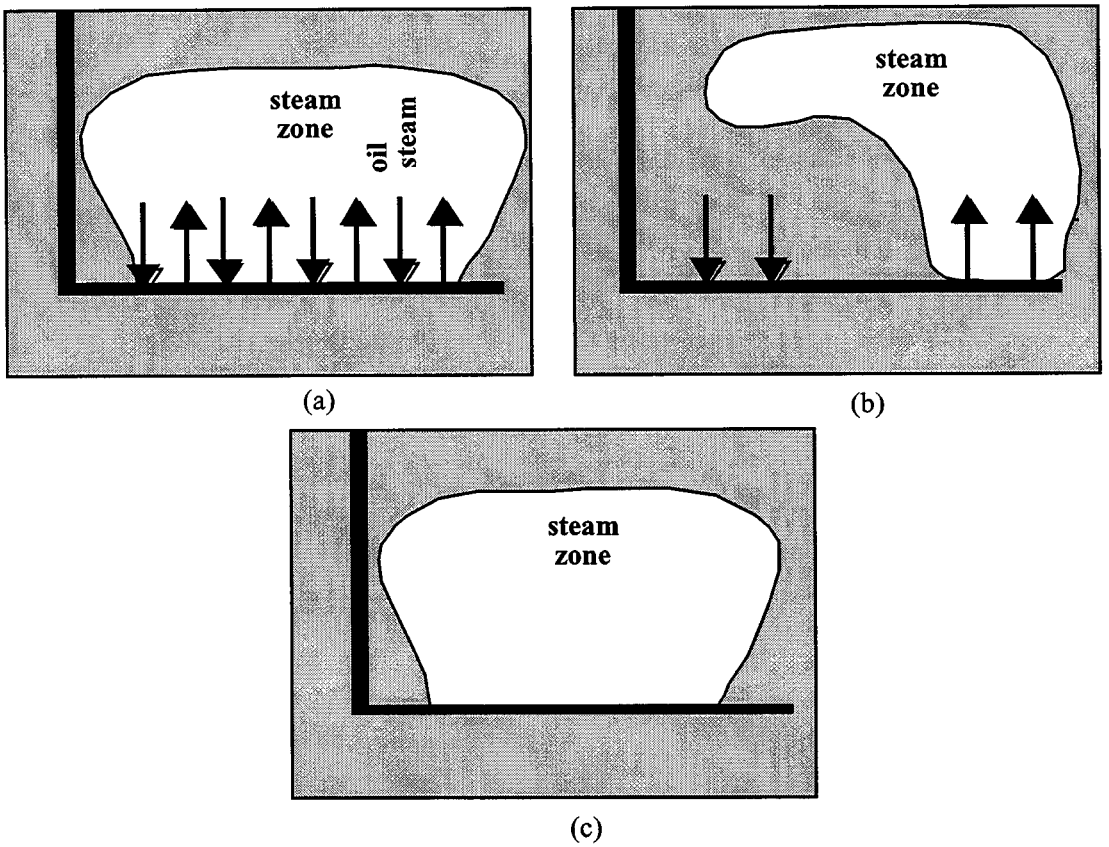

Figure 2-Steam injection and oil production strategies for a single well: (a) counter-current injection/production, (b) co-current injection and production, and (c) cyclic injection/production.

We will simulate and history match results from SAGD processes employing a single well for production and injection. From an engineering perspective, we hope to clarify injection and well completion strategies that lead to optimum recovery with minimum heat input. For example, in the single-well steam assisted gravity drainage (SW-SAGD) process, steam is injected and oil produced from the same well. However, there is no consensus as to where the steam should be injected and oil produced in a well, as shown in Fig. 2. Injection and production could occur in a counter-current fashion along the entire length of the well as shown in Fig. 2(a) or steam might be injected from the toe of the well and production occur in the vicinity of the heel, Fig. 2(b). The interplay between steam injection rate and oil production rate should be explored to obtain guidelines for minimizing steam recirculation. Importantly, continuous steam injection needs to be compared with cyclic steam injection shown schematically in Fig. 2(c). For vertical wells, early cyclic injection is the most efficient process in terms of heat input and recovery rate. This may also be true for horizontal wells. We plan to pursue these issues using both numerical simulation and semi-analytical techniques.

Steamdrive in Fractured, Low Permeability Media. Recent field tests have shown that steam injection can recover substantial amounts of oil held inside low permeability, fractured reservoir rock (Kumar and Beatty 1995; Kovscek et al. 1997b). It is unclear how the basic mechanisms differ from conventional streamdrive in permeable heavy-oil reservoirs and how these differences might be used to an advantage. It seems certain, however, that one of the central advantages of steamdrive over nonthermal recovery methods is that steam does not actually have to contact oil to heat it and improve recovery. Thermal conduction allows steam to heat unswept portions of the reservoir. Upon heating, volumetric

expansion and vaporization of oil improve recovery. There are three areas we need to study: heat transport and oil production mechanisms, conceptual model, and simulation studies. Each is described next.

In the area of heat-transfer mechanisms, we will study fracture (natural or hydraulic) to matrix heat transfer, conduction versus convection heat transfer within the matrix, and the role of matrix permeability on the ease of establishing a steam zone. For oil-production mechanisms, the role of oil composition on vapor-phase formation and the degree of volumetric expansion will be examined.

A beginning point will be numerical study of the steamdrive process in well characterized matrix and fracture geometries, including simulation of heat and steam penetration of single and multiple matrix blocks as a function of permeability contrast between fracture and matrix and capillary entry pressure of the matrix. The basic question: How easy is it to penetrate the low permeability matrix with steam? Previous experiments (Sumnu et al, 1994) indicate that it is difficult for steam to build sufficient pressure to enter the matrix of 800 mD sandstone when very high permeability flow paths are also available. Also examined will be the case of fractures or high permeability zones which are present, but do not necessarily communicate. In either scenario, significant steam condensation will occur during the initial stages of steam injection. Heating will be due to release of latent heat from the steam, condensed hot water imbibition into the matrix, and heat conduction. The relative importance of each mechanism will be characterized.

Oil composition and the fraction of light components will play a very important role in determining the ease with which a vapor phase forms in the matrix. If the oil contains sufficiently light components that flash slightly above the formation temperature, this vaporization will aid in oil production due to volumetric expansion resulting from the formation of a vapor phase. Perhaps more importantly, vaporization of the oil phase may provide pathways for steam to enter the matrix, thereby enhancing heat transfer to the matrix. Even prior to flashing, volumetric expansion due to heating of the oil will promote production. Hence, an important part of the numerical study will be effectiveness of recovery as a function of oil composition and gravity. A way forward is to choose relatively simple characterizations of light, medium, and heavy crude oils and examine numerically the ease of steam-phase formation in the matrix and how recovery due to volume expansion changes as we move from light to heavy oil. If warranted, we may pursue experiments to verify conclusions reached here.

Also in the area of mechanisms, we propose to quantify through experiment and theory the speed and extent to which steam and hot water change the permeability of low permeability, siliceous, rocks. Large internal surface area and high steam and condensate temperatures could lead to substantial rearrangement of the permeability field. Hot steam condensate might dissolve large amounts of silica, the silica can then transport with the aqueous phase, and silica could precipitate in a different portion of the reservoir as the hot condensate cools. Hence, permeability might increase near injectors and decrease within the reservoir. Our current plans call for conducting experiments with hot water injection into representative diatomite samples and to monitor experiments with our CT scanner. In this way, we will measure the time evolution of permeability in a well characterized and controlled environment. The CT scanner will allow us to determine if "wormholes" develop upon injecting hot, silica-free water.

From this study of mechanisms and the interplay of matrix and fracture permeability, sufficient information will be available to assemble an improved conceptual picture of steam, heat, and oil flow in diatomite. The model may include elements of heat and mass flow, matrix dissolution and reprecipitation as a function of temperature, and expansion and contraction of the rock matrix and fractures with pore pressure. The relative importance of each of these factors will be quantified. We will then be able to answer the question of whether current compositional, thermal simulators for permeable systems capture all of the essential physics.

The final or culminating portion of this task is to consider the implications of the above mechanisms on field-scale recovery. With input from industry sponsors, we will identify representative field-type problems to simulate. The factors examined here will depend upon any dominant mechanisms identified. We will use representative field-type problems and conduct simulations. Possible factors to examine include effect of geologic layering and the conductivity between layers, other forms of heterogeneity, steam override, and gravity segregation of water and steam in the wellbore.

Primary Production of Heavy Oil

So-called cold production of heavy oil is attractive because steam injection is costly due to the operating and capital expenses for steam generation facilities. Sometimes primary recovery can be on the order of 10-15% from heavy-oil reservoirs. Most cases of significant cold production are associated with foamy crude oil and horizontal wells (Smith 1988). Here, gas released from solution during pressure depletion remains dispersed as small bubbles rather than uniting to form a single phase. With foamy crude oil, the gas-oil ratio (GOR) is lower and the oil productivity of a well is increased over the unfoamed case (Maini et al. 1993).

Experimental Investigation. A key to developing a mechanistic understanding of foamy-oil behavior is to delineate bubble growth, interaction, and flow mechanisms at the pore level. These are unknown for foamy heavy oil. Here, we will use two-dimensional micromodels with one to one representation of sandstone pore features (Hornbrook et al. 1991) to observe bubble size, nucleation, growth, and flow. Crude oil saturated with methane as well as non-foaming mineral oil will be employed. The micromodels will be subjected to a declining pressure and the dynamics of heavy-oil solution gas drive observed. By using various types of oil, we hope to delineate crude-oil conditions that are conducive to the formation of foamy oil. As pressure and temperature are important to crude-oil behavior, a major portion of the micromodel effort will be in the design of temperature controlled pressure vessel to conduct experiments at relevant temperatures and pressures. The major difficulty is the construction of an apparatus that provides a confining pressure to the micromodel and incorporates a transparent window for viewing the micromodel. The thickness of window, transparent confining fluid, and micromodel must remain thin for imaging with a high-power microscope objective.

Companion experiments will also be conducted in sands and sandstone. The purpose of the experiments is to measure the evolution of oil and gas saturation in situ as well as pressure while undergoing primary production of foaming and non-foaming heavy crude oils. Production rate will be varied to delineate critical rates of production necessary for foamy oil generation. Porous media will be scanned along the length of the core rather than conventional cylindrical cross sections. In this manner, it should be possible to visualize core-spanning gas paths, if they develop, as a function of expansion rate. A visual cell will be used at the outlet to gauge the size of mobile bubbles. Mobile bubble size can then be compared between the micromodel and porous media experiments. Figure 3 illustrates the proposed apparatus. The water jacket is necessary to create a symmetric cross section for CT-scanning.

Model and Simulation of Cold Production. The objective of this task is to translate the experimental observations and results from the above experimental effort into a mechanistic model for cold production of heavy oil. The model should be mechanistic and consistent with physical observations. Since unfoamed oil is a subset of foamy oil, the model should address primary production of all heavy crudes. Information on foam-bubble size and the rheology of bubble-laden crude oil will be translated into a model and subsequently tested in a reservoir simulator. Our approach will be a bubble population balance (e.g., (Kovscek *et al.* 1995)). In a population-balance method, the number density of bubbles (i.e., the number of bubbles per unit volume of gas) is tracked as a function of location and time. Number density is also referred to as bubble texture. The crux of the problem is to develop the requisite mechanistic constitutive equations for gas and oil flow. These equations will be developed and tested against the information and data garnered in the experiments described below.

Reservoir Definition

The central idea of reservoir definition is to apply reservoir engineering techniques to improve our ability to understand reservoir rock and fluid properties and reservoir architecture, and the flow paths and flow barriers that arise from this architecture. Our interest in this topic is to learn the distribution of permeability and how geology and flow patterns determine the success of a recovery process.

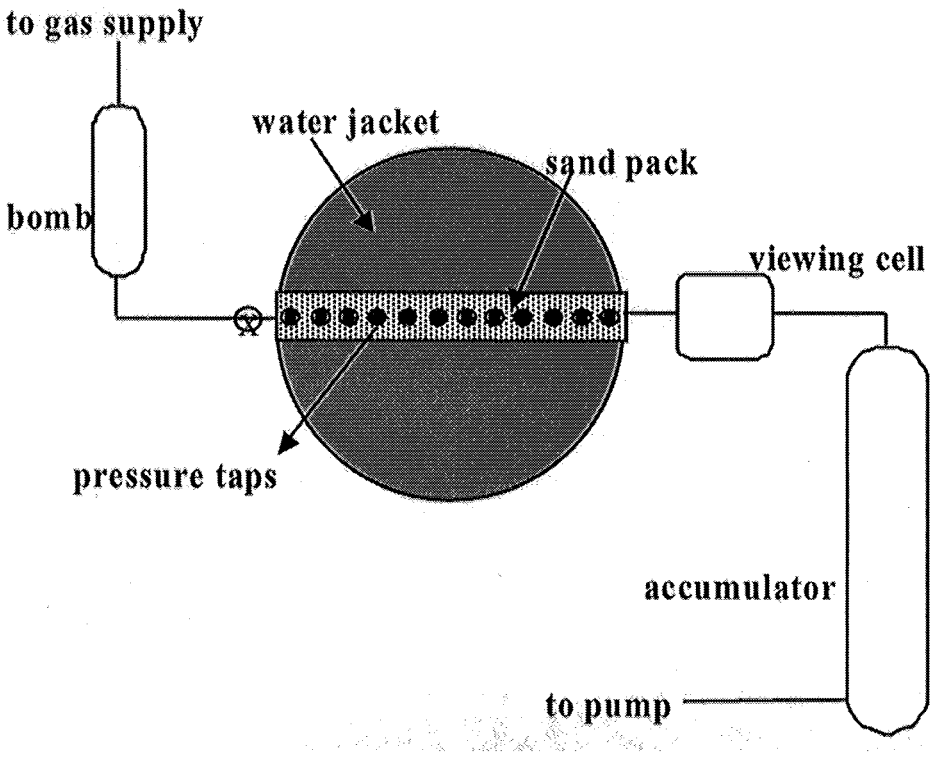

Figure 3: Schematic of proposed apparatus.

History matching using reservoir simulators plays an important role in reservoir engineering. It is important for prediction and data interpretation. In many cases we have tracer or water breakthrough information at producers and pressure information. These data contain much information about the permeability distribution of the reservoir, but it is difficult to infer this distribution. Most approaches to this inverse problem begin with a conventional reservoir simulator and manipulate parameters at the grid-block level corresponding to conventional simulation grids. There are many grid blocks, thus the optimization is slow. Also, conventional finite difference reservoir simulators for flow simulation are relatively slow. Streamline based reservoir simulators have been developed recently that execute much more rapidly, relative to conventional finite-difference based simulation, and are quite accurate in that numerical dispersion is minimized (Batycky et al, 1997). In streamline simulation, the three-dimensional flow simulation is broken down into a number of one-dimensional flow paths. We will apply the concepts of streamlines to infer permeability fields based on tracer breakthrough, water cut, and injection/production pressure information.

The basic idea is to switch the optimization to the streamline level rather than optimizing

way, the production characteristics of wells are decoupled and broken into a series of streamlines. With streamlines, we compute the time of flight of a fluid volume along a streamline, and so we also know the breakthrough time for each individual streamline. The streamline or series of streamlines that under or over predict reservoir performance are thus easily identified. The streamline properties, for instance permeability, are adjusted to match the reference production curve and pressure histories. Once the modifications of the streamline properties are computed, these modifications can be converted to changes in the properties of grid blocks through which the streamline passes. In this way, we dramatically reduce the size of the optimization problem.

In-Situ Combustion

During the most recent meeting of our industry advisory committee, representatives suggested that we study unusual recovery methods that are not practiced widely for improved recovery of heavy oils. Here, we focus on variants of the in-situ combustion process. This effort is necessary to advance the art of heavy-oil recovery and prepare for field implementation of new projects. The following presents the motivation for such work, points out some problems with application of steam injection, and discusses two avenues that we intend to explore.

The most widely used recovery method for heavy oils is steam injection in either a cyclic or steam-drive fashion. Steam injection, however, is not applicable to all reservoirs. The major parameters that determine the applicability of steamflood are depth, pressure, and formation properties such as permeability and initial oil saturation. Each is discussed briefly. When reservoir depth exceeds about 3,000 ft (1,000m), heat loss from the injection well to the surrounding formation causes steam to condense and makes steam injection both difficult and inefficient. Another issue associated with depth is pressure. As pressure increases, the latent heat of water decreases until it vanishes entirely at the critical point (705 °F, 3200 psi). Hence, at high pressure, most of the enthalpy of steam is sensible heat rather than latent heat. This translates to high injection temperature, less efficient heat transport, and significant heat losses from both the injection wells and the formation. Formation permeability is important in two ways. First, steam injectivity is proportional to permeability. Second, clays present in the reservoir may swell in the presence of the fresh water that results from steam condensation. This can reduce injectivity and impair the process. The last factors are oil saturation and porosity. If not enough oil is in place, the energy used to heat the reservoir will be greater than the energy obtained from the oil produced. Steam injection is generally uneconomic in a reservoir where the product of porosity and oil saturation is less than about 0.1.

From the above discussion it is clear that despite its usefulness steam injection is limited to a select group of reservoirs. On the other hand, in-situ combustion is not nearly as limited. Two possible scenarios where in-situ combustion could be feasible, and steam injection not, are offshore fields and reservoirs lying under permafrost. Due to reduced heat losses and the containment of combustion products within the reservoir, in-situ combustion is more energy efficient and involves fewer atmospheric emissions than steam. Additional benefits of combustion are the in-situ upgrading of heavy oils because the heaviest fraction of the crude oil is consumed during the process and reduction in sulfur content.

The development of water soluble catalytic additives to improve performance (Shallcross et al. 1991) and to broaden the in-situ combustion process to horizontal well applications are two pathways for improving in-situ combustion reliability. We will utilize our past experience in metallic salt additives to promote combustion at lower temperatures and study upgrading possibilities for heavy oils or oils containing heavy metals or sulfur.

Solvents reduce heavy-oil viscosity and facilitate production. The solvents can be miscible gases or liquids. Liquid solvents are usually expensive while the price for the oil recovered is low. Consequently, the economics of liquid solvent injection are usually not favorable. Miscibility of gases with heavy oils requires very high pressure. Again, the economics are not good. During solvent injection, the main

problem will be the efficient use of a limited amount of a relatively expensive injected fluid. Reservoir heterogeneities and density and mobility differences between solvent and reservoir oil will cause sweep efficiency problems.

A solvent process combined with in-situ combustion in a cyclic fashion provides a means to exploit the strengths of both processes. One important fact to note is that both solvent injection and in-situ combustion have been proven to be effective in a variety of reservoirs, but the combination of the two methods has never been attempted, to our knowledge. Cyclic injection of solvents, either gas or liquid, followed by in-situ combustion of a small part of the reservoir will increase the near wellbore temperature and also will clean the wellbore region of all the residues and precipitated crude oil fractions left by the solvents. Unlike the classic well to well in-situ combustion, we would only try to improve near wellbore conditions by burning the heavy residues left after the solvent cycle.

The following describes some simple tests that can be used as a screening procedure for this technique. Heavy crudes from reservoirs such as Cold Lake or Hamaca will be mixed with liquid solvents and viscosities of the mixtures will be measured. Filtration of the mixtures will determine whether solid precipitation or formation damage are likely to occur. If precipitation occurs, the mixtures could be filtered through a sand pack of permeability and pore structure close to the field sands. Changes in permeability with the injection will be recorded. When (and if) the ratio of the permeabilities before and after passage of the mixtures declines substantially, the sand pack will be combusted. Fuel concentration and composition as well as an estimate of the air requirements will be obtained. With these data, simple calculations are possible to estimate production in the field, and to make an economic evaluation.

Effort

For the coming year, we anticipate that roughly 25% of our effort will be expended on projects in the category "Multiphase Flow and Rock Properites". Another 20% of our effort will be devoted to "Hot Fluid Injection" while 25% will be in the area of "Mechanisms of Primary Heavy-Oil Recovery". Finally, 20% of our effort will be in Reservoir Definition and 10% in the area of In-Situ Combustion.

References

1. Akin, S., Castanier, L. M. and Brigham, W. E.: "Effect of Temperature on Heavy Oil/Water Relative Permeabilities." SPE 54120, paper presented at the 1999 SPE International Thermal Operations Symposium, Bakersfield, CA, (March 17-19, 1999).

2. Batycky, R. P., Blunt, M. J., and M. R. Thiele: "A 3D Field-Scale Streamline-Based Reservoir Simulator," SPERE (November 1997), 246-254.

3. Bertin, H. J., Apaydin, O. G., Castanier, L. M. and Kovscek, A. R.: "Foam Flow in Heterogeneous Porous Media: Effect of Crossflow." Soc. Pet. Eng. J. **4(2)**, (1999) 75-82.

4. Butler, R. M.: GravDrain's Blackbook: Thermal Recovery of Oil and Bitumen. Calgary Alberta, Canada, GravDrain Inc. (1997).

5. Hornbrook, J. W., Castanier, L. M. and Pettit, P. A.: "Observation of Foam/Oil Interactions in a New, HIgh-Resolution Micromodel." SPE 22631, paper presented at the 66th Annual Technical Conference and Exhibition of the Society of Petroleum Engineers, Dallas (October 6-9, 1991).

6. Joshi, S. D.: "Thermal Oil Recovery with Horizontal Wells." Jour. Pet. Tech. (November 1991) 1302-1304.

7. Kovscek, A. R., Patzek, T. W. and Radke, C. J.: "A Mechanistic Population Balance Model for Transient and Steady-State Foam Flow in Boise Sandstone." Chemical Engineering Science **50**(23) (1995) 3783-3799.

8. Kovscek, A. R., Patzek, T. W. and Radke, C. J.: "Mechanistic Foam Flow Simulation in Heterogeneous Multidimensional Porous Media." SPEJ 2(4) (1997) 511-526.

9. Kovscek, A. R., Johnston, R. M. and Patzek, T. W.: "Evaluation of Rock/Fracture Interactions During Steam Injection Through Vertical Hydraulic Fractures." SPE Production and Facilities (May 1997b) 100-105.

10. Kumar, M. and Beatty, F. D.: "Cyclic Steaming in Heavy Oil Diatomite." SPE 29623, paper presented at the SPE 65th Western Regional Meeting, Bakersfield (March 8-10, 1995).

11. Maini, B. B., Sarma, H. K. and George, A. E.: "Significance of Foamy-Oil Behaviour in Primary Production of Heavy Oils." Jour. of Canadian Pet. Tech. **32**(9) (1993) 50-54.

12. Olsen, D. K., Sarathi, P. S., Schulte, R. K. and Giangiacomo, L. A.: "Case History of Steam Injection Operations at Naval Petroleum Reserve No. 3, Teapot Dome Field, Wyoming: A Shallow Heterogeneous Light-Oil Reservoir," SPE 25786, paper presented at the International Thermal Operations Symposium, Bakersfield (February 8-10, 1993).

13. Prats, M.: Thermal Recovery, Society of Petroleum Engineers, Henry L. Doherty Memorial Fund of AIME, Dallas (1982).

14. Schembre, J. M., Akin, S., Castanier, L. M. and Kovscek, A. R.: "Spontaneous Water Imbibition into Diatomite." SPE 46211, paper presented at the 1998 Western Regional Meeting of the Society of Petroleum Engineers, Bakersfield (May 10-13, 1998).

15. Smith, G. E.: "Fluid Flow and Sand Production in Heavy-Oil Reservoirs Under Solution-Gas Drive." SPE Production Engineering (May 1988) 169-180.

16. Sumnu-Dindoruk, M. H., K. Aziz, W. E. Brigham, and L. M. Castanier: "A Study of Steam Injection in Fractured Media," SUPRI TR101, Stanford University, Stanford, CA (1996).

MULTIPHASE FLOW AND ROCK PROPERTIES

Experimental and Analytical Study of Water Infiltration in In Fractured Systems

Edgar R. Rangel-German and A. R. Kovscek*

Abstract

Capillary imbibition is an important mechanism during water reinjection in fractured porous media. Using an X-ray computerized tomography (CT) scanner, and a novel, CT-compatible core holder, we performed a number of experiments to study air expulsion from rock samples by capillary imbibition of water in a three-dimensional geometry. Different injection rates and fracture apertures were utilized. Two different fracture regimes were identified: "instantly-filled" where the imbibition time is much greater than the time to fill the fracture with water and "filling fracture" where the fracture to matrix transfer grows in length due to relatively slow flow through the fractures. These results were used to validate an approach to calculate the amount of water imbibing into a rock proposed by Rangel-German and Kovscek (2000). A more general semi-analytical model that accounts for both "filling-fracture" and "instantly-filled fracture" regimes in the early-time period is also presented. Although this model couples the matrix and fracture empirically, a way to implicitly couple matrix and fracture is proposed.

Introduction

When considering multi-phase flow in fractured systems, system properties might be quite different from homogeneous porous media. Several studies have focused on understanding the properties of fractured porous media such as capillary pressure, continuity between adjacent matrix blocks, fracture relative permeabilities, and cocurrent or counter-current imbibition (Kazemi et al. 1989; Mattax and Kyte 1962; Hughes 1995; Cil et al. 1996; Cil et al. 1998; Rangel-German et al. 1998). All of these affect the rate of mass transfer between the rock matrix and fractures and determine the amount of water in the matrix.

Capillary imbibition is an important mechanism during water reinjection in fractured porous media. Unless imbibition forces are strong enough to pull water into the matrix, there will be no mass transfer between matrix and fracture. Capillary forces in reservoirs depend on factors such as permeability, pore structure, pore-throat to pore-body size ratio, wettability, and the interfacial tension between the resident and the imbibing phase.

Viscous forces are also important in the flow through fractured media. Viscous forces may counter-act or supplement capillary forces by lowering the amount of water imbibed or forcing water penetration in to the matrix, respectively. Viscous forces are the dominant mechanism affecting flow through fractures and depend on factors such as viscosity, fracture roughness, and fracture conductivity. The last two are a function of fracture geometry.

In any 3-D fractured system, buoyancy forces must also be considered. Gravity might have a strong effect and become the force controlling flow. Buoyancy forces affect the rate with which the displacing phase enters the space previously occupied by the resident phase, vertically. Through a balance with capillarity, gravity sets the equilibrium distribution of wetting and non-wetting phases.

---

* Annual Geothermal Resources Congress, San Francisco (September 2000).

All of these mechanisms must be considered whenever we are to estimate the amount of water imbibed into the matrix of a fractured system. In order to maximize the mass of water imbibing the rock, one must aim to obtain the highest possible matrix-fracture mass transfer. Every system probably has a different optimum combination of these mechanisms at its maximum mass transfer value. Intuitively, injected water will preferentially flow through the fractures rather than the low-permeability matrix in naturally fractured reservoirs when capillary imbibition forces are weak or when injection flow rates are high enough to avoid capillary imbibition. On the other hand, optimum physical conditions for high matrix-fracture mass transfer might not be economical (e.g. slow injection for a very long time).

Handy (1960) in describing air/water systems stated that imbibition could be described by either a diffusion-like equation or a frontal-advance equation, depending on assumptions. However, both solutions predict that the mass of water imbibed depends linearly on the square root of time in one-dimension. This has been verified by other studies (Reis and Cil, 1993; Cil and Reis, 1996; Reis and Haq, 1999; Akin et. al, 2000; Rangel-German and Kovscek, 2000).

Rangel-German and Kovscek (2000) identified the presence of two different fracture flow regimes in cubic rock samples with a single horizontal fracture. The first one, named "filling-fracture" shows a variable length plane source due to relatively slow water flow through fractures; the second flow regime, named "instantly-filled fracture:, where the time to fill the fracture is much less than the imbibition time, shows a constant plane source imbibition. They found that the behavior of the first regime has a linear relationship with time; whereas the behavior of the second regime is very similar to that observed in both counter-current and cocurrent one-dimensional imbibition experiments reported previously in the literature. Instantly-filled fractures display a linear relationship with the square root of time.

In this paper, we discuss further the parameters affecting multi-phase flow in fractured porous media and the way that they can be related to an implicitly coupled matrix and fracture. These parameters are expressed in terms of well known dimensionless numbers such as capillary number, Bond number, and Peclet number. We describe new results of an experimental study of air expulsion from rock samples by capillary imbibition of water in a three dimensional geometry. Flow in the matrix and the fracture is imaged simultaneously. During the experiments, porosity and saturation measurements along the cores were made utilizing an X-ray computerized tomography (CT) Scanner. A novel experimental set-up insuring minimal X-ray artifacts (Rangel-German and Kovscek, 2000) was used to obtained data on water-air displacements in horizontal single-fracture systems.

These experimental results were used to validate an approximate approach to calculate the amount of water imbibing into a rock proposed by Rangel-German and Kovscek (2000), and to write a more general semi-analytical model that could account for both regimes in the early-time period.

Experimental Design

An imbibition cell was designed to insure minimal artifacts while scanning and the collection of maximum saturation information. The details of both the coreholder and set-up are shown in Rangel-German and Kovscek (2000). The basic idea is to use cubic rock samples of 5x5x5 cm, epoxy 5 faces having the bottom open, and create a single horizontal fracture of known and constant aperture along the bottom face. This fracture allows water flow from one horizontal well along the bottom left side of the core to a second horizontal well along the bottom right side of the core. The idea is to have uniform flow along the bottom face of the core. To guarantee few X-ray artifacts, a PVC container was used as opposed to metal, and a cylindrical water jacket in the scanning plane presents a circular cross section object to the scanner. Figure 1 shows frontal and lateral views of the core holder.

A CT Scanner can be used to measure porosity, saturation, and in some cases, concentration distribution, and to track advancing fronts. It can also be used to measure fracture apertures. We used a modified Picker 1200SX Dual Energy CT Scanner. Vertical CT images are taken along the direction of

imbibition (either vertical or horizontal). A single slice provides us with an image of the progress and saturation pattern of imbibition as well as the progress of the water flow in the fracture.

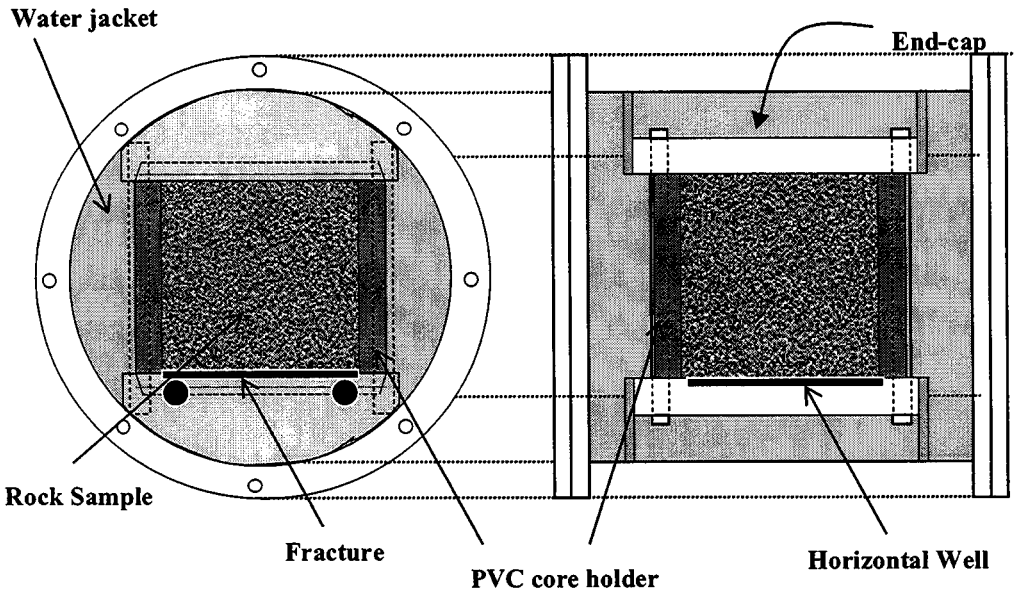

Figure 1. The Coreholder. Frontal and Lateral View.
(After Rangel-German and Kovscek, 2000)

Different experiments at constant water injection rates into the fracture were performed. Using a Constametric pump, rates varied from very slow to very high (0.1 ml/min to 2 ml/min). Different fractures apertures ranging from very narrow (0.025 mm) to wide (0.1 mm) were also used. Different initial water saturations were also applied.

Data Analysis

Porosity and saturation distribution along the core were determined from the experiments. The most common way to calculate porosity from CT Scanner images is (Withjack, 1988):

$$\phi = \frac{CT_{cw} - CT_{cd}}{CT_w - CT_a} \tag{1}$$

where CT_{cw} is the CT number for a 100% water saturated core at a matrix location, CT_{cd} is the CT number for a dry core at a matrix location, CT_w is the CT number for water, and CT_a is the CT number for air. For reference, the CT number for water is around 0 (zero),while the CT number for air is -1000. The water saturations were also calculated from the CT images. The following equation shows how to evaluate water saturation for the water displacing air case.

$$Sw = \frac{CT_{aw} - CT_{cd}}{CT_{cw} - CT_{cd}} \tag{2}$$

where CT_{aw} is the CT number for water and air saturated core at a matrix location.

Experimental Results

Images were collected throughout the experiments. Figure 2 shows a set of these images for a given injection rate and fracture aperture. Calculating the average water saturation (S_w) of the block at each time, and plotting Sw against the square root of time, one obtains the curves shown in Figure 3.

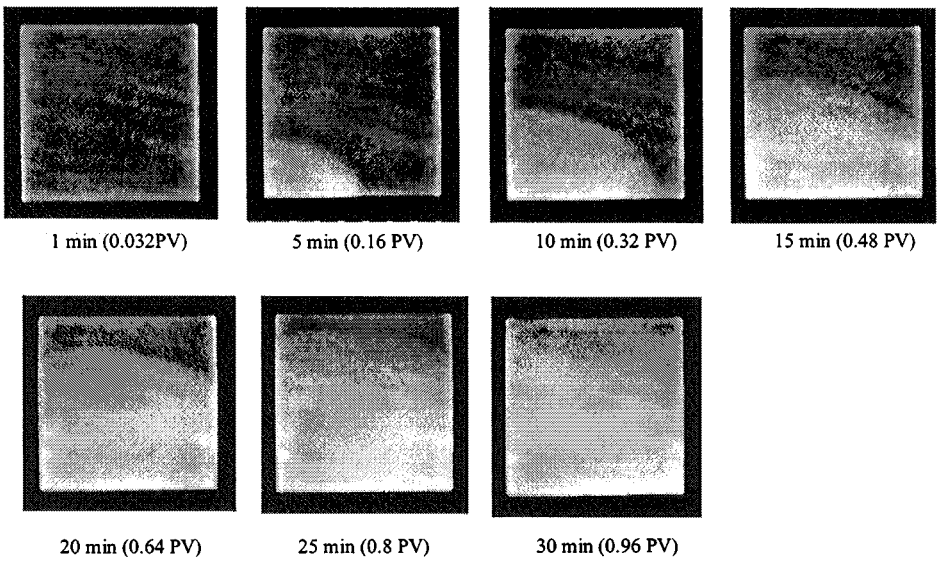

Figure 2. CT Images for "Filling-fracture system for times..
Water injection at 1 cc/min in a fracture 0.1 mm thick.

Figure 3 show the curves for different cases of injection rate, fracture aperture and initial water saturation. These cases are shown in Table 1. The curve labeled 2cc/min, f = 0.025 mm was obtained in a different block of sandstone than the other three experiments; hence, results are slightly different.

Table 1. Different Cases for the Water Imbibition Experiments.

Experiment	Flow Rate [cc/min]	Fracture Aperture [mm]	Fluids System
1	1.0	0.1	Air-water
2	0.5	0.025	Air-water
3	1.0	0.025	Air-water
4	2.0	0.025	Air-Brine

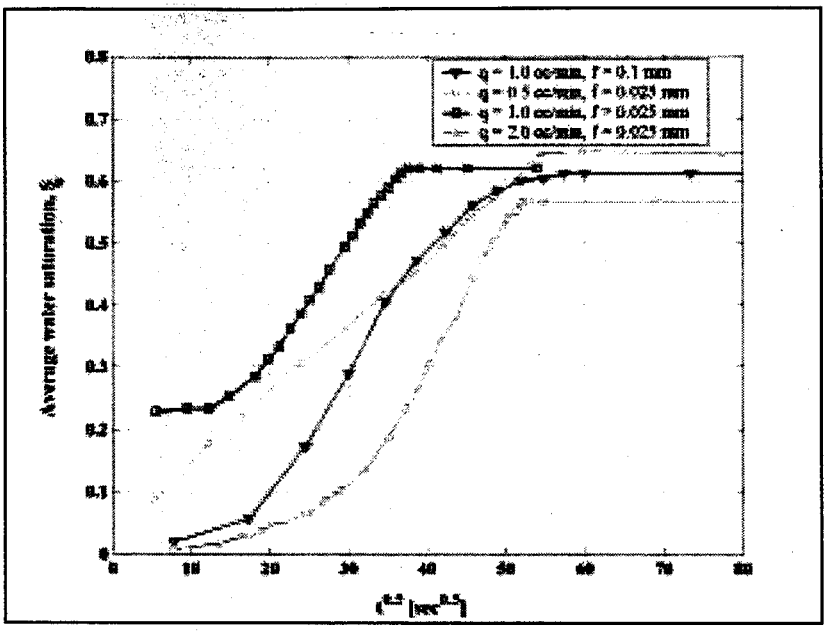

Figure 3. Average Water Saturation versus Square Root of Time.

Semi-Analytical Model

Experimental results have shown that the "filling-fracture" regime has a linear relationship with time, whereas the "instantly-filled fracture" regime has a linear relationship with the square root of time. In general, we have:

i) A constant rate of imbibition for "filling-fracture" regime, R_{ff}:

$$R_{ff} = \frac{\partial \overline{S}_w}{\partial t} \qquad [=] \quad s^{-1} \qquad t \le t_c \tag{3}$$

ii) A constant rate of imbibition for "instantly-filled fracture" regime, R_{if}:

$$R_{if} = \frac{\partial \overline{S_w}}{\partial \tau} \qquad [=] \quad s^{-0.5} \qquad t > t_c \tag{4}$$

where τ is equal to square root of time $t^{0.5}$, and t_c is the critical time at which there is a change of regime. Thus for both regimes and accounting for initial water saturation, S_{wi}, the equation for average water saturation in the matrix block is:

$$\overline{S_w} = t\, R_{ff}\,[1 - H(t - t_c)] + \left[t_c\, R_{ff} + (t - t_c)^{0.5}\, R_{if}\right] H(t - t_c) + \overline{S_{wi}} \tag{5}$$

where H is the Heaviside function; and t_c is the characteristic time for the fracture.

The characteristic time, t_c, is the boundary between both regimes. The fracture fills instantly with respect to the matrix if $t_D = t/t_c$ is much greater than 1 ($t_D >> 1$).

Rangel-German and Kovscek (2000) established the basis to obtain the values of R_{ff} and R_{if}, experimentally. They found expressions for the horizontal and vertical advance as a function of time, i.e.

functions $x_D = x_D(t^{1/2})$ and $y_D = y_D(t^{1/2})$. Based on empirical relations, they tried to describe the imbibition process by a diffusion-like equation with the frontal-advance analyzed experimentally. A linear superposition of 1-D solutions normal to the fracture face of the diffusion equation was applied:

$$\overline{S_w}(Y,t) = erfc\left(\frac{Y}{2\sqrt{\alpha t}}\right) \tag{6}$$

where S_w is the water saturation, Y is the vertical position of the saturation S_w at a given time, in meters; t is the time in seconds, and α is the hydraulic diffusivity in m^2/sec.

Figure 4 shows the average water iso-saturation curves for different times obtained from Eq. 6. The difference between the areas under the curves is directly proportional to mass of water imbibed in the elapsed time between t_1 and t_2. From experimental results, we know that the rate of the mass imbibed is linear with time for the filling-fracture" regime. Thus, the value of the rate of imbibition for the "filling-fracture" regime, R_{ff}, can be calculated as:

$$R_{ff} = \frac{\partial \overline{S_w}}{\partial t} = \lim_{\Delta t \to 0} \frac{\phi}{A_T} \frac{\iint S_w(X,Y,t_2)dx_D dy_D - \iint S_w(X,Y,t_1)dx_D dy_D}{\Delta t} \qquad t \le t_c \tag{7}$$

R_{ff} is a constant for a given constant injection rate, constant fracture aperture, and constant system fluids. The rate of imbibition for the "instantly-filled fracture" regime, R_{if}, is a constant whose value is directly proportional to the imbibition potential, $P_c k S_w$. (Akin et al, 2000). Eq. 7 can also describe R_{if}.

Discussion

Capillary, viscous and gravity forces interact to define the pattern and regime of flow, as well as the fluid distribution. An accurate evaluation of these terms will lead us to obtain a more realistic representation of flow in fractured systems.

The ratio of viscous to capillary forces, which controls the matrix-fracture transfer, is called the capillary number:

$$N_{Ca} = \frac{v\mu}{\gamma} \tag{8}$$

where v is the interstitial velocity, μ is the fluid viscosity, and γ is the interfacial tension between the fluids in the pore space. Similarly, the ratio of buoyancy to capillary forces, which sets the equilibrium distribution of wetting and non-wetting phase, is called the Bond number:

$$Bo = \frac{g\Delta\rho k}{\gamma} \tag{9}$$

where g is the gravitational acceleration, and $\Delta\rho$ is the difference in density between the fluids.

Either in the fracture or in the matrix, these forces will cause a fluid to move. For a given fluid system, structure of the porous medium and geometry, expressions for the rate of imbibition for both regimes can be written in terms of these ratios, which in turn can be written as functions of injection rate and fracture geometry, which are measurable.

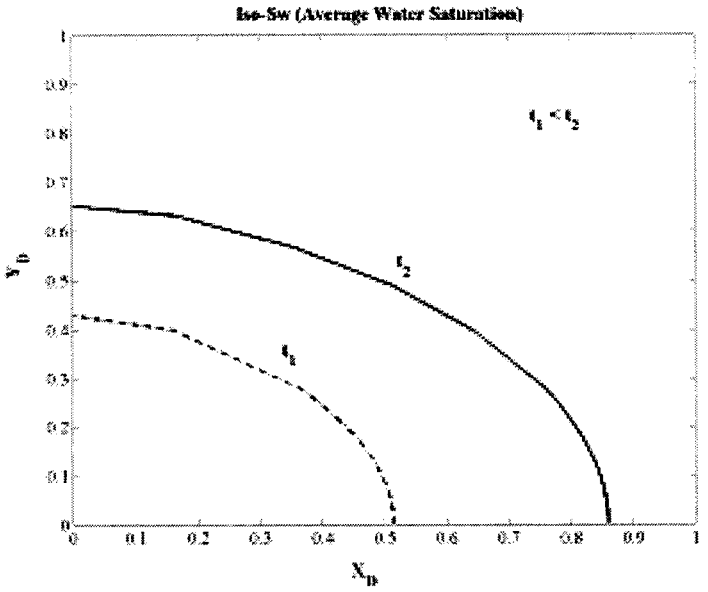

Figure 4. Average Water Saturation for two different times.

If the linear superposition of 1-D solutions normal to the fracture face to describe imbibition is valid, then we can express the ratio of convective to diffusive forces, called Peclet number, as:

$$Pe = \frac{vL}{\alpha_c} \tag{10}$$

where α_c is the capillary diffusivity whose equation is:

$$\alpha_c = \frac{kk_r}{\mu_w}\frac{\partial P_c}{\partial S_w} \tag{11}$$

where k_r is the matrix relative permeability, and P_c is the matrix capillary pressure.

Conclusions

The results of the combined experimental and analytical study show:

1. The apparatus used for this study allows the measurement of flow rates, porosity, and saturation distribution. We can study the progress and saturation pattern of imbibition, as well as the progress of the water flow in the fracture.

2. Phase distribution in the matrix and inside the fracture can be determined by means of a (CT) Scanner.

3. CT Imaging of the imbibition process permits observation of the advance of the water front into the cores and explains the observed trends in water saturation as a function of time.

4. A semi-analytical model to describe the imbibition process in single matrix blocks in the entire early-time period has been proposed.

5. The basis for this new approach is twofold: material balance and empirical correlations.

6. Viscous and buoyancy forces set the equilibrium distribution of phases.

7. Viscous and capillary forces dominate the interaction between matrix and fracture.

References

1. Akin, S., Schembre, J.M., Bhat, S.K., and Kovscek, A.R.: "Spontaneous Imbibition Characteristics of Diatomite," Journal of Petroleum Science and Engineering, to appear 2000.

2. Cil, M. and Reis, J.C.: "A Multi-Dimensional, Analytical Model for Counter-Current Water Imbibition into Gas-Saturated Matrix Blocks," J.Pet. Sci & Eng., **16** (1996) 61-69.

3. Cil, M., Reis, J.C., Miller, M.A., and Misra, D.: "An Examination of Countercurrent Capillary Imbibition Recovery from Single Matrix Blocks and Recovery Predictions by Analytical Matrix/Fracture Transfer Functions," paper presented at the SPE Ann. Tech. Conf. And Exhibition, New Orleans (September 27-30, 1998).

4. Handy, L.: "Determination of Effective Capillary Pressure for Porous Media from Imbibition Data." Pet. Trans. AIME **219** (1960) 75-80.

5. Hughes, R.G.: "CT Measurements of Two-Phase Flow in Fractured Porous Media," MS Report, Stanford University, Stanford, CA, 1995.

6. Kazemi, H., Gilman, J.R., and El-Sharkaway, A.M.: "Analytical and Numerical Solution of Oil Recovery from Fractured Reservoirs Using Empirical Transfer Functions." SPE19849, paper presented at the SPE 64th Ann. Tech. Conf. And Exhibition, San Antonio, (October 8-11, 1989).

7. Mattax, C., and Kyte, J.R.: "Imbibition Oil Recovery from Fractured Water-Drive Reservoirs." Soc. Pet. Eng. J. **2** (1962) 177-184.

8. Rangel-German, E.: " Experimental and Theoretical Investigation of Multiphase Flow in Fractured Porous Media," MS report, Stanford University, Stanford, CA, 1998.

9. Rangel-German, E., Akin, S., and Castanier, L.: "Multiphase-Flow Properties of Fractured Porous Media," paper presented at the SPE Western Regional Meeting, Anchorage, (May 26-28, 1999).

10. Rangel-German, E. and Kovscek, A.: "Matrix-Fracture Interaction in Single Matrix Blocks," paper presented at Twenty-fifth Workshop on Geothermal Reservoir Engineering, Stanford University, Stanford (January 24-26, 2000).

11. Reis, J.C. and Cil, M.: "A Model for Oil Expulsion by Counter-Current Water Imbibition in Rocks: One-Dimensional Geometry," J. Pet. Sci & Eng., **10** (1993) 97-107.

12. Reis, J. and Cil, M.: "Analytical Models for Capillary Imbibition: One-Dimensional Matrix Blocks." In Situ, **23(3)** (1999) 243-270.

13. Reis, J.C. and Haq, S.A.: "Water Advance in a Single Fracture in the Presence of Capillary Imbibition into Adjacent Matrix Blocks." In Situ, **23(3)** (1999) 271-295.

Determination of Relative Permeability from Spontaneous Imbibition Experiments

Josephina M. Schembre

1. Introduction

Simulation of multiphase flow in porous media requires knowledge of relative permeability functions. These functions are necessary to make estimates of productivity, injectivity, and ultimate recovery from oil reservoirs for evaluation and planning of production operations (Honarpour and Mahmood, 1986). Therefore, measurements of relative permeability in the laboratory and/or empirical and theoretical models are an important subject in reservoir modeling.

The laboratory methods used to calculate relative permeability functions are mainly grouped into centrifuge, steady- and unsteady-state techniques. The centrifuge model has been improved, however, concerns regarding the replacement of viscous forces with a range of centrifugal forces still remain for unsteady state displacement processes that are rate dependent (Ali, 1997). Steady state methods offer disadvantages, especially in the case of low permeability rocks, in which it is laborious to reach multiple steady states and, capillary forces and capillary end effects are significant (Firoozabadi and Aziz, 1988; Kamath *et al.*, 1993). Steady state techniques have been improved in order to make corrections for capillary effects (Virnosvky *et al.*, 1995) but they still require successive measurements for different total flow rates. Capillary pressure has a significant effect on saturation distribution and recovery, and capillary forces dominate multiphase flow in low-permeability rocks and fractured reservoirs. In developing unsteady state methods for low-permeability systems, it is necessary to account for capillary pressure when obtaining the relative permeability curve. Thus, most unconventional unsteady techniques do not apply.

Finally, we have also the methods that measure relative permeability by history matching observable parameters such as fluid production, pressure drop and saturation profile history. In such methods, a determined flow description model is required. These methods assume that the relative permeability and capillary pressure curves behave according to a pre-determined function. The limitation imposed on the description of the actual shape of the relative permeability curve causes a bias error and a variance error (Wu, 1977). When the number of parameters in the functional representation increases, the bias error tends to decrease. However, since more parameters are estimated on the basis of the same amount of information, the variance error tends to increases.

In the method we propose each relative permeability value at a particular saturation is treated independently. Fitting to a pre-determined functional shape is not necessary. We present a method for computing two-phase relative permeability curves from experimental in-situ, saturation profiles obtained from spontaneous imbibition experiments. The method consists of two stages:

a. In the first stage, the saturation profile history from a single experiment, in combination with a previously measured capillary pressure, is used for a direct computation of the relative permeability for both phases. The saturation history is collected using a CT imbibition cell where the entire length of the core is scanned along the direction of the flow, a single scan provides the position of saturation at a specific time. Figure 1 shows the outline of the experimental cell. Further information about the experimental equipment and procedure is found in Akin's paper (Akin *et al.*, 2000).

b. The second part of this method is a verification stage, where the relative permeability curve obtained is input for numerical simulation, and a match of the saturation profile is checked.

With this work, we do not only attempt to measure an important petrophysical property of the rock, but to expand our understanding of the mechanisms of spontaneous imbibition.

2. Methodology

The mathematical model used for interpretation of imbibition data is based on the standard one-dimensional flow equation for two inmiscible phases in porous media. We neglect the effect of gravity. For the wetting-phase, we have

$$u_w = -\frac{kk_{rw}}{\mu_w}\frac{\partial p_w}{\partial x} \tag{1}$$

In Eq. (1), u_w is the flow velocity, k is the absolute permeability, k_{rw} is the relative permeability, μ_w is the dynamic viscosity, and $\frac{\partial p_w}{\partial x}$ is the wetting phase pressure gradient.

Substituting $u_w = \phi v_w = \phi S_w \left.\frac{dx}{dt}\right|_{S_w}$ in Eq. (1) results in

$$\phi S_w \left.\frac{dx}{dt}\right|_{S_w} = \frac{kk_{rw}}{\mu_w}\frac{\partial p_w}{\partial x} \tag{2}$$

where, $\left.\frac{dx}{dt}\right|_{S_w}$ is the velocity of saturation S_w and it is a function of time.

Integrating with respect to time, we can express the relative permeability of each saturation S_w as,

$$k_{rw} = \frac{x|_{S_w} S_w}{\int_0^t \left(\frac{\partial p_w}{\partial x}\right)_{S_w}} \frac{\mu_w \phi}{k} \tag{3}$$

In this function, the porosity, viscosity and, permeability are known and are constant. Once the pressure gradient history is known, we obtain the relative permeability. The first part of Eq. (3), $\frac{x|_{S_w} S_w}{\int_0^t \left(\frac{\partial p_w}{\partial x}\right)_{S_w}}$ is, in fact, a constant for a particular Sw. As a result, the objective function is exclusively a function of water saturation. The methodology to determine the relative permeability from the water saturation profile is summarized in the following steps:

1. Experimental positions of each saturation are obtained for different times from spontaneous imbibition experiments. Saturation history is obtained by using the technique of subtraction of images described by Garg *et al.* (1996).

2. Sorting and smoothing of saturation data.

3. Find the position of a particular saturation as a function of time from the experimental data. Data provide the saturation as a function of time and specific positions in the core. We transform this data so that the position is given as a function of saturation value and time.

4. Calculate the relative permeability for each saturation. The integral term in Eq. (3) is evaluated with the trapezoidal method.

5. Simulate the imbibition process numerically and compare the CT derived saturation profile histories with numerically estimated profiles.

3. Numerical Simulator and Model Input

Two numerical simulators were used to model spontaneous imbibition experiments, ECLIPSE 100 and M2NOTS. ECLIPSE 100 is a black-oil developed by Geoquest, Schlumberger. M2NOTS is a simulator program that uses the "integral finite difference" method (Adenekan *et al.*, 1993). It was developed for simulating the coupled transport of water, vapor, air and heat in porous media The advantage of this simulator lies on the fact that the relative permeability and capillary pressure data is input as an equation, which makes the computation of the derivatives in Eq. (3) easier.

4. Validation: Synthetic Cases

The objective of this exercise was to test and validate the method. The relative permeability and petrophysical properties are input to the simulator, saturation histories are created and analyzed, and relative permeability computed from the simulated data. The relative permeability curves obtained are compared with the input curve. Water-air and water-oil spontaneous imbibition cases were considered. The rock properties used in the three cases were descriptive of diatomite. Characteristics of the porous medium and fluid properties are shown in Table 1. Further description of the models and results obtained for each case follows.

4.1 Water-Air

For the water-air case, the contribution of the pressure gradient of the non-wetting phase is not significant to the determination of k_{rw}. Air is inviscid. Consequently, we simplify the pressure gradient in Eq. (3) with

$$\frac{\partial p_w}{\partial x} = \frac{\partial p_{air}}{\partial x} - \frac{\partial p_c}{\partial x} \approx -\frac{\partial p_c}{\partial x} \tag{4}$$

We use M2NOTS for 1002 cells (elements) in testing the water-air case. The fine grid and small time steps limit numerical error. The relative permeabilities for water and gas phases follow the power model function of Fatt and Klikoff (1959) with power-law coefficient of 3. The capillary pressure curve is given by the Leverett function (1941):

$$p_c = p_o \sigma(T) f \tag{5}$$

where, p_o is a constant $\left(\cos\theta \left(\frac{k}{\phi} \right)^{1/2} \right)$, $\sigma(T)$ is the surface tension for water as a function of temperature, and

$$f = 4.013 - 13.68 S_w^* + 21.313 (S_w^*)^2 - 11.548 (S_w^*)^3 \tag{6}$$

The reduced saturation is given as

$$S_w^* = \frac{S_w - S_{wc}}{1 - S_w} \tag{7}$$

A plot of the capillary pressure given by this function and used in the simulation is shown in Figure 2. As these are synthetic cases, we are not concerned that the capillary pressure curve describes drainage. It is assumed that there is no initial water saturation and no residual gas saturation ($S_{wi}=S_{nwr}=0$). comparison of the theoretical water relative permeability with the curve obtained from applying Eq. (3) to the synthetic data is shown in Figure 3. The curves shown are for the case where the gas pressure gradient is neglected and the case where it is included in the calculations. The semi-logarithmic scale is used to accentuate any differences. Both curves follow the theoretical curve with an error of approximately 12 per cent. The largest error is attributed to the computation of the numerical integral. A second cause of error is due to uncertainty in locating the position of a particular saturation as a function of time. Neglecting the pressure gradient of the air leads to insignificant errors.

The non-wetting phase pressure is known from the simulation. Although the non- wetting-phase gradient is neglected when finding the wetting-phase relative permeability, the method can yield the non-wetting phase relative permeability as well. In this case, Eq. (3) is modified to fit the model for the non-wetting phase,

$$k_{rnw} = \frac{\mu_{nw}\phi S_{nw}}{k}\left(\frac{x\big|_{S_{nw}}}{\int_0^t \frac{\partial p_{nw}}{\partial x}\Big|_{S_{nw}}}\right) \tag{8}$$

and,

$$x\big|_{S_{nw}=1-S_w} = x\big|_{S_w} \tag{9}$$

Figure 4 shows the plot of the input and calculated relative permeability curves for the non-wetting phase. To test the calculated curves, simulations were conducted with the new data. Figure 5 compares the input saturation history and that obtained using the computed relative permeability curves. The larger values of k_{rw} at low water saturation affect slightly the leading edge of the saturation fronts at later times. Otherwise, the saturation history is matched exactly.

4.2 Water-Oil

For the water-oil case we use ECLIPSE. We include the non-wetting pressure gradient in Eq. (3).

Figure 6 shows the result obtained for the water relative permeability. Relative permeability is also computed and shown for the case where we chose to neglect the oil pressure. The relative permeability obtained when we neglect the oil-phase pressure gradient agrees with the input curve with the exception of water saturation values greater than 0.7. At high water saturations, the gradients in p_c and p_o are roughly equal. The water relative permeability obtained when we include the oil-phase pressure gradient in the calculations matches the input data somewhat better. The nonwetting phase is not specially viscous allowing the close match with or without incorporating $\frac{\partial p_o}{\partial x}$.

The oil relative permeability computed from Eq. (8) is compared to the input curve in Figure 7. The inaccuracy is larger in this case than in the water-air case, especially at large water saturations. The relative permeability values for the highest S_w values no longer follow the same trend as in the input curve. A close look at the computational output revealed spurious data reported by the simulator for the oil-phase pressure gradient at early times. Initial time-step size is set to the minimum value allowed by the simulator. We make no attempt to eliminate this simulation artifact. This numerical error affects the integral term in Eqs. (3) and (8).

The input water saturation history and that obtained using the computed relative permeability curves are compared in Figure 8. Similar to the water-air case, the larger values of k_{rw} at low water saturation affect slightly the leading edge of the saturation fronts at later times. The combination of the capillary pressure and relative permeability curves of the largest water saturations will affect the overall speed and shape of the imbibition front.

5. Experimental Cases

The next step is the application of the method to experimental data. We use water saturation profiles measured by X-ray CT during spontaneous imbibition experiments in Berea sandstone and diatomite. Only water-air systems are studied in this section.

5.1 Berea Sandstone

One of the advantages of working with Berea sandstone is that relative permeability curves have been reported in the past. We can compare the results with values reported in the literature. Table 2 summarizes the characteristics of the core. Further characteristics and the experimental method used to obtain the water saturation profiles are described in Akin and Kovscek (1999).

The original capillary pressure used is given by Sinnokrot *et al.*, 1969); it was modified for different fluid system and petrophysical properties by using the Leverett J-function (Ma *et al.*, 1991) and, upscaled to non-initial water saturation and a residual gas saturation of S_{gr}= 0.2. The capillary pressure used in this case is shown in Figure 9. The relative permeability curve obtained is compared to data provided from Lerdahl *et al.* (2000) and Oak *et al.* (1988) in Figure 10. The values of the curve obtained are larger than the reference curves. This could be due to the fact that the capillary pressure shows low values for the derivative with respect to water saturation, especially at low water saturations.

A comparison of the CT-determined experimental water saturation profiles and the profiles obtained by simulating the core with the measured relative permeability is shown in Figure 11. The results match well. The pressure gradient within the core was not measured in the experiments. It is not possible to find the non-wetting phase relative permeability.

5.2 Diatomite

There is very little known about petrophysical properties in Diatomite. The use of the classical unsteady state method in the determination of relative permeability for diatomite could lead to inaccurate results. Table 3 summarizes the characteristics of the diatomite core used in the experiments. The same experimental method as in the case of the Berea sandstone was used to obtain the water saturation profiles (Akin and Kovscek, 1999).

For this case, we used a imbibition capillary pressure curve measured with the porous-plate method reported by Akin and Kovscek (1999). It is similar to another curve reported by Kumar and Beatty (1995). The capillary pressure used in the method is shown in Figure 12.

The relative permeability curve obtained is shown in Figure 13. At high water saturation, the relative permeability is found to decrease as Sw increases. The reason for this is shown in Figure 14. Here, the experimental water saturation profile and the profile obtained by simulating the imbibition process are compared. High water saturations within the experiments advance slowly at earlier time. Therefore, retardation exists for saturation greater than 0.7. The solid line gives the relative permeability curve used for simulation. The exponential model in Eq. (10) was used to fit the points

$$k_{rw}(S_w) = 5E^{-5}\exp(8.3355\,S_w) \tag{10}$$

The results seem to match the saturation-history data reasonably well, Figure 14.

Extension of the Method: Forced Imbibition

Thus far, we have assumed spontaneous imbibition in the analysis of the water saturation profile. One of the main concerns when analyzing the water saturation profiles is the maintenance of water supply such that the experimental results represent purely spontaneous imbibition behavior. In this section, we present the numerical solution for the case of slight forced imbibition.

For the case of forced imbibition, we recall that the psi-potential for any fluid is defined as Dake (1978).

$$\Psi = p + \rho g h \tag{11}$$

Assuming that the water level is constant, the water pressure gradient can be approximated by

$$\frac{dp_w}{dx} = \frac{dp_c}{dx} + \frac{\rho g h}{x\big|_{S_w,t}} \tag{12}$$

Where, $x|_{Sw,t}$ is the position of a particular water saturation at a given time, and h the level of the water column measured from the reference point, which is the water-core contact.

Substituting Eq. (12) in Eq. (3) and making the same assumptions, we express relative permeability at any given water saturation and time as

$$k_{rw} = \frac{x\big|_{S_w}\, S_w}{\int_0^t \left(\frac{\partial p_c}{\partial S_w}\frac{\partial S_w}{\partial x} + \frac{\rho g h}{x} \right)_{S_w}} \frac{\mu_w \phi}{k} \tag{13}$$

Equation (13) shows that neglecting the height of the water column in the method leads to larger values in the relative permeability curve. The size of this error depends on the magnitude of the water column compared to the derivative of capillary pressure. In general, the derivative of the capillary pressure is more sensitive to these effects for high water saturation values. This result is very valuable because it extends the application of this method to data collected during forced imbibition experiments.

6. Conclusions

A method has been developed to determine dynamic relative permeability from the water saturation history obtained from spontaneous imbibition experiments. The method was tested using synthetic data for the water-air case. The results were very good, suggesting that this method is very reliable for these systems and that the air pressure gradient can be neglected in the calculations for water relative permeability. The method was tested in the same manner with synthetic data for the water-oil case. A sensitivity study showed that neglecting the oil-phase pressure gradient could lead to error in the high water saturation values for viscous oils. Numerical inaccuracies introduced by the reservoir simulator at early times for the synthetic data did not allow an exact match of the relative permeability end points. This effect is emphasized in the water-oil case. It was also observed for the experimental water-air cases. The method was used to determine the water relative permeability for two experimental cases with Berea sandstone and diatomite. In both cases, the relative permeability curves obtained were used in simulation to verify accuracy. The measured curve reproduced the experimental behavior. In addition, it was shown that this method could be adapted for forced imbibition experiments. This method reduces the required time to conduct measurements and analysis of data.

References

1. Adenekan, A.E, T.W. Patzek and K. Pruess: "Modeling of Multiphase Transport of Multicomponent Organic Contaminants and Heat in the Subsurface: Numerical Model Formulation," Water Resources Research, Vol. 29, No. 11 (November 1993) 3727-3740.

2. Akin, S and A.R. Kovscek: "Imbibition studies of Low-Permeability Porous Media," paper SPE 54590, in Proceedings of the Western Regional Meeting, Anchorage, Alaska (May 26-29, 1999).

3. Akin, S., J.M. Schembre, S. K. Bhat and A.R. Kovscek: "Spontaneous Imbibition Characteristics of Diatomite," Journal of Petroleum Science and Engineering 25 (2000) 149-165.

4. Ali, J. K.: "Development in Measurement and Interpretation techniques in Coreflood Tests to Determine Relative Permeabilities," SPE 39016. Proceedings of the fifth Latin American and Caribbean Petroleum Engineering Conference and Exhibition, Rio de Janeiro, Brazil (August 30 - September 3, 1997).

5. Dake, L. P.: "Fundamentals of Reservoir Engineering", Elsevier, 1978. pp 114-116.

6. Fatt, I. and Klikoff, W. A.: "Effects of Fractional Wettability on Multiphase Flow Through Porous Media," AIME Transactions, Vol. 216, p. 246, 1959.

7. Firoozabadi, A. and K. Aziz: " Relative Permeabilities from Centrifuge Data," SPE 15059, in Proceedings of the 56th California Regional Meeting of the society of Petroleum Engineers, Oakland, (April 2-4, 1988).

8. Garg, A., A.R. Kovscek, M. Nikravesh, L.M. Castanier and T.W. Patzek: "CT Scan and Neural Network Tecnology for Construction of Detailed Distribution of Residual Oil Saturation During Waterflooding," SPE 35737, in Proceedings of the Western Regional Meeting, Anchorage (May 22-24, 1996).

9. Honarpour, M. and S.M. Mahmood: "Relative Permeability Measurements: An Overview", SPE 18565 (1986).

10. Kamath, J., E.F. deZabala and R.E. Boyer: "Water/Oil Relative permeability endpoints of Intermediate- Wet, Low permeability rocks," SPE 26092, in Proceedings of the Western Regional Meeting, Anchorage (May 26-28, 1993).

11. Kumar, M and F.D. Beatty: "Cyclic steaming in Heavy Oil Diatomites," SPE 29623. Proceedings of the Western Regional Meeting, Bakesfield (March 8-10, 1995).

12. Lerdahl, T.R., P. Øren and S. Bakke: "A Predictive Network Model for Three-phase Flow in Porous Media," SPE 59311. in Proceedings of the 2000 SPE/DOE Improved Oil Recovery Symposium, Tulsa (April 3-5, 2000).

13. Leverett, M. C.: "Capillary Behavior in Porous Solids," AIME Trans., Vol. 142 (1941) p.152.

14. Ma S.,M.X. Jiang and N.R. Morrow: "Correlation of Capillary Pressure Relationships and Calculations of Permeability," SPE 22685, in Proceedings of the 66th Annual Technical Conference and Exhibition, Dallas (October 6-9, 1991).

15. Oak, M.J., L.E. Baker and D.C. Thomas: "Three-phase Relative Permeability of Berea Sandstone," SPE 17370. First presented at the 1988, SPE/DOE Enhanced Oil Recovery Symposium held in Tulsa, (April 17-20, 1988).

16. Schembre, J.M.: "Spontaneous Imbibition in Low-Permeability Media", Masters report. Stanford University, California, 1998.

17. Sinnokrot, A. A., H.J. Ramey and S.S. Marsden: "Effect of Temperature Level upon Capillary Pressure Curves," SPE 2517. Proceedings of the SPE 44th Annual Fall meeting, Denver, Colorado (Sept 28-Oct. 1, 1969).

18. Virnosvky, G.A., S. M. Skjaevaland, J. Surdal and P. Ingsøy: "Steady-state relative permeability measurements corrected for capillary effects," SPE 30541 presented at the 1995 SPE Annual Technical Conference & Exhibition, Dallas, 22-25 Oct.

19. Watson, A.T., P.D. Kerig, P.C. Richmond and T.-M. Tao: "An Improved Method for Estimating Relative Permeability From Displacement Experiments," SPE 15064, in proceedings of the 56th California Regional Meeting, Oakland (April 2-4, 1986).

Table 1 : Properties of Rock and Fluids Used in Simulation

Rock properties	Permeability[md]	6.6
	Porosity	0.65
	Length[cm]	8.8
	Compressibility[1/atm]	5E-5
Fluids		
Water	Viscosity[cp]	1.0
	Density[g/cm3]	1.0
Air	Viscosity[cp]	0.02
	Density[g/cm3]	0.002
Oil (Decane)	Viscosity[cp]	0.86-0.9
	Density[g/cm3]	0.8

Table 2 : Characteristics of the Berea Sandstone Core

Porosity	0.22
Permeability[md]	780
Diameter[cm]	2.43
Length[cm]	8.8
Pixel resolution	210

Table 3 : Characteristics of the Diatomite Core

Porosity	0.68
Permeability[md]	6.6
Diameter[cm]	2.43
Length[cm]	9.017
Pixel resolution	225

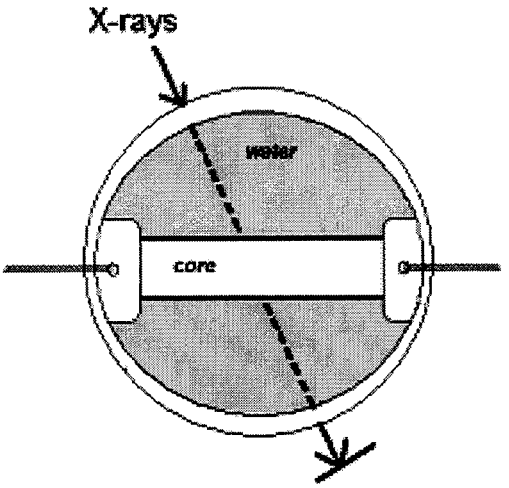

Figure 1: Outline of the imbibition cell

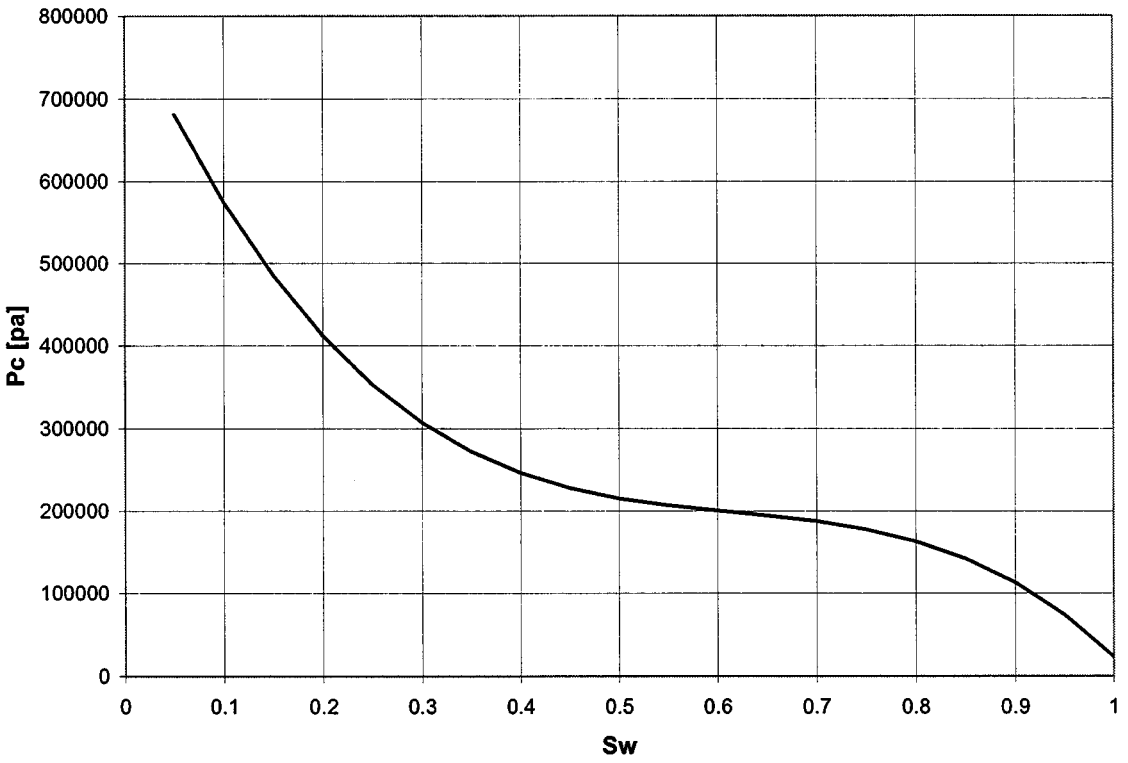

Figure 2 : Capillary pressure used for the synthetic water-air case

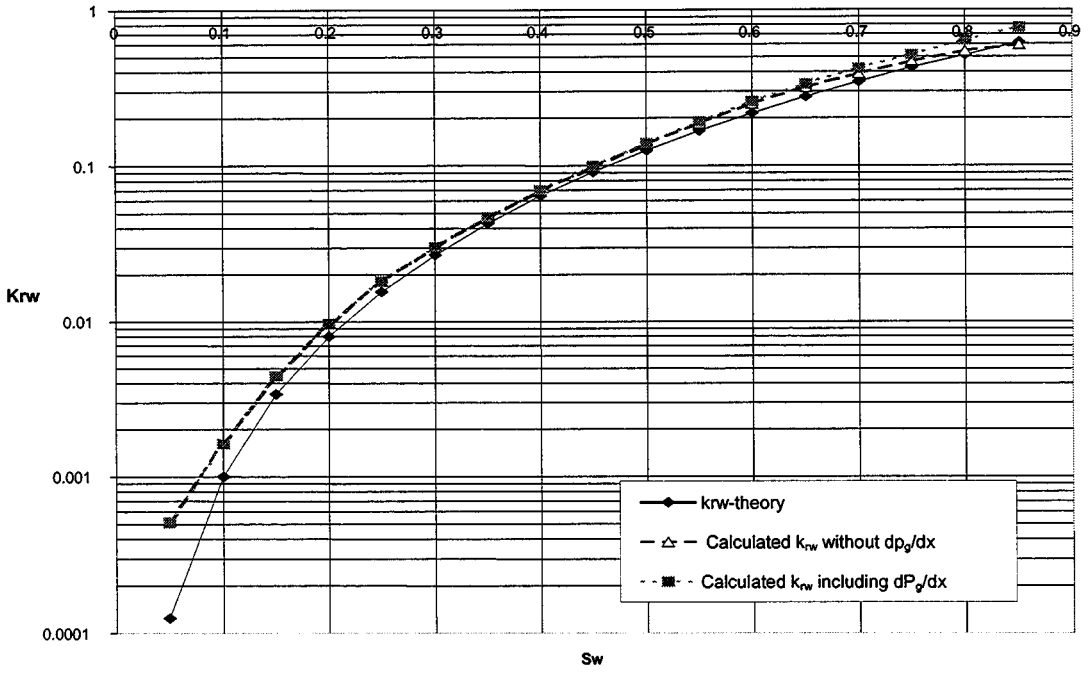

Figure 3 : Input and calculated relative permeability curves for the synthetic water-air case

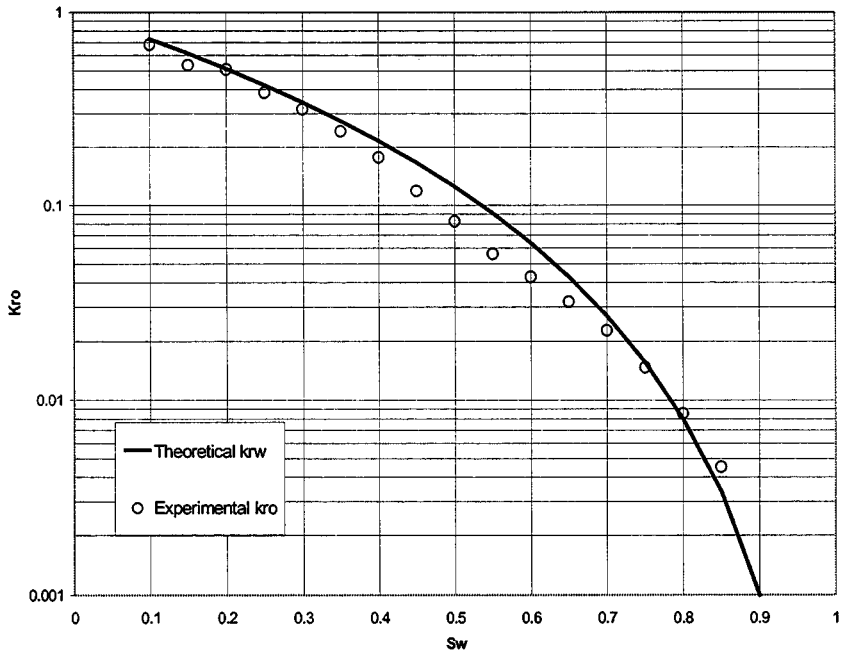

Figure 4: Input and calculated gas relative permeability curves for the synthetic water-air case

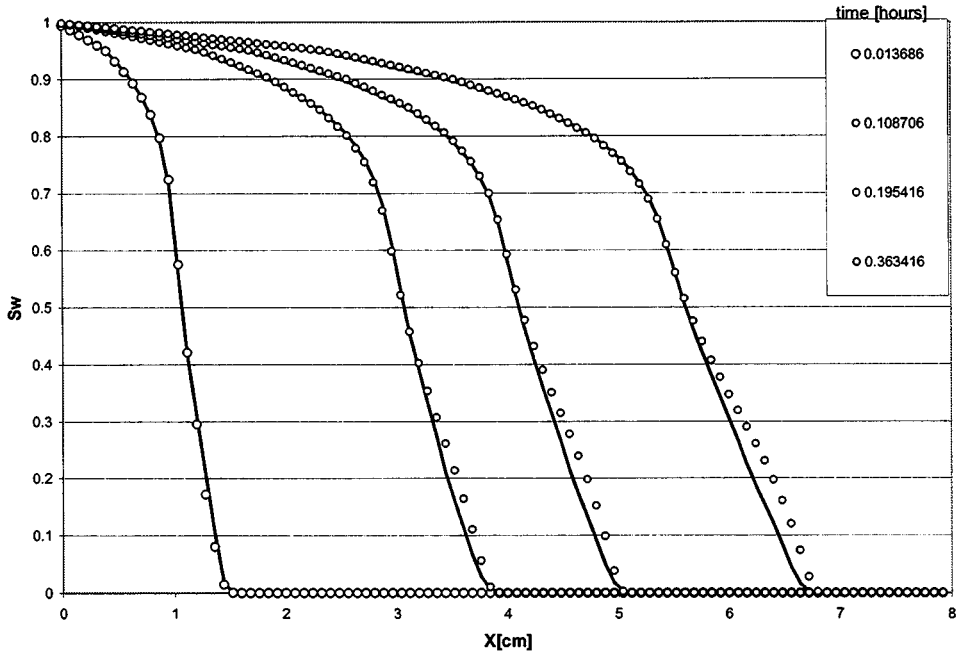

Figure 5: Saturation profiles obtained for original and computed relative permeability curves, solid: computed relative permeability curve

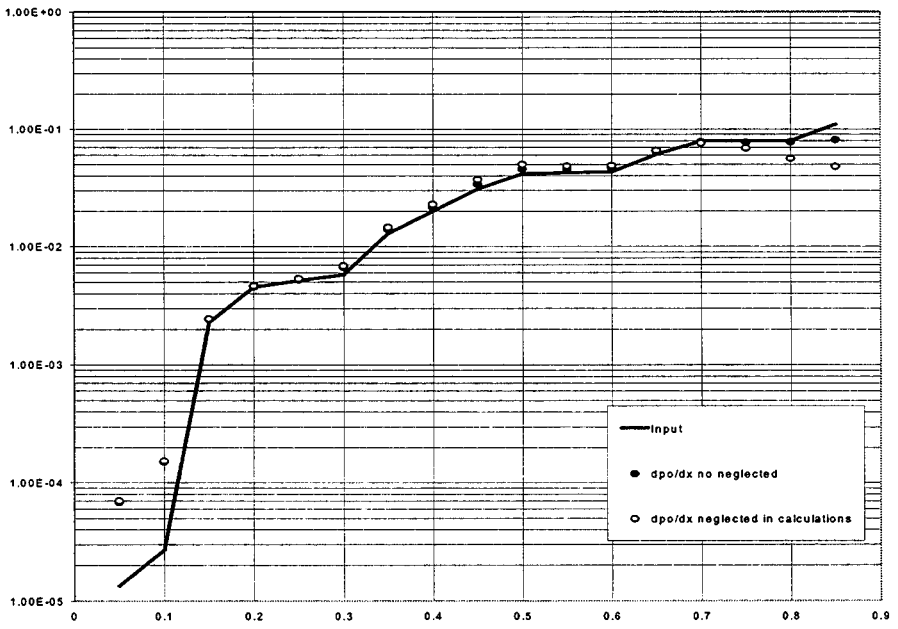

Figure 6: Input and experimental relative permeability curves obtained for the synthetic water-oil case run

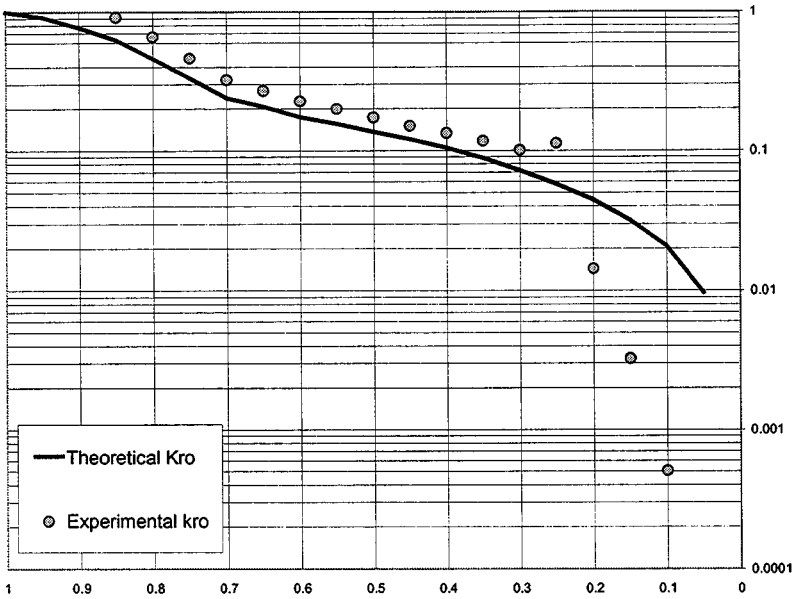

Figure 7: Input and experimental oil relative permeability obtained for the synthetic water-oil case run

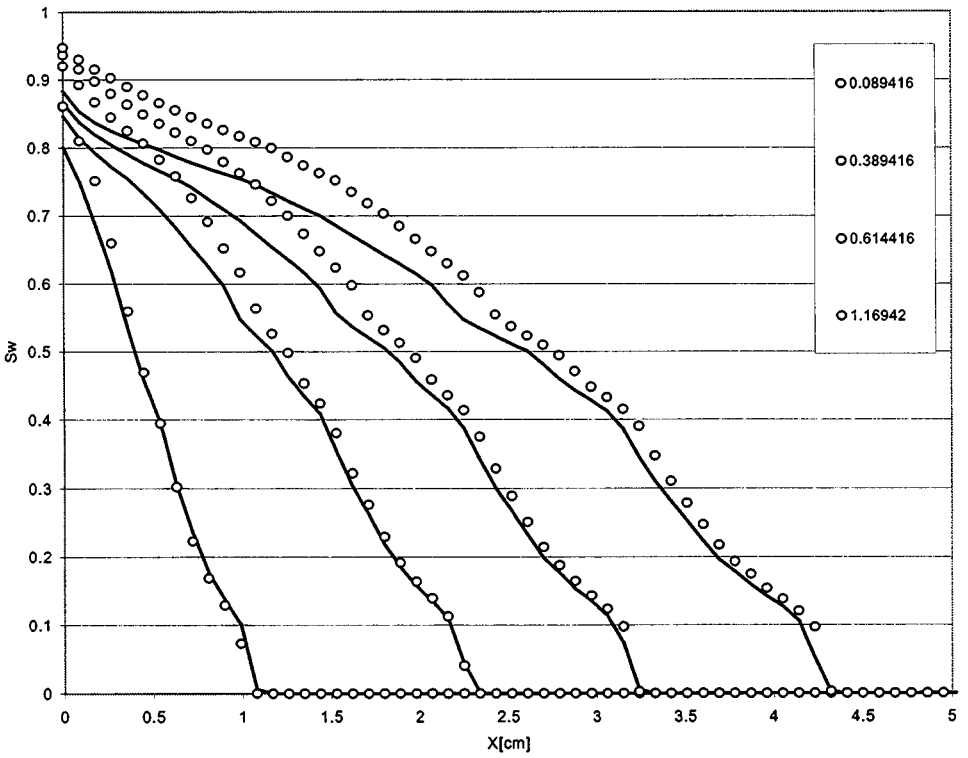

Figure 8: Water saturation profiles obtained for water-oil case using input (solid) and output (symbols) relative permeabilities

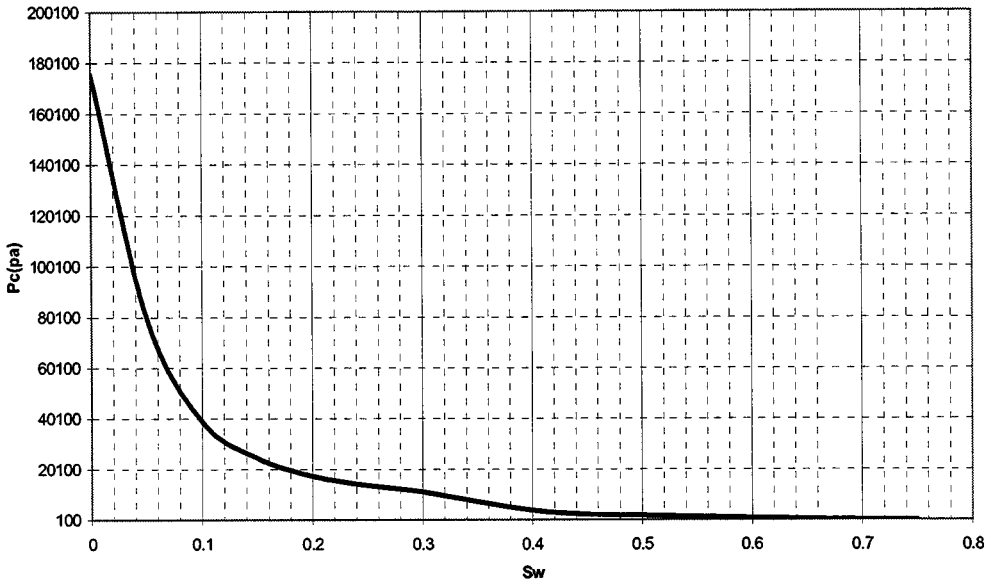

Figure 9: Capillary pressure curve used in Berea Sandstone case

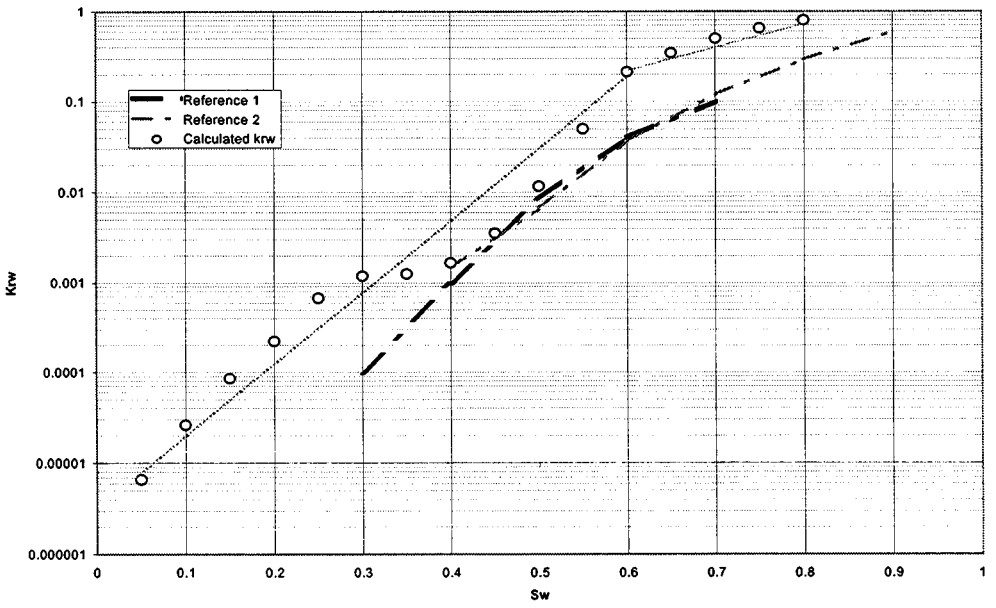

Figure 10: Water relative permeability obtained for the Berea Sandstone case

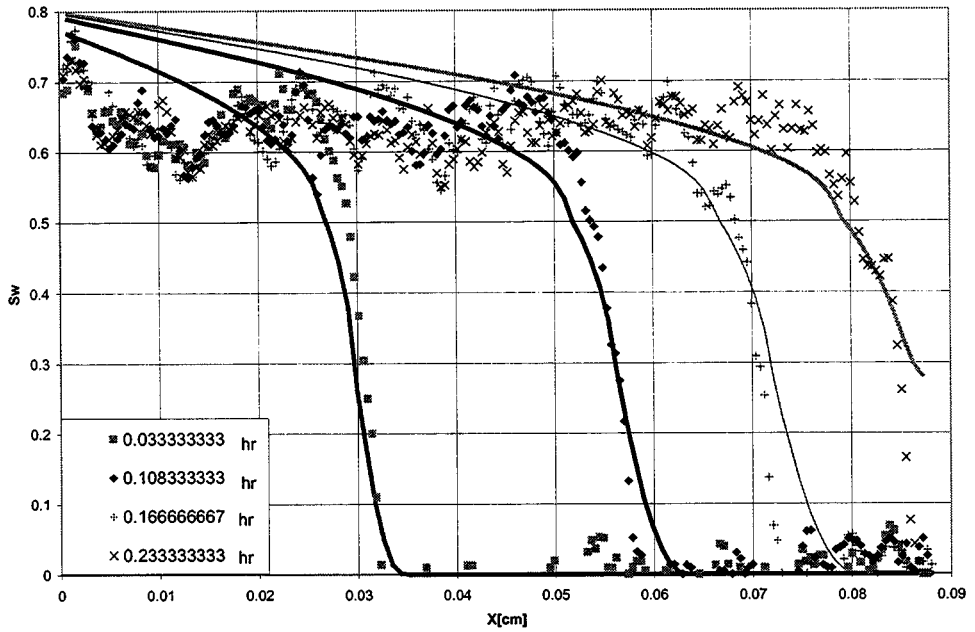

Figure 11: Saturation profile obtained by simulation with measured krw compared to the experimental profile (Berea sandstone)

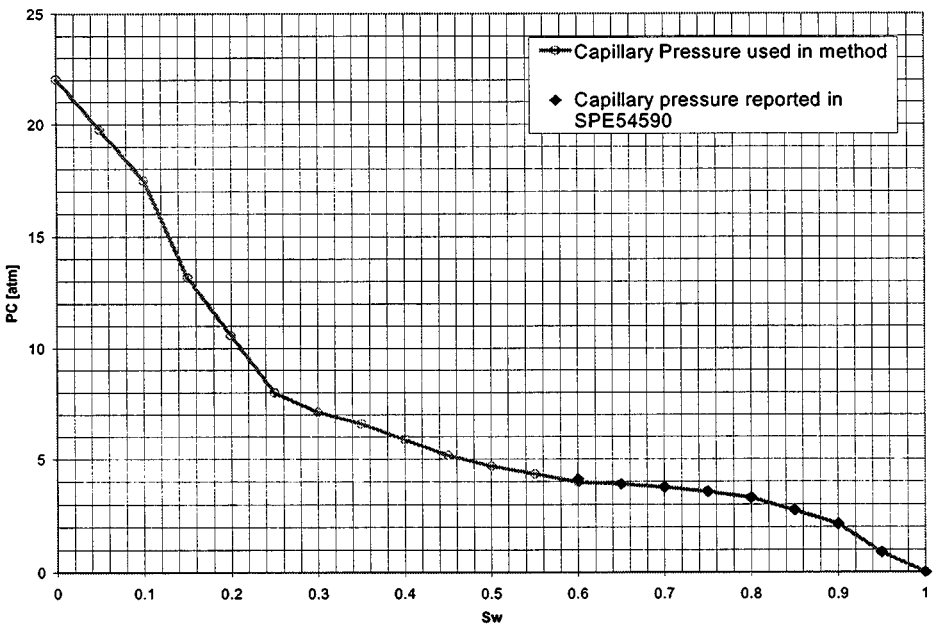

Figure 12: Capillary pressure used in the diatomite case

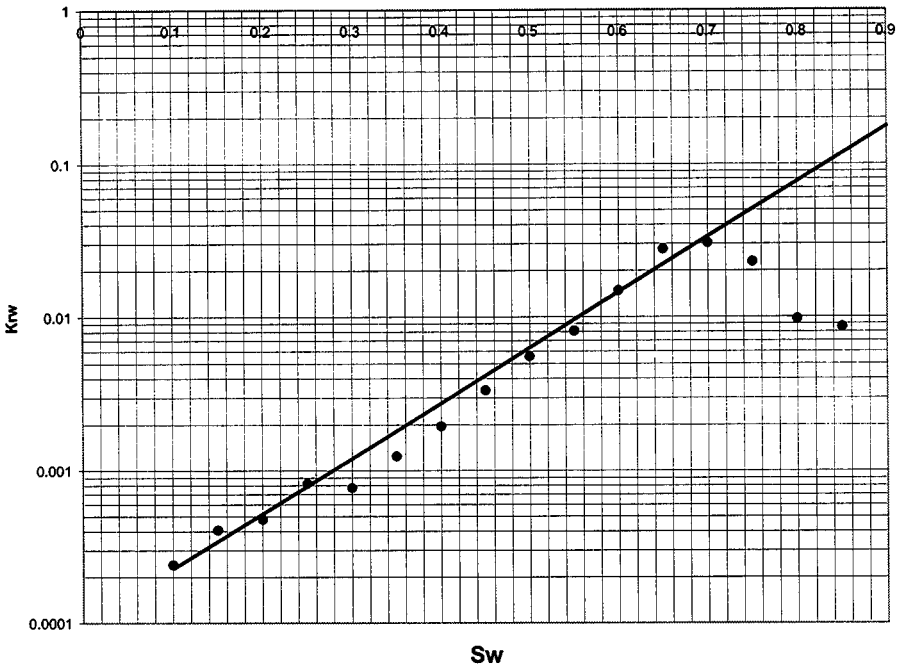

Figure 13: Relative permeability obtained for the diatomite case

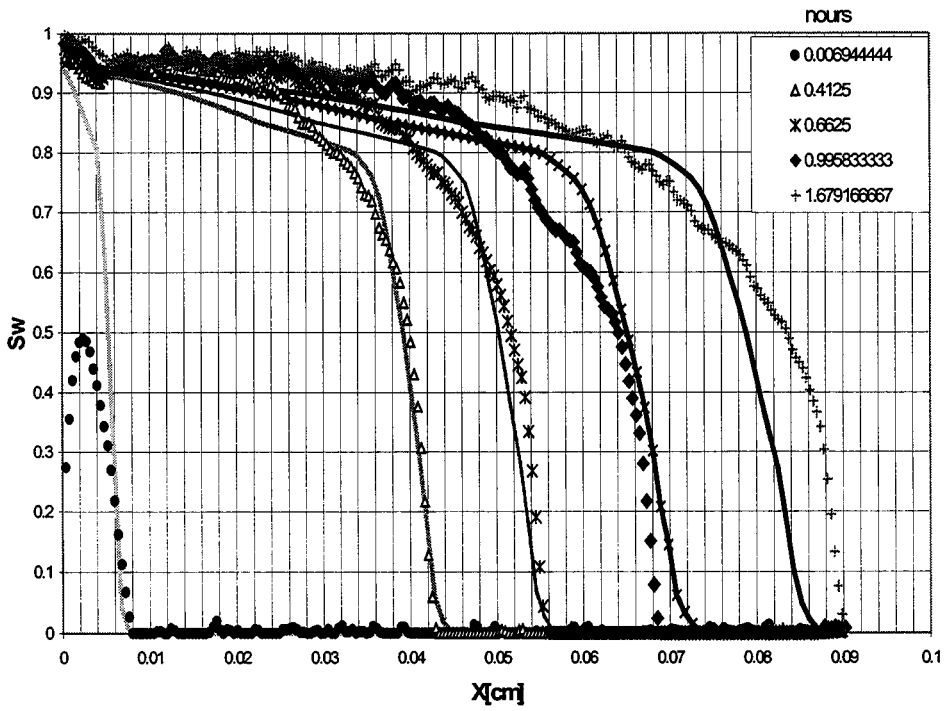

Figure 14: Saturation profile obtained by the method, compared to the experimental profile in diatomites.

Imbibition in Low-Permeability Porous Media

Liping Jia

Abstract

Oil recovery from low permeability reservoirs is strategically important because of the large resources locked in such formations. Imbibition is fundamental to oil recovery from such reservoirs under most secondary and improved recovery processes of practical interest. It is also characteristic of porous medium wettability. The rate and the extent of imbibition depend critically on the viscosity of the wetting and nonwetting phases. In this literature, the work on imaging imbibition in low permeability porous media (diatomite) with X-ray computed tomography has been studied. The viscosity ratio between nonwetting and wetting fluids is varied over several orders of magnitude yielding different levels of imbibition performance. The field cores and crude oil are studied using a novel design cell. A mathematical analysis of counter-current imbibition processes is performed and a modified scaling group incorporating the mobility ratio is developed. This modified group appears to improve scaling accuracy of countercurrent imbibition significantly. The outline for the future work is discussed.

1. Introduction

1.1 Imbibition in Porous Media

Petroleum production has, rightly, focused on the easiest to produce prospects. With more fields approaching maturity and abandonment, recovery options are required for more difficult to produce reservoirs such as low permeability diatomite and chalk formations. For example, estimates place the amount of original oil (OOIP) in the diatomaceous and siliceous shale formations of California at 12 to 18 billion bbl (Ilderton *et al.,* 1996). Although the volumes of oil in place are large, the low permeability creates challenging issues in producing this oil. Injectivity and productivity are generally low, and wells usually require hydraulic fracturing or in-place natural fractures to attain economic rates. Because of the limited injectivity, recovery processes must be designed carefully and natural oil-production forces optimized.

In imbibition, wetting fluid is drawn spontaneously into rock by capillary suction and the non-wetting fluid is expelled. The rate and the extent of imbibition depend critically on the viscosity of the wetting and nonwetting phases. Other factors include: fluid/fluid interfacial tension (IFT), pore structure, the initial water saturation of the rock, and relative permeability curves. Water injection, steam injection, and CO_2 injection in a water-alternating gas (WAG) fashion all rely to some extent on capillary imbibition to aid oil production. Steam injection is, for all practical purposes, carried out under saturated conditions with some fraction of the injected steam in the liquid phase. Likewise, initial heating of a cold reservoir is accompanied by condensation and flow of the resulting hot water away from the injector. In CO_2 injection under both miscible and immiscible conditions, water slugs are usually injected with the aim of controlling CO_2 mobility. Thus, capillary phenomena are important to most recovery techniques of interest in low permeability media.

Imbibition can occur in a reservoir in both counter-current and co-current flow modes, depending on the fracture network and the water injection rates. Hamon and Vidal (1986) presented the results of an experimental and numerical study of homogeneous and heterogeneous samples with different lengths and boundary conditions allowing cocurrent and countercurrent flows. The reliability of a numerical method to scale-up imbibition tests was proved. But, the heterogeneities of the cores should be taken into account. They confirmed that the countercurrent flow experiments were numerically reproduced with the capillary pressure curve generated from the imbibition experiment.

Bourblaux and Kalaydjian (1990) studied co-current and countercurrent imbibition in natural sandstone samples. They reported significantly lower imbibition rates from counter-current experiments as compared to co-current experiments. They suggested that lower counter-current imbibition rates are due to flow patterns and the extra viscous resistance generated when the two phases pass each other. They also observed some difference in final oil recovery from the two processes. Note that Bourblaux and Kalaydjian (1990) use a single mineral oil (Soltrol 130, μ_{nw}=1.5 mPa-s) as the nonwetting phase in their experiments. They did not consider how different oil viscosities might change the imbibition rate and final oil recovery.

Cuiec, Bourbiaux and Kalaydjian (1990) performed experimental studies of imbibition in a low-permeability outcrop chalk. They found that countercurrent mechanism was dominant, with rapid and efficient oil recovery for strongly hydrophilic chalk material. The length and various boundary conditions were investigated. With lower IFT, final recovery increased and the rate of spontaneous imbibition was slower. The imbibition reproducibility was performed with the same sample (dry the sample) and different samples.

1.2 Scale-Up Studies

Rapoport (1955) derived general scaling laws, which account for the effects of gravitational and capillary forces. The correlation between the laboratory and field studies was presented. The scaling laws were applied to incompressible, two-phase flow systems and for the water-oil displacement.

Handy (1960) discussed how to predict imbibition behavior in porous media. The equation for piston-like displacement was derived, from which the conventional scaling group can be developed. The surface wettability was also studied from the imbibition rate.

Mattax and Kyte (1962) proposed the first scaling group for imbibition oil recovery from fractured, water-drive reservoir, based on the work of Rapoport. They also presented satisfactory results with the group for two different core sizes, shapes, and boundary conditions. The identitical water-oil ratio and rock types were used for the experiments. It was the first time that there was experimental evidence to be published to verify the scaling theory for imbibition mechanism.

Empirical scaling models have been proposed to estimate oil recovery rates from blocks that have sizes and shapes different from laboratory core samples (*e.g.*, Morrow *et al.* 1994, Zhang *et al.* 1996, Zhou *et al.* 2000). Kazemi *et al.* (1992) presented numerical and analytical solutions of oil recovery using empirical, exponential transfer functions based on the experimental data given by Aronofsky *et al.* (1958) and Mattax and Kyte (1962). They proposed a shape factor that included the effect of size, shape, and boundary conditions of the matrix. More recently, this shape factor was generalized by Zhang *et al.* (1996) to account for sample shape and boundary conditions more accurately. A dimensionless time, t_D, was proposed that reads

$$t_D = t\sqrt{\frac{k}{\phi}}\frac{\sigma}{\mu_s L_c^2} \tag{1}$$

where k is absolute permeability and σ is interfacial tension. The characteristic length, L_c, is a function of the bulk volume of the rock sample and the area of the block face open to imbibition. The geometric average of phase viscosity, μ_s, is given by the following equation:

$$\mu_S = \sqrt{\mu_w \mu_{nw}} \tag{2}$$

The above scaling equation was used by Zhang et al. (1996) and they report that ultimate oil recovery on a pore volume basis by spontaneous imbibition in Berea sandstone cores is approximately constant for systems with differing lengths, viscosity ratios, and boundary conditions. Zhang et al. (1996)

emphasize that the use of the square root of viscosities in correlation of imbibition is empirical and that air/liquid results did not correlate with those for oil/water systems.

1.3 Importance of the Research

1.3.1 Low Permeability Porous Media

Whereas imbibition has long been recognized as an important recovery mechanism in low permeability reservoirs, most studies were performed on sandstone cores with relatively high permeability (>100 mD) (*e.g.*, Jadhunandan and Morrow 1991, Reis and Cil 1993, Cil and Reis 1996, Garg *et al.*, 1996). Both chalk and diatomite formations have high porosity (35 to 70%) and low permeability (0.1 to 10 mD). Diatomite is a siliceous rock composed mainly of biogenic silica and detrital-rich layers of sand, silt and clay; whereas, chalk is a carbonate. Notable work regarding chalk rock systems includes Cueic *et al.* (1994) who found experimentally that oil recovery by water imbibition is rapid and efficient for strongly water-wetting chalk. Reduction in IFT decreased the rate of imbibition but increased ultimate oil recovery. This effect was attributed to the mobilization of oil ganglia. Milter and Øxnevard (1996) evaluated imbibition recovery of different chalk facies and linked performance to the rock framework and pore system. In regard to diatomite, Akin et al (2000) report the use of a novel X-ray computed tomography (CT) imbibition cell to quantify co-current imbibition rates and saturation profiles as well as to begin linking diatomite imbibition performance to pore structure and roughness. Kamath *et al.* (1995), conducted long-term forced displacements on diatomaceous mudstone samples revealing that water-oil relative permeability end points could be sensitive to flooding velocity. Relative permeability to water increased by as much as 31%with increased flow rate.

Low permeability rocks, such as diatomite, are relatively unstudied in the laboratory because of low injectivity and a host of other difficulties in designing and performing laboratory tests on such samples. The low rates and long turn over time are major contributors to measurement uncertainties. For example, we observed substantial differences in residual oil saturation in diatomite between counter-current imbibition and co-current imbibition. The high residual oil saturation from free imbibition may be due to insufficient imbibition time, or due to the difference in flow patterns. A good understanding of the flow characteristics of the imbibition process and its scaling would be helpful for interpretation.

In this report, we present an experimental and scaling study of counter-current imbibition in diatomite. Despite some similarities between chalk and diatomite, generalization of imbibition performance between these two rock types is not currently possible. Our aim is to collect in-situ water saturation profiles and imbibition performance data across several orders of magnitude of the ratio of wetting to nonwetting fluid viscosity. Within this report, much of the experimental focus is placed on counter-current imbibition to complement previous work on co-current imbibition (Akin et al 2000). We also propose a one-dimensional model to analyze the scaling behavior of counter-current imbibition processes.

1.3.2 Field Core and Crude Oil

In this research, field cores and crude oil from Lost Hills were used in the experiment. The field cores are diatomites with low permeability. There is reservoir fluid in the cores. With the new design of the CT-scanner cell, it is possible for us to investigate the behaviors of the field core with crude oil, while simulating the real reservoir conditions. Satisfactory results were obtained though we still need to improve our apparatus.

2. Experimental Study

Our objectives are to obtain the saturation profile and rate of imbibition in order to determine fluid displacement mechanisms during counter-current water imbibition into air- and oil-filled cores. We use X-ray CT scanning for visualization of displacement patterns. Our porous medium is a well characterized diatomite outcrop sample.

An imbibition cell designed specifically for the CT scanner is used. Both counter-current and co-current imbibition are possible with the setup. The imbibition cell for the field core was slightly renovated, using the same principles. In conventional CT-scanning many scans closely spaced in time are required to determine accurately the position and shape of displacement fronts. Rather than scan in a conventional mode where X-ray CT data is collected in cylindrical volume sections that are normal to the central axis of the core, the entire length of the core is scanned at the same instant as illustrated in Figure 1. Because we scan along the direction of flow, a single slice provides us with a picture of the progress and saturation pattern of imbibition. Nonlinearity in flow behavior and the effect of heterogenities are thereby easily gauged. This change in scan orientation required redesigning the coreholder assembly such that beam hardening and X-shaped imaging artifacts caused by asymmetry in the shape of the scanning plane are minimized. Figure 1 details this special design. There are two separate chambers fashioned from acrylic tubes. The main chamber is the core holder and the second is a water jacket of circular cross section that surrounds the core. Cores are potted inside the acrylic tube with epoxy (Epoxy 907, Miller-Stephenson Chemical Co.). There is no fluid exchange between the two chambers and the outer water-filled chamber allows for some measure of temperature control. The core holder may be placed in either a horizontal or vertical position. For this work, vertical is chosen. An L-shaped mounting bracket allows for bolting of the apparatus to a precision positioning system (Compumotor RP240, Parker-Hannifin Corp). Images obtained with this setup are flat and do not exhibit detectable positioning errors. Further details are given by Akin *et al.* (2000).

The core holder has two endcaps, shown schematically at the top and bottom of the core, for fluids to flow in and out of the core holder. Specifics of the endcaps depend upon whether co-current or counter-current imbibition is studied. For counter-current experiments, an endcap that allows water to be circulated by pump across the core face is used. The endcap contains a fracture-like gap of 5 mm and inlet/outlet flow lines. Thus, a supply of fresh water is maintained at the core face and produced oil is swept out of the endcap. For co-current experiments, endcaps with spider-web shaped channels are used to distribute the flow evenly.

Our CT scanner is a Picker 1200 SX X-ray scanner with 1200 fixed detectors. The voxel dimension is (0.5 mm by 0.5 mm by 10 mm), the tube current is 50 mA, and the energy level of the radiation is 140 keV. The porosity and aqueous-phase saturation fields are measured on a single vertical volume section in the center of the core as a function of time. The acquisition time of one image is 3 seconds while the processing time is around 40 seconds. The total time of measurement is short enough to capture accurately the position of the front and construct the saturation profiles along the core.

Diatomite samples were obtained from the Grefco Quarry (Lompoc, CA). They had no initial oil or water saturation. The rock is consolidated and almost pure white indicating little silt or mud. Some evidence of bedding planes is visible to the naked eye. The samples are from outcrop or near surface formations; hence, silica is in the amorphous or opal-A state. Previous work with this type of diatomite has demonstrated that they are water wet, pore structure is complex, and flow pathways are well connected (Akin *et al.* 2000). The rock is cut in a direction parallel to the bedding plane and shaped into cylindrical cores with diameters of 2.5 cm and lengths of 9.5 cm. The diatomite block could not be cored using conventional drilling and cutting methods because of its friable nature. A piece of the rock is cut by band saw to approximate dimensions. Then it is shaped manually by fixing two circular 1 inch patterns to each end of the rough-cut core. These pieces are used as guides in the shaping process with a file. Final shaping is achieved with sandpaper. Nominal porosity and permeability values are 72% and 6 mD as summarized in Table 1.

2.1 Procedure

The experimental procedure depends slightly upon whether water/air or water/oil imbibition is performed. The core is exposed to house vacuum and a temperature of 50 °C for a minimum of ten hours and usually several days, to ensure a "dry" core at the beginning of the experiment. The end caps are placed on the core holder and the core holder is placed inside the water jacket vertically and leveled. Since, the core holder is surrounded by water during the CT experiments, a leak test is performed by applying a slight gas pressure and checking that the pressure in the core holder is maintained for a period of time. The water jacket is then filled with water and a dry image of the core is taken to obtain the reference dry core CT values.

In all cases, we begin imbibition with the core completely filled with nonwetting fluid (air or oil). This avoids the added complication to interpretation introduced by variable initial water saturation and allows direct comparison to the water-air case. With this well characterized and easily repeatable initial condition we hope to show definitively the effect of viscosity ratio on imbibition performance of diatomite.

2.1.1 Water-Air Experiments

For water-air experiments, water is introduced at the top of the core. Water is supplied by a reciprocating chromatographic pump (Constametric 3200, LDC Analytical) and pumped through the endcap at a rate of 5 cm^3/min. Pressure drop across the endcap is below 100 Pa because flow spaces within the endcap have large dimensions. Thus, ample water is supplied at the core face and free imbibition occurs. The outlet endcap at the bottom of the core is sealed shut ensuring that imbibition is counter current.

Once imbibition begins, CT images are taken periodically. Initially, images are taken at roughly 1 min intervals and the frequency decreases as the rate of imbibition slows. Image collection ceases when CT numbers stabilize. De-aerated water is pumped through the core after imbibition to ensure that the core is completely filled with water.

Saturation profiles during imbibition are constructed from raw CT data according to where CT denotes the CT value for a voxel and the subscripts ob, ar, and wr refer to the object being processed, air-saturated rock, and water-saturated rock, respectively.

$$S_w = \frac{CT_{ob} - CT_{ar}}{CT_{wr} - CT_{ar}} \tag{3}$$

Because images of 100% air and water filled rock are available, a map of porosity for each core can be computed from

$$\phi = \frac{CT_{wr} - CT_{ar}}{CT_w - CT_a} \tag{4}$$

The subscript w refers to the CT number of the water phase whereas a refers to air. Water and air CT numbers are taken as 0 and –1000, respectively. Figure 2 presents porosity images of the cores used in these experiments. Black shading corresponds to a porosity of 0.6 while white is 0.8. Note that the last core exhibits some diagonally oriented planes of high porosity.

2.1.2 Water-Oil Experiments

For water-oil experiments, there is difference when we use outcrop diatomite cores and field cores. A slightly different imbibition cell and experimental process is applied for the experiments.

2.1.2.1 Outcrop Diatomite Cores

Cores are dried as described above. Then oil is introduced to the core through the bottom end cap (Fig. 1) with the top end cap open to atmosphere. Thus, the core is saturated in a co-current fashion. Oil is pumped through the core to dissolve any residual air. At this stage, the lower inlet to the core is sealed shut. The porosity field of cores used for oil-water imbibition are calculated using Eq. (4) upon substitution of CT_o, the CT number for the oil phase, for CT_w and replacing CT_{wr} with CT_{or}, the CT number of the oil saturated rock.

For counter-current imbibition, water is again introduced at the top of the core by pumping water through the endcap at a rate of 5 cm^3/min. Water that did not imbibe and any produced oil exit the end cap. Images are collected periodically throughout the duration of imbibition. It is very difficult to obtain a 100% water-saturated image within the same experiment and a slightly different equation is used to process the raw CT data:

$$S_w = \frac{CT_{ob} - CT_{or}}{\phi(CT_w - CT_o)} \tag{5}$$

where ϕ is the independently measured porosity of each voxel. Equation (5) is comparable with Eq. (3) in terms of accuracy because images obtained here are flat and exhibit minimal artifacts or errors.

Two oils with different viscosities are used. The first is n-decane whose viscosity is 0.84 mPa-s whereas the second is a viscous white mineral oil (Blandol) whose viscosity is 25.2 mPa-s. The effect of using these different oils is solely to adjust the oil-water viscosity ratio. Even though cores are oriented vertically, buoyancy forces within the cores are negligible relative to capillary forces. The Bond number ($=(\rho_w-\rho_o)gk/\sigma$) for water-oil cases is approximately 10^{-10} and 10^{-9} for water-air cases indicating the dominance of capillarity. The relevant properties of the experimental fluids are summarized in Table 2.

2.1.2.2 Field Cores

The imbibition cell for the field core was shown in Figure 11. It uses the same principles for the outcrop cores. The main difference is the core holder. Since the field core contains initial oil or water saturation, we can not pot the core inside the acrylic tube with epoxy as we did with the outcrop cores. Therefore we use the renovated conventional core holder, in which there is rubber sleeve to hold the core. There is PVC tube outside of rubber sleeve, which connects two end caps that have similar structure as those for the outcrop cores. There is free space between the PVC tube and rubber sleeve, which permits us to apply confining pressure. Because the permeability of the field is so small, about 1.5 md, the confining pressure is necessary in order to saturate the core with crude oil. The core is positioned horizontally in order to neglect the gravity effect.

In order to simulate the real reservoir as much as we can, the whole system for the experiment was maintained the same temperature, which is close to the reservoir temperature. The special tubing was used to maintain the oil and water warm. The relationship of the viscosity of the crude oil and temperature was presented in Figure 10. The process of the experiment was shown in Figure 11 and 12 in detail. The countercurrent imbibition was performed using the field core and crude oil. We saturated the crude oil in cocurrent fashion. The procedure is similar to those for the outcrop cores.

2.2 Results

Our chief point of interest from the experiments is counter-current imbibition performance as the ratio of nonwetting fluid to wetting fluid viscosity increases. Figure 3 summarizes the recovery versus time for all experiments. Recovery is normalized by the total volume of nonwetting fluid originally present in the core. Three water/n-decane experiments were conducted to assure repeatability. However, the cores all have different permeability and so water/n-decane results do not fall onto a single curve. As expected, imbibition recovery slows as non-wetting fluid viscosity and flow resistance increases. Nevertheless, imbibition is relatively rapid in all cases despite the low rock permeability. Residual oil saturations are reported in Table 1.

The saturation images obtained from the raw CT data illustrate the strong capillary forces that are operative during imbibition. In all of the images to be discussed, black indicates that S_w is 0 while white indicates that S_w is 1. Figure 4 presents results from air-water imbibition at various points in time. Water enters the core from the top and movement down the core is roughly one-dimensional. The water front is relatively sharp initially and becomes more diffuse as the front moves through the core. Front movement is rapid and it reaches the end of the core at 180 min. By comparing Fig. 4 with Fig. 9 of Akin et al (2000) which presents water-air co-current imbibition results for the same rock, we find that counter-current imbibition is relatively slower and that the imbibition fronts are more diffuse.

Figure 5 shows saturation images from n-decane water imbibition and Figure 6 gives results for the blandol water system. Note the shaded bar in each figure indicating S_w. As the oil viscosity increases by a factor of roughly 20 between Figs. 4 and 5, imbibition displacement effectiveness decreases. Figure 6 lacks a discernable displacement front while such a feature is evident in Fig. 5. At the end of imbibition, recovery in the n-decane case is roughly 0.65 whereas at the higher viscosity recovery is about 0.5. As the nonwetting phase viscosity and fluid flow resistance increases, it becomes increasingly hard for the oil to move in a countercurrent fashion across the region of high water saturation at the inlet of the cores.

There are several aspects of Figs. 5 and 6 that deserve further comment. We note that counter-current imbibition, while generally occurring in a one-dimensional fashion, is sensitive to local inhomogeneities within the rock. In Fig. 5 the displacement front becomes somewhat tilted because the capillary characteristics of the rock are not constant. Compare images at times of 27 min and 158 min within Fig. 5. Careful observation of the images in Fig. 6 reveals that water begins to accumulate near the bottom of the core at roughly 77 min. This is well before the macroscopic front arrives. Apparently some rapid conduit with high permeability allowed water to move down the core rapidly. Indeed this core revealed some high regions that are roughly diagonal to the axis of the core, see Fig. 2. Previous work examining co-current imbibition in this same rock found that imbibition frontal advance was nearly one-dimensional (Akin et al 2000).

Figure 13 shows the images of CT number changes for field cores during oil saturating. It is found that it takes more time to produce oil because the viscosity of crude oil is high as is the initial water saturation. Moreover we found that heterogeneity in the core influences the imbibition. After we started to imbibe the core with water, the first third of the core imbibes water fast. Figure 14 displays the progress of imbibition in the case of the field core with crude oil.

To summarize the experimental results, imbibition performance as gauged by speed of recovery and amount recovered decreases as the non-wetting phase viscosity increases. Water movement through the cores becomes increasingly diffuse with viscosity also.

3. Theoretical Analysis

In this section, we derive imbibition rates by assuming that flow is one dimensional and the fluids are incompressible. Also, assumed is that the wettability and pore structure of the system are similar across the medium. We neglect any effect of gravity. Applying Darcy's law and invoking capillarity results in the following equations:

$$u_w = \frac{-kk_{rw}}{\mu_w}\frac{\partial p_w}{\partial x} = -\lambda_w \frac{\partial p_w}{\partial x} \tag{6}$$

$$u_w = \frac{-kk_{rnw}}{\mu_{nw}}\frac{\partial p_{nw}}{\partial x} = -\lambda_w \frac{\partial p_{nw}}{\partial x} \tag{7}$$

$$u_t = u_{nw} + u_w \tag{8}$$

$$p_c = p_{nw} - p_w \tag{9}$$

where u is Darcy velocity, k is absolute permeability, k_r is relative permeability, μ is viscosity, p is pressure, and λ is mobility. The subscripts nw, w, c, and t represent nonwetting phase, wetting phase, capillary, and total, respectively. Upon combination and rearrangement of Eqs. (6) to (9), we obtain for the wetting phase pressure gradient

$$\frac{\partial p_w}{\partial x} = \frac{-u_t}{\lambda_t} - f_{nw}\frac{\partial p_c}{\partial x} \tag{10}$$

where f represents fractional flow ($=\lambda_{nw}/\lambda_t$) and λ_t ($=\lambda_{nw}+\lambda_w$) is the total mobility.

Consider now the case of counter-current imbibition. The total velocity must be 0 at all points within the one-dimensional media because the fluids are assumed to be incompressible. Setting u_t within Eq. (10) to 0 and back substituting into Eq. (7) results in

$$u_w = \frac{\lambda_w \lambda_{nw}}{\lambda_t}\frac{\partial p_c}{\partial x} \tag{11}$$

Note that Eq. (11) does not neglect the pressure gradient within the wetting phase. The form of Eq. (11) results from the restriction to counter-current flow and it suggests correctly that the imbibition rate depends upon individual phase mobilities and the total mobility of the system.

To proceed, Eq. (11) is multiplied and divided by $\sqrt{k_{rw}k_{rnw}/\mu_w\mu_{nw}}$. This operation and some rearrangement yields

$$u_w = k\frac{1}{\sqrt{\mu_w\mu_{nw}}}\frac{\sqrt{k_{rnw}k_{rw}}}{\sqrt{M}+\frac{1}{\sqrt{M}}}\frac{\partial P_c}{\partial S_w}\frac{\partial S_w}{\partial x} \tag{12}$$

where M ($= (\mu_{nw} k_{rw} / \mu_w k_{rnw})$) is mobility ratio.

The form of Eqs. (11) and. (12) results from the restriction to counter-current flow. It suggests that counter-current imbibition is diffusion-like and controlled by the product of the mobility in both phases. Note that in Eq. (12), the effects of viscosity are for accounted by $\sqrt{\mu_{nw}\mu_w}$ and $\sqrt{M} + \frac{1}{\sqrt{M}}$. The values of the second term are not very sensitive to M, when M is not significantly larger or smaller than unity. However, when the value of M is substantially different from unity, the contribution of $\sqrt{M} + \frac{1}{\sqrt{M}}$ can be significant. The following dimensionless time follows from Eq. (12)

$$t_D = t\sqrt{\frac{k}{\phi}}\frac{\sigma}{L_c^2}\sqrt{\lambda_{rw}^* \lambda_{rnw}^*}\,\frac{1}{\sqrt{M^*} + \frac{1}{\sqrt{M^*}}} \tag{13}$$

where $\lambda_r^* (= k_r^* / \mu)$ is a characteristic mobility for the wetting and nonwetting phases and M^* $(= \lambda_{rw}^* / \lambda_{rnw}^*)$ is a characteristic mobility ratio. Here, end-point relative permeabilities are used when calculating λ_r^* and M^*. Equation (13) is similar to the empirically determined (Zhang et al 1996) scaling of t_D indicated in Eqs. (1) and (2) with respect to phase viscosity. In the limit of M^* approaching unity, t_D varies inversely with the geometric mean of μ_{nw} and μ_w. Note also that Eq. (13) explains water/gas imbibition scaling. For water/gas cases, $\sqrt{M^*} << 1/\sqrt{M^*}$ and the scaling of t_D with viscosity is approximately $1/\mu_w$ as indicated empirically (*c.f.*, Handy 1960).

The mobility ratio depends on the viscosity of the fluids and the wettability of the system. For strongly water-wet systems, the end-point relative permeability of the wetting phase can be significantly less than unity (Dullien 1992). For water-wet sandstone, water relative permeability can be as low as 0.05 at residual oil saturation. Therefore, the mobility ratio can be close to unity even for systems of high viscosity ratio. The diatomite samples used here are strongly water wet and their endpoint relative permeabilities are expected to be low as in the sandstone case.

The above discussion is based on the assumption that the relative permeability and the capillary pressure functions are similar for all of the measurements. In counter-current imbibition, the total water imbibed is controlled by matrix adjacent to the fracture. Thus, if S_w at the inlet does not vary significantly, the oil recovery is proportional to $\sqrt{t_D}$ until the imbibition front reaches the outlet boundary. Because values of $\partial P_c / \partial S_w$ increase as water saturation decreases, the imbibition rate is larger at low water saturation than that of high water saturation. Therefore, the oil recovery may depart from $\sqrt{t_D}$ (see discussion).

To recap, the oil recovery from counter-current imbibition is approximately proportional to the square-root time during the initial infinite-acting period. The dimensionless time for counter-current imbibition can be scaled to by Eq. (13), which is more general and explains the empirical findings Zhang *et al.* (1996).

4. Discussion

Because of the complex nature of experiments associated with low permeability samples and CT scanning, only a limited number can be performed in a reasonable period of time. Additionally, we performed a number of numerical simulations of counter-current imbibition to strengthen our scaling arguments above. The capillary pressure and relative permeability curves reported for sandstone by Bourblaux and Kalaydjian (1990) were used. A two-dimensional permeability field was generated with correlation lengths of 0.05 in both directions and medium permeability of 1.0 mD. The model (100 X 100 cells) has the dimensions of 25 cm (10 in.) in length and 10 cm (4 in.) in width to mimic experiments on a whole core. Wetting liquid viscosity was kept constant (0.75 mPa-s) and nonwetting phase viscosity varies from 1.0, 20 to 200 mPa-s. The end-point mobility ratios are about 0.1, 1.9 and 19.2.

4.1 Scaling of Simulation Data

Previous scaling studies of spontaneous imbibition have focused on the shape factor proposed by Zhang *et al.* (1996) and the results are usually presented on a logarithmic time scale. The scaled recovery curves generally cover about two orders of magnitude. The large time scale can mask the differences between scaled data. In Figure 7(a), we present the simulated oil recoveries from counter-current imbibition using the dimensionless time of Zhang *et al.* The curves indeed fall into a narrow range. However, the same data are shown in Figure 7(b) with a linear time scale. An almost 100% error is indicated between the low and high viscosity oil. For low permeability reservoirs this time error might be as long as the field life. Figure 8 shows the same data scaled by the new dimensionless time with the appropriate end-point mobility ratio. Here, the endpoint relative permeabilities for the wetting and nonwetting phase are 0.05 and 0.65, respectively, consonant with the data of Bourblaux and Kalaydjian (1990). The scaling is almost perfect with slight differences at late times. These differences result from boundary effects on the porous medium.

4.2 Scaling of Experimental Data

In the simulations, the relative permeability functions and the fluid properties are known; therefore, the end-point mobility ratio is defined exactly. For the experiments, relative permeability functions are not known accurately. Nevertheless, the scaling group for time developed in §3 was tested on the available counter-current imbibition data for diatomite. For the water/air experiments, k^*_{rw} is set to 0.14 and k^*_{rnw} is chosen as 0.60. In the water/oil cases, k^*_{rw} and k^*_{rnw} are set to 0.14 and 0.45, respectively. These endpoint values are representative of fine-grained, strongly water-wet diatomite (Schembre and Kovscek 2000). Figure 9 displays the result of this exercise. Note that recovery has been scaled to the fraction of recoverable oil. The recovery from the water/air system and all of the water/oil systems agree reasonably well. Within experimental scatter, the data are reduced to a single curve in spite of the fact that the nonwetting fluid viscosity varies by 4 orders of magnitude. Both the simulation and the experimental data indicate the new dimensionless time can improve significantly the scaling of spontaneous imbibition in low permeability porous media.

The good scaling of recovery from systems with different viscosity ratios suggests that the general shapes of the recovery curves as a function of dimensionless time are similar over the viscosity range studied in this paper. Therefore, the recovery rate by countercurrent imbibition can be scaled by the dimensionless time as well. Considering counter-current imbibition as diffusion processes can be a good approximation, and the initial oil recovery is proportional to the square-root of time.

4. Discussion

Because of the complex nature of experiments associated with low permeability samples and CT scanning, only a limited number can be performed in a reasonable period of time. Additionally, we performed a number of numerical simulations of counter-current imbibition to strengthen our scaling arguments above. The capillary pressure and relative permeability curves reported for sandstone by Bourblaux and Kalaydjian (1990) were used. A two-dimensional permeability field was generated with correlation lengths of 0.05 in both directions and medium permeability of 1.0 mD. The model (100 X 100 cells) has the dimensions of 25 cm (10 in.) in length and 10 cm (4 in.) in width to mimic experiments on a whole core. Wetting liquid viscosity was kept constant (0.75 mPa-s) and nonwetting phase viscosity varies from 1.0, 20 to 200 mPa-s. The end-point mobility ratios are about 0.1, 1.9 and 19.2.

4.1 Scaling of Simulation Data

Previous scaling studies of spontaneous imbibition have focused on the shape factor proposed by Zhang *et al.* (1996) and the results are usually presented on a logarithmic time scale. The scaled recovery curves generally cover about two orders of magnitude. The large time scale can mask the differences between scaled data. In Figure 7(a), we present the simulated oil recoveries from counter-current imbibition using the dimensionless time of Zhang *et al.* The curves indeed fall into a narrow range. However, the same data are shown in Figure 7(b) with a linear time scale. An almost 100% error is indicated between the low and high viscosity oil. For low permeability reservoirs this time error might be as long as the field life. Figure 8 shows the same data scaled by the new dimensionless time with the appropriate end-point mobility ratio. Here, the endpoint relative permeabilities for the wetting and nonwetting phase are 0.05 and 0.65, respectively, consonant with the data of Bourblaux and Kalaydjian (1990). The scaling is almost perfect with slight differences at late times. These differences result from boundary effects on the porous medium.

4.2 Scaling of Experimental Data

In the simulations, the relative permeability functions and the fluid properties are known; therefore, the end-point mobility ratio is defined exactly. For the experiments, relative permeability functions are not known accurately. Nevertheless, the scaling group for time developed in §3 was tested on the available counter-current imbibition data for diatomite. For the water/air experiments, k^*_{rw} is set to 0.14 and k^*_{rnw} is chosen as 0.60. In the water/oil cases, k^*_{rw} and k^*_{rnw} are set to 0.14 and 0.45, respectively. These endpoint values are representative of fine-grained, strongly water-wet diatomite (Schembre and Kovscek 2000). Figure 9 displays the result of this exercise. Note that recovery has been scaled to the fraction of recoverable oil. The recovery from the water/air system and all of the water/oil systems agree reasonably well. Within experimental scatter, the data are reduced to a single curve in spite of the fact that the nonwetting fluid viscosity varies by 4 orders of magnitude. Both the simulation and the experimental data indicate the new dimensionless time can improve significantly the scaling of spontaneous imbibition in low permeability porous media.

The good scaling of recovery from systems with different viscosity ratios suggests that the general shapes of the recovery curves as a function of dimensionless time are similar over the viscosity range studied in this paper. Therefore, the recovery rate by countercurrent imbibition can be scaled by the dimensionless time as well. Considering counter-current imbibition as diffusion processes can be a good approximation, and the initial oil recovery is proportional to the square-root of time.

The scaling of the simulation results suggests that the end-point mobility ratio contributes to imbibition rate significantly. The end-point mobility ratio is also a measure of the wettability of the systems. For strongly water wet rocks, such as clean sandstone, the relative permeability to water can be very small, resulting in small end-point mobility ratios. On the other hand, for weakly water-wet systems, the water-end point relative permeability can be large, resulting in large end-point mobility ratios. One needs to know the system wettability before scaling laboratory data to the field situation.

4.3 Counter-Current Versus Co-Current

In designing an oil recovery process from low permeability formations, we need to optimize the natural recovery potentials. Do we encourage counter-current or co-current imbibition in waterflooding a reservoir? Which gives faster recovery? And which recovers more oil?

In simulating both counter-current and co-current imbibition, we used the same relative permeability and capillary pressure curves. Results from co-current imbibition, not shown here, consistently indicated about 20% more oil recovery compared to countercurrent imbibition. We carefully examined the simulated residual oil saturation distributions and found that countercurrent imbibition is much more sensitive to local heterogeneity and traps more oil as a result. Experiments and simulations indicate that co-current imbibition reaches residual oil saturation much faster than counter-current imbibition, as others have shown (*e.g.*, Bourblaux and Kalaydjian 1990). Thus, strictly applying measured residual oil saturation from counter-current imbibition experiments to the field can be pessimistic, because some degree of co-current flow might exist in the field. Nevertheless, counter-current imbibition may be the preferrable recovery mechanism in low permeability reservoirs with relatively viscous oil. As discussed before, oil recovery from counter-current imbibition is proportional the square-root of time, while co-current imbibition with viscous oil is proportional to time. Counter-current imbibition recovers oil faster than co-current imbibition for t_D less than 1. As oil viscosity increases, this period of time increases as indicated in Eq. (13).

For low permeability reservoirs such as diatomite, the permeability is about 1 mD and the oil viscosity is about 10 to 20 cp. Experience has shown that pressure gradients of more than 4500 kPa/m (200psi/ft) are needed for conducting laboratory displacement experiments (Kamath *et al.* 1995). The reservoir pressure gradient cannot be more than 110 kPa/m (5 psi/ft), in practice. Clearly, oil recovery in a displacement fashion is very difficult. However, extensive fracturing of the formation and encouraging counter-current imbibition may improve access to the reservoir and promote increased field-wide recovery.

5. Conclusions

This paper reports experimental measurements of countercurrent imbibition in diatomite using novel CT imaging techniques. Imaging with X-ray CT permits quantitative monitoring of the advance of wetting liquids. Experiments were conducted with wetting and nonwetting fluids whose viscosities spanned 4 orders of magnitude. The advance of wetting liquid slows and saturation patterns become increasingly diffuse as the ratio of nonwetting to wetting liquid viscosity increases. Counter-current imbibition appears to be much more sensitive to core-scale heterogeneities as compared to co-current results in the same rock type reported elsewhere (Akin *et al.* 2000).

A theoretical analysis of the flow characteristics of imbibition processes was also conducted. A new formulation for the dimensionless time appropriate to counter-current imbibition resulted. The new scaling was used to correlate experimental and simulation results. It improves correlation significantly by taking end-point fluid-phase mobilities and the mobility ratio into account. The scaling also explains the empirical observation that water/oil imbibition time scales inversely with the geometric mean of water and oil viscosity, whereas water/air imbibition scales inversely with water viscosity.

Application of laboratory-based residual oil saturation measurements from counter-current imbibition tests to the field can lead to pessimistic predictions. This is true especially for low permeability rocks containing relatively viscous oil. While this work helps to clarify the role of mobility ratio, other factors such as rock type, wettability, and initial saturation are not well understood. In low permeability systems, t_D can be less than 1 for a portion of the total recovery time. Because, counter-current imbibition initially scales as $\sqrt{t_D}$, it recovers oil faster than processes that scale linearly with time provided that t_D is less than 1.

6. Future Plans

More cores from the same field will be studied and crude oil will be used in order to understand this diatomite reservoir as well as possible. Other kinds of rock will be used for finding a more general scaling, which is not only valid for diatomite reservoir, but also for other sandstone reservoir. Outcrop cores will be used with crude oil so that we can observe more clearly how the crude oil influences the results.

We will try to find the scaling group for cocurrent imbibition flow also, which can complete the study. Simulation will be applied on diatomite samples in order to verify the scaling group.

7. Nomenclature

CT	CT number
k	permeability
k_r	relative permeability
L_c	characteristic length
M	mobility ratio
P_c	capillary pressure
S_w	water saturation
t	time
u	Darcy velocity
ϕ	porosity
λ	mobility
ρ	mass density
σ	surface tension
μ	phase viscosity

subscripts

a	air phase
ar	CT value of air-saturated rock
D	dimensionless
nw	nonwetting phase
o	oil phase
ob	CT value of image being processes
or	CT value of oil saturated rock
s	denotes geometric mean of phase viscosity
t	total
w	wetting phase
wr	CT value of water-saturated rock

References

1. Akin, S, Schembre, J. S., Bhat, S. K., and Kovscek, A. R.: "Spontaneous Imbibition Characteristics of Diatomite," J. Pet. Sci. & Eng. **25** (2000) 149-165.

2. Cil, M. and Reis, J. C., 1996. "A Multi-Dimensional, Analytical Model for Counter-Current Water Imbibition into Gas-Saturated Matrix Blocks," J. Pet. Sci & Eng., **16** (1966) 61-69.

3. Cuiec, L., Bourbiaux, J. B. and Kalaydjian, F. J.: "Oil Recovery by Imbibition in Low Permeability Chalk." Soc. Pet. Eng. Form. Eval. **9** (September 1994) 200-208.

4. Dullien, F. A. L.: Porous Media Fluid Transport and Pore Structure, 2nd Ed. Academic Press Inc, San Diego, CA. (1992).

5. Garg, A., Zwahlen, E. and Patzek, T. W.: "Experimental and Numerical Studies of One-Dimensional Imbibition in Berea Sandstone". presented at the 16th Annual American Geophysical Union Hydrology Days, Fort Collins (April 15-18, 1996).

6. Ilderton, D. C., Patzek, T. W., Rector, J. W. and Vinegar, H. J.: "Passive Imaging of Hydrofractures in the South Belridge Diatomite." Soc. Pet. Eng. Form. Eval. **11** (March 1996) 46-54.

7. Jadhunandan, P. P. and Morrow, N. R.: "Spontaneous Imbibition of Water by CrudeOil/Brine/Rock Systems." In Situ **15**(4) (1991) 319-345.

8. Kamath, J., deZabala, E.F., and Boyer, R. E., 1995. "Water/Oil Relative Permeability Endpoints of Intermediate-Wet, Low-Permeability Rocks," Soc. Pet. Eng. Form. Eval. **10** (March 1995) 4-10.

9. Kazemi, H., Gilman, J. R. and El-Sharkaway, A. M.: "Analytical and Numerical Solution of Oil Recovery from Fractured Reservoirs Using Empirical Transfer Functions". Soc. Pet. Eng. Res. Eng. **7**(2) (May 1992) 219-227.

10. Mattax, C. C. and Kyte, J. R.: "Imbibition Oil Recovery from Fractured Water-Drive Reservoirs." Soc. Pet. Eng. J. **2** (June 1962) 177-184.

11. Milter, J. and Øxnevard, R. L.: "Spontaneous Imbibition in Two Different Chalk Facies." Petroleum Geoscience **2** (1996) 231-240.

12. Morrow, N. R., Ma, S., Zhou, X. and Zhang, X.: "Characterization of Wettability from Spontaneous Imbibition Measurments". CIM 94-475, paper presented at the 45th Annual Technical Meeting of the Pet. Soc. of the CIM, Calgary, Alberta Canada (June 12-15, 1994).

13. Reis, J. C. and Cil, M.: "A Model for Oil Expulsion by Counter-Current Water Imbibition in Rocks: One-Dimensional Geometry," J. Pet. Sci & Eng., **10** (1993) 97-107.

14. Schembre, J. M. and Kovscek, A. R.: Unpublished results (2000).

15. Zhang, X., Morrow, N. R. and Ma, S., Nov 1996. "Experimental Verification of a Modified Scaling Group for Spontaneous Imbibition." Soc. Pet. Eng. Res. Eng. **11** (November 1996) 280-285.

16. Zhou, X., Morrow, N. R., and Ma, S.: "Interrelationship of Wettability, Initial Water Saturation, Aging Time, and Oil Recovery by Spontaneous Imbibition and Waterflood." Soc. Pet. Eng. J. **5** (2000) 119-207.

Table 1. Diatomite Core Properties

Core	Experimental condition	Average permeability, mD (10^{-15} m^2)	Average porosity, fraction	Residual saturation, S_{nwr}
1	air/water	6.0	0.64	0.05
2	n-decane/water	6.1	0.72	0.30
3	blandol/water	7.9	0.77	0.34
4	n-decane/water	2.5	0.78	0.38
5	n-decane/water	4.3	0.68	0.36

Table 2. Properties of Experimental Fluids

	ρ (kg/m^3)	μ (mPa-s)	σ liquid-air (mN/m)	σ liquid-water (mN/m)	CT (H)
air (STP)	1.82	0.018	-	72	-1000
n-decane	730	0.84	23.7	51.4	-283
blandol	780	25.	19.8	45.69	-212
water	1000	1.0	72	-	0

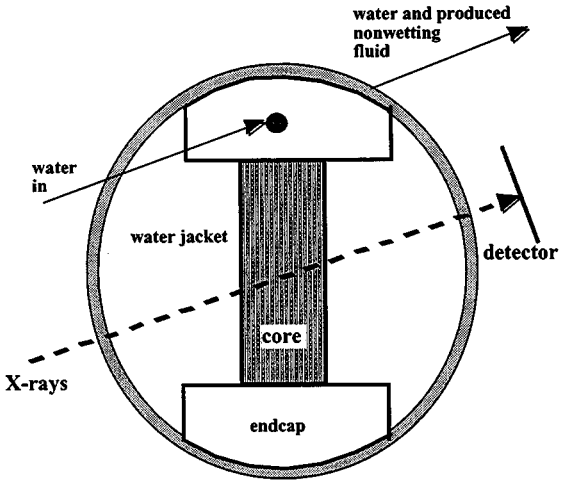

Figure 1. Schematic of imbibition cell set up for countercurrent imbibition.

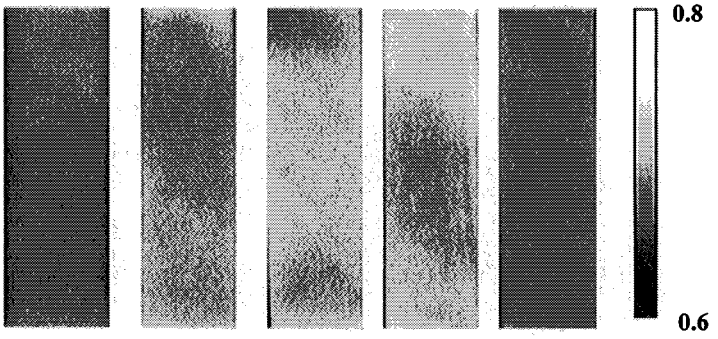

Figure 2. Porosity images of diatomite cores (left to right) used for countercurrent imbibition: (1) air/water, (2) n-decane/water, (3) blandol/water, (4) n-decane/water, and (5) n-decane/water.

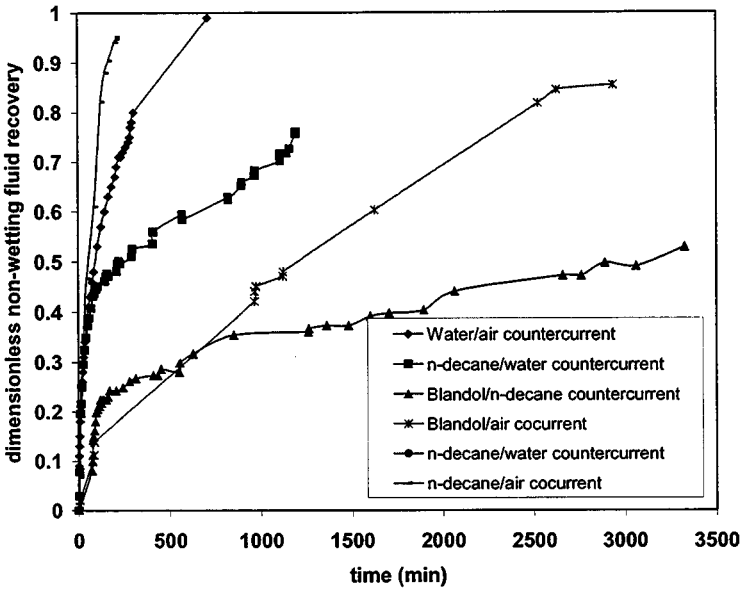

Figure 3. Nonwetting fluid recovery versus absolute time.

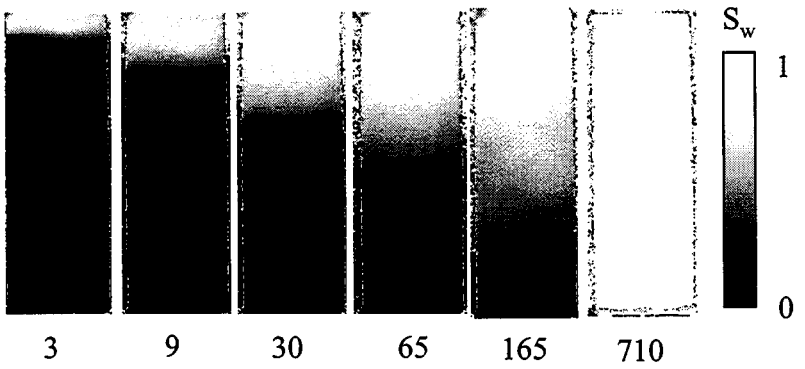

Figure 4. CT-derived water saturation images of counter current water/air imbibition in diatomite. Time is given in minutes beneath the images.

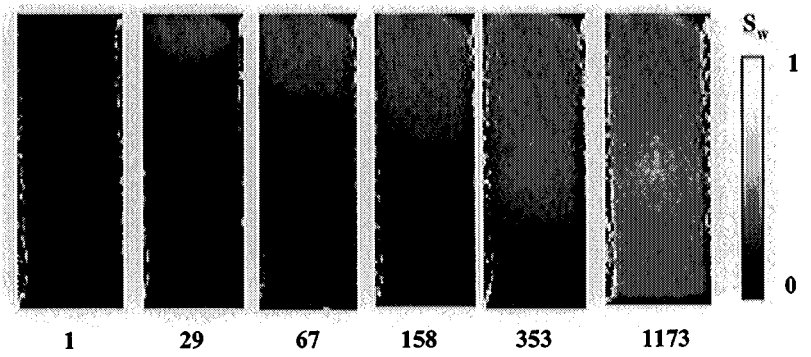

Figure 5. CT-derived water saturation images of counter current water/n-decane imbibition in diatomite. Time is given in minutes beneath the images.

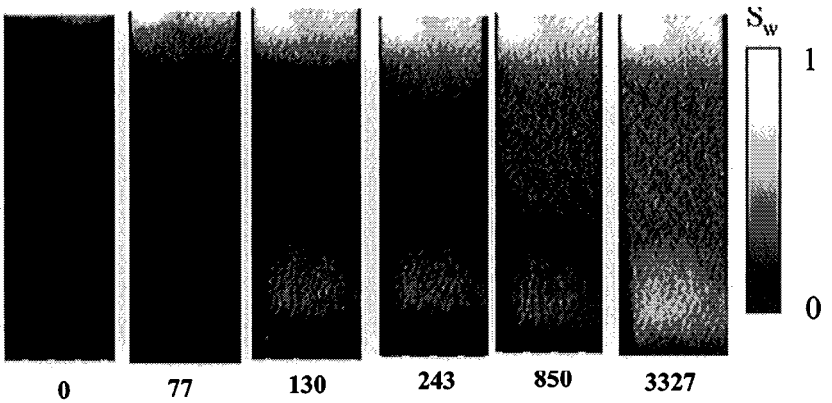

Figure 6. CT-derived water saturation images of counter current water/blandol imbibition in diatomite. Time is given in minutes beneath the images.

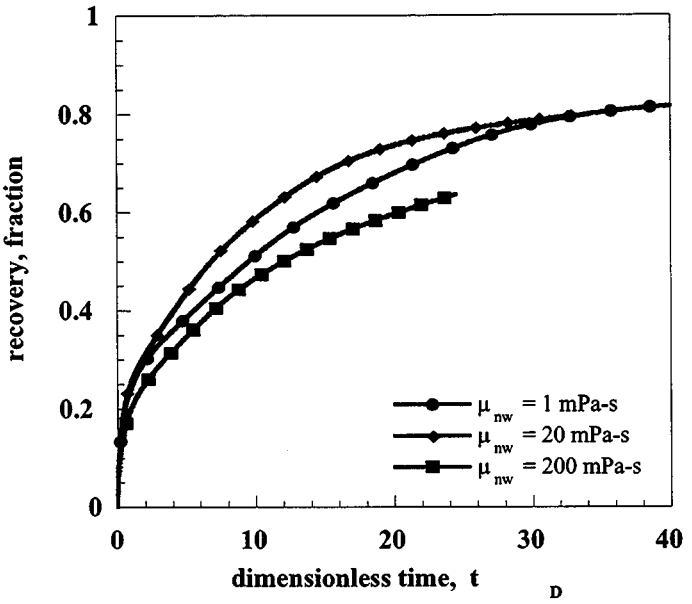

Figure 7 Scaling of the simulated oil recovery using the dimensionless time of Zhang *et al.* (1996).

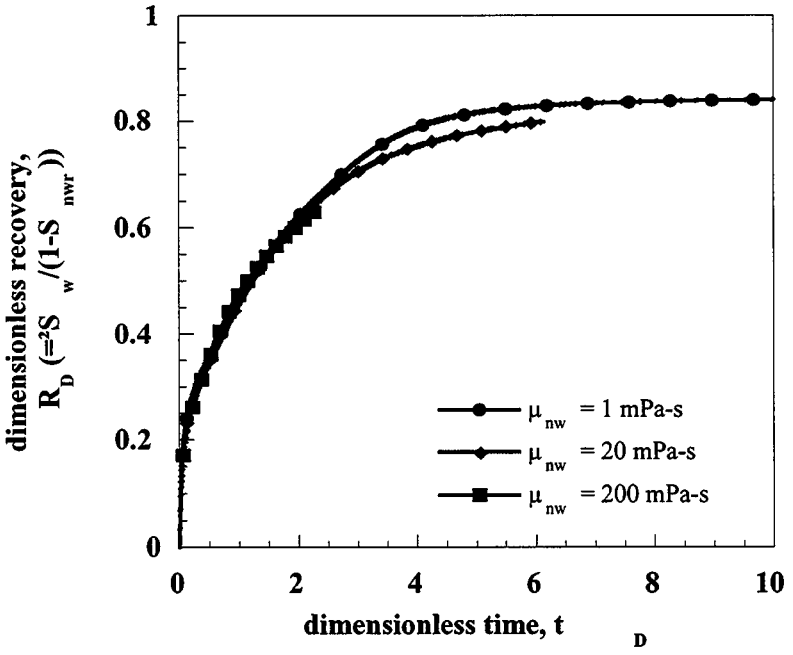

Figure 8 Scaling of the simulated oil recovery using the proposed dimensionless time.

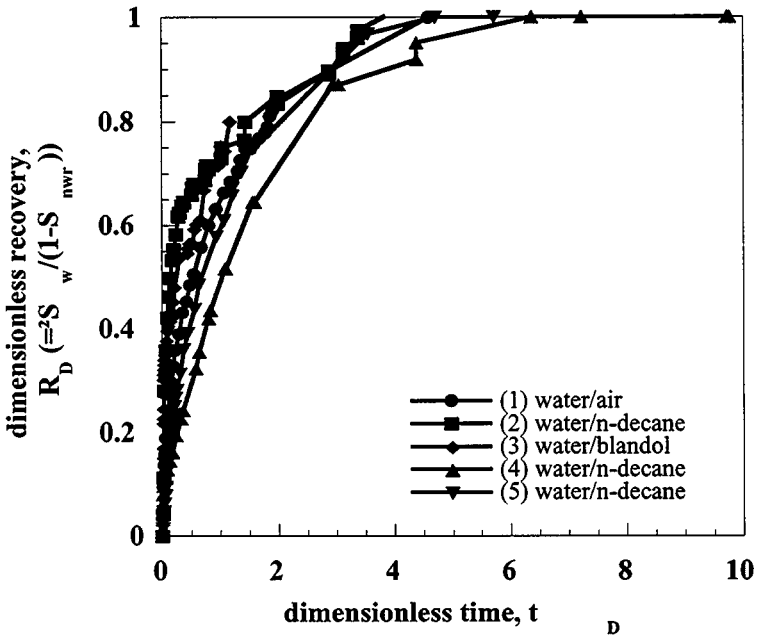

Figure 9. Correlation of recovery by countercurrent imbibition from diatomite. Nonwetting-phase viscosity varies by 4 orders of magnitude.

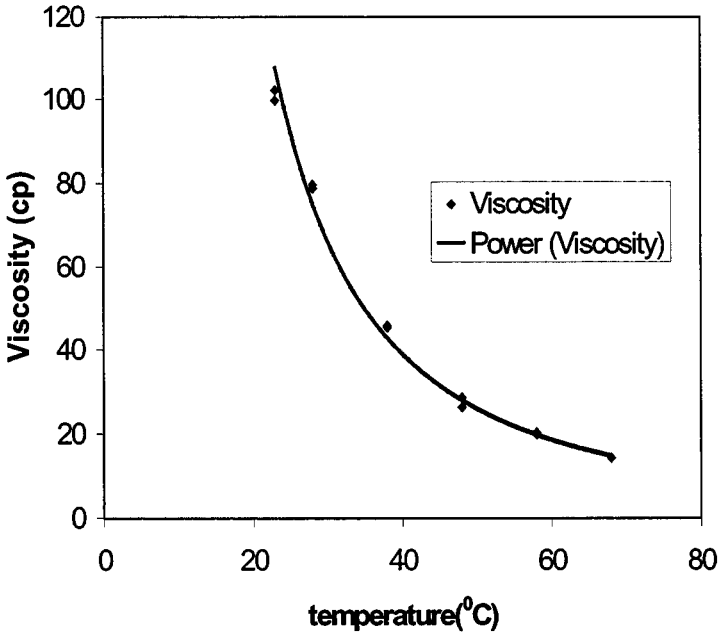

Figure 10 Viscosity versus temperature (Lost Hills crude oil).

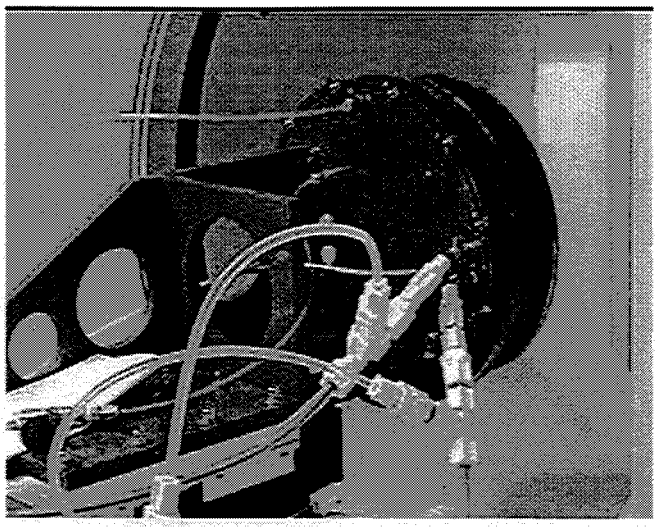

Figure 11 The imbibition cell for field core studies.

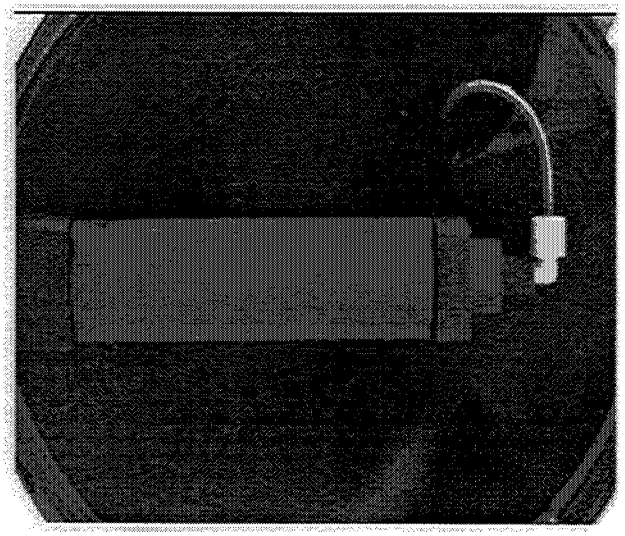

Figure 12 Frontal view of the imbibition cell.

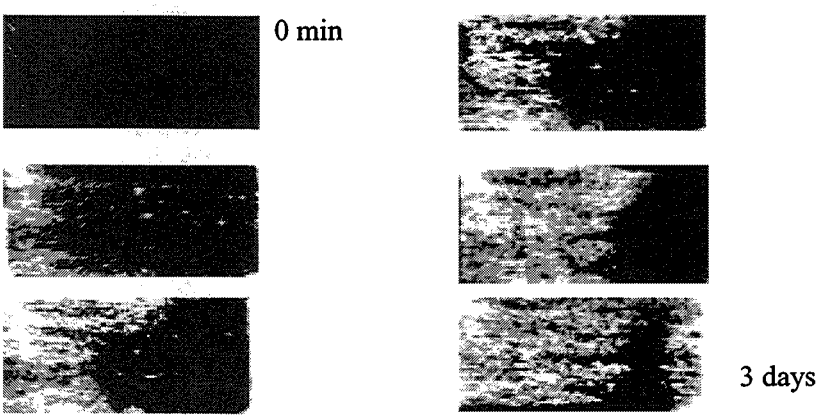

Figure 13 CT number changes during saturation.

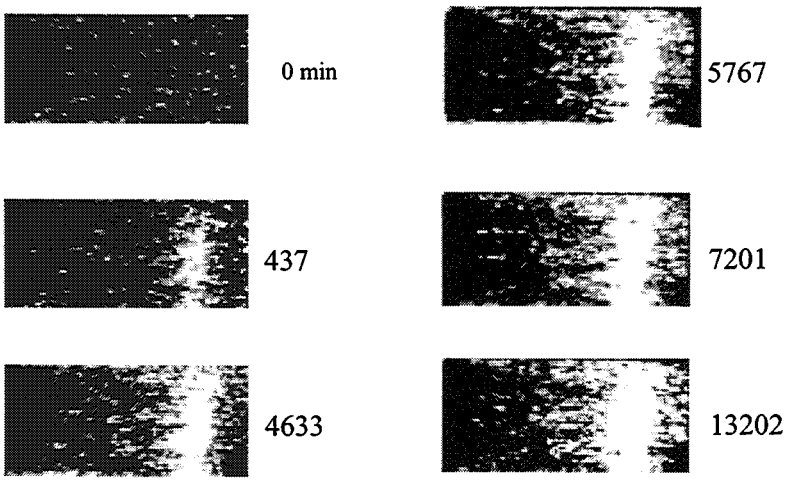

Figure 14 *Sw* difference images with time.

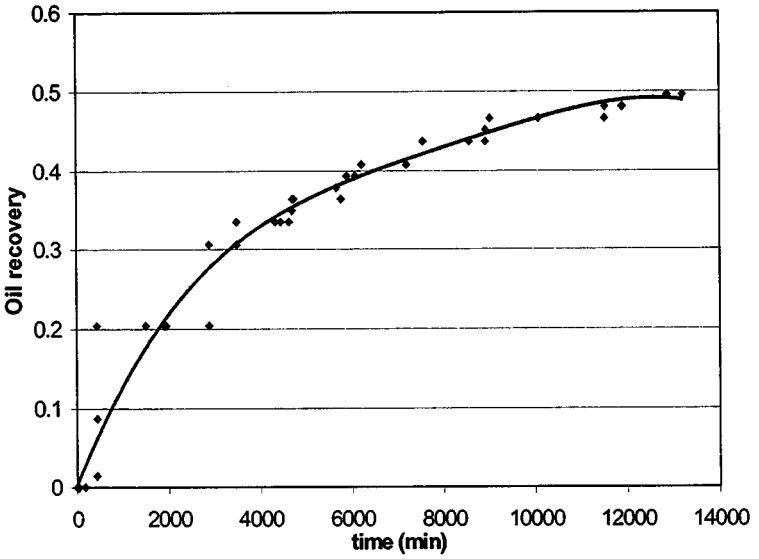

Figure 15 Oil recovery versus time (Field core, countercurrent flow).

Use of Computerized Tomography in Petroleum Engineering Research

S. Akin[1] and A. R. Kovscek

Abstract

Imaging the distribution of porosity, permeability, and fluid phases is important to understanding single and multiphase flow characteristics of porous media. X-ray computerized tomography (CT) has emerged as an important and powerful tool for nondestructive imaging because it is relatively easy to apply, can offer fine spatial resolution, and is adaptable to many types of experimental procedures and conditions. This paper gives an overview of CT technology for imaging porous media, the principles behind the technology, and effective experimental design. By critically reviewing prior work with this important tool, we hope to provide a better understanding of its use and a pathway to improved analysis of CT-derived data. Because of the wide variety of image processing options, they are discussed in some detail.

1. Introduction

The use of X-ray computerized tomography (CT) or computer-assisted tomography for observing single and multiphase fluid flow in rock and nondestructively viewing its interior is a relatively new technique in petroleum engineering and the associated geological sciences. Radiological imaging using computerized tomography was first developed in England in 1972 by Hounsfield. In comparison to conventional X-ray radiography, CT scanners generate cross-sectional images of the object by measuring the attenuation of a beam of X-rays as it is rotated around the object at angular increments within a single plane. From a set of these measurements, back projection algorithms that generally use Fourier transform algorithms are used to reconstruct a cross-sectional image. Sedgewick and Dixon (1988) compared three X-ray-based techniques for measuring fluid saturations: single-beam attenuation, xeroradiography, and CT. They concluded that the methods gave similar results, but that the advantage of CT was resolution on the millimeter scale. Additionally, three-dimensional images can be generated by interpolating among cross-sectional images.

CT scanners are classified according to the placement of the source-detector combination. First generation scanners used a source and 3 to 6 detectors. The images of the specimen were acquired in a translate-rotate fashion. The source and detectors were fixed and the sample was rotated at angular intervals about its central axis in order to acquire data for a cross-sectional image. It usually took several minutes to finish a single scan. Second generation scanners improved the scan time and image quality by keeping the same geometry but incorporating up to 70 detectors. Third and fourth generation CT scanners further improved the scan time and the image quality by rotating the X-ray source in a circular path rather than the sample. Third generation scanners use an arc of detectors whereas fourth generation machines use a ring of up to 1440 detectors. Scan and processing times are in the range of 30 to 40 seconds. With the introduction of fifth generation scanners, a ring of sources and detectors are used and the scan time is significantly reduced. Thus, there is no need for a rotation or translation and the scan times are so fast that even a heart beat can be scanned. Second through fourth generation scanners are used in petroleum engineering research. Advanced CT scanners, such as spiral CT (KlingenbeckRegn, 1999) where continuous volumetric scanning is possible and fifth generation, have not been utilized in petroleum engineering research yet.

[1]Petroleum and Natural Gas Engineering Department, Middle East Technical University

So-called industrial scanners are intended for analysis of inanimate objects only and have also been used for flow imaging. They differ from a medical scanner in several regards. Notably, the sample is rotated in this type of scanner as opposed to the X-ray source as in third and fourth generation medical scanners. Because they will never be used to examine living subjects, the energy of their X-ray sources is generally higher allowing the penetration of metal and relatively thick objects. Thus, laboratories housing industrial scanners general require greater shielding. On the other hand, the intensity of these sources is generally less and therefore longer scan times are required compared to a medical scanner to achieve similar accuracy. This makes the monitoring of fast displacement processes or frontal advance somewhat more difficult than with a medical scanner. These factors probably contribute to industrial scanners being utilized for flow imaging to a much lesser extent.

The remainder of this review is organized in the following fashion. First X-ray absorption theory as it relates to CT scanning is discussed. Next, imaging artifacts are discussed as is experimental design. The various applications and image processing options are then given. Our goal is to provide a comprehensive overview of the use of CT for imaging porous media and multiphase fluid flow, however we do not attempt a complete compilation of every paper that reports using CT for imaging porous media.

1.1 Theory

An X-ray is defined as the emission and propagation of energy through a medium in the form of waves that have a frequency larger than visible light and intermediate between ultraviolet and gamma rays (Weast, 1987). When a CT scanner is operated, X-rays penetrate a thin volumetric slice of an object at different angles as the X-ray source rotates around the object. A series of detectors then records the transmitted X-ray intensity. Thus, many different X-ray ray attenuations are made available for mathematical reconstruction and enhancement.

The basic quantity measured in each volume element (voxel) of a CT image is linear attenuation coefficient as defined by Beer's law

$$\frac{I}{I_o} = \exp^{-\mu h} \tag{1}$$

where I_o is the incident X-ray intensity and I is the intensity remaining after the X-ray passes through a thickness, h of homogeneous sample, and μ is the linear attenuation coefficient. For a heterogeneous medium, the energy transmitted along a particular ray path is

$$\ln\left(\frac{I}{I_o}\right) = \int_0^L \mu(h(x,y))dh \tag{2}$$

where h(x,y) are the coordinates of the attenuation coefficient in two dimensions, L is the path length from source to detector, and dh is a distance along this path length.

Beer's law assumes a narrow X-ray beam and monochromatic radiation. In practice, the actual beam is polychromatic consisting of, for instance, a spectrum of photons ranging from 20 KeV to 120 KeV. Detectors also have an associated efficiency that is energy dependent. The true situation can be represented

by an equation of the form

$$I = \int_{e_l}^{e_h} \frac{dI_0}{dE} \varepsilon(E) \exp\left(-\int_0^h \mu(x,y,E) dL \right) dE \tag{3}$$

In Eq. (3), dI_0/dE represents the spectral distribution of the incident radiation, $\varepsilon(E)$ is the efficiency of the detector at a particular energy E, e_l and e_h represent the relevant spectrum of energy with subscripts l and h signifying low and high, respectively. The attenuation coefficient is now a function of position and energy.

In practice, Eq. (2) is used to reconstruct images and it is assumed that some particular effective energy characterizes the X-ray beam as a whole. Essentially, Eq. (2) is discretized into n volume elements each with unknown attenuation coefficient. Measurement of the attenuation of multiple ray projections provides sufficient data to solve multiple equations for attenuation coefficient. Images are usually reconstructed with a filtered back propagation method. The method projects a uniform value of attenuation over each ray path so that the calculated, uniform value is proportional to the measured attenuation. Each matrix element receives a contribution from each ray passing through it. Images obtained are blurred because of the assumption that attenuation is uniform over the entire length of the ray. A convolution or filtering process is then used to modify the ray sum data and improve images. These filter functions are complex, depend on many parameters given the final result desired, and are usually proprietary. As an example, a filter function might enhance edges to sharpen an image.

After image reconstruction, relative values of linear attenuation coefficient are known for each pixel. The CT computer converts attenuation coefficients into corresponding numerical values, or CT numbers by normalizing with the linear attenuation coefficient of water, μ_w as shown below

$$CT = 1000 \frac{(\mu - \mu_w)}{\mu_w} \tag{4}$$

The units of Eq.(4) are Hounsfield (H) units. Each Hounsfield unit represents a 0.1% change in density with respect to calibration density scale. Table 1 lists the CT numbers for some common materials. Note the increase in CT number with mass density.

The linear attenuation coefficient is a function of both the electron density (bulk density), and effective atomic number, Z, in the following form (Vinegar and Wellington, 1987):

$$\mu = \rho\left(a + bZ^{3.8} / \ E^{3.2}\right) \tag{5}$$

where "a" is Klein-Nishina coefficient and "b" is a constant. By scanning at two different energy levels, E, (high and low) one image proportional to density and one image proportional to effective atomic number can be obtained. For X-ray energies above 100 keV, X-rays interact with matter by Compton scattering which depends on electron density. For energies well below 100 keV, the interaction is dominated by photoelectric absorption, which depends on the effective atomic number. Equation 5 states that the heavier elements have greater photoelectric cross section and the fraction of photoelectric contribution increases rapidly as the X-ray energy is lowered.

Assessment of porosity and in-situ phase saturation is possible once CT numbers are measured. Various expressions employed for saturation determination by CT are given later in connection with the review. All derive from the idea of subtraction. The CT numbers measured during an experiment for a partially saturated, say oil and water, porous medium consist of contributions from the rock, oil, and water phases. Subtraction allows us to isolate contributions from a particular phase. For example, by subtracting an image of rock containing both oil and water from an image of water saturated rock, the contribution of rock is removed from the resultant image. Then, normalizing by the difference in CT numbers between fully

water and oil saturated rock gives the fraction of the pore space filled with water and scales quantities to lie between 0 and 1.

2. Types of Error

Measurements with X-ray CT are subject to a variety of errors and image artifacts including "beam hardening", star-shaped or so-called "X-artifacts", positioning errors, and machine errors. These are discussed briefly.

The majority of CT scanners were developed for medical purposes and were originally intended for qualitative and not quantitative imaging. Because the X-ray source delivers a spectrum of X-ray energies (polychromatic) rather than monochromatic energy, the lower energy, or soft, portions of the X-ray spectrum are absorbed at the air/sample interface. Thus, the X-ray spectrum attenuates toward the lower energy portions of the spectrum. This introduces an error in linear attenuation measurement called "beam hardening" or "cupping" because the remaining high-energy photons shift the average energy of the beam toward "harder" X-rays. It is realized more often in relatively large objects and is manifest as dark bands around the periphery of objects. For example, the image in Fig. 1 displays typical beam hardening effects. It results in falsely high CT numbers (Herman, 1980).

The artifact amplitudes increase with scanned volume or slice width. Object scatter can be reduced in third generation CT geometry by collimating the detector elements. For fourth generation CT geometry, only poor anti-scatter collimation is possible and a numeric correction is necessary (Ohnesorge *et al.* 1999). A number of methods can be applied directly to reduce "beam hardening" effects. Reconstruction algorithms provide corrections for "beam hardening". Thus, reconstructive processing and beam filtering prior to scanning reduce the occurrence of low energy photons entering the sample. These methods, however, are not optimized for dense materials, such as reservoir rocks. Special core designs, such as surrounding the core holder with a cylindrical water jacket (Schembre *et al.* 1998, Akin *et al.* 2000) or with a crushed rock jacket, (Kuru *et al.* 1998) can minimize "beam hardening" effects. Aluminum (Akin *et al.*, 1998A) and composite carbon fiber core holders are also used for such purposes (Withjack, 1988, Akin and Demiral 1997).

Beam hardening can also be reduced by simply moving to higher energy X-ray sources. With fewer low energy photons, the degree of attenuation of the X-ray beam is reduced. Correspondingly, the average energy of the beam shifts little at material boundaries. In this regard, an industrial scanner might be superior to a medical scanner. Another method to reduce "beam hardening" is to calibrate the machine to a CT number larger than that of water, see Eq. (4). For this purpose, a doped or spiked water solution (potassium iodide or potassium bromide, or equivalent) or quartz sample can be used. The weight percentage of the solution should be selected to match the CT number of the rock, refer to Table 1. In turn, an image results where CT numbers of a homogeneous sample do not vary with the depth of penetration (i.e. a flat image). Quartz is useful for this purpose if the rock under consideration is a sandstone. Vinegar and Wellington (1987) discuss choice of dopants and calibration in detail.

Object shape can also lead to artifacts. The cross-sectional geometry of the scanner gantry is circular and the machine delivers the best images of objects that are also circular and symmetric in cross section. When square or rectangular cross sections of objects are presented to the scanner, X-shaped artifacts are witnessed in the images obtained. An example is given in Fig. 2. Note that the rock is homogeneous, but that the image contains darkly shaded portions in the shape of the letter X. Dashed white lines mark dark portions to guide the eyes.

X-shaped artifacts originate from the image reconstruction and back propagation process. During processing to obtain CT numbers of individual voxels, it is assumed that an average attenuation can be applied along each ray path. In square or rectangular images, the length of diagonals is greater then the

length of sides. Thus, as the beam is moved in angular intervals around the object, the amount of material encountered varies with the angular interval. The average attenuation then varies depending on the ray path even though the material is heterogeneous. Because the diagonals represent the greatest amount of material, CT numbers are largest there.

Positioning errors can be introduced during the process of image subtraction to obtain fluid-phase saturations or porosity. Essentially, the position of an object within subtracted images must be constant. Objects being scanned must either remain perfectly stationary or be connected to a positioning and alignment system for repeatable placement in a given position. An alternative is to employ image processing routines to center and align objects of interest prior to subtraction. This option works best for objects with cylindrical cross-sectional volume and images where the object is only slightly displaced relative to other images. The last point comes about because CT numbers obtained for an object depend slightly upon where the object is placed relative to the center of the gantry.

3. Experimental Design and Image Quality

In designing an experimental setup to be used in a CT scanner, the errors discussed above must be considered in combination with other factors such as timing, spatial resolution, and image quality. If the measurements are of static properties such as density, atomic number, porosity, or steady-state saturation, the timing of scans is not important. On the other hand, dynamic experiments, such as unsteady state relative permeability experiments and corefloods, follow the evolution of a phase as a function of position and time. Special designs are sometimes required to track rapidly moving fronts accurately. In order to monitor precisely front position and shape, Schembre *et al.* (1998), and Akin *et al.* (2000) designed an apparatus that allows the entire length of a core to be visualized in a single scan, as shown in Fig 3. Note the horizontally oriented core holder in the center of the cylindrical crosssection. On either end of the coreholder, there are endcaps for fluid distribution and maintaining position. The coreholder/endcap assembly is housed within a cylindrical water jacket for temperature control and minimization of image artifacts.

If conventional scanning of cross sections along the length of a core is employed, one can estimate the location of the flood front and the time it takes to scan the front. Then a greater number of scans can be collected in the location of the front. Another method is to stop the experiment at a particular moment to take scans (Siddiqui *et al.*, 1996 and Closmann and Vinegar, 1993). However, capillary and viscous forces cause redistribution of fluids within the core and can effect the results dramatically. Thus, this procedure is not generally recommended.

Spatial resolution is particularly important if the CT data will be used to measure fracture aperture (Hunt *et al.*, 1987). The minimum values that medical scanners can resolve are between 1 to 2 mm in spatial resolution. In the study of Hunt *et al.*, the minimum fracture aperture that could be resolved quantitatively was on the order of 0.5 mm. An alternative to direct measurement is the missing mass technique suggested by Johns *et al.* (1993). This technique, unlike the conventional measurement, lets fracture apertures as low as 0.01mm to be inferred by using a medical CT scanner. Jasti *et al.* (1993) describe a specially constructed industrial scanner where the scanned object is viewed on, apparently, a spatial resolution of 0.01 mm. In contrast to a medical scanner where a two-dimensional fan-shaped X-ray beam illuminates an object, their high resolution system uses a cone-shaped microfocal X-ray beam. Images obtained are three-dimensional because reconstruction is performed onto a specified three-dimensional grid. This eliminates the need for interpolating between two-dimensional images. Such an instrument might be useful for examining some of the relatively large features of the microstructure of a porous medium, a detailed examination of porosity, and analysis of static fluid distribution within porous media. Scan times are relatively long (20 min) making frontal tracking difficult.

Perhaps the most important factor in terms of image quality is the geometry of the experimental setup. Since the geometry of the scanner and reconstructions is circular, it is better to have round objects and to center the apparatus within the scanner gantry. This minimizes "x-artifacts". Note the circular cross section that the apparatus presents to the scanner in Fig. 3. The core holder is immersed in a cylindrical water jacket to minimize "beam hardening". Similar designs without a water jacket were reported by Hove *et al.* (1987, 1990). Another factor that affects the image quality is the usage of the medical-scanner patient table to carry experimental setups. Although the image table is transparent to X-rays, it causes a wave-like artifact to appear in the images (i.e. superimposed on the object) if the scan diameter is small. The table causes the CT numbers to be lower and noisier than those without the table. The best way to minimize the effect is to remove the table from the scan plane.

4. Flow Characterization

Next, the various applications are reviewed. CT scanning has the distinct ability to visualize many core phenomena that are otherwise undetectable by standard practices, such as front tracking and flow profiling. Visualization can be grouped into quantitative and qualitative categories. Several authors presented CT studies that include coreflood front tracking and displacement efficiency during miscible and immiscible displacement experiments (Burger *et al.* 1994, Franshan and Jelen 1986, Hove *et al.* 1987, 1990, Withjack 1988, Withjack and Akervoll 1988, Liu *et al.* 1990, Hicks *et al.* 1990, Demiral *et al.* 1991, Hicks and Deans 1994, Walsh and Withjack 1994, Bertin *et al.* 1998, Schembre *et al.* 1998, Rangel-German *et al.* 1998, Akin *et al.* 2000), mud invasion visualization (Auzerais *et al.*, 1991, Krilov *et al.* 1991, Kuru *et al.* 1998), and production of sand along with oil (Tremblay *et al.* 1998).

Quantitative studies include Wang *et al.* (1984) who reported local oil saturations using an X-ray CT scanner. They also presented images of viscous fingering, time derivatives of local composition, and residual oil distribution for the case of water displacing oil from a porous medium. Vinegar and Wellington (1987) reported measurement of three-phase saturations utilizing X-ray CT. They also described the image processing system, X-ray transparent high-pressure flow equipment, choice of fluid dopants, and X-ray energies for scanning of coreflood experiments. Examples were given of tertiary miscible carbon dioxide displacements in Berea sandstone. Withjack (1988) recorded the use of CT for saturation measurements to be used in the computation of steady state two-phase relative permeabilities. CT saturation results agreed with conventional measurements within 2 saturation percent. He also reported that the CT scanner provided an improved understanding of miscible corefloods.

Some studies concentrated on the use of CT derived multiphase saturation data for steady or unsteady state relative permeability determination. Fresnhan and Jelen (1986) proposed a method to determine saturation changes during the course of a waterflood using a second generation CT. They used production history to calibrate the change in attenuation with a corresponding change in saturation. Relative permeabilities obtained by trial and error were used to simulate the saturation profile along the core. The model predicted overall recovery, but it overestimated recovery in the first one third of the core. The authors attributed this problem to improper modeling of end effects. Mohanty and Miller (1988) obtained porosity and saturation profiles during steady state relative permeability tests. They calculated relative permeability curves for mixed-wet cores using the JBN method at three different flooding rates (low, intermediate, and high). For all cases, the flood front was not piston like, as observed in CT images. MacAllister *et al.* (1990) measured two-phase steady state gas-water relative permeabilities using a CT scanner to calculate three-dimensional fluid saturation distributions during experiments. Similarly, Kamath *et al.* (1993) analyzed three dimensional saturation profiles generated from CT scanning of waterfloods, oil floods, and miscible corefloods. They calculated relative permeability end points of the low permeability mixed-wet diatomaceous mudstones using the steady-state method. From the axially nonuniform saturation distribution images at the end of the floods, they concluded that end effects were present.

Cuthiel *et al.* (1993) performed a series of steam corefloods. Trial and error steam relative permeabilities were used to fit experimental saturation and pressure profiles to model data. Clossman and Vinegar (1993) measured steam and water relative permeabilities in natural cores at steam drive residual saturation under in-situ conditions. They found that steam relative permeabilities were in agreement with published experimental results. In related work, Ambusso *et al.* (1996) and Satik (1998) determined steady-state steam-water relative permeabilities in sandstone. They used a CT scanner to identify portions of the core with uniform saturation profiles that were, thus, appropriate for computation of relative permeability.

Siddiqui *et al.* (1996), Akin and Demiral (1997) and Sahni *et al.* (1998) used CT derived three-phase saturation data to estimate three-phase relative permeabilities whereas Barbu *et al.* (1999) examine three-dimensional phase-saturation patterns in three-phase flow. Similarly, DiCarlo *et al.* (2000A&B) used CT to elucidate the effect of porous medium wettability on three-phase relative permeability in a gravity drainage mode.

5. Porosity and Core Characterization

Next, we consider the quantitative determination of porosity. Porosity can be measured using conventional methods such as Boyle's Law porosimetry (API, 1960), or thin-section analysis (Van Golf-Recht, 1982), but it can be measured more descriptively on a local basis using CT methods. Withjack (1988) performed CT porosity measurements from two scans at the same location obtained with different fluids saturating the porous medium. The following equation based on Beer's law is used to determine the porosity for each volume element (voxel):

$$\phi = \frac{CT_{wr} - CT_{ar}}{CT_w - CT_a} \tag{6}$$

The subscripts w and a represent water-phase and air-phase CT numbers, whereas wr and ar refer to water- and air-saturated rock, respectively. Close agreement (±1-porosity percent) was reported between the CT derived porosities and those determined volumetrically.

On the right of Figure 3 is shown a sample porosity image obtained by applying Eq. (6) to a homogeneous diatomite core. Note in the raw dry and water saturated images on the left and middle of Fig. 3 that the endcaps used for positioning the core and delivering and producing fluids are evident. There are also bubbles apparent in the epoxy-filled annular region between the core and acrylic sleeve. The image of porosity on the right contains no image remnants of the gas bubbles or the endcaps because the dry and water saturated images are flat, free of beam hardening effects, x-shaped artifacts, and perfectly aligned.

Lu *et al.* (1992) used a dual scan with single energy level technique that was proposed by Moss *et al.* (1990) to calculate porosity based on Eq. (6). Using xenon gas as a contrast agent, they determined porosity images for conventional core samples and samples that exhibited dual-porosity features. More recently Watson and Mudra (1994) investigated gas storage in Devonian shales using a CT scanner and utilized Eq. (6). Alternatively, Vinegar and Kehl (1988) determined porosity using a method in which the bulk density of the material, ρ_b, must be calculated using several calibration coefficients obtained prior to scanning. The fluid and grain density of the material (ρ_f, ρ_g) must be known too.

In standard CT porosity measurement, the core sample should be 100% saturated with a contrast agent such as xenon gas or with (doped) brine. Special equipment for cleaning and saturating samples is sometimes needed. Akin *et al.* (1996) proposed a dual energy scan porosity measurement method at energy levels 1 and 2 based on estimation of a matrix CT number, CT_M. In this technique, there is no need to clean and saturate the samples with a contrast agent. The equations to solve on a pixel by pixel basis are

$$\phi = \frac{\Delta U}{\Delta N}$$

$$\Delta U = \left(CT_B^2 - CT_M^2\right)\left(CT_{ph1}^1 - CT_{ph2}^1\right) + \left(CT_{ph2}^2 - CT_{ph1}^2\right)\left(CT_B^1 - CT_M^1\right) \quad (7)$$

$$\Delta N = CT_{ph1}^2\left(CT_M^1 - CT_{ph2}^1\right) + CT_{ph2}^2\left(CT_{ph1}^1 - CT_M^1\right) + CT_M^2\left(CT_{ph1}^1 - CT_{ph2}^1\right)$$

where the subscript B refers to a given voxel and subscripts ph1 and ph2 refer to the CT numbers of pure phases.

The distribution of porosity and even raw CT images help greatly to characterize the nature (homogeneous vs heterogeneous) of a porous medium (Bergosh and Lord 1987, Karacan and Okandan 1999). Figure 4 presents a set of raw CT images taken of a carbonate core at 1 cm spacing. The presence and location of vugs is evident. Note that dark shading corresponds to high density regions and white to low. As will be discussed later, 3D image reconstructions can be used to examine further these and other phenomena.

5. 1 Permeability Distribution

Permeability cannot be measured directly but its distribution may be estimated with the help of a CT scanner. Withjack *et al.* (1990) presented a permeability distribution determination based on measuring in-situ flood-front velocities by CT scanning. In this technique, a core is assumed to be formed by a bundle of streamtubes with negligible variation of cross-sectional area along the length of each streamtube. The streamtube permeability of each voxel can be calculated from the following equation with the knowledge of average core permeability ($k_{average}$), individual streamtube porosities (ϕ_i), and the time for the solvent to flow along a given length of core (t_i).

$$k_1 = \frac{k_{average} A_T}{A\left(1 + \frac{\phi_2 t_1}{\phi_1 t_2} + \frac{\phi_3 t_1}{\phi_1 t_3} + \ldots + \frac{\phi_n t_1}{\phi_1 t_n}\right)} \quad (8)$$

Other permeabilities can then be computed from

$$\frac{k_n}{k_1} = \frac{\phi_n t_1}{\phi_1 t_n} \quad (9)$$

This technique relies on accurate estimation of individual voxel porosities and thus should be used with care. Another technique for in-situ permeability distribution determination is based on measurement of in-situ tracer concentrations with a CT scanner (Johns *et al.* 1993, and Mohanty and Johnson, 1991). In this technique, a density-matched viscous flood is conducted and monitored with a CT scanner. Complete water or oil saturated core scans are taken and then scans are taken at different intervals in time as the displacement is conducted with the same oil doped with a contrast agent. The concentration of the dopant is then calculated from the following equation.

$$C_s = \frac{CT_{osr} - CT_{or}}{CT_{sr} - CT_{or}} \quad (10)$$

The subscripts osr, or, and sr refer to the CT numbers of rock containing oil and solvent, oil-saturated rock, and solvent-saturated rock, respectively. In-situ macroscopic dispersivity values can also be computed by scanning the core at 10% and 90% concentrations and measuring the distance between the concentration

contours (Mohanty and Johnson, 1991). Yet another way of computing the permeability field is to use an empirical permeability-porosity correlation as suggested by Hicks and Deans (1994).

6. Determination of Two Phase Saturations

Many methods have been used for determining fluid saturations during multiphase coreflood experiments. These include transparent models, resistivity, X-ray absorption, nuclear magnetic resonance, X-ray and gamma ray attenuation. Honarpour *et al.* (1986) summarize these methods. All impose restrictions and provide only localized average values for the saturations. In comparison to the above-mentioned techniques, CT measurement of saturation is fast, accurate, easy to calibrate, and offers fine spatial resolution. There are several different CT methods for in situ saturation determination.

6.1 Linear Interpolation Between Pure States

In this technique, it is assumed that the CT number of the core lies on the straight line connecting complete saturation by phase 1 (say water) to complete saturation by phase 2 (say oil). Thus, a single energy scan is sufficient to measure two phase saturations as shown below.

$$CT_{owr} = (1-\phi)\mu_r + \phi S_o \mu_o + \phi S_w \mu_w \tag{11}$$

$$1 = S_w + S_o \tag{12}$$

where the subscript owr refers to rock containing both oil and water phases. Here, μ_r, μ_o, and μ_w are the attenuation coefficients for the rock matrix, core fully saturated with oil and water, respectively, and S_o and S_w are oil and water saturations, respectively. Thus the saturation of oil of each voxel can be obtained as follows

$$S_o = \frac{CT_{wr} - CT_{owr}}{CT_{wr} - CT_{or}} \tag{13}$$

One way to obtain the value of CT_{or} after scanning the water saturated core (to obtain CT_{wr}) is complete cleaning and drying of the core followed by saturation of the core with oil. Because this procedure usually requires removal of the core from its original position, it is subject to positioning errors.

Figure 5 presents example water saturation maps acquired for different diatomite cores during countercurrent water imbibition. The completely wet and dry images presented in Fig 3 are used in the denominator of Eq. (13). The water saturation scale is given on the right. Note that no effect of gravity on the imbibition front is found because capillarity dominates fluid saturation patterns. Wang *et al.* (1984) and Macallister *et al.* (1990) also demonstrated the use of Eq. (13) for various laboratory corefloods.

Another way to obtain the value of CT_{or} was reported by Alvestad *et al.* (1991). The CT value of the rock completely saturated with oil is interpolated from the dry CT and water saturated CT images with knowledge of pure phase CT numbers using the following equation.

$$CT_{or} = CT_{dry} + \frac{CT_o - CT_a}{CT_w - CT_a}\left(CT_{wr} - CT_{dry}\right) \tag{14}$$

6.2 Fluid CT Numbers

If the porosity distribution of the rock is already available, a different form of Eq. (13) that does not need complete water and oil saturated images can be used:

$$S_w = \frac{CT_{ow} - CT_{or}}{\phi(CT_w - CT_o)} \tag{15}$$

In order for the Eq. (15) to yield accurate results, the images must be perfectly flat (i.e. free of beam hardening effects). The CT numbers for water and oil (or air) should be obtained inside the core holder without the core for best results. It should be noted that if the saturation values computed with Eq. (15) decrease towards the center of the slice, beam hardening effects are present and the results are incorrect.

Figure 6 is a 3D reconstruction of S_w during a hot water flood computed using Eq. (15) (Akin *et al.* 1998). White indicates high water saturation and colors correspond to S_w as indicated by the color bar in the figure. Each reconstruction is a different time and flow is from right to left in each image. Temperature increases from 70 °F (21 °C) for images on the left to 122 °F (50 °C) in the middle and 150 °F (66 °F) on the right. The decrease in S_o and corresponding increase in S_w is quite clear.

6.3 Linear Regression

The procedure described previously assumes that no information is available except for the two pure states. Usually, average saturations at residual states are known from other laboratory techniques like Dean-Stark extraction. Therefore, complete drying of the core and resaturation with oil can be avoided by scanning the core at connate water saturation, S_{wc} that can be easily obtained from material balance. At connate water saturation, Eq. (13) can be written

$$S_o = \frac{(CT_{ow} - CT_{wr})(1 - S_{wc})}{CT_{swcr} - CT_{wr}} \tag{16}$$

where the subscript wrsc denotes a CT measurement of a core at connate water saturation. This approach assumes that the connate water saturation is uniform throughout the core. This assumption will lead to errors if there is a saturation gradient. Ganapathy *et al.* (1991) showed that in naturally heterogeneous sandstone cores the oil saturation profile at the start and the end of a coreflood was not uniform. Similarly, Qadeer *et al.* (1995) showed that there were large saturation gradients along the length of a Berea sandstone core for several corefloods monitored with a CT scanner. Similar non-uniform saturations were reported by Sprunt *et al.* (1991) for Middle Eastern carbonates and by MacAllister *et al.* (1990). Thus, the use of Eq. (16) is limited and must be undertaken with caution.

7. Determination of Three Phase Saturations

Several different methods exist for calculating three phase saturations using a CT scanner. These techniques can be categorized into four major groups: One immobile phase method, matched CT-fluids method, linear interpolation method, and dual-energy scan methods.

7.1 One Immobile Phase Method

In this technique, it is assumed that one phase is immobile and its value is constant throughout the core. With this assumption, the immobile phase's CT number is included in rock CT number in Eq. (13). Thus, it is assumed that only changes in the saturation of the remaining phases alter the CT values. The saturations of the mobile phases can be obtained by implementing the two-phase CT saturation methods given by Eqs. (11) to (13).

7.2 Linear Regression

In this method, a two-phase flood is conducted until irreducible water saturation, S_{wirr}, is achieved and a scan, CT_{oirr} is taken at this saturation. Then, three-phase flow is initiated and the water and oil saturations are obtained using the following equations and assuming that the saturations are linearly related to CT numbers. The remaining saturation can be obtained by material balance. This method was used by Siddiqui *et al.* (1996) to obtain three phase saturations of water, benzyl alcohol, and decane.

$$S_w = S_{wirr} + \left(\frac{CT - CT_{oirr}}{CT_{wr} - CT_{oirr}}\right)(1 - S_{wirr}) \tag{17}$$

$$S_o = \left(\frac{CT_{wr} - CT}{CT_{wr} - CT_{oirr}}\right)(1 - S_{wirr}) \tag{18}$$

7.3 Dual Energy Scan Method

Three-phase saturations can be most accurately obtained by scanning the core at two energy levels that are linearly independent from each other. Vinegar and Wellington (1987) presented a dual-energy method where fluid CT numbers can be used to obtain three phase saturations. They eliminated the term for the gas-phase scan by assuming that the attenuation of the gas is zero. Eq. (13) can be adapted for three phases and two energy levels as shown below:

$$CT_1 = (1-\phi)\mu_{r1} + \phi S_o \mu_{o1} + \phi S_w \mu_{w1} + \phi S_g \mu_{g1} \tag{19}$$

$$CT_2 = (1-\phi)\mu_{r2} + \phi S_o \mu_{o2} + \phi S_w \mu_{w2} + \phi S_g \mu_{g2} \tag{20}$$

$$1 = S_o + S_w + S_g \tag{21}$$

Here subscripts 1 and 2 refer to measurements at high and low-energy levels. It should be noted that the difference in linear attenuation coefficients or CT numbers should be large enough to ensure linear independence of the above equations. In other words, the high and low energy levels must measure different physical properties (Compton scattering and photoelectric absorption) as discussed in the Theory section. Therefore, at least one of the phases must be doped with a strong photoelectric absorber such as potassium bromide. The equations to obtain the saturation of each voxel are

$$S_o = \frac{(CT_{w1} - CT_{g1})(CT_2 - CT_{g2}) - (CT_{w2} - CT_{g2})(CT_1 - CT_{g1})}{(CT_{o2} - CT_{g2})(CT_{w1} - CT_{g1}) - (CT_{o1} - CT_{g1})(CT_{wr2} - CT_{g2})} \tag{22}$$

$$S_w = \frac{(CT_{o2} - CT_{g2})(CT_1 - CT_{g1}) - (CT_{o1} - CT_{g1})(CT_2 - CT_{g2})}{(CT_{o2} - CT_{g2})(CT_{w1} - CT_{g1}) - (CT_{o1} - CT_{g1})(CT_{wr2} - CT_{g2})} \quad (23)$$

where CT_1 and CT_2 refer to data for the three-phase system at high and low energy. It should be noted that, the rock is not considered in the denominator of Eqs. (22) and (23). Use of this method, is demonstrated by Akin and Demiral (1997, 1998) in a Berea sandstone plug. A different form of the above equation that includes images of gas, water, and oil saturated rock can also be used. Thus, the set of equations that use rock influence instead of pure fluid CT numbers are

$$S_o = \frac{(CT_1 - CT_{gr1})(CT_{wr2} - CT_{gr2}) - (CT_2 - CT_{gr2})(CT_{wr1} - CT_{gr1})}{(CT_{or1} - CT_{gr1})(CT_{wr2} - CT_{gr2}) - (CT_{or2} - CT_{gr2})(CT_{wr1} - CT_{gr1})} \quad (24)$$

$$S_w = \frac{(CT_2 - CT_{gr2})(CT_{or1} - CT_{gr1}) - (CT_1 - CT_{gr1})(CT_{or2} - CT_{gr2})}{(CT_{or1} - CT_{gr1})(CT_{wr2} - CT_{gr2}) - (CT_{or2} - CT_{gr2})(CT_{wr1} - CT_{gr1})} \quad (25)$$

The experimental procedure is somewhat complicated, because three end-point calibration scans are needed at each energy level. This method has been used to measure three-phase saturations using during gravity drainage experiments (Sahni *et al.* 1998, DiCarlo *et al.* 2000A, DiCarlo *et al.* 2000B).

It should be noted that multiphase liquid saturations need to be corrected using room temperature values for the case of steam injection or high temperature corefloods. This can be achieved by either obtaining the reference CT values at the corresponding temperatures or correcting the saturations after calculation. Closmann and Vinegar (1993) discuss this issue in more detail.

8. Discussion

The accuracy of the CT derived parameters such as porosity and multiphase fluid saturations can be obtained theoretically. Error analyses for different porosity measurement techniques are presented in detail by Akin *et al.* (1996). They propose two techniques. In the first technique, measurements from two scans at identical positions are compared to determine the random error. In the second technique, multiple scans of a single core position that comprise a representative statistical population of the same pixel are analyzed. They reported that the conventional CT porosity measurement technique is subject to 3.8% error if the CT number measurement has an error of 1.6%. Withjack (1988), in establishing the correctness of Eq. (6), measured porosity of Berea sandstone and dolomite samples with CT and volumetric methods. He reported agreement within 1%.

Error analysis for CT derived multiphase saturation measurements based on Eqs. (13), (22), and (23) are presented by Sharma *et al.* (1997). They reported that two-phase saturation errors were between 0.7 to 2.1%. On the other hand three-phase saturations measured during a steam injection experiment were subject to an error up to 18.7 % in magnitude. Absolute errors were roughly the same for all values of phase saturation, and therefore, the largest percentage errors occur for measurements of low saturation.

Experiments in medical CT scanners have largely been conducted in a horizontal fashion. While most scanners are designed to allow some degree of inclination with respect to the vertical, it is difficult to find scanners where the gantry can be oriented in a true vertical fashion, that is, parallel to the floor. Chiefly, this a mechanical design problem in that the bearings supporting the gantry will not allow it to

rotate while in vertical mode. Notable exceptions are the work of Sahni *et al.* (1998), DiCarlo *et al.* (2000A&B), and Kantzas *et al.* (1988) where true vertical positioning was employed.

This overview of previous work suggests many best practices for obtaining high-quality data from CT. In brief, apparatus that present circular cross sections to the scanner eliminate or greatly reduce x-artifacts originating from unequal X-ray path lengths through scanned materials. With some care in the design of coreholders, beam hardening effects can be reduced greatly along with x-artifacts and flat artifact-free images obtained. In this regard, it is strongly suggested to design positioning systems that do not rely on standard medical CT patient couches. These couches are prone to errors in positioning apparatus repeatedly and introduce wave-like artifacts in images. At the very least, patient couches should be removed from the scan plane.

For quantitative representation of porosity or fluid-phase saturation, image processing equations that use fully saturated porous media as end states give the most accurate and least ambiguous results. Specifically, Eq. (6) should be used for porosity, Eq. (13) for determination of two-phase saturation, and Eqs. (24) and (25) for three-phase saturation. If it is difficult or impossible to obtain one of the necessary fully-saturated images, then pure fluid CT numbers and the local porosity field should be used to back-calculate the fully saturated porous media image. For example, Eq. (15) could be used for two-phase saturation and Eqs. (22) and (23) for three-phase saturation.

8.1 Frontiers

There are a number of frontiers that remain in CT scanning of porous media. The first is complete volumetric monitoring of dynamic experiments. Current 1st through 4th generation scanners collect data from thin volumetric sections. Generally, coverage of a porous medium with such scans is incomplete because of the need to sample the entire core at a relatively rapid rate. Interpolation between, essentially, two-dimensional cross sections is required to infer three-dimensional information; hence, detail is lost. Spiral CT (KlingenbeckRegn *et al*, 1999) provides the opportunity for subsecond acquisition times of multiple slices. This development puts complete volumetric scanning of "fast" displacement processes within reach. To date, there have been no reports of experiments utilizing this tool.

Another frontier is routine scanning at spatial resolutions on the order of 0.1 to 0.01 mm. With such detailed information fracture networks and other fine-scale heterogeneity could be characterized and flow in them resolved. This objective will be quite difficult to obtain with a medical scanner as there is little driving force in the medical community to obtain resolution finer than about 0.25 mm with these devices. In this regard, industrial scanners may provide a pathway forward. Machines have been introduced with resolution of around 0.1 mm. Problems to overcome for measurement of in-situ saturations might include shorter scan times as discussed earlier, accurate repeatable positioning of the object to be scanned, and positioning of the source/receiver assembly which is variable in some industrial scanners. Recently developed computed microtomography (CMT) for imaging of porous media offers spatial resolution on the order of 5 μm (Coles *et al* 1996, 1998). Unfortunately, synchrotron X-rays are required and porous medium sample sizes to date have only been about 2.5 cm in both diameter and length. The need for synchrotron radiation probably limits usage as a widespread porous media characterization and flow monitoring method.

CT scanning is advanced sufficiently to provide information on convective transport properties and multiphase fluid saturation structures in porous media. This is not the case, however, with diffusive transport processes. Recent work (Nakashima 2000) showed how CT imaging could be used to measure diffusion coefficients of ions in water saturated rocks and clays. Thus far, the technique is limited to relatively heavy ions, such as iodine (I-) where the mass attenuation coefficient is large. Extension to other and perhaps lighter ions could provide advantages over other conventional laboratory techniques for measuring ion diffusion coefficients.

Image processing remains an area where progress could be made. The requirements of medical and petrophysical scanning are not identical. To date, most image processing to convert raw attenuation data to CT numbers has relied upon the proprietary algorithms developed by scanner manufacturers. These image processing routines are not optimized for dense materials such as rock and the aluminum or plastic used in coreholders. Improvements might be made by simply considering image reconstruction for flow in porous media applications separate from the medical community.

9. Summary

Review of CT scanning as a qualitative and quantitative tool in petroleum engineering research is given. The development and application of X-ray computed tomography for the determination of rock properties and the study of coreflooding dynamics are discussed in detail. Multiphase saturation, porosity and permeability determination using different methods with a CT scanner is presented. The advantages and disadvantages of these methods as well as their accuracy are discussed. Finally, factors affecting experiments are discussed and techniques to handle such problems are suggested.

Nomenclature

Roman

a	: Klein-Nishina coefficient
A	: area
b	: constant, 9.8×10^{-24}
C	: concentration
CT	: CT number
e	: energy, limits of integration
E	: energy level
h	: thickness
I	: x-ray intensity
k	: permeability
L	: length
S	: saturation
t	: time
Z	: atomic number

Greek

ε	: efficiency
ϕ	: porosity
μ	: linear attenuation coefficient
ρ	: density

subscripts and superscripts

0	: incident radiation
1, 2	: low and high energy levels
avg	: average
b	: bulk
e	: experimental
f	: fluid
g	: gas or grain
l, n	: index
o	: oil
ow	: oil + water
os	: oil + solvent
r	: rock
ph1	: phase 1
ph2	: phase 2
s	: solvent
swc	: connate
w	: water
wrsc	: connate water + rock
B	: base
M	: matrix

References

1. Akin S., Castanier, L. M. and Brigham, W.E.: "Effect of Temperature on Heavy-Oil/Water Relative Permeabilities", SPE 49021, proceedings of the 1998 SPE Annual Technical Conference and Exhibition, New Orleans (September 27-30, 1998).

2. Akin, S., and Demiral, B.: "Effect of Flow Rate on Imbibition Three-Phase Relative Permeabilities and Capillary Pressures," SPE 38897 proceedings of the 1997 SPE Annual Technical Conference and Exhibition, San Antonio (October 5-8, 1997) 575-584

3. Akin S, and Demiral B. "Application of Computerized Tomography to the Determination of Three Phase Relative Permeabilities" paper 122, proceedings of the 8th International Symposium on Flow Visualization, Sorrento, Italy (September 1-4, 1998).

4. Akin, S., Demiral, B., and Okandan, E.: "A Novel Method of Porosity Measurement Utilizing Computerized Tomography", *In Situ*, Vol. 20, No 4 (1996) 347-365.

5. Akin S., and Kovscek A.R.: "Imbibition Studies of Low-Permeability Porous Media," paper SPE 54590 proceedings of the 1999 SPE Western Regional Meeting, Anchorage (May 26-28, 1999).

6. Akin, S., Schembre, J.M., Bhat, S. K., and Kovscek, A. R., "Spontaneous Imbibition Characterisitcs of Diatomite," *J. Pet. Sci. Eng.*, Vol 25 (2000) 149-165.

7. Alvestad J., Gilje E., Hove, A.O., Langeland O., Maldal T., and Schilling B.E.R.: "Coreflood Experiments With Surfactant Systems for IOR: Computer Tomography Studies and Numerical Modelling" proceedings of the 6th European IOR Symposium held in Stavanger, Norway (May 21-23, 1991) 789-800.

8. Ambusso, W., Satik, C, and Horne, H. "Determination of Relative Permeability for Steam-Water Flow in Porous Media," SPE 36682, Proceedings of the 1996 SPE Annual Technical Conference and Exhibition, Denver (October 6-9, 1996).

9. American Petroleum Institute: "API Recommended Practice for Core Analysis Procedures," API Report No 40, American Petroleum Institute, Dallas (1960), 17, 28-30.

10. Auzerais F.M., Dussan E.V., and Reischer A.J.: "Computed Tomography for the Quantitative Characterization of Flow Through a Porous Medium," SPE 22595, proceedings of the 66th Annual Technical Conference and Exhibition of SPE held in Dallas (October 6-9, 1991) 83-95.

11. Barbu, A., Hicks, P. J. Jr., and Grader, A. S.: "Experimental Three-Phase Flow in Porous Media: Development of Saturated Structures Dominated by Viscous Flow, Gravity, and Capillarity," Soc. Pet. Eng. J., 4(4) (December 1999) 368-379.

12. Bergosh J.L. and Lord G.D.: "New Developments in the Analysis of Cores From Naturally Fractured Reservoirs," SPE 16805 proceedings of the 62nd Annual Technical Conference and Exhibition of the SPE, Dallas (September 27-30 1987) 563-570.

13. Bertin H.J., Apaydin O.G., Castanier L.M., and Kovscek A.R.: "Foam Flow in Heterogeneous Porous Media: Effect of Crossflow" *Soc. Pet. Eng. J.*, 4(2), (June 1999) 75-82.

14. Burger, J. E., Bogeswara, R., and Mohanty, K. K.: "Effect of Phase Behavior on Bypassing in Enriched Gas Floods," Soc. Pet. Eng. Res. Eng. 9 (May 1994) 112-118.

15. Closmann, P. J. and Vinegar, H. J.: "A Technique for Measuring Steam and Water Relative Permeabilities at Residual Oil in Natural Cores: CT Scan Saturations," Journal of Canadian Petroleum Technology 32, No. 9 (November 1993) 55-60.

16. Coles, M. E., Hazlett, R. D., Spanne, P., Muegge, E. L., and Furr, M. J., "Characterization of Reservoir Core Using Computed Microtomography", SPE J. (September 1996) 295-301.

17. Coles, M. E., Hazlett, R. D., Spanne, P., Soll, W. E., Muegge, E. L., and Jones, K. W., "Pore-level Imaging of Fluid Transport Using Synchrotron X-ray Microtromography", J. Pet. Sci. & Eng. 19 (1998), 55-63.

18. Cuthiell, D., Sedgwick, G., Kissel, G., and Wooley, J.: "Steam Corefloods With Concurrent X-ray CT Imaging," Journal of Canadian Petroleum Technology 32, No: 3 (March 1993) 37-45.

19. DiCarlo, D. A., Sahni. A., and M. J. Blunt, "The Effect of Wettability on Three-Phase Relative Permeability," Soc. Pet. Eng J., 5(1) (March 2000 A) 82-91.

20. DiCarlo, D. A., Sahni. A., and M. J. Blunt, "Three-Phase Relative Permeability of Water-Wet, Oil-Wet, and Mixed-Wet Sandpacks," Trans. Porous Media, 39 (2000 B) 347-366.

21. Frenshan, P. B., and Jelen, J.: "Displacement of Heavy Oil Visualized by CAT Scan," paper presented at the 37th Annual Technical Meeting of the Petroleum Society of CIM, Calgary, (June 8-11, 1986) 605-620.

22. Ganapathy S., Wreath D.G., Lim M.T., Rouse B.A., Pope G.A., and Sepehrnoori K.: "Simulation of Heterogeneous Sandstone Experiments Characterized Using CT Scanning," SPE 21757, proceedings of the Western Regional Meeting held in Long Beach (March 20-22, 1991) 79-90.

23. Garg A., Kovscek A. R., Nikravesh M., Castanier L. M., and Patzek T. W.: "CT Scan and Neural Network Technology for Construction of Detailed Distribution of Residual Oil Saturation During Waterflooding," SPE 35737, proceedings of the SPE Western Regional Meeting, Anchorage (May 22-24, 1996).

24. German ER, Akin S, and Castanier L.M.: "Multiphase-Flow Properties of Fractured Porous Media," SPE 54591 proceedings of the 1999 SPE Western Regional Meeting, Anchorage (May 26-28, 1999).

25. Herman, G.T.: "Image Reconstruction from Projections," The Fundamentals of Computerized Tomography, Academic Press, NYC (1980) 76-83, 161-179.

26. Hicks, P. J., and Deans, H. A.: "Effect of Permeability Distribution on Miscible Displacement in a Heterogeneous Carbonate Core," Journal of Canadian Petroleum Technology 33, No: 8, (October 1994) 28-34.

27. Hicks Jr., P.J., Deans, H. A., Narayanan, K.R.: "Distribution of Residual Oil in Heterogeneous Carbonate Cores Using X-Ray CT," 1992 International Technical Meeting Jointly Hosted By The Petroleum Society Of CIM and The Society Of Petroleum Engineers, Calgary (June 10-13 1992).

28. Hicks, P. J., Naranayan, R., and Deans, H. A.: "An Experimental Study of Miscible Displacements in Heterogeneous Carbonate Cores Using X-Ray CT," SPE 20492, paper presented at the 65th Annual Technical Conference and Exhibition of SPE, New Orleans (September 23-26, 1990) 231-245.

29. Hounsfield, G.N.: "A Method of and Apparatus for Examination of a Body by Radiation Such as X or Gamma Radiation," British Patent No. 1,283,915, London (1972).

30. Hove, A.O., Nilsen, V., and Leknes, J.: "Visualization of Xanthan Flood Behavior in Core Samples by Means of X-Ray Tomography," *SPERE*, (November 1990) 475-480.

31. Hove, A.O., Ringen, J.K., and Read, P.A.: "Visualization of Laboratory Corefloods With the Aid of Computerized Tomography of X-Rays, " *SPERE* (May 1987) 148-154.

32. Honarpour M. Koederitz L., and Harvey A.H.: Relative Permeability of Petroleum Reservoirs, CRC Press (1986) 143 pp.

33. Hunt, P. K., Engler, P., and Bajscrowicz, C.: "Computed Tomography as a Core Analysis Tool: Applications and Artifact Reduction Techniques, SPE 16952, paper presented at the SPE Annual Technical Conference and Exhibition, Dallas (September 27-30, 1997).

34. Jasti, J. K., Jesion, G., and Feldkamp, L.: "Microscopic Imaging of Porous Media with X-Ray Computer Tomography," Soc. Pet. Eng. Form. Eval. (September 1993) 190-193.

35. Johns R.A., Steude J.S., Castanier L.M., and Roberts P.: "Nondestructive Measurements of Fracture Aperture in Crystalline Rock Cores Using X-Ray Computed Tomography" Journal of Geophysical Research 98, No. B2 (February 10, 1993) 1889-1900.

36. Kamath, J., Zabala, E.F., and Boyer, R.E.: "Water/Oil Relative Permeability Endpoints of Intermediate-Wet Low-Permeability Rocks," Soc. Pet. Eng. Form Eval, 10(1) (March 1995) 4-10.

37. Kantzas, A., Chatzis, I., Macdonald, F., and Dullien, F. A. L., "Using a Vertical Scanner for Horizontal Scanning in Non-medical Applications of Computer Assisted Tomography" CSNDT J., (March and April 1988), 20-25.

38. Karacan C.O. and Okandan E.: "Heterogeneity Effects on the Storage and Production of Gas From Coal Seams," SPE 56551, paper presented at the 1999 SPE Annual Technical Conference and Exhibition, Houston, (October 3-6, 1999).

39. KlingenbeckRegn K, Schaller S, Flohr T, Ohnesorge B, Kopp AF, Baum U: "Subsecond Multi-Slice Computed Tomography: Basics And Applications", European Journal of Radiology, 31, no. 2 (August 1999) 110-124.

40. Krilov Z., Steiner I., Goricnik B., Wojtanowicz A.J., and Cabrajac S.: "Quantitative Determination of Solids Invasion and Formation Damage Using CAT Scan and Barite Suspensions," SPE 23102, proceedings of the 1991 Offshore Europe Conference, Aberdeen, Scotland (September 3-6. 1991).

41. Kuru, E, Demiral B, Akin S., Kerem M., and Cagatay B.: "An Integrated Study of Drilling-Fluid Shaly Rock Interactions: A Key to Solve Wellbore Instability Problems", Oil Gas European Magazine, 24, No 1 (March 1998) 25-29.

42. Lu, X.C., Pepin, G.P., and Moss, R.M.: "Determination of Gas Storage in Devonian Shales With X-Ray Computed Tomography," SPE 24810, paper presented at the 67th Annual Technical Conference and Exhibition of SPE, Washington, DC, (October 4-7, 1992) 455-466.

43. MacAllister, D.J., Miller, K.C., Graham, S.K., and Yang, C.T.: "Application of X-ray CT Scanning to the Determination of Gas-Water Relative Permeabilities," SPE 20494, paper presented at the 65th Annual Technical Conference and Exhibition of SPE held in New Orleans (September 23-26, 1990), 255-267.

44. Mohanty K.K, and Johnson S.W.: "Interpretation of Laboratory Gasfloods With Multidimensional Compositional Modeling," SPE 21204, proceedings of the SPE Symposium on Reservoir Simulation, Anaheim (February 17-20, 1991) 19-34.

45. Mohanty, K.K. and Miller, A.E.: "Factors Influencing Unsteady Relative Permeability of a Mixed-Wet Reservoir Rock," SPE 18292, paper presented at the 63rd Annual Technical Conference and Exhibition of SPE, Houston (October 2-5, 1988).

46. Nakashima, Y.; "The Use of X-ray CT to Measure Diffusion Coefficients of Heavy Ions in Water-Saturated Porous Media," Engineering Geology, 56(1-2) (April 2000) 11-17.

47. Ohnesorge B, Flohr T, KlingenbeckRegn K: "Efficient Object Scatter Correction Algorithm For Third And Fourth Generation CT Scanners", European Radiology, 9 , no. 3 (1999) 563-569.

48. Qadeer, S., K. Aziz, J. Fayers, L.M. Castanier, and W.E. Brigham: "An error analysis of relative permeabilities calculated using conventional techniques," proceedings of IEA Enhanced Oil Recovery, Bergen (August 28-31, 1994).

49. Sahni A., Burger, J. E., and Blunt, M.J.: "Measurement of Three Phase Relative Permeability during Gravity Drainage using CT Scanning." SPE 39655, proceedings of the 1998 SPE/DOE Improved Oil Recovery Conference, Tulsa (April 19-22, 1998).

50. Satik, C., "A Study of Steam-Water Relative Permeability," SPE 46209, proceedings of the SPE Western Regional Meeting, Bakersfield (May 10-13, 1998).

51. Sharma B.C., Brigham W.E., and Castanier L.M.: "CT Imaging Techniques for Two-Phase and Three-Phase In-Situ Saturation Measurements" Report SUPRI TR 107, Stanford University, Stanford, California, 1997.

52. Schembre, J.M., Akin, S., Castanier, L.M., and Kovscek A.R.: "Spontaneous Water Imbibition into Diatomite" SPE 46211, proceedings of the 68th Annual SPE Western Regional Meeting, Bakersfield (May 9-15, 1998).

53. Sedgwick, G E. and Dixon, E.M.: "Application of X-ray Imaging Techniques to Oil Sands Experiments," Journal of Canadian Petroleum Technology, 27, no. 2, (March and April 1998) 104-110.

54. Siddiqui S., Hicks P.J., and Grader A.S.: "Verification of Buckley-Leverett Three-Phase Theory Using Computerized Tomography" Journal of Petroleum Science and Engineering 15 (1996) 1-21.

55. Sprunt E.S., Desal K.P., Coles M.E., Davis R.M., and Muegge E.L.: "CT-scan-Monitored Electrical-Resistivity Measurements Show Problems Achieving Homogeneous Saturation," SPE Formation Evaluation (June 1991) 134-140.

56. Van Golf-Recht, T.D.: Fundamentals of Fractured Reservoir Engineering, Elsevier Scientific Publishing Co., Amsterdam, The Netherlands, (1982) 151.

57. Vinegar, H.J., and Wellington, S.L.: "Tomographic Imaging of Three-Phase Flow Experiments," Rev. Sci. Instrum., 58 [1] (January 1987) 96-107.

58. Walsh, M.P., and Withjack, E.M.: "On some Remarkable Observations of Laboratory Dispersion Using Computed Tomography [CT]," Journal of Petroleum Technology, 33, no. 9 (November 1993).

59. Wang, S.Y., Huang, Y.B., Pereira, V., and Gryte, C.C.: "Application of Computed Tomography to Oil Recovery From Porous Media," Applied Optics, 24, No: 23 (December 1985) 4021-4027.

60. Watson, A.T., and Mudra, J.: "Characterization of Devonian Shales With X-Ray Computed Tomography," Soc. Pet. Eng Form Eval, (September 1994) 209-212.

61. Wellington, S.L., and Vinegar, H.J.: "X-Ray Computerized Tomography," JPT (August 1987) 885.

62. Withjack, E.M.: "Computed Tomography for Rock Property Determination and Fluid Flow Visualization," Soc. Pet. Eng Form Eval (December 1988), 696.

Table 1. CT numbers for common materials.

material	CT (H) 130 KeV	CT (H) 100 KeV	density (kg/m^3)
air	-1000		1.82
n-hexane	-285		660
n-decane	-283		730
water	0		1000
1wt% KBr in water	70	91	1005
2wt% KBr in water	142	183	1013
8wt% KBr in water	565	725	1058
PVC	620		1400
quartz	1589	1836	2190
Berea sandstone	1608	1835	2120
Colton sandstone	1629	1840	2270
Navaho sandstone	1858	2102	2360
Red Navaho sandstone	1912	2156	2390
Indiana limestone	1531	1750	2220
alumina	2478	2866	2820

Notes: CT numbers for minerals and rocks measured at a tube current of 250 mA on a Philips Tomoscan with a 16 cm field of view. Other values measured on a Picker 1200 SX at a tube current of 65 mA and a 16 cm field of view.

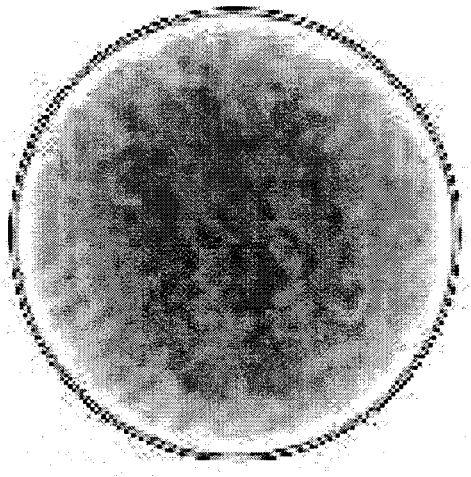

Figure 1. Example of beam hardening in scanning a homogeneous object. Note the lighter shading just inside the core holder.

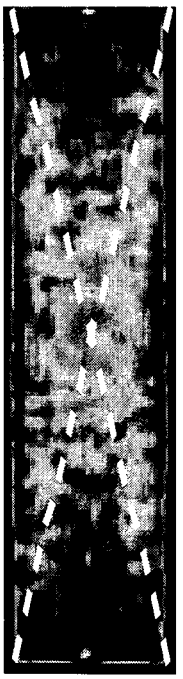

Figure 2. Example of an x artifact in scanning a homogeneous object. Dashed white lines are drawn to guide the eyes.

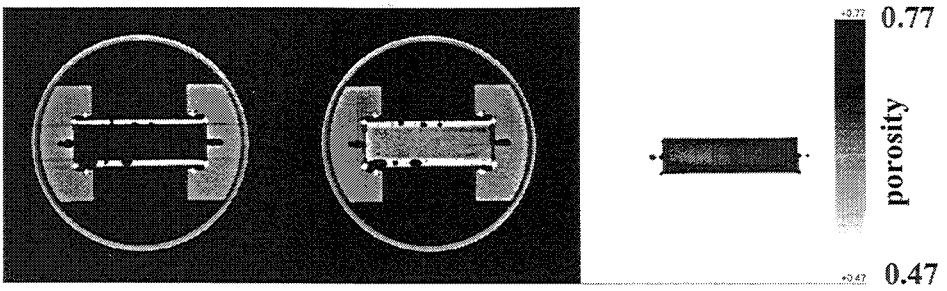

Figure 3. Scan of imbibition cell that allows imaging of entire core length. Dry image (left), water saturated image, (middle), and porosity image (right).

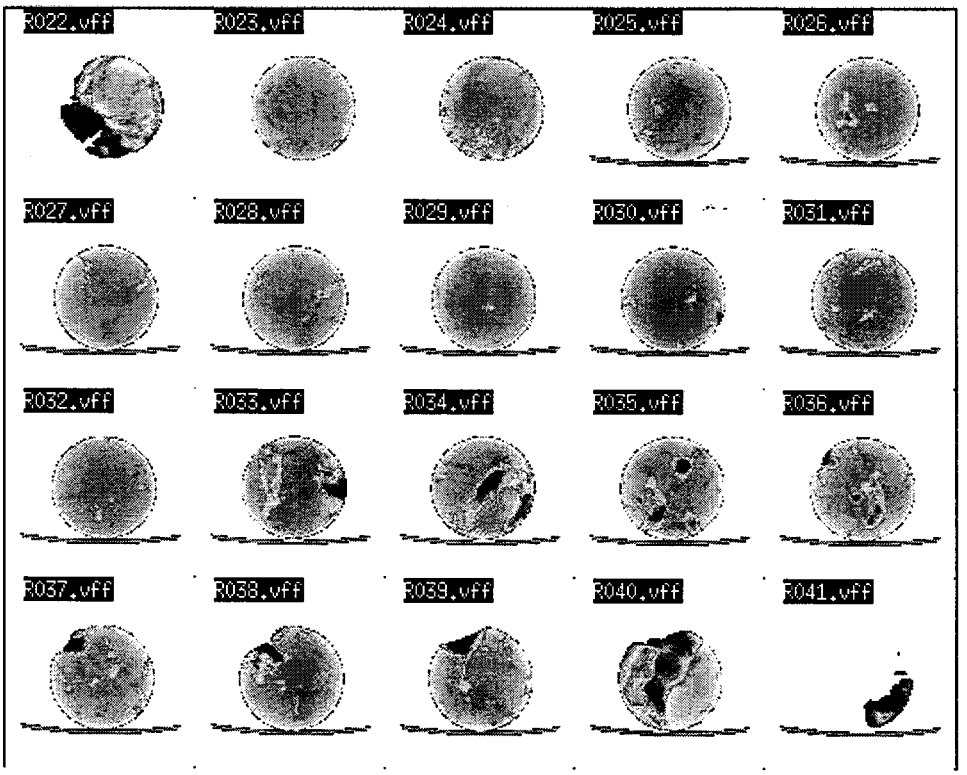

Figure 4. Scans of carbonate core at 1 cm spacing.

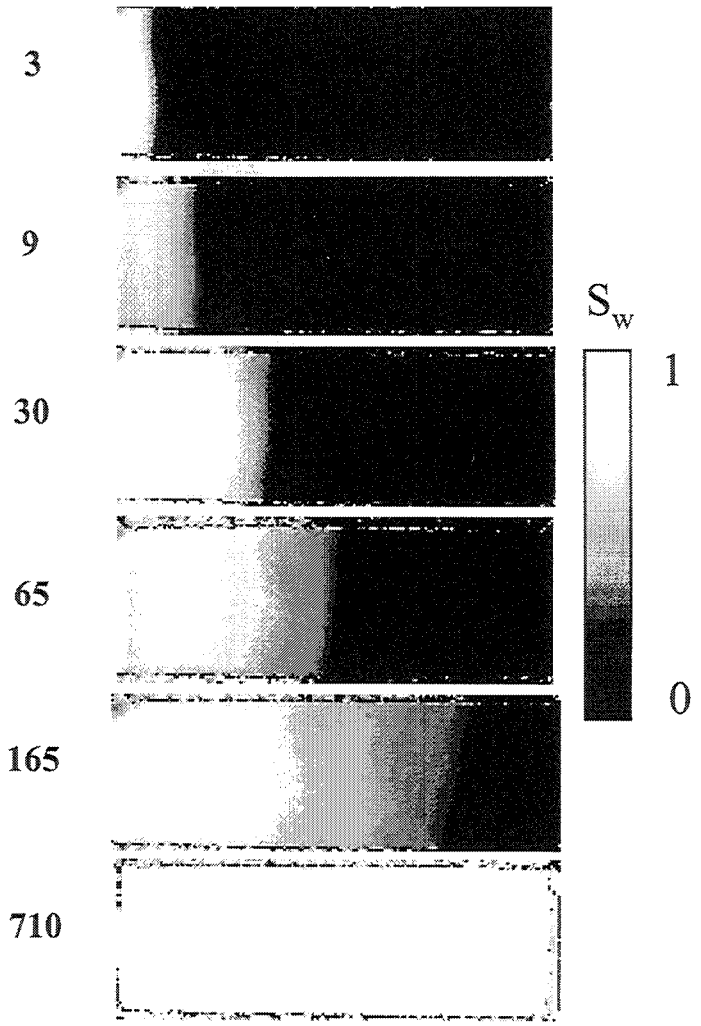

Figure 5. CT-derived water saturation images of spontaneous imbibition in diatomite. Water displacing air. Time in minutes is given next to each image.

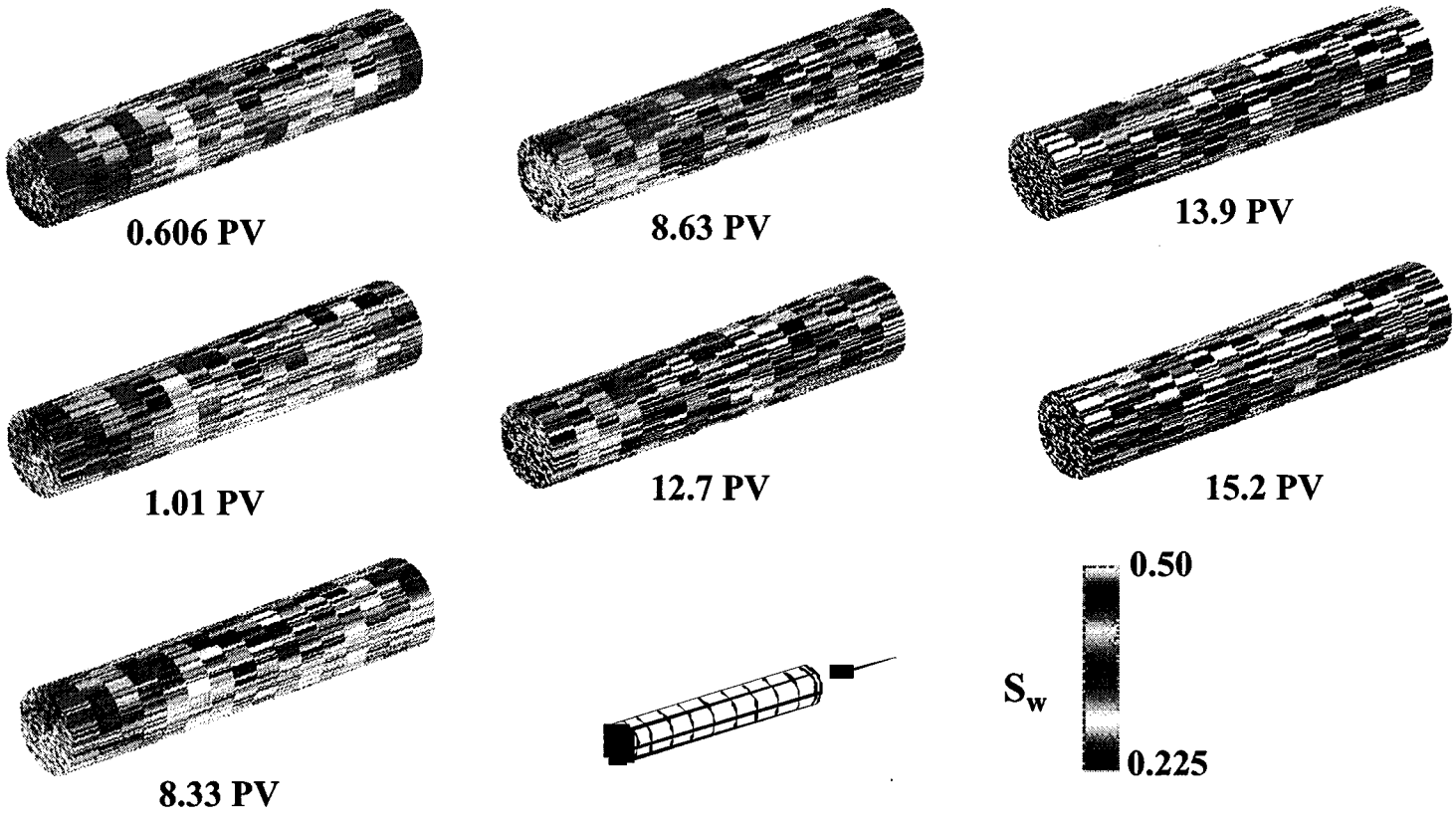

Figure 6. 3D reconstruction of water saturation in a sandpack undergoing hot-water flood.
Times are given as pore volumes of water injected. Water temperature is increased during the experiment.
Left images: 70 °F (21 °C). Center: 122 °F (50 °C). Right 150 °F (66 °C).

HOT FLUID INJECTION

Light-Oil Steam Injection into Diatomite Reservoirs

B. Todd Hoffman

Abstract

A class of reservoirs composed of diatomite rock contain a high proportion of relatively light oil. Characteristics of diatomites include high porosity (~50%) and low permeability (~1 md). In the San Jouquin Valley (Kern County, CA), diatomite reservoirs lie between 500 and 2000 feet deep and initial reservoir pressures are roughly 500 to 1000 psi. Pilot steamflooding in diatomite has shown a great deal of success; however, the mechanisms that caused the floods to be successful have not yet been determined. Though light-oil steamflood (LOSF) is not new technology, it is an area without a great deal of research. Heavy-oil steamflooding, especially in shallow reservoirs, is a proven technology with a number of large commercial projects across the globe, however LOSF has still not reached that stage. A handful of field cases and a number of experimental results amount to all the research in LOSF. Unlike heavy oil there have been very few large-scale continuous commercial light oil projects reported in the literature.

This review lays out how steamflooding and particularly light oil steamflooding has emerged. Also discussed are the mechanisms that provide for the recovery of oil in a steamflood, and the mechanisms that are the most important for particular reservoir characteristics. A number of LOSF pilot tests will be evaluated, along with the factors that contributed to the successes and failures of the particular floods. Some special circumstances associated with diatomite reservoirs will be mentioned along with the fractures properties of this rock type. The review will end with some concluding remarks and areas of planned research.

Introduction

In 1952, steamflooding was initiated as an enhanced recovery technique. The famous pilot at Yorba Linda Field in California began the steam injection process into oil reservoirs. Through the 1950's and 1960's steamflood technology was in the initial experimental phase with a number of pilot tests. This early work determined that steam injection is generally most efficient in highly permeable rock ($k > 1$ Darcy) and thick sands, usually greater than 30 feet. Once industry had gained enough confidence from these pilot tests, it was ready to make some significant investments in steam flooding. By the 1970's a number of fields were benefiting from steamdrive technology, and production peaked (Figure 1) in the mid 1980's and has since been fairly constant. This production has been almost exclusively from the heavy oil realm (Blevens, 1990).

Light oil steam flood also had its roots in California. In the 1960's, one of the first LOSF field trials was initiated at the Brea Field near Los Angeles. Brea consisted of steeply dipping sands that had an average permeability around 70 md and a typical porosity value about 22% (Volek and Pryor, 1972). The development of LOSF was not as rapid as with heavy oil. Heavy oils benefited tremendously from steam injection, compared to waterflood, because of the oil viscosity reduction caused by the increase in reservoir temperature. Unlike heavy oils, light oils produce very successfully from water drives, and because water drives are seen as less risky with less initial investment than steam injection, LOSF were developed more sparsely (Hanzlik, 1981). Regardless, there are a number of applications where LOSF seem to be as good if not a better route than waterflooding, for example highly dipping reservoirs and unconsolidated sandstones. Application in low-permeability highly-fractured reservoirs, such as diatomite, is still to be proven.

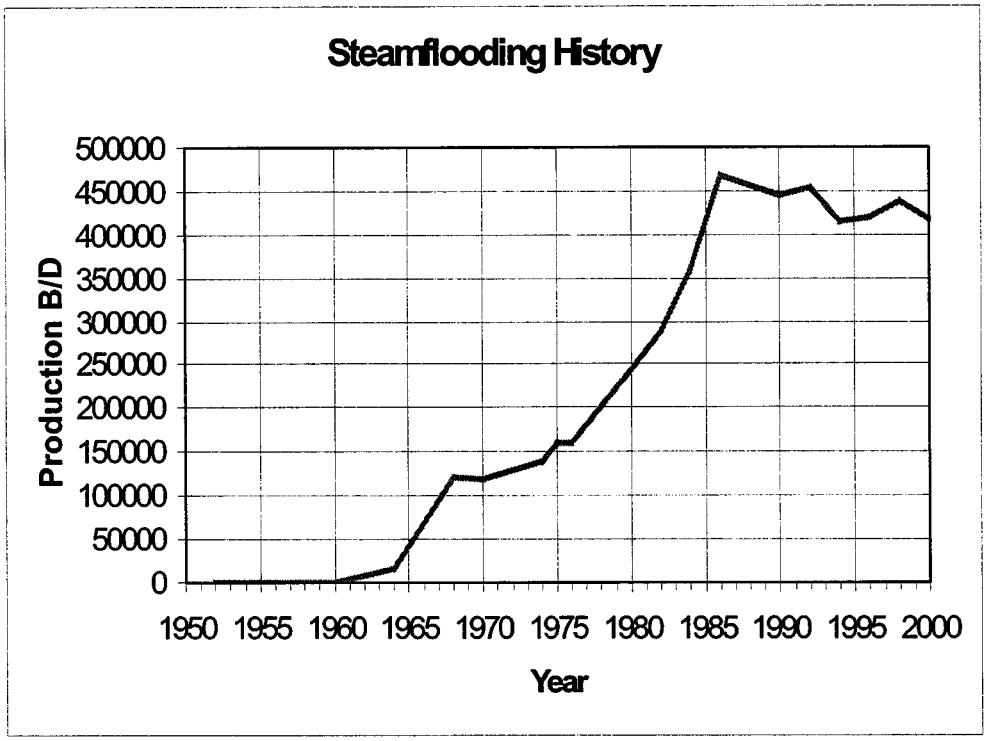

Figure 1. Steamflood Production from initiation at Yorba Linda through 1990 (Moritis, 2000)

Low-permeability fractured reservoirs contain a large volume of oil around the world, yet production from these reservoirs has been modest. Primary production is notoriously low, usually 5% - 10% of original oil-in-place. Additionally, waterfloods in these reservoirs usually suffer from low injectivity, poor sweep, and fracture-to-producer linkage which all tend to make the project uneconomic. All of these factors have facilitated an attempt to use enhanced recovery techniques, such as steam injection, to increase the recoverable reserves.

Mechanisms

Whether steamflooding is applied to heavy or light oils and high or low permeable reservoirs, the general mechanisms remain the same. The difference lies in the amount a particular mechanism effects a particular hydrocarbon reservoir (Blevins, *et al.,* 1984) . Figure 2 qualitatively displays the roles certain mechanisms play for light to heavy oils. As depicted thermal expansion and vaporization are the most important for light oil and viscosity reduction plays the primary role for heavy oils. In the literature there is a significant detail paid to steamflooding mechanisms. Wu presented a critical review of steamflood mechanisms (Wu, 1980). He and others have identified the following, which should be considered a

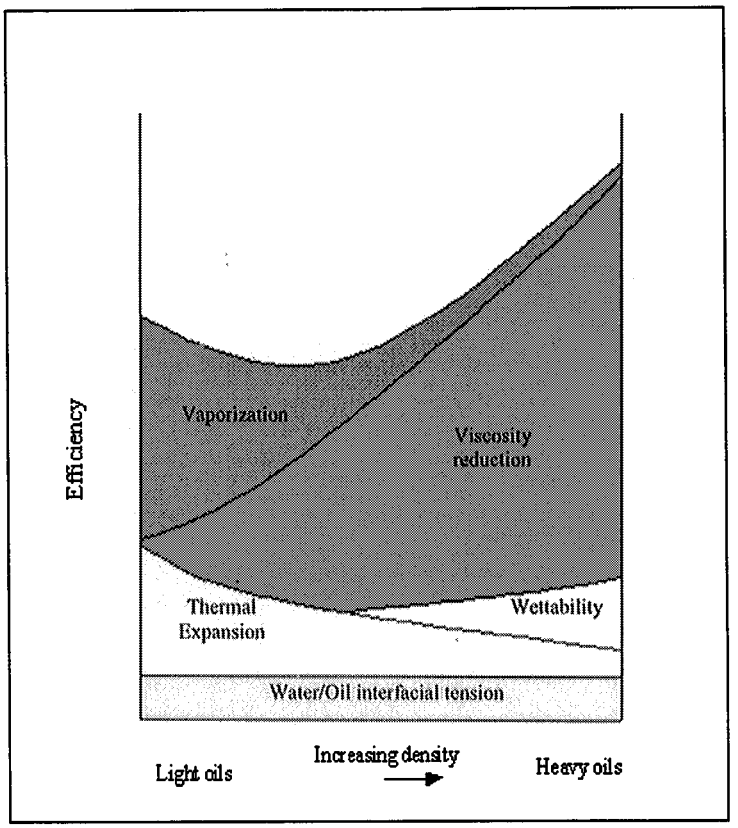

Figure 2. Contributions of different mechanisms to the improvement of oil displacement by a heated fluid instead of cold water (Burger *et al.*, 1985).

thorough but not exhaustive list:

(1) viscosity reduction;
(2) distillation (vaporization);
(3) distillate (in situ solvent) drive;
(4) steam (gas) drive;
(5) thermal expansion;
(6) relative permeability and capillary pressure variation; and
(7) gravity segregation.

In high viscosity reservoirs, the objective of steamflooding is to increase oil production by reducing oil viscosity allowing oil drainage at significantly higher rates. Conversely, for low viscosity oils the primary objective is to reduce residual oil saturation below that obtainable by ordinary waterflooding through steam distillation and steam distillation drive. In fractured systems or highly heterogeneous reservoirs, thermal conduction allows heat to sweep areas of the reservoir not contacted by steam. In this case, thermal expansion and possibly vaporization, are important recovery mechanisms.

Distillation

Farouq Ali (1968) estimated that 5% – 10% of heavy oil production could be attributed to steam distillation, and as much as 60% of the oil recovery from some light oils may be attributed to the same mechanism. Since the distillation process is so instrumental to the success of LOSF, some time will be

spent discussing it further. When steam is constantly injected into a continuous oil-bearing reservoir layer, four separate zones develop in the reservoir as shown in Figure 3. The way these zones are formed is of particular interest to LOSF. When the initial steam contacts the cold reservoir, the steam is condensed to hot water. As the reservoir is heated up, some steam will remain in the vapor phase and a steam zone begins to develop. In this steam zone, the high temperature causes some of the hydrocarbons to be vaporized. As more steam is injected, the vaporized oil is carried forward along with the steam. A portion of the steam and distillate condense at the steam front causing a distillate bank to form. The vaporization, transport, and condensation of the hydrocarbon fractions is a dynamic process that displaces the lighter hydrocarbons and generates a distillate bank that miscibly drives the reservoir oil to the production wells (Duerksen and Hsueh, 1983). The combination of the distillate bank drive and steam vaporization leaves very low residual oil saturation in the reservoir.

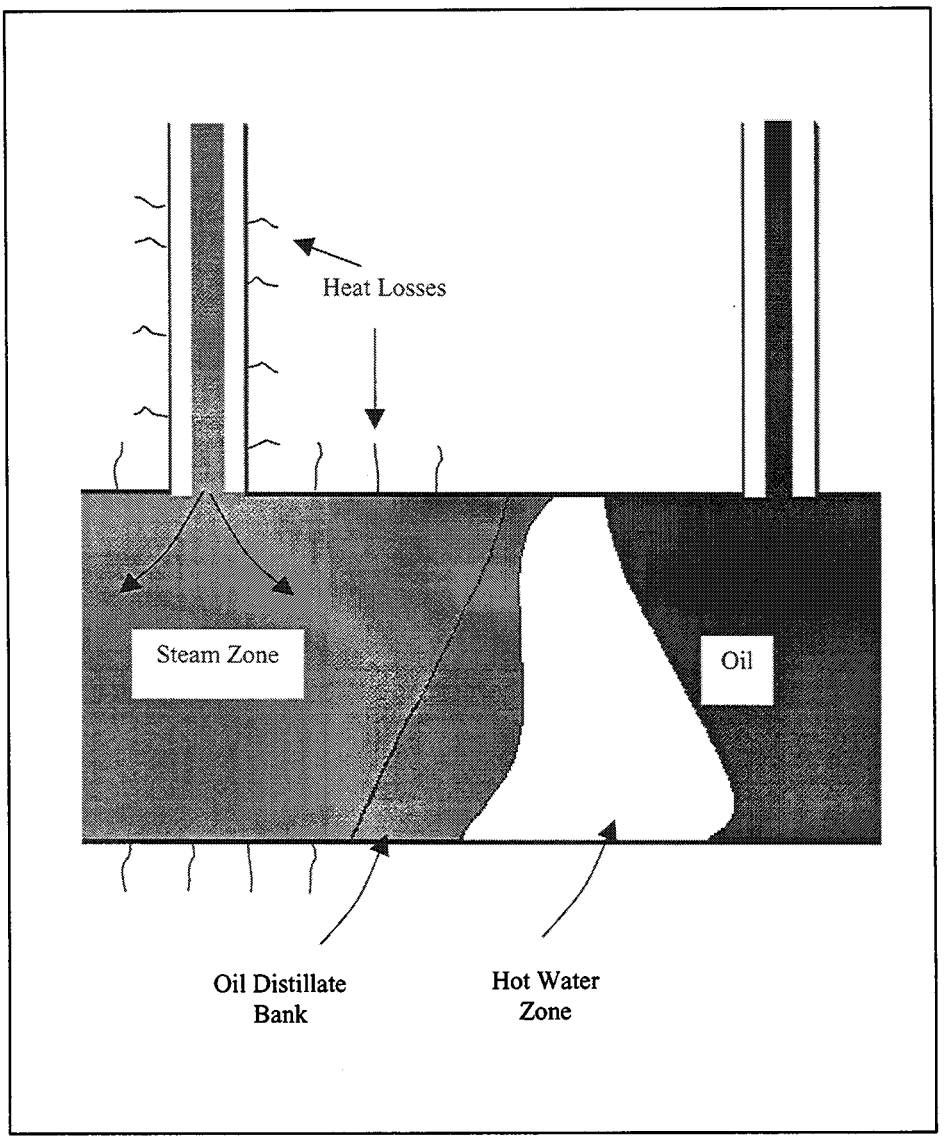

Figure 3. Schematic of light-oil steamflooding
(Volek and Pryor, 1972).

Wu and Brown (1975) stated that distillate yield, the amount of recovery from distillation and distillate drive, is a function of oil composition, and not a function of porous media, initial oil saturations, or steam injection rate. They plotted steam distillation yield against a correlation parameter, V_w/V_{oi}, which is defined as the ratio of the cumulative water distilled to the initial oil volume. This parameter can be used to compare the sensitivity of certain properties. Additionally, Wu and Brown (1975) stated that the yield does not necessarily correlate with the API gravity. However, Duerksen and Hsueh (1983) found they could correlate API gravity and distillate yield, Y. First they calculated a distillation factor, F, which takes into account the system's pressure and temperature affects. Then using an F which represented typical steamfloods in shallow California reservoirs, they determined that

$$Y = 2 * (°API). \quad (1)$$

As a general rule, this correlation works well for low-wax content crude oils. A more rigorous yet still simple correlation that includes wax content is

$$Y = 0.98 + 2.19 * (°API) - 1.09 * (\% Wax). \quad (2)$$

Duerksen and Hsueh also suggested that Wu and Brown might have been able to correlate API gravity with distillate yield if they had included wax content into their calculations.

Thermal Expansion

As the reservoir temperature increases, thermal expansion occurs in all phases of the reservoir, oil, gas, water and rock; however, the rock will play an insignificant role as a recovery mechanism. Figure 4 shows the amount of thermal expansion for various oils and water at 500 psi. For a 300° F increase in temperature, the fluid will expand about 10% to 15%. In addition to the liquid expansion, thermal gas expansion can be significant, especially in supporting an expanding steam/gas cap recovery mechanism.

Field Studies

There are about 25 documented LOSF field trials, and only about half were considered successful (Table I) (Olsen *et al.*, 1992). We will discuss a number of these to determine where the successes and failures occurred and the major factors that contributed to the outcome of the field tests. Also, we will discuss some heavy-oil steamfloods in diatomite and end with a review of a light-oil steam pilot in a diatomite reservoir.

Brea

In 1964 Shell instituted a steam flood in the Brea Field (Volek and Pryor, 1972), which is located about 25 miles east of Los Angeles. The reservoir chosen, Lower B Sand East, contains steeply dipping (66°) sands with a porosity of 22% and permeability around 70 md. The sediments are marine turbidite deposits, and the sands are 300-800 feet thick. The area of interest was developed between the 1920's and the 1940's and had produced 19% of initial oil from depletion gas drive and gravity drainage. The initial pilot study consisted of two injectors and 13 producers with another injector being added within two years. Wellbore failures plagued the start-up of the field study, but once the troubles were worked out, the test worked successfully.

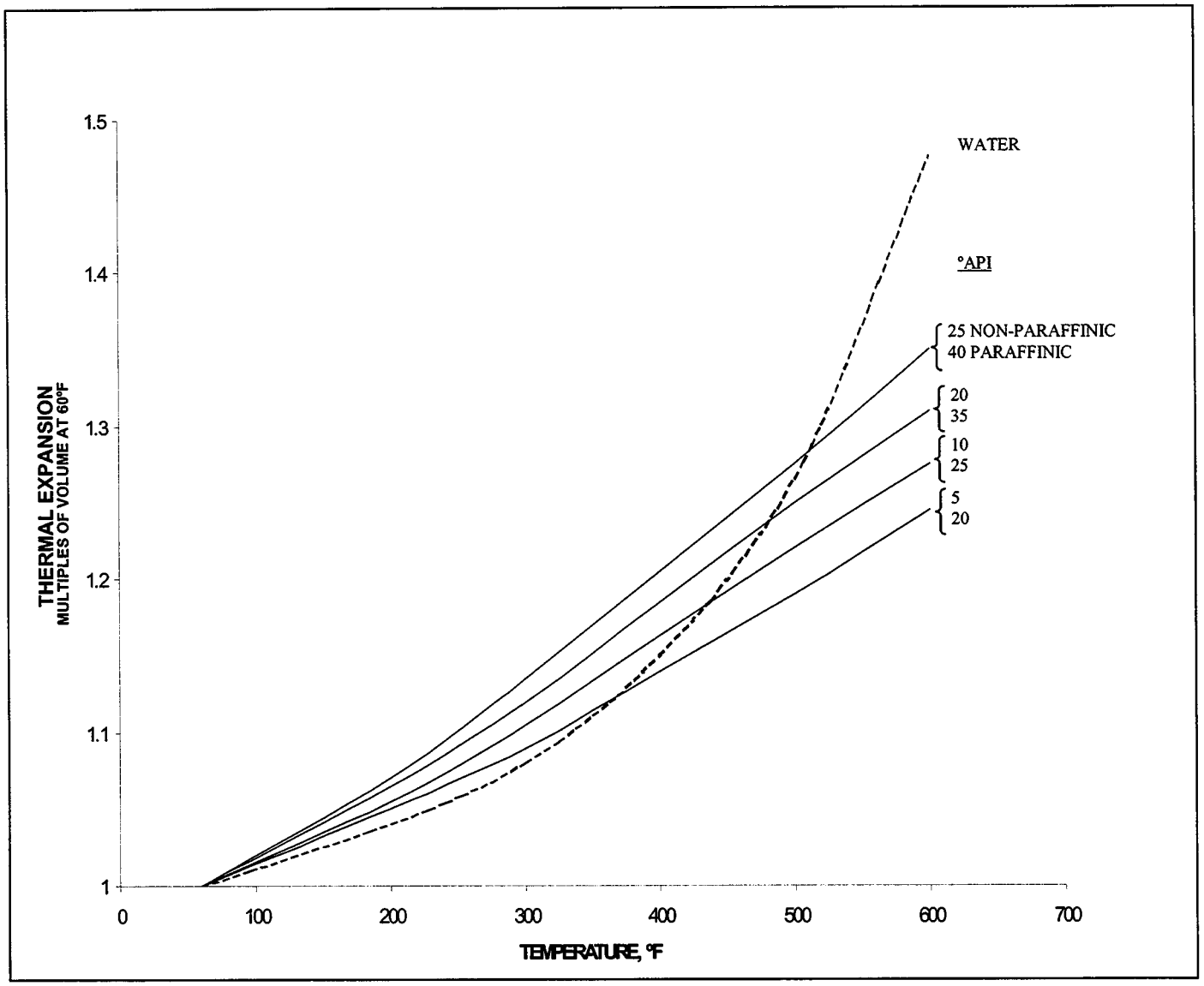

Figure 4. Thermal Expansion of Liquid Crude Oil Fractions (Wu, 1977).

Table I. Steamdrive field projects in light-oil sandstone reservoirs (Olsen *et al.*, 1992)

Field	Area (acres)	Gravity (°API)	Permeability (md)	Depth (ft)	Technical Success
Homer Field, LA	40	37	NA	1250	-
Teapot Dome, WY	120	33	63	325	Y
Garland Field, WY	35	22	10	4250	N
Elk Hills, CA	20	27	5000	2800	N
Lacq Superieur, France	30	22	10	2000	Y
Schoonebeek, Netherlands	15	25	5000	2400	Y
East Coalinga, CA	10	16-30	9000	900-2200	Y
Brea, CA	30	24	70	4600	Y
Smackover, AR	NA	20	5000	2000	Y
Triumph, PA	NA	41	7898	600-750	N
Shamburgh, PA	NA	45	14	900	N
El Dororado, KS	1.6	37	500	650	N
Frankling Heavy Pool, PA	NA	20	800	450-600	N
Duri, Indoesia	>4000	23	1550	625	Y
Sheills Canyon, CA	18	34	140	850	Y
Fyzabad, Trinidad	18	24	412	2500	-
Caddo-Pine Island, LA	NA	21	500	800	N
Georgsdorf, Germany	144	27	1200	2100-2800	Y
Ruhlermoor, Germany	980	25	700	1700-2460	Y
Ruhlertwist, Germany	237	25	5000	2650	Y
Emlichheim, Germany	121	24.5	6020	400	Y
Loco, OK	4	20	750	200-300	Y
Carmopolis, Brazil	40	22	NA	2500	Y
Lost Hills, CA	15	20	50	1200	-
Buena Vista Hills, CA	5	27	20	3000	N

After over five years of steam injection, a maximum temperature of 623° F was recorded in a temperature observation well. No heat was observed down dip; the heat, aided by the density difference between the steam vapor and the hydrocarbon liquid, moved only updip from the injection well. During the same time frame, the oil gravity from one production well changed from 23.5 to 25.9 °API. This demonstrates that the lighter components were being distilled from the oil in the steam zone and recondensed at the steam front. Residual oil saturation was reduced to 8%, which was found by drilling and coring observation wells in the swept area of the reservoir. This data shows that distillation was the significant recovery mechanism in the Brea steamflood. At the very least, the pilot study was a technical success; it showed that light-oil could be successfully produced from steam injection.

Teapot Dome

Naval Petroleum Reserve No. 3, Teapot Dome field, is a U.S. government owned oil field located 35 miles north of Casper, Wyoming (Olsen *et al.*, 1992; 1993). Production started in the 1920's, but full production was not initiated until 1976. The reservoir is characterized by a sandstone that is highly fractured and faulted and has low permeability, around 5-50 md. As a result, primary and secondary production left considerable reserves in the ground. In 1980, screening and planning for enhanced oil

recovery (EOR) projects began. Steam drive did not pass the initial screening due to poor estimated economics. Pilot projects for in situ combustion and polymer flood were initiated in 1982, but they only lasted a couple of years because of poor economic conditions and early breakthrough, respectively. Injection of steam was used to preheat the formation before the start of the in situ combustion, and the steam injection produced significant oil. There was enough response from the injection to implement a steamdrive pilot in 1985.

The Shannon Sandstone is the shallowest (300 - 500 feet) and most productive of the nine producing zones. It accounts for approximately 55% of the production. The Shannon consists of two highly fractured heterogeneous sandstone intervals separated by shaley siltstone. The steamflood was implemented with five different steam generators, and a number of separate line-drive patterns. In one pattern, 5A, heat input was increased by increasing steam quality from about 50% to about 75%. This led to a 37% increase in pattern production, which shows how closely production is tied to steam quality and hence, heat input. The major mechanism for this flood were reported as steam distillation, repressurization, thermal expansion of the oil, imbibition, oil viscosity reduction, alteration in the oil relative permeability, and dry heat distillation. Overall steamdrive in Teapot Dome's Shannon Reservoir was moderately economic with a breakeven cost approximately equal to $12/bbl.

Buena Vista Hills

Buena Vista Hills Field in Kern County, California was Chevron's first light oil (27 ° API) steamflood (Hong, 1986; Blunschi, 1987; Ziegler, 1988). In 1981, the company successfully conducted a six-month steam injection test that showed that steam could be injected into the reservoir at rates and quality necessary for an efficient recovery of the oil. Encouraged by these preliminary results in early 1985 they decided to implement a pilot project, which involved 12 inverted 5-spot patterns over a 65-acre area. The sandstone reservoir is approximately 100 feet thick and 2500 feet deep, and its porosity and permeability are on the order of 34% and 86 md, respectively. Extensive reservoir simulation modeling was carried out prior to development, and recoveries were estimated to be 50% of original oil with a large portion of the recovery attributed to steam distillation. However, early breakthrough and generally lower than expected recovery was observed. These were attributed to reservoir geology where almost all of the steam channeled through thin, highly permeable thief zones, and did not effectively contact major portions of the reserves. Unfortunately, they did not achieve the piston-like steam-front advance that was expected, which caused the economics of the project to be seriously hindered and finally caused the project to be terminated. The field trial did not even last two years, starting in April 1985 and ending in January 1987. Oil recoveries expected from numerical simulation and those seen in the field are displayed in Figure 5.

Shiells Canyon

The Sheills Canyon Field, located in Ventura County, California, was selected for steam drive because of the volatile nature and the low viscosity of the crude oil (34° API) (Konopnicki *et al.*, 1979). In addition, the 35° dip of the selected formation was ideal for expanding steam/gas cap recovery. Steamflood was initiated on March 3, 1973 in Zone 203 of the Sespe formation. The reservoir is approximately 850 feet deep and about 150 feet thick with an average porosity of 20% and an average permeability of 140 md. The reservoir is bounded on all sides by faults and assumed to be fluid sealing at flood pressures. There are 37 acres in the fault block with 29 considered floodable. Primary production began in April 1961 and produced 9.5% of initial oil before steamflood commenced.

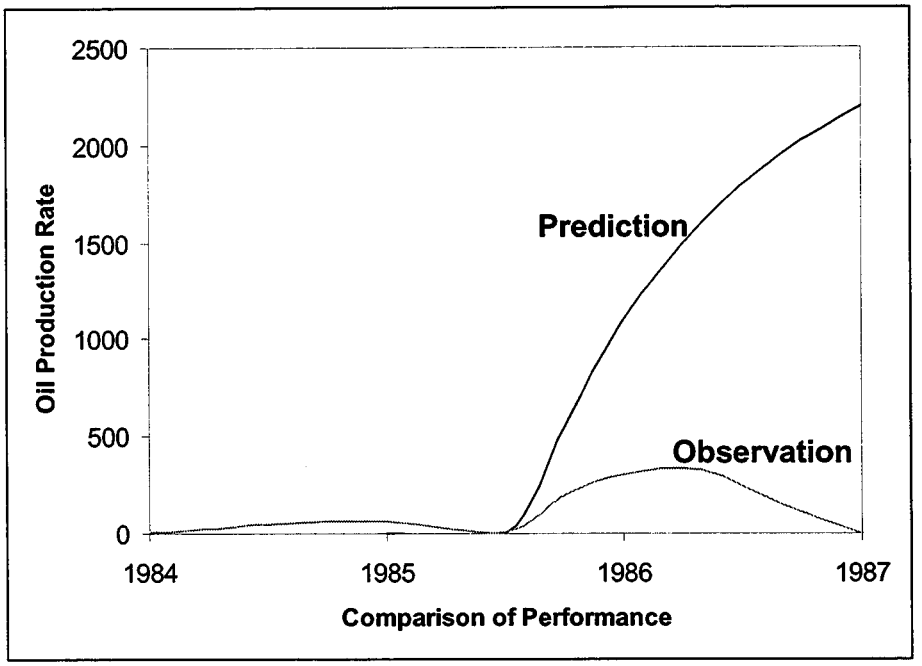

Figure 5. Buena Vista Predicted and Observed Oil Production (Dehghani and Ehrlich, 1998).

Before the pilot started, three types of studies were carried out to determine if Shiells Canyon was suitable for steam injection. First, a steam distillation experiment was conducted to estimate the distillable fraction in the Shiells Canyon crude oil. At anticipated reservoir conditions, the distillable fraction rapidly increased to 47% and then slowly climbed to 57%. Next, simulation was used to compare distillation from Shiells Canyon crude to Brea Field oil, and they found that at the same temperature, Shiells Canyon oil exhibits more favorable distillation characteristics. The last study used steamflooded linear sand packs, and measured temperature and pressure along the packs. The results showed the flood with the highest backpressure required the most injection to get to equivalent oil saturations, which shows the advantages of maintaining low back pressures, and thus low fluid levels, in the producing wells. Also, it showed how produced oil density could help predict when steam breakthrough will occur.

The pilot initially consisted of one injector and five producers. Due to the good response, another injector and five more producers were added. Over the life of the pilot, total injection for the two wells averaged about 750 B/D. Production jumped from 12 B/D prior to steam injection to 230 B/D by the middle of 1977, while the water cut remained below 50%. Due to a casing failure in the first injection well an offset well was drilled 25 feet from the original well. This well was cored and indicated an average residual oil saturation of 3% compared to 45% prior to steamflooding. The Shiells Canyon LOSF appeared to be quite successful.

Elk Hills

The last field test we will discuss is the Elk Hills Oil Field (Gangle, *et al.*, 1992; Burzlaff *et al.*, 1992). Like Buena Vista, Elk Hills is located in Kern County, and like Teapot Dome, Elk Hills is part of

the Naval Petroleum Reserve. The field is situated 3000 feet down and had produced 19% of the original oil during primary recovery. The high primary production is due to the superb reservoir properties. The permeability is around 1 Darcy (1000 md), and the porosity is about 30%. The steamdrive pilot lasted from 1987 to 1991 when it was ended due to marginal economics. Actual field production data compared poorly with predictions from numerical simulation. The differences were explained by poor well recoveries, which resulted from wellbore scale and lack of steam confinement to the pilot pattern. A post project simulation found that steam distillation and distillation drive were of little importance because of limited sustained steam zone temperature in the pilot area. Therefore, the majority of oil response had been due to waterflooding by condensed steam. The same properties that were good for primary production hindered the steamdrive by quickly dissipating and cooling the steam and its heat effects. While the field test underperformed expectations, economics indicated that the pilot was a break-even venture if production response outside the pattern is incorporated into the overall project.

Cymric

Cyclic steam injection is used to produce heavy oil (14 °API) from the diatomite reserve in Cymric Field, San Joaquin Valley, CA (Kumar, 1995). A highly instrumented cyclic steaming well and two closely spaced observation wells were monitored to observe fluid flow and recovery response. In addition, a three-dimensional simulation model based on this well was constructed to determine the importance of recovery mechanisms, reservoir properties, and modeling parameters in steam stimulation of heavy-oil diatomite. The Cymric reservoir occupies the crest of a double plunging anticline that formed as a result of NE-SW compression associated with movement on the San Andreas Fault. Consistent with diatomite reservoirs, Cymric has high porosity (40%-65%) and low permeability (0.1 md – 1.0 md). Its oil saturation is approximately 55% and has an initial reservoir pressure equal to 450 psi. The reservoir is between 1050 and 1250 feet deep.

The test well, A-S, was located near the crest of the anticline. The two observation wells, A-O and A-D were 23 and 30 feet away, respectively. The plane dip at the test site was 36°. Temperature response was seen at well A-O almost immediately, whereas almost no increase in temperature was observed at well A-D. Consequently, it was determined that a steam induced fracture was created along the direction from well A-S to well A-O. This observation was supported by a vertical seismic profile conducted in a nearby well. The Cymric Simulation Model was based on and constrained by the data gathered from the injection and observation wells. The reservoir was represented by a single porosity model and a single vertical fracture emanating from the well in the direction discussed above. The fracture length was estimated from well test analysis, and the fracture height was based on data from observation wells. Because the fracture plays such an important role in the fluid flow, a good knowledge of the induced fracture dimension and orientation is very important for field development.

The main mechanisms to get the oil from the matrix to the fracture were countercurrent imbibition, and thermal fluid expansion. While convective heat only flows during the injection part of the cycle, conductive heat flows over the entire duration of the cycle, which enhances the effects of thermal expansion. The total recovery and timing of the recovery are both strongly influenced by matrix permeability. Since higher matrix permeability results in more convective heat transfer, an order of magnitude change in matrix permeability will double the amount of production and reduces the time to production peak. Overall, cyclic steam injection into heavy-oil diatomite has shown to be quite successful in the Cymric Field.

South Belridge Field

At least two separate steam injection pilots have been completed on South Belridge Field by two separate companies. South Belridge is located in the San Joaquin Valley and contains up to 2 ½ billion barrels of initial oil-in-place. It is characterized by high porosity (50% – 65%) and high oil saturation (up

to 70%), however its permeability is very low (less than 1 md). Regardless, its high porosity and oil saturation coupled with a thick (1,000 feet) oil column may make it a good candidate for the steam drive process (Johnston and Shahin, 1995). Both projects were completed in the late 1980's and early 1990's.

Heavy-Oil Pilot

The first pilot to be discussed was completed by Mobil was conducted in a portion of the reservoir containing heavy oil (12 °API) (Murer, 1997). The initial purpose of the test was to determine the viability of cyclic steam injection into an unfractured interval of diatomite containing heavy oil, but the test performed sluggishly and the well was eventually hydraulically fractured and propped. After two additional cycles, a nearby production well was drilled, and a two-well continuous steam injection process was initiated and operated for over a year. The initial injection rate was 400 barrels of equivalent cold water per day (B/D), but this was reduced to 200 B/D due to fears that they may unintentionally fracture into the overlying high permeability zone. Production remained fairly constant at about 15 barrels of oil per day (B/D), except for once, when the production well had to be shut in for a short time (< 1 month). After the well came back on line, it was able to produce about 40 B/D for a few months.

Overall the steamflood performance was poor with an oil-steam-ratio (OSR) of 0.08, but in a two-well pattern much of the efficiency of the injected steam is lost. Implementing a five spot pattern could have increased OSR two or three times. However, there were some positive aspects resulting from the pilot study. The post-fractured cyclic operations were quite good, and the production increase after shut-in indicated that some type of cycling operation may be successful. In this process the producers are shut in and steam is injected until some pressure limit is attained; then the producers are brought back on production. In essence, it is a multiwell cyclic project. Also, the authors concluded that if the process was applied to a lower viscosity oil, the steamflood performance could become an economic process. This is the situation we will examine next.

Light Oil Pilot

Shell implemented steam injection in South Belridge to evaluate it as a potential recovery process in light oil (Johnston and Shahin, 1995). Before Shell and Mobil combined operations at this location under the name Area, Shell had approximately 900 acres of South Belridge diatomite under waterflood. The ultimate recovery after waterflood was about 15% of original oil-in-place. Generally, waterfloods in diatomites have suffered from low water injectivity, poor vertical and areal sweep, extensions of injection fracture, and short-circuiting due to injector-producer linkup. Steam injection may mitigate some of these problems. Preliminary simulation studies showed that an additional 30% of original oil-in-place may be recoverable with steam drive bring the ultimate recovery up to 45%. The idea is that steam injection can outperform waterflood in diatomite due to three main reasons. First, steam injection is usually a stable process; as a result, channeling and fingering of the steam is much less prevalent than with water. Second, heat can propagate through the rock by thermal conduction, which in this low permeability rock is a significant effect. The heated fluids, especially gas, expand and expel oil from the rock matrix. Numerical simulation has shown that in the early life of a steam drive, this mechanism (thermal expansion) is the most important to recovery. Third, distillation of the reservoir oil by steam can lead to extremely low residual oil saturations. The vaporized oil condenses at the steam front and contributes to the increased oil production.

The pilot project has been divided into three separate phases with results of Phase III not yet published. Phase I was a limited interval (150 feet) test that consisted of one injector placed between two previously existing production wells. Furthermore, 9 observation wells were used to monitor heat front growth and changes in saturation. Phase II had two injectors, two producers, and eight observation wells. Within two months of starting Phase I, temperature response was seen in an observation well 15 feet west of the injector. Temperature increase was noticed in all of the observation wells except a few on the outer edge of the pattern. Steam injectivity remained high except for an eight month period when a malfunction

caused the steam separator to output steam that contained some impurities. The impurities plugged the reservoir and temporarily reduced the injectivity. Production at all producers from both phases responded positively to steam injection. The Phase II wells indicate that the steam drive process worked better than predicted, exceeding oil-steam-ratio estimates. However, steam breakthrough occurred in one zone of one production well. Fortunately, the breakthrough was isolated by setting a bridge plug above the zone, but this zone may cause problems when the steamflood is expanded. An increase in H_2S was also observed in the production wells, especially where steam breakthrough occurred. This could cause addition problems in the expansion of the flood. In general, Phases I and II have shown to be very promising, but a full scale project is needed to fully evaluate the commercial viability of the light-oil steam drive process in the South Belridge Field. Therefore, Phase III will try to quantify the remaining uncertainties associated with this process. Some issues being addressed are verifying the production seen in Phase II and mitigating unwanted fracture extension and steam breakthrough. Phase III will cover 15 acres and have 9 oil producers, 12 steam injectors and 12 observation wells.

Diatomite

Pure diatomite is a hydrous form of silica composed almost entirely of the skeletal remains of unicellular aquatic plants called diatoms. These skeletal remains collect at the sea bottom along with silts, sands, and muds. A general observation is that the fewer the impurities with the diatoms, the higher the porosity and permeability. Porosity can range from 25% for the silty diatomite to 65% for the clean diatomite. An interesting property of diatomite is that it can have very high porosity, but unfortunately, its permeability is extremely low, ranging from 0.01 – 10 md. This is due to the extremely small size of the diatoms and diatom fragments. Another important feature of diatomite is a high pore-volume rock compressibility, yet a network of high permeability natural fractures. This apparent inconsistency is because of the brittle nature of diatomite when it encounters non-compressive loads. The San Joaquin Valley diatomite reservoirs consist of a series of stacked layers separated by virtually impermeable shale layers. This makes fluid and heat communication among layers in the vertical direction exceptionally poor (Kovscek *et al.*, 1996a; 1996b). Diatomite is a complex rock-type that makes understanding the oil recovery mechanism very challenging.

Steamfront Stability

Steamflooding is considered to be a stable displacement process on a microscopic and core scale. The tendency of steam to "finger" beyond the front is suppressed by condensation of steam within the finger (Farouq Ali, 1982). However, depending on the rock properties this may or may not be the case. Burger *et al.* (1985) published a method that relates steam front stability and rock properties. Start with the mobility divided by the Darcy velocity for both the displaced and displacing fluid, and then take the ratio of the displaced value over the displacing value, so that you have the following equation:

$$\frac{\dfrac{k_{rw}}{\mu_w \bullet V_w}}{\dfrac{k_{rs}}{\mu_s \bullet V_s}} > 1 \tag{3}$$

where the subscripts w and s stand for water and steam, respectively. If the result is greater than one then the process is considered stable. Upon assumption that the relative permeability for the displacing fluid is approximately equal to that of the displaced fluid, useful information can be drawn from

$$\frac{\mu_S \bullet V_S}{\mu_W \bullet V_W} \tag{4}$$

Burger *et al.* presented an expression to calculate the ratio of Darcy velocities, V_S/V_W, and it is shown below

$$\frac{V_v}{V_w} = \frac{1+\dfrac{1-\phi}{\phi}\dfrac{(hc)_s(T_h - T_r)}{\rho_{v,Tr}H^{Tr}_{v,Th}}}{1+\dfrac{1-\phi}{\phi}\dfrac{(hc)_s(T_h - T_r)}{\rho_{w,Tr}H^{Tr}_{v,Th}}} \tag{5}$$

where

ϕ is porosity,

$(hc)_s$ is average heat capacity per unit volume of solid matrix

T_h is steam temperature,

T_r is reservoir temperature,

$H^{Tr}_{v,Th}$ is steam vapor enthalpy from reservoir temperature to steam temperature,

$\rho_{v,Th}$ is vapor density at steam temperature,

$\rho_{w,Tr}$ is water density at reservoir temperature,

μ_v is vapor viscosity, and

μ_w is water viscosity.

This method was used to determine if steamflood in diatomite is a stable displacement process. The enthalpy and temperature of the saturated steam, along with the density and viscosity of both water and vapor, are calculated from correlations found in Ejogu and Fiori (1987). The correlation for most of these properties is only a function of pressure. The viscosity correlations are a function of both temperature and pressure. Consequently, the results of the equation are only a function of porosity, heat capacity of the solid matrix, reservoir temperature, and pressure. Reservoir temperature has little effect on displacement stability. Heat capacity, within its known range, also changes the calculations only a small amount. Therefore, I plotted the stability parameter versus pressure for the range of porosities expected (25% - 65%). The outcomes are presented graphically in Figure 6, and lead to some interesting results. For a pressure of 500 psi, the steam front is stable for all porosity values in our range. At 2500 psi, the front will be unstable for all porosity values. Steam injection pressures ranging from 500 to 1200 psi have been reported for diatomite projects (Kovscek *et al.*, 1996a; 1996b). Figure 6 indicates that the more porous diatomite layers could be close to the stability limit and unstable at the largest injection pressures.

Planned Research

This research will try to determine the recovery mechanisms that are the most dominant when steam flooding a diatomite reservoir containing light oil (20°-30° API), and/or the mechanisms that have little or no effect on recovery. Figure 2 from Burger *et al.* (1985) showing the relative importance of different mechanisms for light to heavy oils indicates that thermal expansion and distillation are the primary recovery mechanisms in light oil sandstone. These two mechanisms will serve as a starting point for the research. There has been speculation that some initial gas saturation was present in the reservoir as trapped free gas. This has lead to the theory that thermal gas expansion could be an important recovery mechanism.

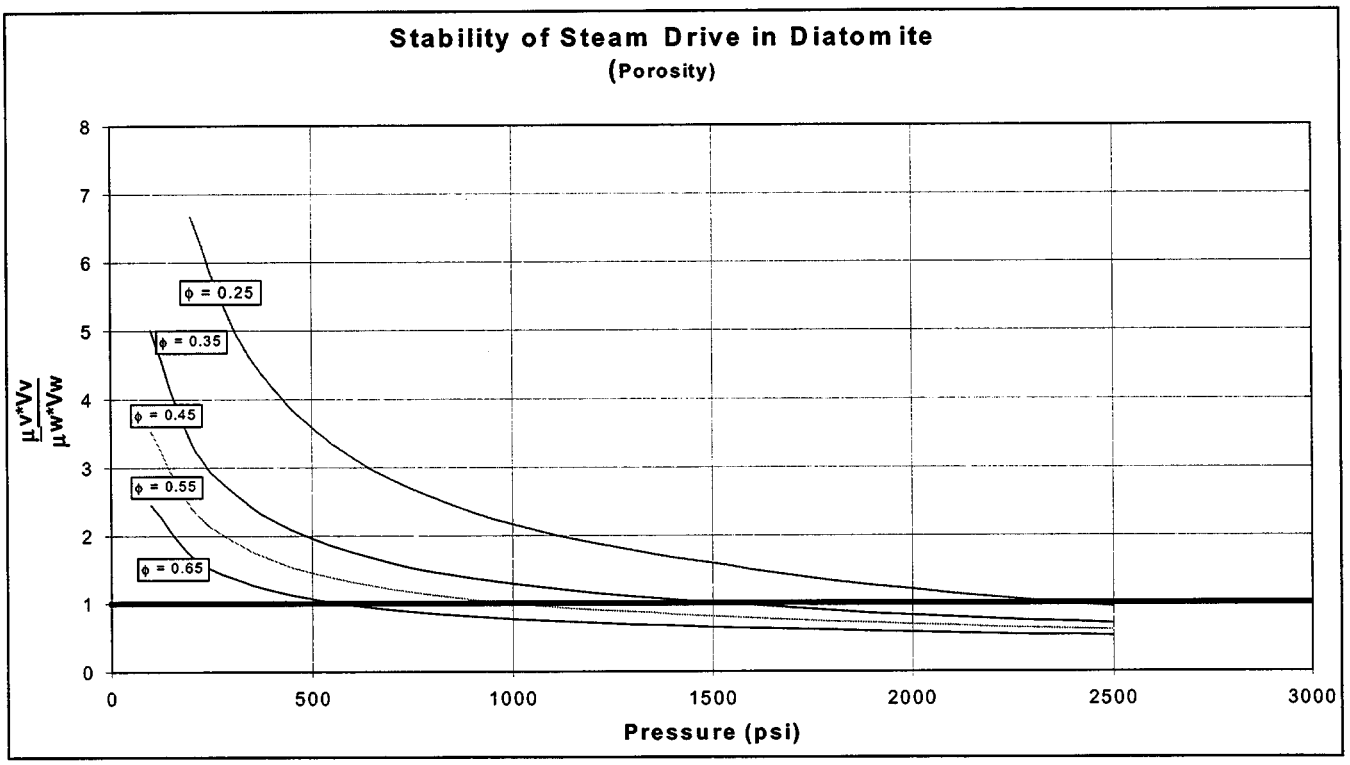

Figure 6. Steam drive stability in diatomite

Figure 3 displays the four zones that develop: steam zone, distillate zone, hot water zone, and oil zone. This research will also attempt to find how the particular zones in the steam drive process form. Because the well spacings are so close in most diatomite reservoirs, it has been hypothesized that the distillate zone does not have enough critical time to form. We will determine at what critical time and length the specific zones begin to occur and when each particular zone reaches the producer. Also, we will find the size of different zones and whether all the zones even develop.

Thermal reservoir simulation will be the method employed to perform this research, specifically the simulator CMG Stars will be used. Figure 7 displays some possible configurations that may be used in the simulations. In some cases, all the heat will be kept inside the reservoir (perfect insulating boundries), and in others, certain amount of heat will dissipate out of the confined reservoir. Undoubtedly as simulations are performed, more questions will arise that will lead to additional studies. However, the previous material lays out a good road map.

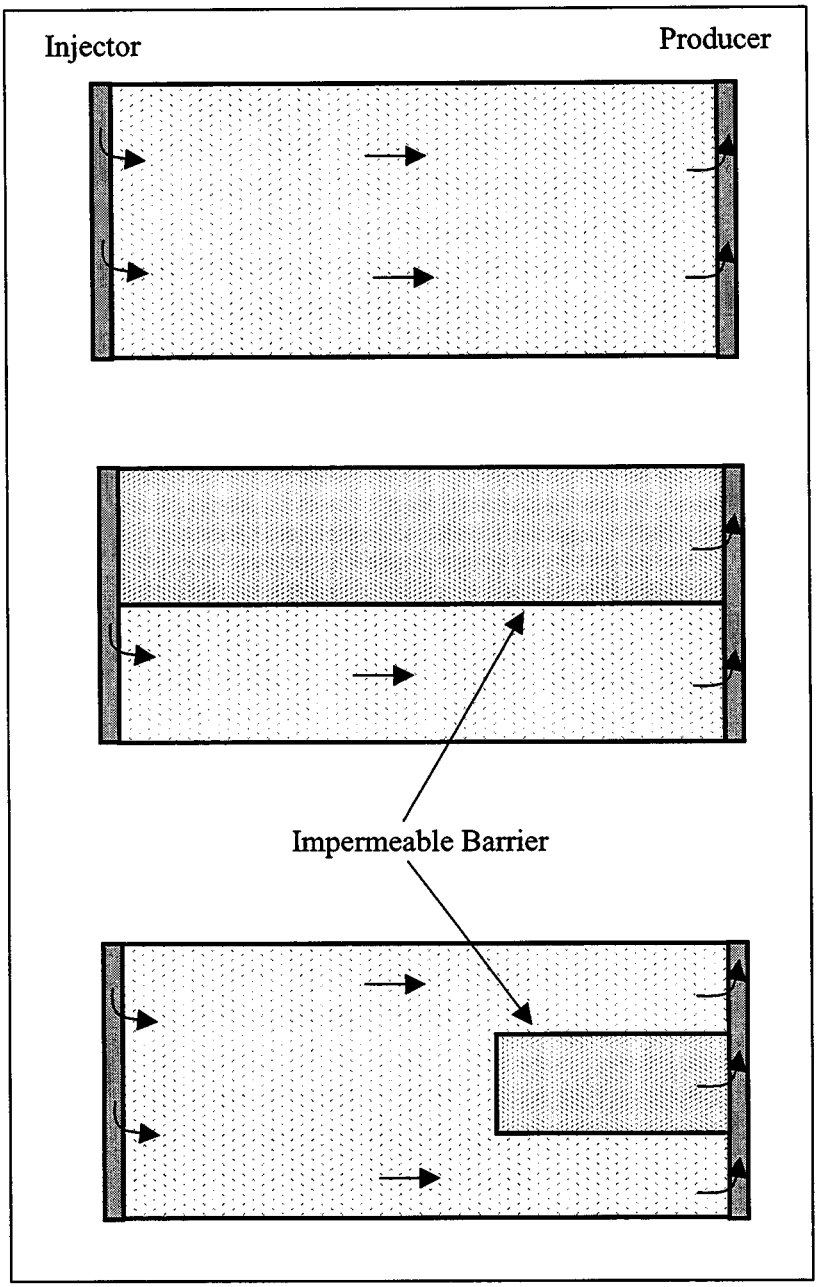

Figure 7. Simulator Configuration

Closing

Early work in studying steamfloods in oil reservoirs defined the major mechanisms that lead to oil recovery. Thermal expansion, oil distillation, and viscosity reduction are three important mechanisms that cause steam injection to outperform waterfloods. A literature review shows that a fair amount of work has been completed on light oil steam injection including a number of field studies with both positive and negative results. Also, research has been published regarding diatomite rock properties, which include high porosity and low permeability. Some initial results of this project show analytically that at high pressures, the steam front may become unstable, which could lead to steam fingering and early breakthrough. Additional planned research will attempt to incorporate the complexities of diatomite with the light-oil steam injection process. Specifically, steam zone formation and recovery mechanisms, such as thermal expansion and distillation, will be examined using a numerical simulator.

References

1. Blevins, Ted R.: "Steamflooding in the U.S.: A Status Report," J. Pet. Tech. (May 1990) 548-554.

2. Blevins, T. R., Duerksen, J. H., and Ault J. W,: "Light-Oil Steamflooding—An Emerging Technology," J. Pet. Tech. (July 1984) 1115-1122.

3. Blunschi, J. H.: "Simulation of a 12-Pattern Field Trail of Light Oil Steamflooding," SPE 16735, paper presented at 62nd Annual Conference and Exhibition at Dallas (September 27-30, 1987).

4. Burger, J., Sourieau P., and Combarnous, M.: Thermal Methods of Oil Recovery, Editions Technip, Paris, France (1985) 89-125.

5. Burzlaff, A. A., Bergeson, Intera, and Harris B. R. Jr.: "Thermal Simulation of Elk Hills Light-Oil Steamdrive Pilot," SPE 24036, paper presented at Western Regional Meeting in Bakersfield (March 30-April 1, 1992).

6. Dehghani, Kaveh, and Ehrlich, R.: "Evaluation of Steam Injection Process in Light Oil Reservoirs" SPE 49016, paper presented at 1998 Annual Technical Conference and Exhibition in New Orleans, (September 27-30 , 1998).

7. Doll, T. E., *et al.*: "An Update of Steam Injection Operations at Navel Petroleum Reserve No. 3, Teapot Dome Field Wyoming: A Shallow Heterogeneous Light-Oil Reservoir," SPE 30286, paper presented at International Heavy Oil Symposium in Calgary (June 19-21, 1995).

8. Duerksen, J. H. and Hsueh, L.: "Steam Distillation of Crude Oils," J. Pet. Tech. (April 1983) 265-271.

9. Ejogu, G.C., and Fiori, M.: "High-Pressure Saturated-Steam Correlations," J. Pet. Tech. (December 1987) 1585-1590.

10. Farouq Ali, S. M. Jr.: "Practical Considerations in Steamflooding," Producers Monthly (January 1968) 13-16.

11. Farouq Ali, S. M.: "Steam Injection Theories—A Unified Approach," SPE 10746, paper presented at California Regional Meeting in San Francisco (March 24-26, 1982).

12. Gangle, F. J., *et al.*: "Light-Oil Steamdrive Pilot Test at NPR-1, Elk Hills, California," SPE Reservoir Engineering (August 1992) 315-320.

13. Hanzlik, Edward J.: "Steamflooding As an Alternative EOR Process for Light Oil Reservoirs," SPE 10319, paper presented at the 56th Annual Fall Technical Conference and Exhibition, San Antonio (October 5-7, 1981).

14. Hong, K. C.: "Numerical Simulation of Light Oil Steamflooding in the Buena Vista Hills Field, California," SPE 14104, presented at International Meeting on Petroleum Engineerng in Beijing (March 17-20, 1986).

15. Johnston, R.M., Shahin, G.T.: "Interpretation of Steam Drive Pilots in the Belrigde Diatomite," SPE 29621, paper presented at Western Regional Meeting in Bakersfield (March 8-10, 1995).

16. Konopnicki, D. T., *et al.*: "Design and Evaluation of the Shiells Canyon Field Steam-Distillation Drive Pilot Project," J. Pet. Tech. (May 1979) 546-552.

17. Kovscek, A. R., Johnson, R. M., and Patzek, T.W.: "Interpretation of Hydrofracture Geometry During Steam Injection Using Tempreature Transients I. Model Formulation and Verification," Marcel Dekker, Inc. (1996a) 251-285.

18. Kovscek, A. R., Johnson, R. M., and Patzek, T.W.: "Interpretation of Hydrofracture Geometry During Steam Injection Using Tempreature Transients II. Asymmetric Hydrofractures," Marcel Dekker, Inc., (1996b) 289-309.

19. Kumar, M., Beatty, F.D.: "Cyclic Steaming in Heavy Oil Diatomite," SPE 29623, paper presented at Western Regional Meeting in Bakersfield (March 8-10, 1995).

20. Moritis, Guntis: "Biennial EOR Production Report – EOR weathers low oil prices", Oil and Gas J., Tulsa (March 20, 2000) p. 15.

21. Murer, A.S., *et al.*: "Steam Injection Project in Heavy-Oil Diatomite," SPE 60853, paper originally presented as paper SPE 38302 at Western Regional Meeting in Long Beach (June 25-27, 1997).

22. Olsen, D. K., *et al*: "Case History of Steam Injection Operations at Navel Petroleum Reserve No. 3, Teapot Dome Field, Wyoming: A Shallow Heterogeneous Light-Oil Reservoir," SPE 25786, paper presented at Internation Thermal Operations Symposium in Bakersfield (February 8-10 1993).

23. Olsen, D.K., *et al.*: "Light Oil Steamflooding: A Laboratory Study of Oil Recovery from Oil-Wet and Water-Wet Porous Media from a 2-D Physical Model," SPE 23692, paper presented at Latin American Petroleum Engineering Conference in Caracas, Venezuela (March 8-11, 1992).

24. Volek, C. W., and Pryor, J. A.: "Steam Distillation Drive—Brea Field, California," J. Pet. Tech. (August 1972) 899-906.

25. Wu, Ching H.: "A Critial Review of Steamflood Mechanisms," SPE 6550, paper presented 47th Annual California Regional Meeting in Bakersfield (April 13-15, 1977).

26. Wu, Ching H., and Brown, Alfred: "A Laboratory Study on Steam Distillation in Porous Media," SPE 5569, paper presented at 50th Annual Fall Metting of SPE in Dallas (September 28 - October 1, 1975).

27. Ziegler, V. M.: "Injection Well Testing in a Light Oil Steamflood, Buena Vista Hills Field, California," SPE 18140, paper presented at 63rd Technical Conference and Exhibition in Houston (October 2-5, 1988).

MECHANISMS OF PRIMARY HEAVY OIL RECOVERY

A Mechanistic Modeling and Experimental Study of Solution Gas Drive

P. Arora and A. R. Kovscek*

Abstract

Solution gas drive in reservoirs containing heavy and viscous oil is not well understood. This paper develops a mechanistic population balance model for describing the process of bubble nucleation and growth. The model is applied to both light and viscous oils. The primary modeling concept is a continuum bubble population balance. Appropriate rate equations are derived for two theories of bubble nucleation described in the literature—instantaneous nucleation (IN) and progressive nucleation (PN). The results of simulations for the IN and PN models are compared to experimental data reported elsewhere for light oil and to new data for viscous oils. Model parameters are all physically based. Within the IN model, the number density of bubbles must be specified while the PN model requires the cavity size distribution of the porous medium as input. The PN model matches the experiments somewhat better, but is more demanding computationally. Interestingly, the population balance description of either model does not require a critical supersaturation to be exceeded before the onset of bubble nucleation and growth. Supersaturation is the difference between the equilibrium and dynamic liquid pressure of a system. Liberation of gas from solution at the thermodynamic bubble point and the bubble growth equations presented here well describe the kinetics of the gas phase and pressure response of the systems examined.

Introduction

Bubble nucleation, growth, and mobilization of gas are important phenomena encountered in oil production by solution gas drive. The drive energy for oil production during pressure depletion is supplied by the release of gas from solution and the expansion of reservoir fluids. The gas phase forms by heterogeneous nucleation along pore walls. As the pressure declines further, bubbles grow due to diffusion of gas from the oil to the bubbles. Generally, bubbles grow large enough to span several pores, unite into a continuous phase, and then flow.

An interesting type of solution gas drive is exhibited by some reservoirs containing heavy oil. A heavy crude oil has a density from roughly 940 to 1000 kg/m^3 (10 to 20° API) and is far more viscous than a conventional crude oil. Wellhead samples are often described as resembling a chocolate mousse due to their frothy appearance, dark brown opaque color, and the relative stability of the foam produced (Maini *et al.* 1993). Such heavy oils are, thus, frequently termed foamy oils. The term foamy oil is retained in this work for historical reasons. However, gas-bubble microstructure and bubble flow properties may not resemble foam (Sheng *et al.* 1999; Tang and Firoozabadi 1999). Specifically, "foamy oil" refers to a dispersion of small bubbles (of variable size and frequency) of natural gas formed by nucleation within heavy crude oils. Hence "bubbly" oil is probably more descriptive. Foamy oil behavior leads to anomalous large primary oil production (Maini *et al.* 1993; Huang *et al.* 1998). Primary recoveries for solution gas drive heavy-oil reservoirs range from 5 to 25 % of the original oil in place (OOIP), whereas 0 to 5% of the OOIP can be produced if the oil is not foamy (Maini 1996, Firoozabadi 2001).

The conditions for significant primary production are not clear. Initially, it was believed that production of reservoir sand along with oil might be necessary for foamy oil behavior. More recently, several reservoirs have been identified that exhibit high recovery of heavy oil as foamy oil, but produce little or no sand (Claridge and Prats 1995). Thus, flow mechanisms can be considered independently from sand production. The rate of oil production appears to contribute to foamy oil formation. Rapid depletion of

reservoir pressure during primary production leads to larger than usual recoveries (Maini *et al.* 1993; Urgelli *et al.* 1999). Nevertheless, there are currently no estimates for the rates necessary to improve production response.

Although we are certain nucleation generates bubbles, the microstructure of the dispersed gas within the porous medium is unknown. In the case of aqueous foams, a detailed accounting of the pore-level morphology of foam and the mechanisms for changing bubble size were keys to unlocking, understanding, and predicting aqueous foam flow behavior (Kovscek *et al.* 1995). A similar understanding of gas-bubble microstructure would likely benefit our understanding of heavy-oil solution gas drive. The foamy-oil case is more complicated in some regards. Gas bubbles are generated by nucleation, and thus, are smaller than pore throat and body dimensions initially. Once formed, these bubbles may grow larger than pore size by gas diffusion and the coalescence of multiple bubbles into a single bubble.

The focus of this work is the development of a mechanistic modeling framework to elucidate solution gas drive behavior in viscous oils and address the question of gas-bubble microstructure. We incorporate pore-level bubble nucleation, growth, and gas transport mechanisms into a continuum displacement model consistent with standard simulation of multi-phase flow in porous media and verify the theoretical predictions by comparison to experimental results. Prior and new results are discussed. The model is based upon a bubble population balance framework (Patzek 1988, Randolph and Larson 1971). In population balance methods, the number density of bubbles is tracked as a function of location and time. This approach is elegant because the bubble conservation equation is analogous to the usual continuum mass balance equations for chemical species flowing in porous media (Patzek 1988; Falls *et al.* 1988). Importantly, a population balance approach allows us to blend previous, and new, experimental knowledge on heavy-oil solution gas drive with nucleation and growth models for single and multiple bubbles in porous media.

Dynamics of Bubble Formation

Before proceeding to describe the theoretical framework and experimental design, it is useful to review models of bubble nucleation and growth. In bulk solution, gas nuclei appear due to thermal fluctuations (Scriven 1959; Wilt 1986). The nucleus is stable if its size is large enough to prevent collapse under the force of capillary pressure. For gas/oil systems, homogeneous nucleation requires a supersaturation of several thousand kPa provided that the system is not close to critical (Kamath and Boyer 1995). Supersaturation is the difference between the pressure at which liquid and gas are in equilibrium and the actual liquid-phase pressure. Because there is no constraint on bubble curvature by a porous medium, bubble radius follows a square root of time dependence. This is the usual time scaling for processes controlled by molecular diffusion.

In porous media, values of supersaturation are not large, compared to bulk solution, indicating heterogeneous nucleation (Kamath and Boyer 1995). Pore wall topology and capillary forces in combination with diffusion characteristics, such as the competition for solute between bubbles, determine the gas-phase occupancy of a porous medium. Bubble size and curvature are not equivalent as they are in the bulk. There are two principal models for pressure and volume evolution during gas phase formation in solution gas drive: (i) instantaneous nucleation (IN—Firoozabadi and Kashchiev 1996) and (ii) progressive nucleation (PN—Li and Yortsos 1995).

Instantaneous nucleation assumes that all bubbles nucleate at essentially the same time and do not originate from preexisting bubbles trapped in crevices or the roughness of pore walls (Firoozabadi 1997). Bubbles nucleate on randomly located active sites on the surface of grains when the supersaturation reaches a prescribed level. In the IN model, the critical supersaturation for the formation of nucleated bubbles is a function of the rate of pressure decline. In practice, the supersaturation is obtained from experiment and the number of bubbles nucleated is an adjustable parameter. Bubbles grow by diffusion and at late times by expansion resulting from the compressibility of the gas. Diffusional bubble growth is modeled as three-

dimensional with shape factors to account for nonspherical bubble shapes. It follows that the theory models bubble growth in a compact fashion such that bubbles are of roughly equal size throughout the porous medium. The assumption of compact growth results in a straightforward theory for bubble volume as a function of time.

On the other hand, progressive nucleation assumes that bubbles are released from sites such as crevices or roughness on pore walls with poor liquid wetting characteristics. These sites become activated when the local supersaturation exceeds the capillary pressure of the site. The source of gas may be pre-existing trapped microbubbles or a nucleated gas phase (Li and Yortsos 1995). The condition for activation of a nucleation site (crevice) of radius W is

$$p_v - p_l = \frac{2\sigma}{W} \tag{1}$$

where σ is the gas-oil interfacial tension, p_v denotes the pressure inside the bubble, and p_l is the liquid pressure. Because the size of such crevices holding trapped gas varies, bubbles are released from pore walls at different degrees of supersaturation. The scaling of bubble growth in porous media is expected to be different than in bulk due to the underlying pore microstructure. Satik *et al.* (1995) examined the mass-transfer driven growth of a single gas cluster in a porous medium under the application of a far-field supersaturation. They found that the pattern of bubble growth changes as bubble size increases. Because bubbles are constrained by the porous medium, they do not grow as analogous spherical bubbles, but rather, adopt disordered shapes frequently described as ramified or fractal (Li and Yortsos 1995, Satik *et al.* 1995). The fractal dimension of growing gas clusters in porous media is 2.5 as opposed to 3 for spherical bubble growth (Li and Yortsos 1995). Bubble growth is complicated by both the geometry of pore space and the availability of solute. Recently, Tsimpanogiannis and Yortsos (2001) developed an effective continuum model that incorporates many of the details of heterogeneous nucleation and gas-phase growth as described above. Calculations reproduced the trends available from depletion experiments in the literature.

El Yousfi *et al.* (1997) undertook a series of experiments in transparent two-dimensional representations of pore space (*i.e*, micromodels) saturated with a solution of carbon dioxide in water. They nucleated bubbles at a fixed supersaturation by connecting the micromodel to a gas reservoir maintained at a pressure significantly less than the initial pressure of the micromodel (300 kPa). Bubbles appeared progressively over a relatively short period of time and then grew by diffusion. Observations were interpreted as four distinct steps. First, stabilized microbubbles of the order of 1 μm (below the resolving power of the microscope) in size were always present. Next, these submicroscopic bubbles grew by diffusion, but remained trapped in pore-wall roughness by capillary forces. Progressively, bubbles were released from the pore walls when the pressure drop became sufficient to overcome capillary forces. Finally, the bubbles released from pore walls continued to grow by diffusional mass transfer.

The series of events described is more similar to PN than to IN especially in regard to the release of preexisting small bubbles from pore walls. However, the duration of bubble production (1 hour) was about 15% of the length of time required to deplete the micromodel of pressure. Hence, they stated that the process might be approximated by IN if the longer time behavior is of interest.

Other Models

A variety of other models of solution gas drive in porous media have been introduced. For the heavy-oil case, a common approach is to adjust regular two-phase parameters such as fluid and rock compressiblity, oil/gas relative permeability, and oil viscosity to match available data (Sheng *et al.* 1999, Tang and Firoozabadi 1999). Sometimes aphysical parameter values result.

Smith (1988) proposed that the gas remains dispersed within the oil phase as a large population of bubbles that are smaller than pore throats. Bubbles and gas then transport freely with the oil phase.

Claridge and Prats (1995) used a similar model suggesting that asphaltenes adhere to surface of gas bubbles thereby stabilizing them at a small size. The oil-phase viscosity was envisioned to drop substantially as asphaltenes deposited on bubble surfaces. Kraus *et al.* (1993) introduced a pseudo bubble point model where gas releases from solution at the thermodynamic bubble point but remains entrained in the oil. The fraction that remains dispersed decreases linearly with declining pressure.

Sheng *et al.* (1996, 1999) proposed a dynamic model incorporating rate processes controlling the transfer of solution gas to dispersed gas and dispersed gas to free gas. Bubble nucleation is instantaneous and bubble radius increases proportional to the square root of time as if the bubbles are not constrained by the porous medium. The dispersed gas accumulates into free gas exponentially with time; the pressure gradient is assumed to have no effect on the growth of free gas. Multiphase flow is described with usual relative permeability relationships. The dispersed gas flows along with the oil-phase and viscosity is assumed equal to the oil viscosity. The adjustable parameters describing gas phase growth vary with the pressure decline rate and it is stated that the usefulness for field prediction is limited (Sheng *et al.* 1999).

Population Balance Model of Solution Gas Drive

The power of a population balance formulation lies in quantifying directly the evolution of bubble size as pressure declines. Gas mobility is assessed from the concentration of bubbles. Further, the method is mechanistic in that documented and/or proposed pore-level events are portrayed in bubble nucleation, growth, and coalescence equations. The method provides a general framework where the relevant physics of heavy-oil solution gas drive can be tested and expressed. Deriving continuum-averaged equations that accurately represent pore-level physics is a difficult task that forms the majority of this work.

Conservation Equations. A bubble population balance is merely a conservation equation incorporating bubble accumulation, transport, generation, and coalescence mechanisms (*c.f.*, Patzek 1988, Randolph and Larson 1971). It must be solved in addition to the usual continuum gas and oil component mass balances. Patzek (1988) presents a generalized derivation applied to aqueous foams in porous media for enhanced oil recovery (EOR) by gas injection. It is applicable to the current problem and need not be repeated here. Our task is to construct rate and constitutive equations that appropriately capture solution gas drive physics. In solution gas drive, bubbles are initially stationary and later flow when they become long enough to be mobilized at the prevailing pressure gradient. The balance is divided logically into stationary and flowing bubbles. For the stationary bubbles, it is written as

$$\frac{\partial}{\partial t}(\phi S_s n_s) = \phi S_g (r_{ns} - r_{cs} + r_{Ds} - r_m) \tag{2}$$

where t denotes time, ϕ is the porosity (void fraction) of the porous medium, and S_s is the saturation of gas held in stationary bubbles. The bubble density, n_s is the average number of stationary bubbles per unit volume of gas. The inverse of n_s is the average volume of gas contained in a bubble. Bubble size ranges from essentially zero for submicroscopic bubbles to infinite for continuous gas. Correspondingly, bubble textures range from infinite for submicroscopic bubbles to zero for continuous gas. The time derivative on the left of Eq. (2) represents the net rate at which the density of stationary bubbles increases or decreases. The right of Eq. (2) expresses the mechanisms that affect bubble size. The symbol r refers to the rate of change of bubble texture while the subscript *ns* refers to the nucleation of stationary bubbles, *cs* coalescence of stationary bubbles, *Ds* the change of bubble size due to gas diffusion, and *m* the mobilization of stationary bubbles. Rates are expressed on a per volume of gas basis. The balance for flowing bubbles is written similarly,

$$\frac{\partial}{\partial t}(\phi S_f n_f) + \nabla \bullet (u_f n_f) = \phi S_g (r_{gf} - r_{cf} + r_{Df} + r_m) \tag{3}$$

where the subscript *f* signifies flowing bubbles and *u* is superficial velocity. The second term on the left of Eq. (3) tracks the convection of bubbles. On the right, nucleated bubbles are always initially stationary so there is no term for nucleation of flowing bubbles. However, flowing gas might be subject to snap-off or other mechanisms of bubble refinement (Kovscek and Radke 1994). For generality, the term r_{gf} is included for generation of flowing bubbles. The total gas saturation, S_g, is given by the sum of S_s and S_f.

Mass balance equations are also required for the chemical species. The balance for gaseous species is linked to the bubble equations through the rates for bubble nucleation and diffusive growth. The system is modeled as a single component oil with a single component gas dissolved in it. Expansion to more than a single oil component is straightforward. During the process of gas evolution, the total amount (moles) of gas component are conserved and this is expressed as,

$$\frac{\partial}{\partial t}(\phi S_o \rho_o X_{g,o} + \phi S_g \rho_g) + \frac{\partial}{\partial x}(\rho_o u_o X_{g,o} + \rho_g u_g) = \frac{Q_o X_{g,o} \rho_o}{V_p} \tag{4}$$

Here, ρ is the molar density, $X_{g,o}$ is the moles of dissolved gas per mole of gas-free oil, u is the Darcy velocity, Q_o is the volumetric oil withdrawal rate, and V_p is the total core volume. The subscripts o and g refer to oil and gas component, respectively. It is assumed that no oil partitions into the gas phase. The mass balance for the oil component is similar,

$$\frac{\partial}{\partial t}(\phi S_o \rho_o) + \frac{\partial}{\partial x}(\rho_o u_o) = \frac{Q_o \rho_o}{V_p} \tag{5}$$

Note that $X_{o,o}$ is 1 because we have used a gas-free oil basis.

Bubble Rate Equations. To continue, we consider nucleation and growth of stationary bubbles with first the IN and then the PN model. For the case of instantaneous nucleation, the rate of nucleation is zero except at the instant where bubbles are nucleated. The rate of bubble growth is obtained by differentiating the inverse of bubble volume, v_b, with respect to time.

$$r_{Ds} = \frac{\partial}{\partial t}\left(\frac{1}{v_b}\right) = -\frac{1}{v_b^2}\frac{\partial v_b}{\partial t} \tag{6}$$

Equation (6) is, in fact, general and applies to any model of bubble growth. Because bubble volume is always positive, it teaches that bubble growth (positive $\partial v_b/\partial t$) without change of identity decreases bubble density. As the volume of a bubble expands, the number of bubbles per unit volume of gas decreases because bubble texture is inversely related to volume. From the IN model, it follows that,

$$r_{Ds} = -3a\left[\int_0^t G(t')dt'\right]^{-4} G(t)\frac{\partial G(t)}{\partial t} \tag{7}$$

where a is a shape factor accounting for irregular shape of gas bubbles in porous media and t' is a variable of integration. The function $G(t)$ is the growth rate of bubble radius (Firoozabadi and Kashchiev 1993)

$$G(t) = (\omega + \nu)K\Delta p^{\omega}(t)t^{\nu-1} \tag{8}$$

where K is a kinetic constant of bubble growth evaluated using Eq. (A-4) of Firoozabadi and Kashiev (1996). Equation (8) represents an attempt to generalize growth rate across a variety of bubble-growth regimes. Hence, the power-law exponents ω and ν vary according to the physical situation. Here, they are set here to values of 0.5 each representing diffusion-controlled growth of an isolated bubble (Firoozabadi and Kashchiev 1996). The expression for supersaturation is given by,

$$\Delta p(t) = p_{bp} - \beta(V - V_{bp}) - p(t) \tag{9}$$

Here p_{bp} is the bubble point pressure, V is the total system volume at any time, V_{bp} is the volume at bubble point, β is the slope of the equilibrium P-V curve of the system, and $p(t)$ is the liquid pressure.

In the PN model, it is possible to nucleate continually bubbles and so both the rate of creation of new bubbles by nucleation and the growth of preexisting bubbles must be considered. We assume that nucleation crevices are distributed according to some probability distribution, $F(W)$ (Li and Yortsos 1995).

It follows that the number of sites, N, activated according to the mechanism given by Eq. (1) is,

$$N(t) = B \int_{2\sigma/\Delta p(t)}^{\infty} F(W)dW \tag{10}$$

where B is a constant expressing the total number of sites per volume of rock and $\Delta p(t)$ is the prevailing supersaturation. The rate of creation of nucleation sites is found by differentiating $N(t)$ with respect to time. Assuming that the bubbles created remain stationary and prevent further nucleation because they occupy the pore space where they were created, the rate of bubble nucleation is

$$r_{ns} = \frac{(1-\phi)}{\phi S_g}\frac{dN}{dt} = \frac{(1-\phi)}{\phi S_g} B \frac{2\sigma}{\Delta p^2(t)} F\left(\frac{2\sigma}{\Delta p(t)}\right)\frac{d}{dt}\Delta p(t) \tag{11}$$

For the PN model, the total volume of gas phase, V_{gs}, can be found by summing over all the nucleated bubbles as below,

$$Vgs = \int_{W}^{Wm} a\left[\int_{0}^{t} G(t' - t_{nuc}(W'))dt'\right]^3 F(W')dW' \tag{12}$$

where W_m is the maximum crevice size, W is the crevice size corresponding to the current level of supersaturation and $t_{nuc}(W')$ is the time at which a crevice of size W′ nucleates. In addition to the sequence of bubble generation, the scaling of bubble growth with respect to time differs among PN and IN models. The value of the parameter ν in the expression for $G(t)$ is made 0.4 to account for bubble growth time scaling in the PN model. Hence, bubble volume scales correctly at $t^{1.2}$ and radius at $t^{2.5}$ within the population balance model for PN. The expression for v_b is obtained by dividing V_{gs} by $N(t)$ and the result substituted into Eq. (6) to obtain r_{Ds}.

Once bubbles grow large, coalescence of bubbles can occur when bubbles meet. When stationary bubbles are widely separated such that the gas saturation of a region is not large, the rate of coalescence is zero. Coalescence should increase as the porous medium fills with gas if there is no mechanism to stabilize bubbles. For this work, the rate of coalescence is set to zero as if bubbles remain widely separated. Simulations are checked after the fact to verify that gas saturation remains low.

Constitutive Relationhips and Assumptions. Constitutive equations for compressibility, phase fluxes, and oil mobility are needed to proceed. The gas phase is assumed ideal. A volume balance is used to compute oil-phase compressibility, and we treat rock and fluid contributions separately. The compressibility of the system, c_f, is taken as

$$c_f \approx -\frac{1}{V_p}\left(\frac{\Delta V_p}{\Delta p}\right) = c_{f,r}(1-\phi) + \frac{\phi S_g}{p} + \phi S_o c_{f,o} \tag{13}$$

Here $c_{f,r}$ is the rock compressibility, $1/p$ is the ideal-gas compressibility, and $c_{f,o}$ is the apparent oil-phase compressibility. During iteration within any particular time step, the change in the total system volume is a known quantity. The remaining terms in Eq. (13), except $c_{f,o}$, are known; hence, the apparent oil-phase compressibility is easily calculated.

Several additional assumptions were made in order to begin testing of the proposed model. Initial bubble volume, the number of flowing bubbles, and the amount of continuous gas in the system were all set to zero. Again, coalescence of bubbles is negligible. This is a good assumption for viscous oils because we simulate only the period prior to the onset of gas flow. In effect, the solution is valid only in the period prior to the start of bubble flow and we examine early-time behavior. Thus, we avoid the question of a critical gas saturation in the model for gas relative permeability (Firoozabadi *et al.* 1992; Kamath and Boyer 1995; Li and Yorstos 1995; Du and Yortsos 1999). For the IN model, all bubbles nucleated at the thermodynamic bubble point of the oil. Thus, the critical supersaturation threshold for bubble nucleation was zero for all the runs and we avoid the introduction of another parameter. This does not imply equilibrium as bubble must grow according to the kinetic expressions above.The validity of this assumption will become obvious in the discussion of results.

The flux of the oil phase is calculated according to the multiphase expression for Darcy's law (Dake 1978). Because the gas-phase flux is zero, no relative permeability function for gas is needed. Figure 1 gives the relative permeability relationship for oil used throughout this work. The function is representative, roughly, of oil flow in an oil-gas system within sands and sandstones (*c.f.*, Corey 1954). Nucleated gas reduces the effective permeability to the oil phase somewhat.

Experiments with Viscous Oil

Experiments were conducted with a viscous white mineral oil and carbon dioxide (CO_2) in order to develop a data base against which the population balance model could be tested. The mineral oil chosen was Kaydol. It had a viscosity of 220 mPa-s at ambient conditions. The solubility of CO_2 in Kaydol as a function of pressure is given in Figure 2. The solid line is drawn to guide eyes. Carbon dioxide was used because of its large solubility in Kaydol and the ease with which it was employed in the laboratory. This system does not display any evidence of foaminess with bulk foaming tests. For instance, shaking a beaker of Kaydol at ambient conditions under an atmosphere of CO_2 did not produce foam. All bubbles dispersed in the oil by shaking coalesced in less than 30 s.

The porous medium was an unconsolidated, permeable sandpack with a length of 40.5 cm and a diameter of 5.08 cm. The porous medium was constructed of an aluminum tube and large grain-size sand. Eleven pressure ports were distributed along the length of the sandpack at equal intervals. Pressure was measured using a single quartz crystal transducer (Paroscientific, Redmond, WA) connected to a multiplexing valve (Scannivalve, Liberty Lake, WA). This setup eliminated the need for multiple pressure transducers and the uncertainty of calculating pressure drop among various pressure measuring devices. The sandpack was connected to a high-pressure syringe pump (ISCO, Lincoln NE) that was operated in "refill" mode so that the system volume was expanded at a constant volumetric rate of 6.00 cm^3/hour. The gas-oil system was easily split and the volume of oil produced measured. A three-way valve allowed the selection

between the syringe pump and a backpressure regulator (Grove Valve, Oakland, CA). The backpressure regulator was used during the process of saturating the sandpack with oil.

The sandpack was prepared by first baking the sand at 750 °C in an oven for 6 to 8 hours to remove any organic impurities. After cooling, it was poured dry into the sandpack with constant agitation from pneumatic vibrators. Porous medium permeability (to liquid) and porosity are 25.7 μm^2 and 33.1 %, respectively. CO_2 was injected into the dry sandpack to displace any air. The inlet to the system was closed and vacuum was drawn on the sandpack overnight. A classic reciprocating chromatography pump is used to inject gas-free oil into the sandpack. The system was then brought up to the initial system pressure of roughly 4.14 MPa (600 psi) using the backpressure regulator. No gas-phase CO_2 was present in the system at this point because of the combination of vacuuming, large CO_2 solubility in the oil, and the system was compressed by a factor of 40. The CO_2 saturated Kaydol was then introduced to the sandpack and at least two pore volumes of Kaydol flushed through the system. The backpressure regulator and the pressure measuring device assured us that we remained above the bubble point at all times during this process.

Experiments were conducted in a pressure depletion mode with the inlet to the sandpack closed. The syringe pump expanded the system at a specific volumetric rate and the pressure at each port was measured roughly every 4 minutes.

Results

Next, we discuss the results of simulations for both the IN and PN models. The population balance equations are expressed in two dimensions with a finite difference scheme using the standard simultaneous solution method (Aziz and Settari 1990). Nonlinear terms are treated implicitly. The primary variables of the simulation are P_l, n_t, and $X_{g,o}$. The simulation results are compared to previous experimental data (Firoozabadi *et al.* 1992) for light oils and to new data for viscous oils.

Instantaneous Nucleation. Before proceeding to comparison of experimental and simulation results, we establish the general trends expected for pressure response, bubble radius, and gas saturation. Parameters are listed in Table 1 along with the oil composition. Initially the core is totally filled with gas-saturated oil. At time t = 0, withdrawal of oil from the core is started at a constant volumetric flow rate of 1.44 cm^3/day (5.1 x10^{-5} ft^3/day). The results of a typical IN simulation are shown in Figures 3 to 6. Figure 3 is a plot of average pressure of the core as a function of time, refer to the line for 10,000 bubbles nucleated per ft^3 of rock (0.353 bubbles/cm^3). Other bubble nucleation densities are discussed subsequently. The run is started at a pressure of 1100 psi (7.58 MPa) and all the bubbles nucleate when the pressure drops to the bubble point of 1071 psi (7.38 MPa). Although bubbles nucleate at the thermodynamic bubble point, this does not apply equilibrium, as discussed below. The growth of bubbles causes the trapped gas phase to increase in size. There is competition between two opposing forces. The withdrawal of oil causes the pressure to fall while the transfer of dissolved gas from the oil to the gas phase fills volume and causes pressure to increase. Gas transfer is driven by the difference in chemical potential among gas in solution and the gas phase. When the gas phase volume is sufficiently large, the pressure of the system increases. Growth of the gas phase combined with increasing compressibility allows a rebound in pressure. Eventually oil withdrawal dominates and consequently the pressure decreases again. The rate of pressure decline at this late stage is not as high as that prior to nucleation because the two-phase system is substantially compressible.

Figure 4 is plot of gas saturation versus time for the 10,000 bubbles/ft^3 (0.353 bubbles/cm^3) nucleation case with a volumetric expansion rate of 1.44 cm^3/day (5.1x10^{-5} ft^3/day). There is no gas in the system prior to bubble nucleation (t = 80 min). Immediately following nucleation and up to roughly 150 min, the gas saturation increases at a rate greater than linear. Subsequently, the gas saturation increases steadily reaching a value of about 0.44 % at the end of the simulation run. Figure 5 shows the growth of a typical bubble in time. There is no bubble until the bubble point pressure is reached. Growth of the bubble is fast initially because gas in the bubble is far from equilibrium with liquid. Growth slows at later times as the system approaches equilibrium and the bubble grows mostly due to pressure decline caused by oil

withdrawal. The size of all bubbles in the system is nearly the same, although, small variations in bubble size are caused by the difference in pressure across the core.

The number of bubbles nucleated per unit volume of rock, N_o, is an adjustable parameter in the IN model. Figure 3 illustrates the effect of varying N_o with all other parameters fixed. When the number of bubbles nucleated is increased, the pressure rebound occurs earlier, the apparent critical supersaturation is less, and the rebound in pressure achieves a higher level. By critical supersaturation, we simply mean the difference between the thermodynamic bubble point and the first minimum in pressure with respect to time. More bubbles imply a larger gas saturation in the system.

Figure 6 shows the effect of varying the system expansion rate, Q_o, on the average pressure of the core. As Q_o increases, the rate of pressure decline becomes larger and hence the pressure falls to lower values before rebounding. Note also the apparent increase in supersaturation as the withdrawal rate increases. The competition between bubble growth and volume expansion increases with withdrawal rate because the gas-oil system is farther from equilibrium.

With the general trends in hand, the model can be compared to available experimental data. Firoozabadi *et al.* (1992) conducted pressure depletion experiments on a Berea sandstone core saturated with a $C_1/C_2/n\text{-}C_{10}$ mixture. In these experiments, the oil withdrawal rate was fixed and the pressure of the core was recorded as a function of time prior to the start of bubble flow. The bubble point is 1071 psi (7.4 MPa) as employed above. The core and hydrocarbon mixture properties are also given in Table 1.

Figure 7 shows a comparison of the IN model simulation with the experimental data for a withdrawal rate of 1.44 cm^3/day (5.1 x10^{-5} ft^3/day). The number density of nucleated bubbles per volume of rock is fixed to 350 bubbles/ft^3 (0.0124 bubbles/cm^3) rock for this run. The simulation result matches the data quite well until a volume expansion of about 0.75 cm^3 (2.6x10^{-5} ft^3) and tends to deviate somewhat thereafter. The pressure from the simulation is higher than the experimental data at late time, but the error is only about 2 %.

An important point to note is that no critical supersaturation is imposed on the system for the simulation runs. Firoozabadi *et al.* (1992) asserted that bubbles nucleated at the pressure corresponding to the minima on the P vs. t curve (6.9 MPa, 1010 psi). Thus, according to them, the value of supersaturation was around 60 psi (0.41 MPa). In these simulations, bubble growth begins at the bubble point pressure. Although bubbles nucleate at the thermodynamic bubble point of the mixture, gas and liquid are not in equilibrium. Bubbles grow according to the kinetic equations above, and the volume of gas as a function of time lags behind what is expected for equilibrium conditions. There is competition between pressure increase due to mass transfer of gas to the bubbles and pressure decrease due to the expanding system volume. These competing effects result in the characteristic pressure minimum and rebound witnessed in solution gas drive. One advantage of our approach is that it eliminates the need for determining experimentally, the value of critical supersaturation as a function of rate for every system.

Figure 8 shows the variation of gas saturation along the core at different times. The gas saturation is highest at a dimensionless length of 1 corresponding to the outlet of the core. Supersaturation is highest near the outlet where the liquid pressure is lowest, hence, gas saturation is relatively high. The run was stopped at t = 2010 mins because this corresponds to the recorded time when gas began to exit the core. The average gas saturation at the end of simulation (Fig. 8) is around 1.26%. This matches well with the value of 1.3% reported by Firoozabadi *et al.* (1992). The low values of gas saturation and the relatively small number of bubbles nucleated indicate the validity of neglecting bubble-bubble coalescence during the initial stages of solution gas drive.

Figure 9 shows the results of the simulation and experimental pressure data for a liquid withdrawal rate of 7.2 cm^3/day (2.54x10^{-4} ft^3/day). The bubble number density of nucleated bubbles was adjusted to 1000 bubbles/ft^3 (0.0353 bubbles/cm^3) to obtain a match with data. All the other parameters are governed by the properties of either the liquid or the porous medium and are not affected by a change in the withdrawal rate. Again, gas bubbles nucleate and begin to grow at the thermodynamic bubble point. The

pressure match for this case is again quite good. Gas saturation profiles with time are rather similar to Fig. 8 and so are not shown here for reasons of brevity. The final gas saturation corresponding to a volume expansion of 3.25 cm^3 ($1.1x10^{-4}$ ft^3) is around 1.8 % which is close to the value of 2 % reported by Firoozabadi *et al.* (1992).

Note, the bubble density increases as the liquid withdrawal rate increases for the IN model. The explicit implication is that more nucleation sites are activated as the withdrawal rate is increased. Additionally, we observe that the bubble population balance approach has directly modeled the increase in apparent critical supersaturation evident in the data (compare Figs. 7 and 9).

Next, the model was applied to a system with a relatively low surface tension. A run was conducted for a liquid mixture with σ equal to 2.1 dyne/cm (2.1 mN/m). The match between the simulated and the experimental pressure data is shown in Figure 10. The properties of the oil mixture and the parameters for the simulation run are summarized in Table 2. The bubble density is 10,000 bubbles per ft^3 of rock (0.35 bubbles/cm^3) which is higher than the previous cases. The implication is that N_o increases with a reduction in surface tension. Calculation and experiment agree well.

Now, the IN bubble population balance model is applied to the viscous-oil solution gas drive experiments. The properties of the mineral oil (Kaydol) are summarized in Table 3 which also lists the properties of the sand pack. The number of bubbles nucleated is 14,000 per ft^3 of rock (0.49 bubbles/cm^3) consistent with the large volumetric expansion rate. Figure 11 is a plot of average core pressure versus time for a run with an oil withdrawal rate of 6 cm^3/hr ($2.1x10^{-4}$ ft^3/hr). The match between the experiment and the simulation is quite good. The simulation overestimates the pressure after t = 80 mins. Gas begins to flow at about 5.25 hrs (314 min) corresponding to a gas saturation of 6%. Our model does not match the data well after 5.25 hrs because it does not have mobile gas. From Figure 12, it can be seen that the simulated gas saturation at 5.25 hrs is 10% which is above the experimentally observed value of 6%.

Summarizing this portion of the modeling exercise, the IN bubble-population-balance model matches experimental data for both light and viscous oil, especially in regard to pressure response. We find no need to incorporate a critical supersaturation. This effect arises naturally within the model when gas nucleates at the bubble point. The main parameter requiring adjustment is the number of bubbles nucleated. The shift in N_o with withdrawal rate and interfacial tension is explained physically. Next, we look at the PN model and its match to the same data.

Progressive Nucleation

The PN model requires a probability distribution function of crevice sizes in the porous medium as input along with the other parameters. In practice, this crevice size distribution is discretized into 1000 equally spaced intervals, a cavity size is correlated with each interval, and the activation supersaturation corresponding to each interval is calculated according to Eq. (1). All grid blocks are assumed to have the same crevice distribution. Each grid-block stores information about the current minimum size of the activated crevice and the history of nucleation in it. The total gas-phase volume is found by summing bubble volumes over all the discrete levels of crevice size. The above scheme is, thus, an approximation of the integral form of the PN model equations. However, it is computationally expedient.

The PN simulation results were first compared to the light oil experimental data of Firoozabadi *et al.*(1992). The properties of the core and oil are the same as in Table 1. The crevice probability density distribution is assumed to be distributed in a log-normal fashion. The actual distribution used for the light-oil runs is shown in Figure 13. The time step for the PN model simulations was kept very small (0.005 hrs) to assure convergence to the correct solution. Figure 14 shows the average pressure versus time for Q_o equal to 1.44 cm^3/day ($5.1x10^{-5}$ ft^3/day). The match is quite good at early times and late times with deviations in the intermediate period. Nucleation for the PN model starts below the thermodynamic bubble point of the liquid when the supersaturation first exceeds the capillary barrier of the maximum crevice size in the

medium. For the current runs, nucleation occurred at practically the bubble point as the maximum crevice size was quite large. This may, however, be different for other systems. Figure 15 shows plots of gas saturation versus distance for this run. The gas saturation at the end of the run is approximately 1.31% which is very close to the value of 1.3% (Firoozabadi *et al.* 1992). Note that the gas saturation profile in Fig. 15 is similar to that for the IN model in Fig. 8. Profiles are relatively flat and S_g is low.

Another run was performed for the same oil system with a Q_o equal to 7.2 cm^3/day ($2.5x10^{-4}$ ft^3/day). The pressure results are shown in Figure 16. Every parameter, except the withdrawal rate, was identical to the Q_o equal to 1.44 cm^3/day run ($5.1x10^{-5}$ ft^3/day). The pressure match is again good and the gas saturation at the end of the run, 1.8 %, agrees well with the experimentally observed value of 2%.

Next, the PN bubble-population-balance model was used to examine viscous oil behavior. The crevice probability density distribution for the porous medium is shown in Figure 17. This is different from the light-oil case because the porous medium is different. The former case is a sandstone, while the current is a high permeability sandpack. Figure 18 shows a comparison of the PN model simulation with the experimental data for the viscous mineral oil, Kaydol. The pressure match is very good until t = 315 min after which gas bubbles begin to flow. The gas saturation in the core, not shown here, at 5.25 hrs is 8.4 % which is higher than the experimentally observed value of 6 %.

Discussion

Both the IN and PN bubble-population-balance models match experimental trends for the light and viscous oil experiments reasonably well. The pressure and overall saturation matches for the PN model are better. The advantage of the PN model is that once the crevice distribution of the porous medium and the properties of the fluid are fixed, there is no need to adjust any parameters. The number of bubbles nucleated is a function of the number of sites activated. For the IN model, the number density of nucleated bubbles is an adjustable parameter that has to be evaluated for every run. Physical bases were used here to determine N_o among runs depending on Q_o and σ. An advantage of the IN model is its simplicity. There is no need to keep track of the bubble size distribution in each grid-block and this makes the simulations much faster than the PN model. As discussed earlier, the time step size was made small to assure convergence for the PN simulations. The simulation run times for the PN model were approximately 15 times larger than those for the IN model.

Figure 19 helps to explain why both IN and PN models yield similar results. It shows a plot of supersaturation versus time for the viscous oil PN simulation. The supersaturation increases after bubble nucleation until about t = 75 min. where it reaches a maximum of 88 psi (0.61 MPa). In PN theory, bubble nucleation occurs only while supersaturation is increasing. Subsequently, supersaturation declines rapidly to a value of 10 psi (0.69 MPa). It then remains relatively constant throughout the remainder of the simulation. In terms of time, bubbles are nucleated from 40 min to 75 min, although bubbles do grow continually. The period of bubble nucleation is a relatively short interval compared to the total time required to deplete the system. This computational result is in agreement with the experimental observations of Yousfi *et al.* (1997) and assertions of Firoozabadi (2001).

Note that the cavity size distributions for PN simulations given in Figs. 13 and 17 are similar for two reasons. First, both porous media originate from sands. Although the sandstone has somewhat lower permeability and porosity, the roughness or crevice characteristics of the grains in each porous medium are likely similar. Second, the calculations reveal that bubbles are nucleated in only the largest crevices. For instance, the minimum cavity size nucleated during calculations for the viscous oil case is $0.06\ \mu m$ ($6.0x10^{-6}$ cm, $2.0x10^{-7}$ ft). Relative to the entire distribution of cavity sizes shown in Fig. 17, this minimum size is quite large. The minimum cavity sizes nucleated in the light-oil cases are similarly large. Thus, the PN calculations shown here are somewhat insensitive to the details of the shape of the crevice size distribution. Of course, with a different depletion rate, or other conditions, a greater fraction of the crevice size distribution may be sampled.

We caution that the results illustrated here should not be considered general because they do not span the entire range of possible physical conditions. For instance, all of the fluid systems are relatively ideal with a limited number of chemical components and no complex organic molecules, such as asphaltenes, resins, or organic acids. Also, a wide variety of pressure depletion rates are not explored and all of the experimental data originates from clean sands or sandstones. Nevertheless, the modeling and experimental results indicate that the initial stages of the solution gas drive process can be described in a consistent fashion across the spectrum of light to viscous oils. Absolute time scales for diffusive bubble growth and pressure depletion are different, of course, as viscosity varies, but the underlying physical phenomena appear to be similar. In turn, the rate of depletion is quite important because gas diffusion and volumetric expansion mechanisms compete to determine pressure response.

All the simulations above were carried out at constant oil withdrawal rates. To study depletion with a pressure boundary condition, the Peaceman well model (Aziz and Settari 1990) was added to the simulator. The pressure at the open end of the core was decreased at a constant rate (dp/dt). In all runs, the properties of the system were the same as those for the viscous oil simulations. In general, the cumulative recovery of oil, before the onset of gas flow, increases with an increase in dp/dt as there is larger pressure drop across the core. An increase in oil viscosity causes a decrease in cumulative oil production as expected from Darcy's law. A more detailed analysis of the system with the pressure boundary condition is given elsewhere (Arora 2000).

Future Work. Although the population-balance framework developed is general, a number of simplifying assumptions were made with regard to gas mobility. The next step, is to add gas mobility to the simulator and allow the possibility of multiple generation of bubbles at the same site once gas exits a particular region of porous medium. This is most easily achieved by adding the concept of critical gas saturation to gas relative permeability. Adding gas mobility makes it possible to compare model predictions to the late-time data from the viscous oil experiments as well as additional experimental data in literature on heavy oil (Urgelli *et al.* 1999, Treinen *et al.* 1997). Gas mobility might also allow further differentiation between IN and PN models. Other enhancements to the model include bubble coalescence as gas saturation rises.

On the experimental side, we intend to explore solution gas drive in the viscous white oil at different expansion rates. By employing oils of different viscosity, the role of oil viscosity on recovery and the ease of creation of the gas phase will be defined. Also, we wish to impose experimentally a prescribed rate of pressure decline so as to provide an additional mode of comparison to simulation.

Conclusion

Solution gas drive is a production mechanism commonly encountered in oil reservoirs that is not very well understood for the case of heavy oil. A mechanistic population balance model has been developed that incorporates instantaneous and progressive mechanisms for solution gas drive. The population balance approach is physical in that the nucleation and growth of the gas phase are modeled explicitly. Of course, expressions are required that model bubble mechanics accurately. The population balance equations are analogous to the mass balance equations for reservoir simulation and so can be incorporated into existing reservoir simulation framework.

Both the IN and PN bubble-population balance models were applied successfully to experimental data for the initial period of solution gas drive (before the onset of gas flow) in light and viscous oils. The IN model showed good matches to pressure data for both light and viscous oils. The average gas saturation at the onset of gas flow for the two cases was also close to the experimentally observed values. The number density (N_o) of bubbles nucleated per volume of rock is an adjustable parameter. It increased when the oil withdrawal rate increased; likewise, N_o increased when the surface tension of oil decreased. An important feature of our IN model is that no critical supersaturation threshold is required to match experimental data. All bubbles nucleate at the thermodynamic bubble point of the gas-liquid system.

The match of the PN model results to experimental data for light and heavy oils was very good and judged superior than those for the IN model. Extra computational work was associated with this improved agreement. Bubbles were released from cavities when the supersaturation overcame the capillary forces associated with a particular crevice size. The period of active bubble nucleation for the PN model, however, was relatively small compared to the total time of the pressure depletion runs. This is in agreement with experimental observations in the literature (Yousfi *et al.* 1997).

References

1. Arora, P., "Mechanistic Modeling of Solution Gas Drive in Viscous Oils", M.S. Report, Stanford University (Jun. 2000).

2. Aziz, K. and Settari, A., *Petroleum Reservoir Simulation*, Elsevier Applied Science, London, 1990.

3. Claridge, E.L. and M. Prats, "A Proposed Model and Mechanism For Anomalous Foamy Heavy Oil Behavior," SPE 29243, in Proceedings of the International Heavy Oil Symposium, Calgary, Alberta (Jun., 1995).

4. Corey, A. T., "The Interrelation Between Gas and Oil Relative Permeabilities," *Producers Monthly*, 19(1), 38-41, (1954).

5. Dake, L.P., *Fundamentals of Reservoir Engineering*, Elsevier Scientific Publishing, Amsterdam, 1978.

6. Du, C. and Y.C. Yortsos, "A Numerical Study of the Critical Gas Saturation in a Porous Medium," *Transport in Porous Media*, 35, 205-225, (1999).

7. Falls, A.H., G.J. Hirasaki, T.W. Patzek, P.A. Gauglitz, D.D. Miller, and T. Ratulowski, "Development of A Mechanistic Foam Simulator: The Population Balance and Generation By Snap-Off," Soc. Pet. Eng. Res. Eng., 3(3), 884-892, (1988).

8. Firoozabadi, A., B. Ottesen, and M. Mikklesen, "Measurement of Supersaturation and Critical Gas Saturation," *Soc. Pet. Eng. Formation Evaluation*, Dec(337-344), (1992).

9. Firoozabadi, A. and D. Kashchiev, "Kinetics of the Initial Stage of Isothermal Gas Phase Formation," *J. Chem. Phys.*, 98(6), 4690-4699, (1993).

10. Firoozabadi, A. and D. Kashchiev, "Pressure and Volume Evolution During Gas Phase Formation in Solution Gas Drive Processes," *Soc. Pet. Eng. J.*, 1(3), 219-227, (1996).

11. Firoozabadi, A., "Author's Reply to Pressure and Volume Evolution During Gas Phase Formation in Solution Gas Drive Processes," Soc. Pet. Eng. J., 2(2), 228-231, (1997).

12. Firoozabadi, A., "Mechanisms of Solution Gas Drive in Heavy Oil Reservoirs," J. Can. Pet. Tech., 40(3), 15-20, (2001).

13. Huang, W.S., B.E. Marcum, M.R. Chase, and C.L. Yu, "Cold Production of Heavy Oil From Horizontal Wells in the Frog Lake Field," Soc. Pet. Eng. Res. Eval. & Eng., 1(6), 551-555, (1998).

14. Kamath, K. and R.E. Boyer, "Critical Gas Saturation and Supersaturation in Low-Permeability Rocks," *Soc. Pet. Eng. Form. Eval.*, 10(4), 247-253, (1995).

15. Kovscek, A.R. and C.J. Radke, Fundamentals of Foam Transport in Porous Media, in *Foams: Fundamentals and Applications in the Petroleum Industry*, L.L. Schramm, Editor., American Chemical Society: Washington D.C. p. 115-163, 1994.

16. Kovscek, A.R., T.W. Patzek, and C.J. Radke, "A Mechanistic Population Balance Model for Transient and Steady-State Foam Flow in Boise Sandstone," *Chemical Engineering Science*, 50(23), 3783-3799, (1995).

17. Kraus, W.P., W.J. McCaffrey, and G.W. Boyd: "Pseudo-Bubble Point Model for Foamy Oils," CIM 93-45, in Proceedings of the 44th Annual Tech. Conf. of the Petroleum Society of CIM, Calgary, AB (May 9-12, 1993).

18. Li, X. and Y.C. Yortsos, "Theory of Multiple Bubble Growth in Porous Media by Solute Diffusion," *Chem. Eng. Sci.*, 50(8), 1247-1271, (1995).

19. Maini, B.B., H.K. Sarma, and A.E. George, "Significance of Foamy-oil Behaviour in Primary Production of Heavy Oils," Journal of Canadian Petroleum Technology, 32(9), 50-54, (1993).

20. Maini, B.B., "Foamy Oil Flow in Heavy Oil Production," *Journal of Canadian Petroleum Technology*, 35(6), 21-24, (1996).

21. Patzek, T.W., Description of Foam Flow in Porous Media by the Population Balance Approach, in *Surfactant-Based Mobility Control: Progress in Miscible-Flood Enhanced Oil Recovery*, D.H. Smith, Editor., American Chemical Society: Washington, D. C. p. 326-341, 1988.

22. Randolph, A. D. and Larson, M. A., *Theory of Particulate Processes*, Academic Press: New York p. 41-64 (1971).

23. Satik,C.,Li,X. and Yortos,Y.C., "Scaling of single-bubble growth in a porous medium", *Phys. Rev. E*, **51**(4), pp 3286-3295, (1995).

24. Scriven, L.E., "On the Dynamics of Phase Growth," Chem. Eng. Sci., 10(1/2), 1-13, (1959).

25. Sheng, J.J., R.E. Hayes, B.B. Maini, and W.S. Tortike: "A Dynamic Model to Simulate Foamy Oil Flow in Porous Media," SPE 36750, in Proceedings of the Soc. Pet. Eng. Ann. Tech. Conf. and Exhibition, Denver, CO (Oct. 6-9, 1996).

26. Sheng, J.J., Maini, B.B., Hayes, R.E. and Tortike, W.S., "Experimental Study of Foamy Oil Stability", *JCPT*, **36**(4), pp 31-37, (1997).

27. Sheng, J.J., B.B. Maini, R.E. Hayes, and W.S. Tortike, "Critical Review of Foamy Oil Flow," Transport in Porous Media, 35, 157-187, (1999).

28. Smith, G.E., "Fluid Flow and Sand Production in Heavy-Oil Reserviors Under Solution-Gas Drive," *Soc. Pet. Eng. Production Engineering*, 3(2), 169-180, (1988).

29. Tang, G.Q. and Firoozabadi, A., "Gas and Liquid-Phase Relative Permeabilities for Cold Production from Heavy Oil," SPE 56540, presented at the SPE Annual Technical Conference and Exhibition, Houston (October 3-6, 1999).

30. Treinen, R.J., Spence, A.P., de Mirabel, M., and Huerta, M., "Hamaca: Solution Gas Drive Recovery in a Heavy Oil Reservoir, SPE 39031, presented at the Fifth Latin American and Caribbean Petroleum Engineering Conference and Exhibition, Rio de Janeiro, Brazil (August 30-September 3, 1997).

31. Tsimpanogiannis, I. N. and Yortsos, Y. C., "An Effective Continuum Model for the Liquid-to-Gas Phase Change and Growth in a Porous Medium Driven by Solute Diffusion," Proceedings of the IMECE'01, New York, NY (Nov. 11-16 2001).

32. Urgelli, D., M. Durandeau, H. Foucault, and J.-F. Besnier, "Investigation of Foamy Oil Effect from Laboratory Experiments," SPE 54083, in Proceedings of the Soc. Pet. Eng. International Thermal Operations and Heavy Oil Symposium, Bakersfield, CA (Mar 17-19, 1999).

33. Wilt, P.M., "Nucleation Rates and Bubble Stability in Water Carbon Dioxide Solutions," *J. Coll. Int. Sci.*, 112(2), 530-538, (1986).

34. Yousfi, A.E., C. Zarcone, and S. Bories, "Physical Mechanisms for Bubble Growth During Solution Gas Drive," SPE 38921, in Proceedings of the Soc. Pet. Eng. Ann. Tech. Conf. and Exhibition, San Antonio, TX (Oct 5-8, 1997).

Nomenclature

A = shape factor of a bubble
A_{cs} = rate constant for bubble coalescence
B = constant, number of sites/volume of rock ($1/L^3$)
c_f = compressibility (LT^2/M)
D = diffusion coefficient of gas in liquid (L^2/T)
F = cavity size probability density (1/L)
G = growth rate of bubble (L/T)
J = flux (mol/L^2T)
K_s = solubility constant ($mol\text{-}L^2/ML^2$)
n = bubble density, number of bubbles/volume of gas ($1/L^3$)
N = number of bubbles nucleated per unit rock volume ($1/L^3$)
p = pressure (M/LT^2)
Q = volumetric flow rate (L^3/T)
r = rate of change of bubble texture ($1/L^3T$)
S = saturation
t = time (T)
u = superficial velocity (L/T)
v = volume (L^3)
V = volume (L^3)
W = cavity size (L)
X = concentration (mol/mol)

Greek letters

β = slope of two phase equilibrium line (ML^2/T^2)
Δp = supersaturation (M/LT^2)
ν = growth parameter power
σ = interfacial tension (L/T^2)
ρ = molar density (mol/L^3)
ω = growth parameter power

Subscripts

b = bubble
bp = bubble point
c = coalescence
D = diffusion

f	=	flowing
G	=	generation, gas
g,o	=	gas in gas-free oil
l	=	liquid
m	=	mobilization
ns	=	nucleation of stationary bubbles
nuc	=	nucleation
o	=	oil
o,o	=	oil in gas-free oil
o	=	core
r	=	rock
s	=	stationary
v	=	vapor

TABLE 1
Simulation Parameters for Bubble Population Balance Model—Establishment of General Trends.

Parameter	Value	Parameter	Value
Length of core (cm)	49.40	β (psi/cm^3)	14
Cross Sectional Area (cm^2)	12.01	K_s (lb-mol/psi-ft^3)	1.6231×10^{-4}
Porosity	0.23	D (ft^2/sec)	6.5×10^{-8}
Pore Volume (cm^3)	136.46	ω	0.5
Permeability (md)	605	ν	0.5
Composition of oil	C_1 28.2%; C_2 0.02%; n-C_{10} 71.46%		
Bubble point pressure (psi)	1071		
Surface tension (dyne/cm)	13	grid size	40 by 3

TABLE 2
Simulation Parameters for Bubble Population Balance Model to Match Low Interfacial Tension Data.

Parameter	Value	Parameter	Value
Length of core (cm)	49.40	β (psi/cm^3)	45.9
Cross Sectional Area (cm^2)	12.01	K_s (lb-mol/psi-ft^3)	1.6231×10^{-4}
Porosity	0.23	D (ft^2/sec)	6.5×10^{-8}
Pore Volume (cm^3)	136.46	ω	0.5
Permeability (md)	605	ν	0.5
Composition of oil	C_1 65.14%; C_2 0.22%; n-C_{10} 34.29%	N_o (bubbles/ft^3-rock)	10000
Bubble point (psi)	3655		
Surface tension (dyne/cm)	2.1	grid size	40 by 3

TABLE 3

Simulation Parameters for Bubble Population Balance Model to Match Viscous Oil Experimental Data.

Parameter	Value	Parameter	Value
Length of core (cm)	40.6	β (psi/cm^3)	3.53
Cross Sectional Area (cm^2)	20.3	D (ft^2/sec)	6.5×10^{-8}
Porosity	0.331	ω	0.5
Pore Volume (cm^3)	264	ν	0.5
Permeability (d)	25.7	viscosity (cP) @ 20°C	220
Composition of oil, gas solubility	CO_2/Kaydol refer to Fig. 2		
Bubble point (psi)	525		
Surface tension (dyne/cm)	50	grid size	40 by 3

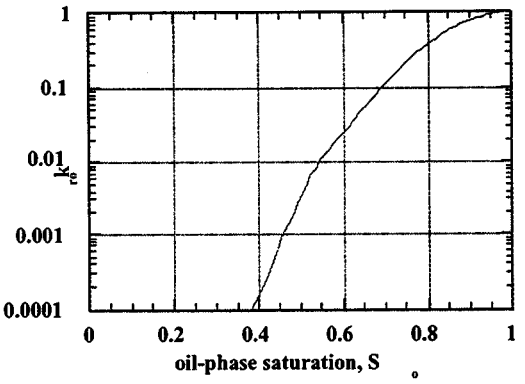

FIG. 1. Oil-phase relative permeability function.

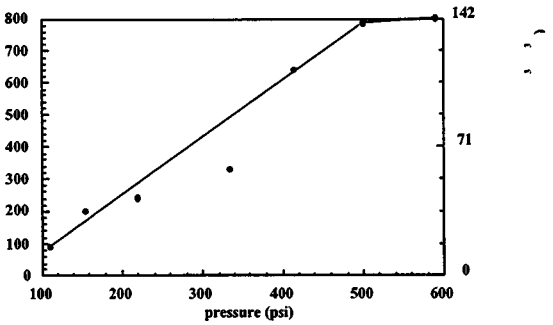

FIG. 2. Solubility of CO2 in Kaydol as a function of pressure.

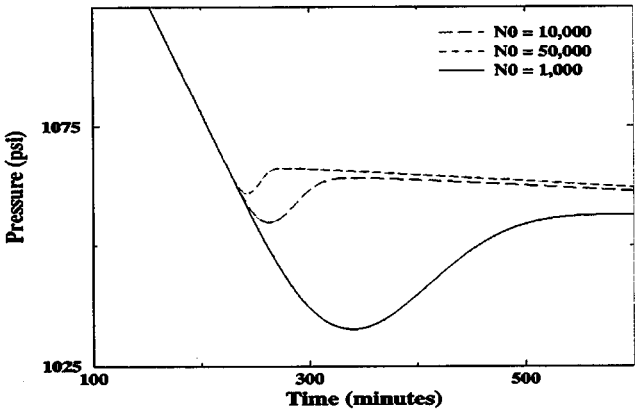

FIG. 3. Plot of average pressure versus time illustrating the effect of varying number of bubbles nucleated, IN population balance model. Withdrawal rate is 1.44 cm3/day (5.1x10-5 ft3/day).

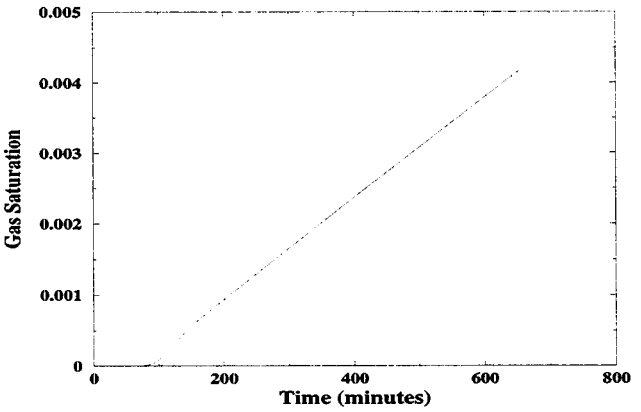

FIG. 4. Average gas saturation in the core versus time for an oil withdrawal rate of 1.44 cm3/day (5.1x10-5 ft3/day), IN population balance model. The number of bubbles nucleated is 10,000 bubbles/ft3 of rock (0.353 bubbles/cm3).

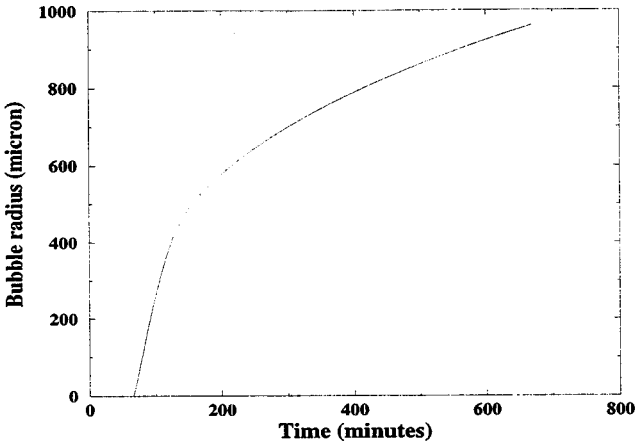

FIG. 5. Gas bubble size with time for an oil withdrawal rate of 1.44 cm3/day (5.1x10-5 ft3/day), IN population balance model. The number of bubbles nucleated is 10,000 bubbles/ft3 of rock (0.353 bubbles/cm3).

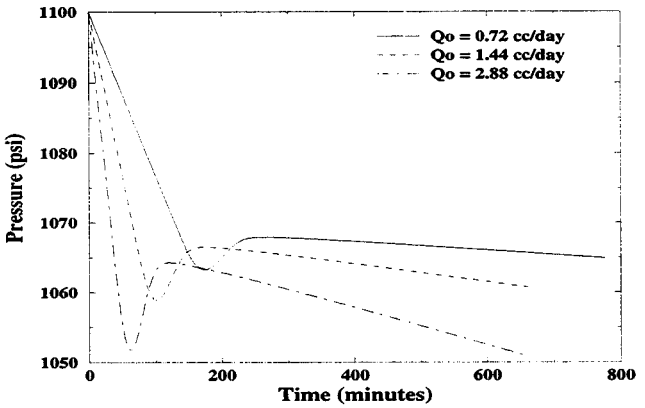

FIG. 6. Plot of average pressure versus time illustrating the effect of varying the expansion rate, IN population balance model. The number of bubbles nucleated is 10,000 bubbles/ft3 of rock (0.353 bubbles/cm3).

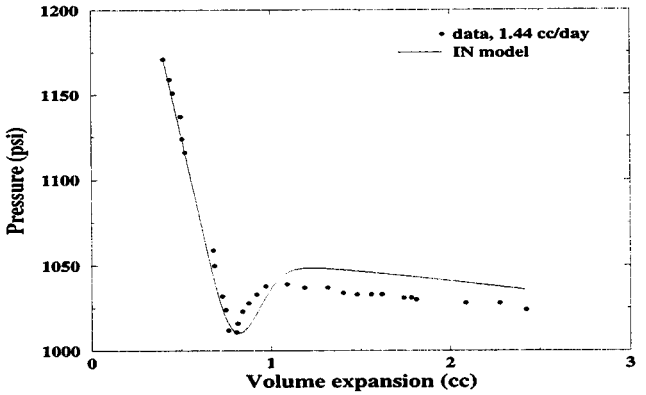

FIG. 7. Match of the IN bubble population balance model to the experimental pressure data of Firoozabadi et al. Withdrawal rate is 1.44 cm3/day (5.1x10-5 ft3/day).

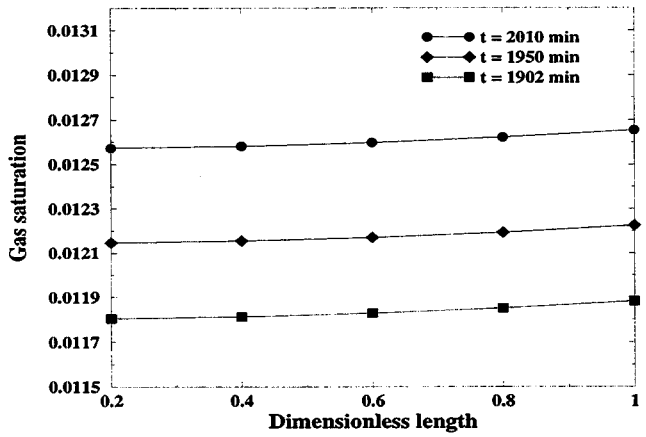

FIG. 8. IN population balance model prediction of average gas saturation along length of core. Withdrawal rate is 1.44 cm3/day (5.1x10-5 ft3/day).

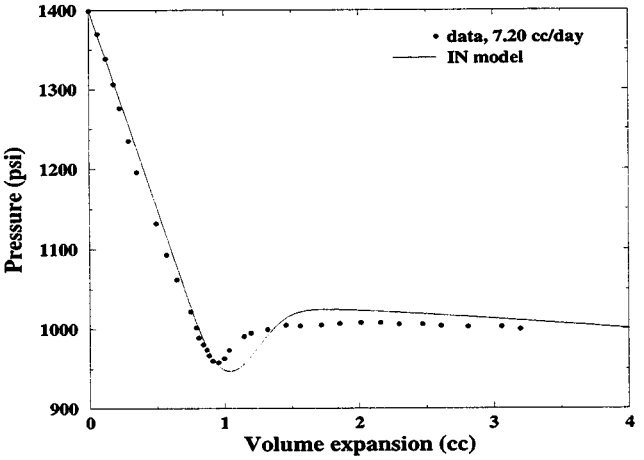

FIG. 9. Match of the IN bubble population balance model to the experimental pressure data of Firoozabadi et al. Withdrawal rate is 7.2 cm3/day (2.5x10-4 ft3/day).

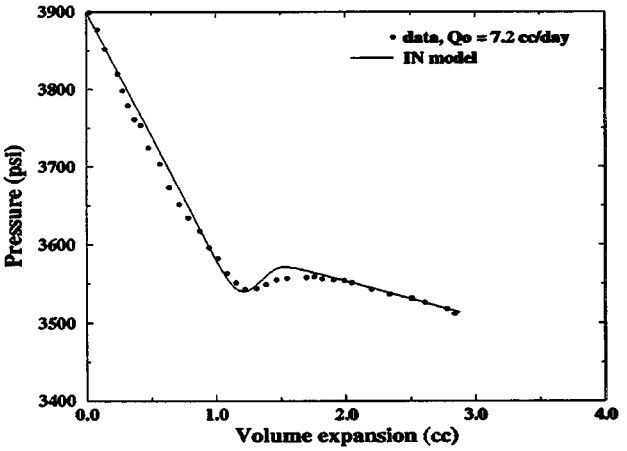

FIG. 10. Match of the IN bubble population balance model to the experimental pressure data of Firoozabadi et al. Low surface tension system. Withdrawal rate is 7.2 cm3/day (2.5x10-5 ft3/day).

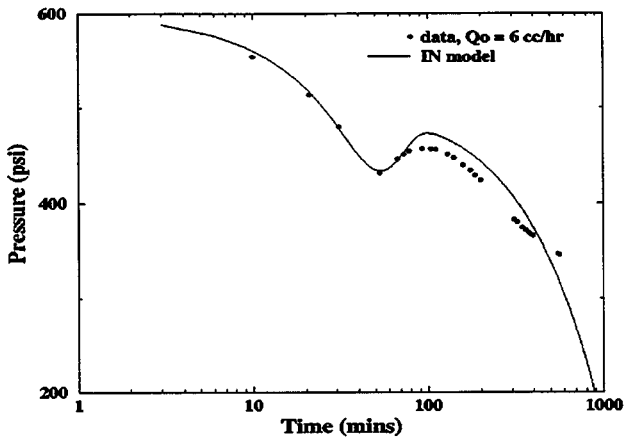

FIG. 11. Match of the IN bubble population balance model to viscous-oil solution gas drive pressure data. Withdrawal rate is 6 cm3/hour (2.1x10-4 ft3/hr).

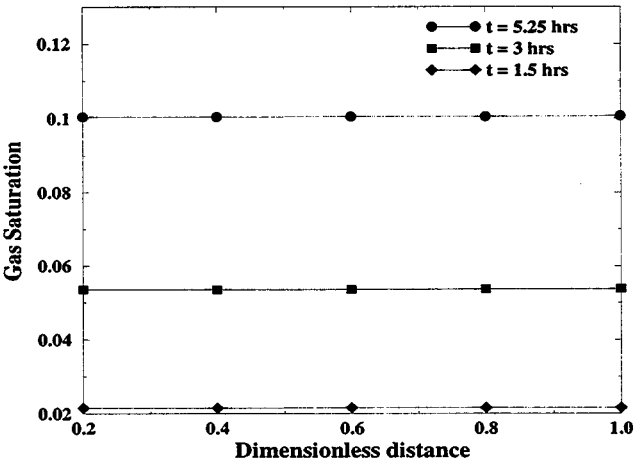

FIG. 12. IN population balance model prediction of average gas saturation along length of core for viscous-oil solution gas drive. Withdrawal rate is 6 cm3/hour (2.1x10-4 ft3/hr).

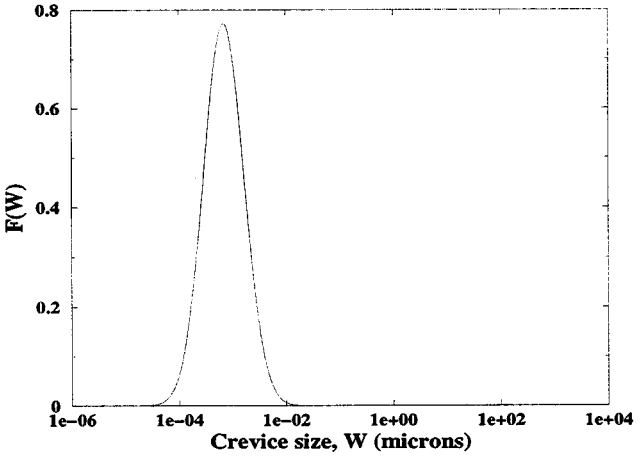

FIG. 13. Crevice size probability distribution function for PN simulations of the experimental data of Firoozabadi et al.

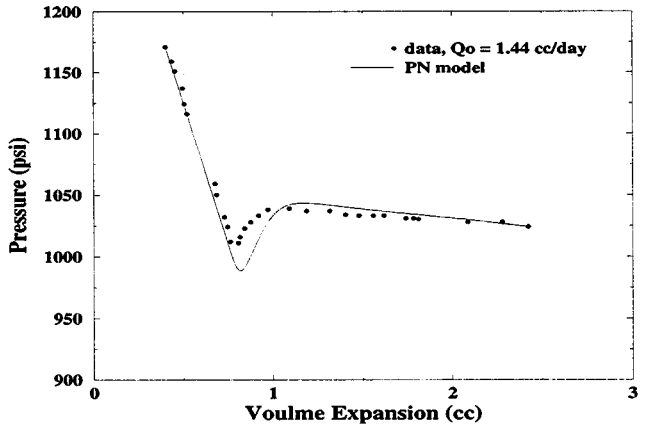

FIG. 14. Match of the PN bubble population balance model to the experimental pressure data of Firoozabadi et al.23. Withdrawal rate is 1.44 cm3/day (5.1x10-5 ft3/day).

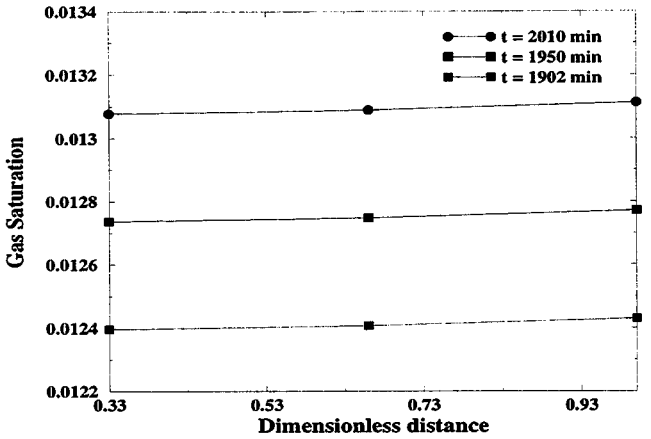

FIG. 15. PN population balance model prediction of average gas saturation along length of core. Withdrawal rate is 1.44 cm3/day (5.1x10-5 ft3/day).

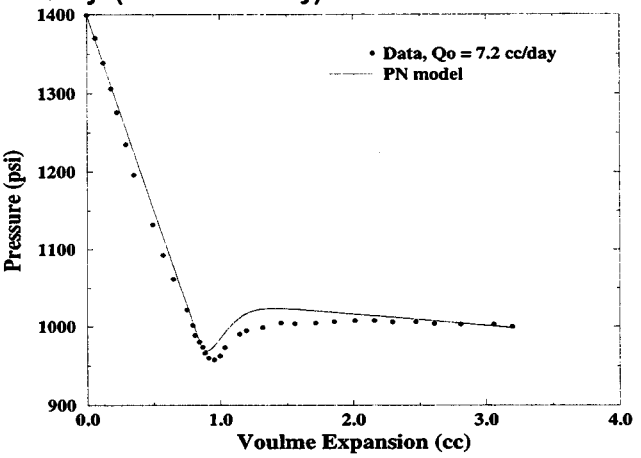

FIG. 16. Match of the PN bubble population balance model to the experimental pressure data of Firoozabadi et al. Withdrawal rate is 7.2 cm3/day (2.5x10-4 ft3/day).

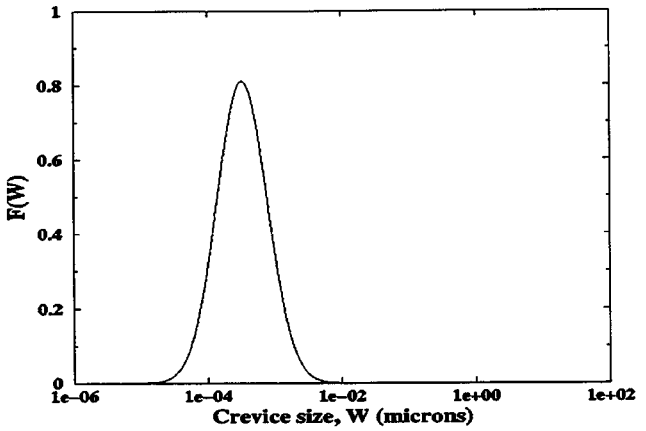

FIG. 17. Crevice size probability distribution function for PN simulations of the viscous oil experiments.

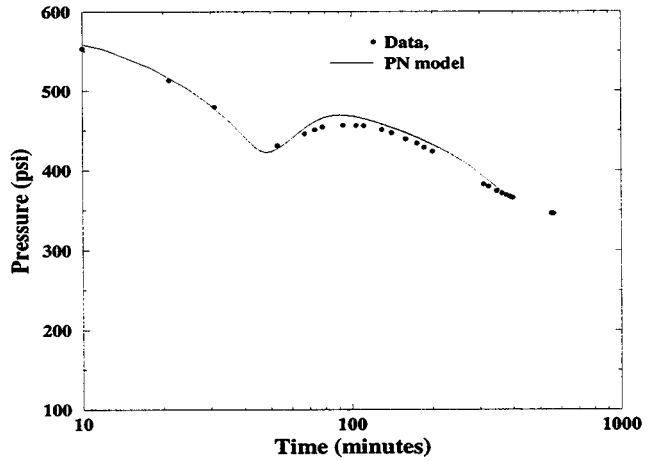

FIG. 18. Match of the PN bubble-population-balance model to viscous-oil solution gas drive pressure data. Withdrawal rate is 6 cm3/hour (2.1x10-4 ft3/hour).

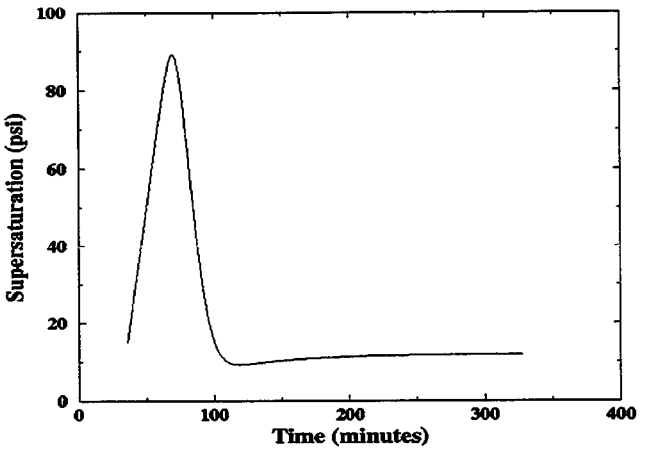

FIG. 19. Supersaturation versus time for the viscous oil PN simulation run.

Mathematical Modeling of Gas Bubble Coalescence in Heavy Oil Reservoirs under Solution-Gas-Drive

Omar Hayat

Introduction

Primary production from heavy-oil reservoirs operating under a solution-gas-drive mechanism exhibits unexpectedly high primary recovery with slower pressure decline rate, lower than expected producing gas oil ratios and higher oil production rates (Bora and Maini, 1997).

Heavy-oil reservoirs in Canada and Venezuela exhibit this phenomenon. The process of solution gas drive involves nucleation of gas bubbles as the pressure in the reservoir falls below the bubble point. It is postulated these small bubbles are trapped and tend to remain dispersed in the oil due to the large viscosity of the continuous oil phase. Initial development of many of these reservoirs under solution-gas drive has a great economic advantage because implementation of traditional thermal methods can be avoided or delayed, resulting in cost saving. At Frog Lake, Alberta Canada a study by Huang *et al.* concluded that cold production, the simultaneous production of oil and sand with the aid of progressive cavity pumps, can produce heavy oil (12° API, 20,000 to 50,000 cp) without the introduction of any external thermal energy. Another study in the Hamaca area of the Orinoco Belt in Eastern Venezuela (Mirabal, 1996) attributed the high productivity found in the reservoir to foamy-oil behavior of the crude. It was reported that primary production mechanism of the Hamaca reservoirs is controlled by the in-situ formation of a non-aqueous oil foam under solution gas drive conditions, improving oil mobility, therefore leading to high well productivity. The contribution of foamy-oil behavior as a primary production mechanism is up to 10% of the OOIP in the Hamaca Area .

Several of these reservoirs are said to have shown a "foamy oil" behavior. This "foam" is oil continuous with the gas fraction close to solution gas-oil ratio and the consistency of a "chocolate mouse" at the wellhead. This kind of reservoir shows abnormally high production rate as well as effective recovery factor (Urgelli *et al.*, 1999).

To explain the above phenomenon a number of mechanisms have been suggested (Poladi-Darvish and Firoozabadi, 1999) which can be divided into two main categories. Geomechanical effects such as sand dilation and development of wormholes comprise the first category. The second category suggests that the special properties of the flowing fluids, the gas and heavy oil, are the main reasons for high production. Both of these categories are not mutually exclusive and are described in some detail below.

The first theory postulates that this favorable behavior of heavy-oil reservoirs driven by solution-gas-drive is because of sand production. Economical production of heavy oil is possible by allowing formation sand to be produced along with the fluid. Dusseault (1978) shows that heavy oil (10-15° API) in cohesionless sandstones (>30% porosity) can be exploited by permitting sand to enter the wellbore along with fluids. He showed that with 1-3% sand production the flow rate goes up from 0.3 – 2 m^3/d to 5-15 m3/d. This higher rate with sand production is attributed to four major factors enhanced drainage radius, grain movement, gas bubble expansion, and continuous pore deblocking.

The second theory suggests that sand production is not the predominant mechanism responsible for high oil rates and recoveries in heavy oils. It focuses more on the way the two phases i.e. oil and gas interact. According to this theory retention of the evolved gas phase in a dispersed form in the oil would lead to maintaining the reservoir energy. Although Dake (1978) does not explicitly discuss heavy oils he has shown that to obtain a high primary recovery, as much gas as possible should be kept in the reservoir. Maintaining the cumulative gas oil ratio the ratio of cumulative gas production to cumulative oil production) as low as possible, helps keep the gas in the reservoir. By keeping the gas in the reservoir the total reservoir system compressibility is large and results in greater cumulative production for a given pressure drop.

The second category, is the focus of this research. Smith (1986) argues that it is certainly the case that extensive sand production modifies the reservoir in the vicinity of the casing, but it has been shown in the laboratory that no amount of sand remolding or fines removal would increase the permeability to the extent observed in pressure analysis. It is more likely that the laboratory determined core permeabilities are overestimates of the undistributed in-situ values and it is most commonly observed that the fines migration in the reservoir leads to reservoir plugging and not reservoir cleaning.

Its now an accepted fact that in the solution gas drive process, the main source of energy driving the oil towards the wellbore is the evolution and expansion of the gas initially dissolved in the oil (Bora and Maini, 1997). The role of the gas bubbles in the oil displacement process is a focus of many research efforts, for the simple reason that understanding the pore level physics of how these bubble nucleate, grow and coalesce is the key to developing better oil recovery techniques from heavy oil reservoirs.

In studying the bubble nucleation and growth process, research efforts have been directed towards trying to examine directly the pore level events by using micromodels. These micromodels are mostly made of glass and in some cases etched out in silicon. Such visualization experiments have also been accompanied by numerical simulation of the experiments. Li and Yortsos carried out experiments of bubble growth by pressure depletion in 2-D etched-glass micromodels and in Hele-Shaw cells (bubble growth in bulk liquid) (Li and Yortsos, 1995). The work also included development of a pore network numerical model to simulate the growth of multiple gas clusters under various conditions. Du and Yortsos also studied the dependence of critical gas saturation (gas saturation at which the onset of bulk gas flow occurs) on the geometric parameters of the porous media in detail (Du and Yortsos, 1999). Bora and Maini (1997) carried out a series of flow visualization experiments to examine the pore scale behavior of the solution gas drive process in heavy oils.

Experimental and modeling effort has also focused on understanding the nucleation mechanism for the gas bubbles. There are two models explaining the nucleation of bubbles. One is instantaneous nucleation (IN), which states that all the bubbles nucleate at essentially the same time and do not originate from preexisting bubbles trapped in crevices or the roughness of pore walls. Firoozabadi and Kaschiev (1995) did some significant work to explore IN. The progressive nucleation process assumes that the bubbles are released from sites such as crevices or roughness on pore walls with poor liquid wetting properties that become activated when the local supersaturation exceeds the capillary pressure of the site (Li and Yortsos, 1995).

The most important issue, however, is the understanding of bubble coalescence in porous media. The presence of dispersed gas bubbles in the oil during pressure depletion results in increased production rates in heavy oil reservoirs.

Bora *et al* (1997) made several observations about bubble coalescence. They described bubble coalescence as a three-step process. According to them, first, the bubbles have to come close to each other. This occurs naturally during migration of the bubbles in fast depletion tests and growth of adjoining bubbles by diffusion in slow depletion tests. When the bubbles are close enough and collide, the second step of the coalescence process begins. This involves draining and thinning of the liquid film separating the two bubbles. This thinning can be a slow process, which requires a finite length of time. According to them whether or not bubbles will coalesce depends whether the hydrodynamic forces pull the two bubbles apart

before the liquid film has drained to a critical film thickness. At critical thickness the final step leads to coalescence of two adjoining bubbles.

George and Kovscek (1999) developed an apparatus to allow the use of silicon-wafer micromodels over a wide range of pressures, as required for solution gas drive experiments. Expected pore-level phenomena, such as snap-off and "breathing" of liquid films were successfully observed. Visual observations of gas bubble formation and evolution at a nucleation site were recorded. Experimental results indicated that oil-phase viscosity affects the rate at which pressure changes during pressure decline. Viscosity was also found to affect possibly the ability of bubbles to coalesce.

Building on that, Arora and Kovscek (2000) developed a mechanistic population-balance model to describe solution gas drive behavior in viscous oils and address the question of gas-bubble microstructure. The objective of this work was to incorporate pore-level bubble nucleation, growth, and transport mechanisms into a continuum displacement model consistent with standard simulation of multi-phase flow in porous media and to verify the theoretical predictions by comparison to experimental results. The results for the IN and PN models were compared to experimental data reported elsewhere for light oil and to new data for viscous oils. It was found that PN model matches the experiments somewhat better, but is more demanding computationally.

The work presented in this paper is directed towards developing a better understanding of solution gas drive behavior in heavy oils. While there is experience and data from micromodels and numerical simulation, the pore-level physics needs to be explored further. The objective of this work is to develop a mathematical model to explain the coalescence of gas bubbles trapped in narrow throats filled with heavy oil. An interesting phenomenon observed in previous micromodel experiments was the effect of viscosity on bubble coalescence (George, 1999). A study by Kumar and Pooladi-Darvish (1999) on the effects of viscosity and diffusion coefficient on the kinetics of bubble growth in heavy oil, reported that the effect of oil viscosity on bubble growth can be ignored. It concluded that viscous forces and in general hydrodynamic forces have little or no effect on bubble growth in heavy oils at late times. This observation was based on studying the numerical model for growth of a single bubble in heavy oil and light oil for gradual decline in pressure. These seemingly different observations make it all the more necessary to explore the effect of viscosity on bubble coalescence in porous media.

Here, mathematical model is developed to study the phenomenon of bubble coalescence in a narrow, non-circular throat filled with oil. The model computes the time required for the oil lens between the bubbles to drain. The computed time for coalescence is compared with visual data available from micromodel experiments.

The next section describes the assumptions and mathematical derivation of the equations.

The third section describes the micromodel experiment. The fourth and the last section consists of discussion of results and comparison to experimental data.

Model Formulation

The goal of this work is to develop a mathematical model that describes the coalescence of gas bubbles trapped in the originally oil filled pores in reservoir media. Consider Fig [1a] to understand the geometry of the trapped bubbles in the pore, this geometry is the basis for developing the model.

The following assumptions are made to solve this problem: Oil is the wetting phase and gas is the non-wetting phase and there is no aqueous phase present. The pore has a square cross-sectional area. This is a valid assumption because real pores in porous media have corners. Pore geometry is shown in Fig 2. Bubbles are acted on by the oil-phase pressure gradient and diffusional bubble growth is slow enough to be neglected. Pore cross-sectional areas in our models are also square. The flow out of the oil lens is through

the four pore corners, and oil films that line the straight section of the bubble-pore wall interface are thin enough to be ignored in flow calculations.. Any effect of gravity is ignored considering the very small pore diameters in reservoir media. Finally we assume that no thin-film forces are present to stabilize gas-oil interfaces.

The problem is solved for one of the trapped bubbles and the solution is valid for the second bubble by virtue of symmetry. Fig 1b shows the geometry of flow lines as the two trapped bubbles move towards each other under the pressure gradient across the bubble. At the plane of symmetry the flow lines interact to generate a stationary flow plane with respect to the z-axis. At this point the problem becomes analogous to a "squeeze film". Denn (1908) explores the problem of a squeeze film in detail.

In the problem under discussion, gas bubbles move towards the symmetry plane and the oil flows out through the four corners. Fig [1b] shows the geometry of the flow problem.

The boundary conditions for the problem illustrated in Fig 1 are that at

$$v_z = v_r = 0 \tag{1}$$

at the symmetry plane.

The oil-gas bubble interface moves towards the symmetry plane, with velocity V(t). Therefore at the moving surface(z = H(t)):

$$v_z = V(t) \tag{2a}$$

$$v_r = 0 \tag{2b}$$

Solving the Navier stokes creeping flow equation for the above boundary conditions, the following expressions for v_z, v_r and V_t are reached (Denn, 1908).

$$v_z = -3V(t) [\, z/H(t)]^{2} [1-2z/3H(t)] \tag{3}$$

$$v_r = [3rzV(t) / H^2(t)] [1 - z/H(t)] \tag{4}$$

$$V(t) = - dH/dt = [2F/3\pi\eta R^4] H^3 \tag{5}$$

In the above equations, H(t) is the distance between the symmetry plane and the bubble front at time t, v_z is the velocity of fluid in z-direction, v_r is the velocity of fluid in the radial direction, V(t) is the velocity of the moving bubble, μ is the viscosity of the fluid, F is the imposed force, responsible for bubble movement, and R is the radius of the bubble.

At this point, boundary conditions and the flow equations are established for this problem.

The task now is to calculate the expression for time t, needed for the two bubbles each of radius R and separated by distance H_o, to drain the oil lens so that coalesce may occur. The answer comes from Stefan Equation [16], derived for the squeeze-film problem using the boundary conditions and flow equations described above:

$$H(t) = [(1/H_o^{2)} + (4Ft/ 3\pi\mu R^4)]^{-1/2} \tag{6}$$

Solving for t gives

$$t = (3\pi\mu R^4/4F) [\, 1/H^2 - 1/H_o^2] \tag{7}$$

In the above equation R, H and Ho can be measured and quantified from visual micromodel experiments. The viscosity of the oil, μ, can be readily measured. The only unknown that needs some mathematical treatment is the imposed force F.

In short, F is simply the pressure difference times the cross-sectional area of the pore and is given by

$$F = (\Delta P - \Delta P_c)\, \pi R^2 \tag{8}$$

Where ΔP is the total pressure gradient across the bubble and ΔP_c is the pressure gradient of oil in four pore corners. The resistance to flow in the pore corners opposes thinning of the lens.

The expression for the term ΔP_c can be calculated from the expression for flow resistance coefficient β, given by Ransohoff and Radke (1988),

$$\Delta P_c = (q\mu\beta L) / (a^2 A_w) \tag{9}$$

where q is the volumetric oil flow rate through the corners, β is the dimensionless flow resistance coefficient, L is the length of the bubble, and A_w is the area of the corners occupied by the oil.

The volumetric flow rate q out of the oil lens is given by

$$q_w = \int_0^{H(t)} 2\pi R v_r \, dz \tag{10}$$

Substituting Eq (4) for v_r and integrating, we obtain

$$q_w = [6\pi R^2 V(t) / H^2(t)]\, [z^2/2 - z^3/3H(t)] \tag{11}$$

Putting in the limits from 0 to H(t), Eq (11) reduces to

$$q_w = \pi R^2 V(t) \tag{12}$$

Substituting Eq (5) for V(t) gives;

$$q_w = 2FH^3(t) / 3\mu R^2 \tag{13}$$

Putting the value of q_w back into the expression for ΔP_c, Eq (9), we obtain

$$\Delta P_c = (2F\, H^3(t)\beta L) / (3\, a^2\, R^2\, A_w) \tag{14}$$

Where a is the interfacial radius of curvature as shown in Fig 2b.

Substituting F with $(\Delta P - \Delta P_c)\, \pi R^2$ in the above expression gives

$$\Delta P_c = [(2\pi H^3(t)\beta L) / (3\, a^2 A_w)]\, [\Delta P - \Delta P_c] \tag{15}$$

Let $\lambda = [(2\pi H^3 \beta L) / (3\, a^2 A_w)]$ and rearranging the above equation

$$\Delta P_c = [\lambda(t)/(1+\lambda(t))]\, \Delta P \tag{16}$$

At this point we have established a relationship between ΔP and ΔP_c and can find the time required to drain any lens. The next step is to establish the values for each of the remaining parameters. Once this is done, calculations can be made for comparison with experimental findings.

Values of parameters are established from experimental observations. The pressure gradient across the bubble, ΔP can be obtained by measuring the gradient across the entire micromodel and equating the $\Delta P/L_{model}$ with $\Delta P/L_{throat}$. For example the micromodel used here is a 1.6-inch square with pressure drop of about 70 psi across its length. The ratio $\Delta P/L_{model}$ for this model is about 44.45 psi/in, for a typical throat of length 100 μm the value of ΔP is about 0.2 psi.

Ransohoff and Radke (1988) have computed the value of β as a function of surface viscosity, pore half angle, contact angle, and degree of roundedness in both graphic and tabular form. For this problem, a no slip condition is assumed and the value for sharp corners is used (degree of roundedness, $R_0 = 0$). From Ransohoff and Radke, for surface viscosity = 0, $\beta = 93.93$. See Fig 2b for the geometry of the problem.

The value for interfacial radius, a, can be calculated from the work of Ransohoff *et al.* (1987). This work tabulates the values for the equilibrium dimensionless interfacial entry curvature, $C_{dm} = C_m R$, in a variety of noncircular cross sections, where R is the local radius for the largest inscribed circle of the capillary. For the case under discussion, it is the radius of the throat. As the throat is assumed to have a square cross-section, $C_{dm} = 1.89$ from Ransohoff et al. Interfacial radius a is related to C_m by simple relationship $a \cong 1/C_m$. For typical pore radius of 10 μm, a = 5.3 μm.

The area wetted by the oil at the four corners, A_w is related to interfacial radius a by simple expression $A_w = 4[a^2 - \pi a^2/4]$. For typical pore dimensions mentioned above, A_w equals 24.02 μm^2.

Its clear that value of β will remain independent of pore geometry for this problem because of the assumption that the throat has sharp corners. Other parameters are dependent on pore geometry and will change from one case to another. The procedure to evaluate them, however, remains unchanged.

Experimental Apparatus

The experimental apparatus consists of a micromodel, pressure vessel, optical equipment and a system of hardware that controls fluid flow and pressure (George, 1999). The micromodel is a 5 cm by 5 cm etched pore pattern in silicon-wafer, which is anodically bonded to a borosilicate glass plate. Fig [3a] is an optical micrograph of the model. Fig [3b] is a SEM micrograph of the model and shows the shape and pattern of the pore network. Note the pore wall roughness and sharp unrounded pore corners.

In order to perform solution gas drive experiments at elevated pressure, a pressure vessel is designed to house the micromodel. The pressure vessel has an operating pressure of 1000 psig. It has a thick sapphire window located directly above the micromodel. See Fig [4] for pressure vessel configuration. Confining fluid is present on both surfaces of the micromodel.

A microscope is positioned on top of the vessel and pore events in the micromodel can be observed through the sapphire window of the pressure vessel.

Kaydol, a 200 cP mineral oil, was saturated with CO_2 at the desired pressure for a minimum of 20 hours. If the micromodel contained air, CO_2 was injected and allowed to sweep the micromodel to displace the air. The upstream pressure was increased to the desired injection pressure, and the injection of live liquid was initiated. Sufficient time was allotted for the micromodel to fill with the liquid, and for some fluid to exit the micromodel. The three-way valve on the downstream side of the pressure vessel was turned such that the outlet of the micromodel was connected to the syringe pump. The pump was then run until the

outlet pressure reached the inlet pressure. The valve on the upstream side of the pressure vessel was shut. At this point the volume between the valve and the syringe pump, including the porous medium, pressure gauges, and tubing was closed. Once the inlet and outlet pressure equilibrated ($\Delta p = 0$), the syringe pump was run in refill mode at a low flow rate, to provide a controlled volume expansion.

The upstream and downstream pressures were recorded against time, and the VCR recorded pore-level visual observations. These visual observations are used to verify the mathematical model developed in this work.

Results and Discussion

Equations derived previously are used to calculate the time for coalescence of gas bubbles trapped in a narrow pore. The geometrical dimensions used are taken from a particular micromodel experiment see Fig 5.

The results are plotted in Fig 6a for the following values of the parameters.

Parameter	Value
Viscosity, η	220cP
Bubble Length, L	100 μm
Bubble Radius, R	10 μm
Interfacial Radius, a	5.29 μm
Wetting Area, A_w	24.02 μm^2
Pressure Gradient, ΔP(across bubble)	0.2 psi

The time required for the bubble to travel from its initial position to the plane of symmetry is calculated. There are no chemical agents present in the viscous mineral oil to stabilize the interface and prevent coalescence. Thus coalescence is assumed to occur when the bubble interfaces (gas-oil) touch. The time interval for coalescence is found by computing time versus interface position according to Eq (7) from the initial position to 1μm of separation. We then extrapolate the solution to an interface separation zero. At very small thickness of the oil lens the squeeze film approximation of this problem breaks down and infinite coalescence times are predicted. With this procedure the calculated time for coalescence is roughly 34s, whereas the experimentally measured time is 32s. The two agree well.

Fig 6b shows the plots for the same geometry of the pore and bubbles but varying viscosities of the liquid. There clearly exists a linear relationship between the time for coalescence and oil viscosity. As the viscosity increases bubbles see greater resistance from the surrounding viscous oil and the time for coalescence goes up.

The dependence of time for coalescence on viscosity of oil is in agreement with observed high recoveries for heavy oil reservoirs under solution gas drive. These heavy oil reservoirs are able to maintain their high-energy state because gas bubble coalescence is delayed by viscous oil. The more time these bubbles take to coalesce the more time is available for the reservoir to stay energetic and produce at high rates, resulting in higher productivity and higher recovery.

Future Work

At this stage a mathematical model has been developed to predict the time for coalescence of trapped bubbles in narrow noncircular pores and it has been verified against one experimental observation. A good match is found. One observation is, however, not enough to validate the model. We need matching against several more experimental observations before it can be satisfactorily validated. There are some differences between the flow field of the squeeze film problem and bubbles in oil and the model needs further refinement to take those into account. Furthermore, at a distance very close to the plane of symmetry or in other words when the two bubbles come very close to each other, the time for coalescence goes to infinity. This behavior needs to be explained and if it asks for some changes in the model, then the necessary changes need to be incorporated.

References

1. Arora P., A Mechanistic Modeling and Experimental Study of Solution Gas Drive. MS Thesis, Stanford University, September 2000.

.2. Bora, R. and Maini, B.B., "Flow Visualization Studies of Solution Gas Drive Process In Heavy Oil Reservoirs Using a Glass Micromodel;" SPE 37519, paper presented at the SPE International Thermal Operations and Heavy Oil Symposium, Bakersfield (February 10-12, 1997).

3. Dake, L.P., Fundamentals of Reservoir Engineering, 1978, by Elsevier, P 84.

4. Denn, Morton M., Process Fluid Mechanics, published by Prentice Hall, 1980, 255 –261.

5. Dusseault, M., Cold Production and Enhanced Oil Recovery, JCPT (November 1993) p. 16.

6. Du, C., Yortsos, Y.C., "A Numerical Study of the Critical Gas Saturation in a Porous Media.," *from* Transport in Porous Media 35 (1999) 205-225.

7. Firrozabadi A., Kaschiev D., Pressure and Volume Evolution During Gas Phase Formation in Solution Gas Drive Process., SPE 26286, Sept 28, 1995.

8. George, D.S., "Visualization of Solution Gas Drive In Viscous Oils," MS Thesis, Stanford University, September 1999.

9. Huang W.S. and Marcum B.E., "Cold Production of Heavy Oil from Horizontal Wells in the Frog Lake Field," SPE 37545, paper presented at the SPE International Thermal Operations and Heavy Oil Symposium, Bakersifled (February 10-12, 1997).

10. Kumar, R., Pooladi-Darvish, M., "Effect of Viscosity and Diffusion Coefficient on the Kinetics of Bubble Growth in Solution-gas Drive in Heavy Oil.," 8th Saskatchewan Petroleum Conf. of CIM in Regina, Canada, (October 18-20, 1999).

11. Li, X. and Yortsos, Y.C., "Visualization and Simulation of Bubble Growth in Pore Networks.", AICHE Jouranl. (February 1995.

12. Mirabal, Rodriguez, H., "Production Improvement Strategy for Foamy Hamaca Crude Oil: A Field Case," SPE 37544, paper presented at the SPE International Thermal Operations and Heavy Oil Symposium, Bakersfield (February 10-12, 1997).

13. Mirabal, Rodriguez, H, " Impact of Foamy Oil Mechanism on the Hamaca Oil Reserves, Orinoco Belt,"Venezuela., SPE 36140, paper presented at the Fourth Latin American and Caribbean Petroleum Engineering Conference, Port-of-Spain, Trinidad and Tobago (April 23-26, 1996)..

14. Poladi-Darvish, M., and Firoozabadi, A., Solution-gas Drive in Heavy Oil Reservoirs. JCPT **38**, No. 4 (April 1999).

15. Ransohoff, Radke and Gauglitz, "Snap-Off of Gas Bubbles in Smoothly Constricted Noncircular Capillaries," AIChE Journal, **33**, No. 5 (May 1987).

16. Ransohoff, T.C. and Radke, C.J., "Laminar Flow of a Wetting Liquid along the Corners of a Predominantly Gas-Occupied Noncircular Pore," Journal of Colloid and Interface Science, **21**, No.2, (February 1988).

17. Smith G.E., "Fluid Flow and Sand Production in Heavy Oil Reservoirs Under Solution Gas Drive," SPE 15094," paper presented at the 56th California Regional meeting of SPE, Oakland (April 2-4, 1986).

18. Urgelli, D. and Durandeau, M., "Investigation of Foamy Oil Effect from Laboratory Experiments,". SPE 54083, paper presented at the SPE International Thermal Operations and Heavy Oil Symposium, Bakersifeld (March 17-19, 1999).

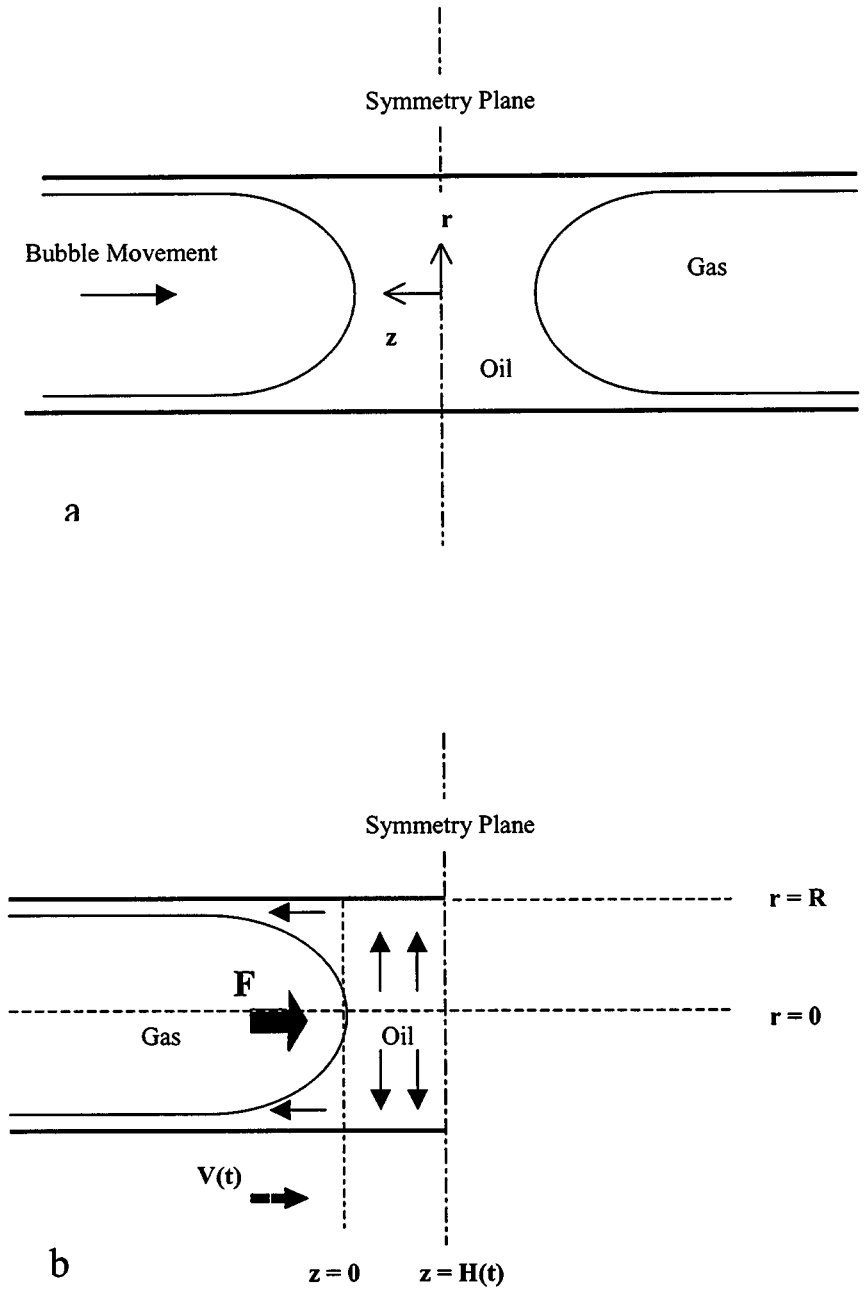

Figure 1 a) Geometrical configuration of two gas bubbles moving towards each other in a narrow pore.
b) Schematic representation of fluid flow and how the plane of symmetry acts as a static plate.

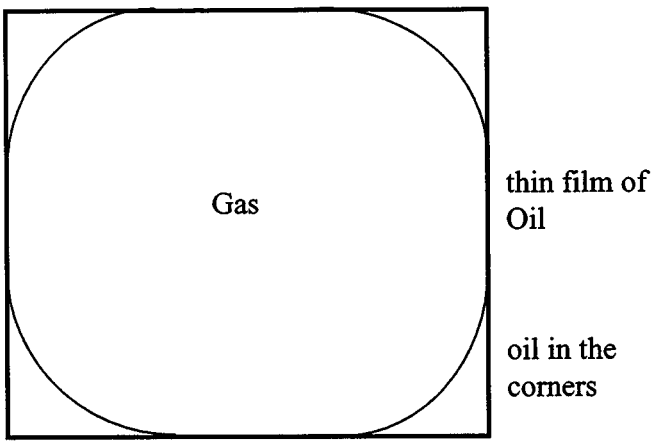

a

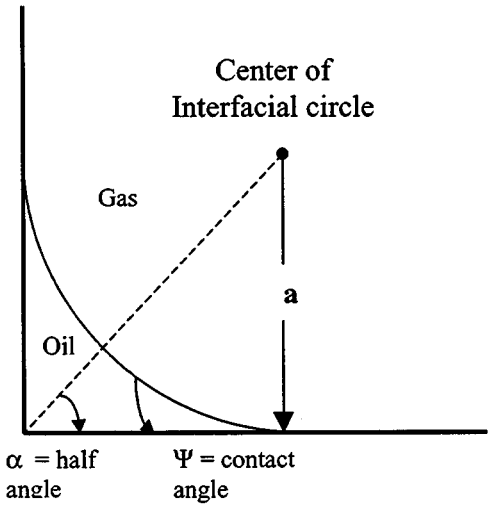

b

Figure 2 a) Cross-sectional view: wetting-liquid distribution in a square throat withthe trapped gas bubble in it.

b) Geometry of the corner flow problem. Showing the half angle,α, the contact angle,Ψ and the primary radius of curvature, a. Flow is in the positive z-direction into the plane of the figure.

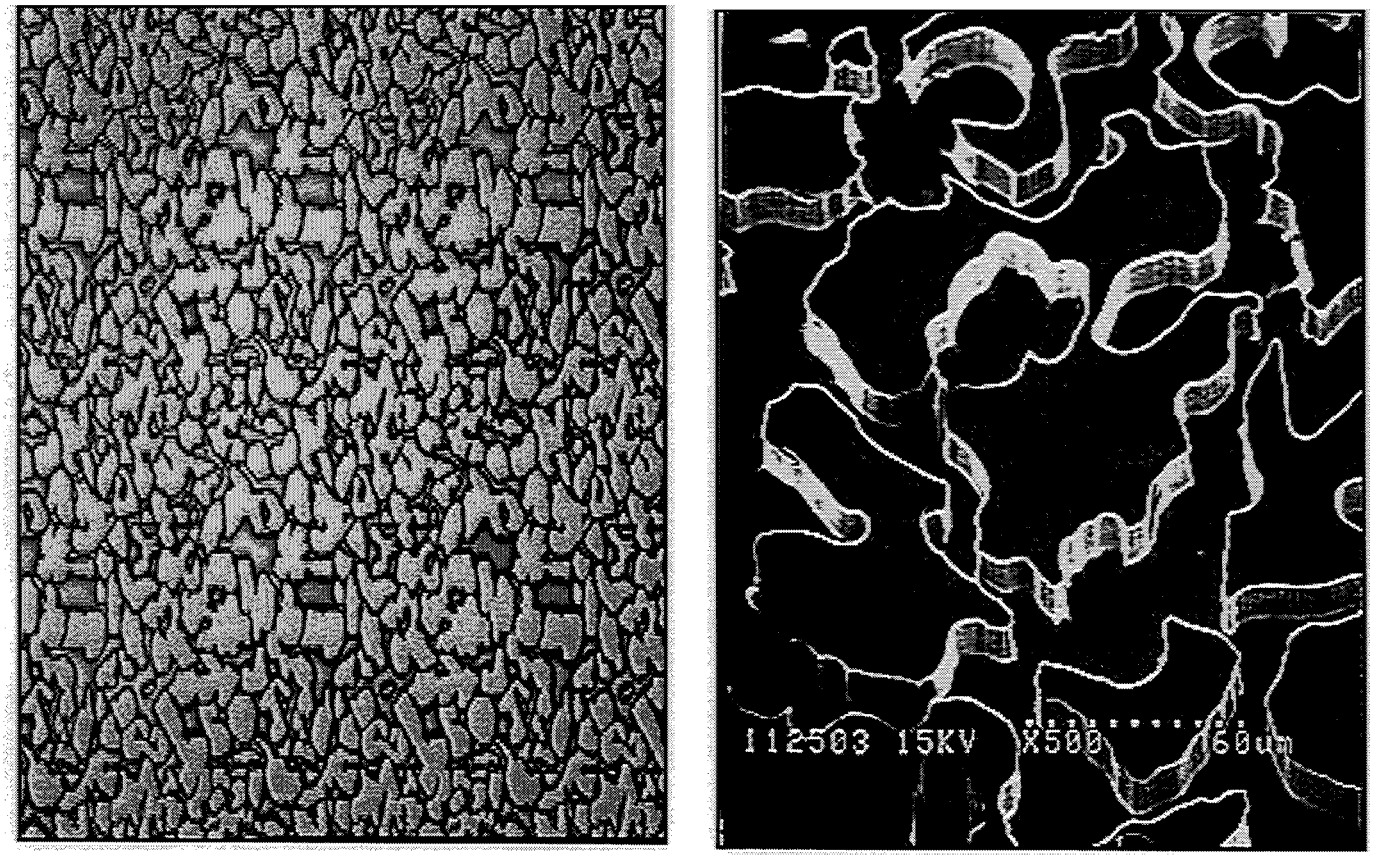

Figure 3 a) Optical micrograph of the micromodel.
b) SEM micrograph of the micromodel.

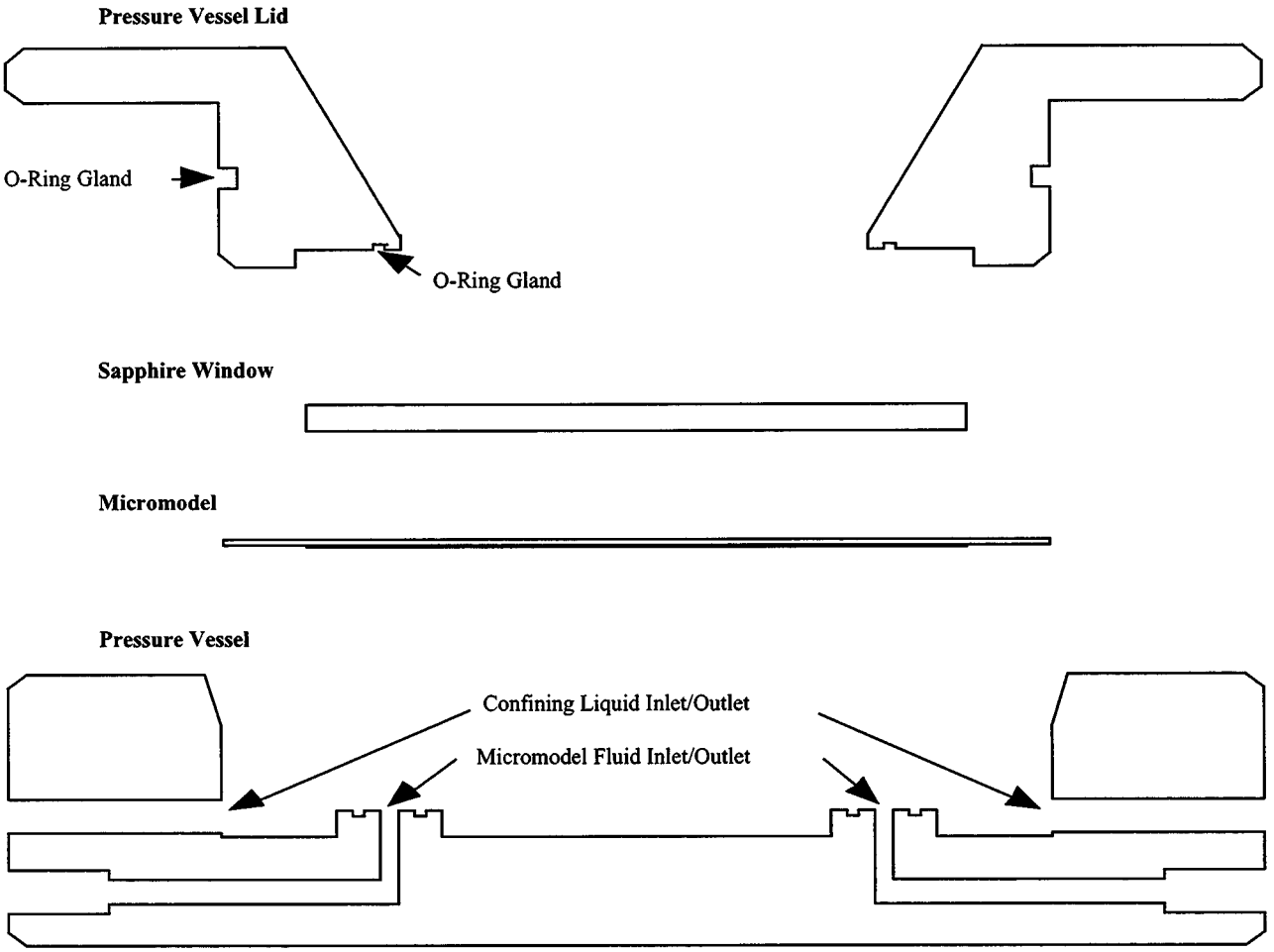

Figure 4 Exploded view of the pressure vessel components

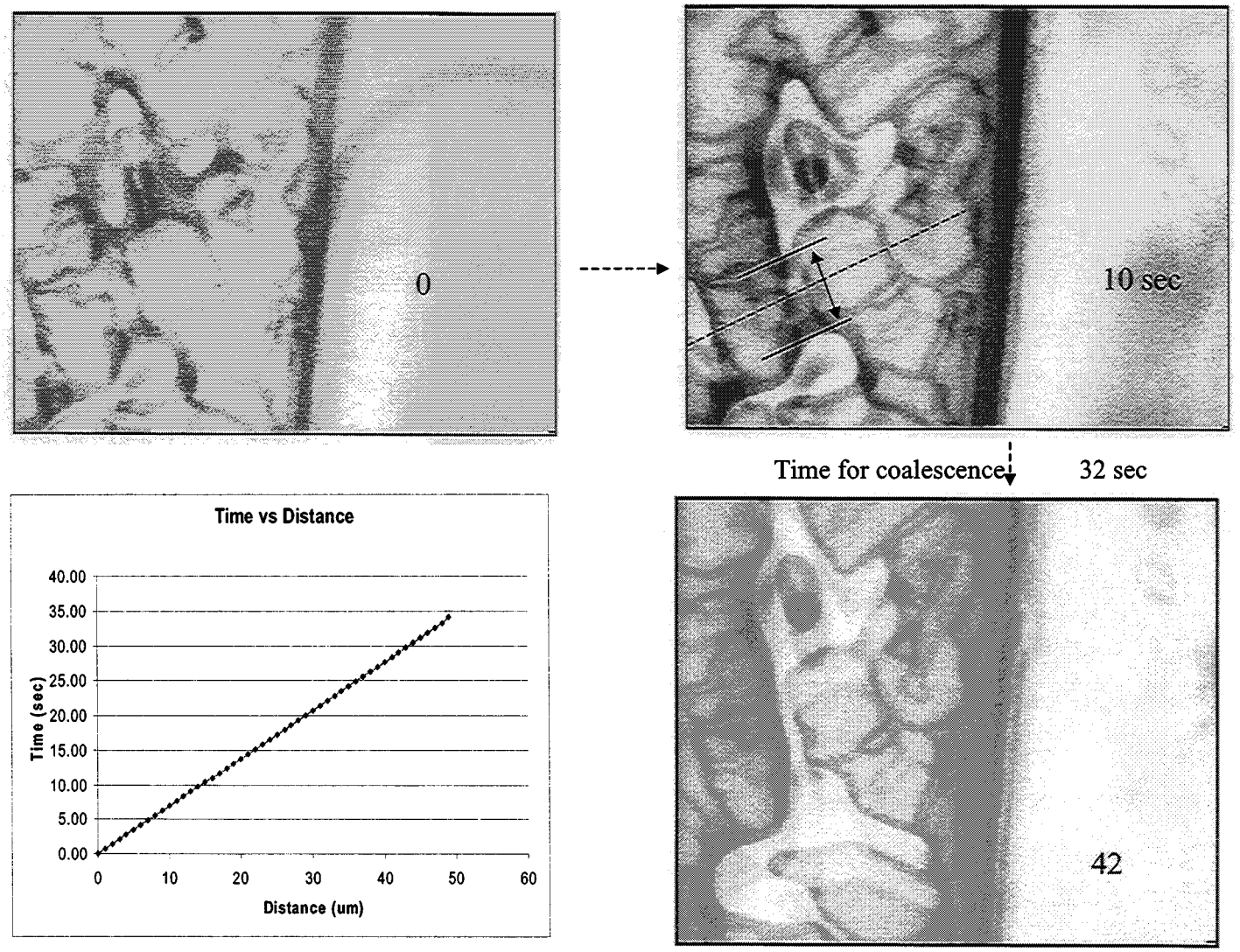
0
10 sec
Time for coalescence
32 sec
Time vs Distance
Time (sec)
40.00
35.00
30.00
25.00
20.00
15.00
10.00
5.00
0.00
0
10
20
30
40
50
60
Distance (um)
42

Figure 5

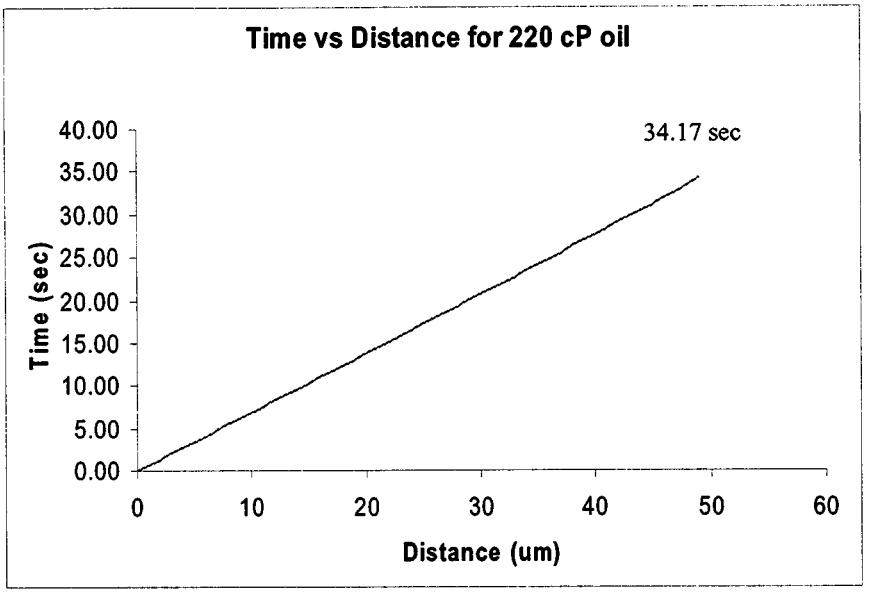

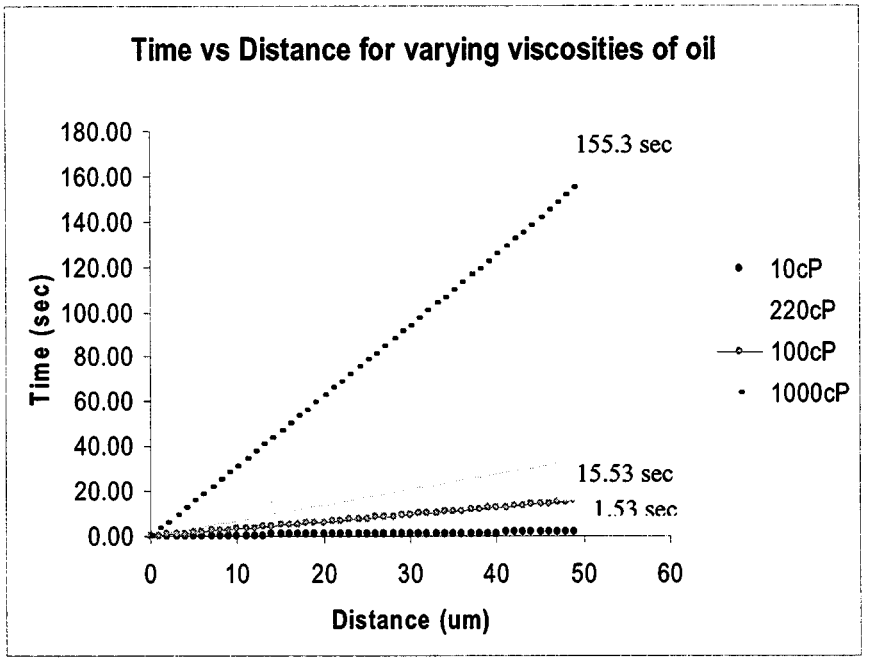

Figure 6

a) Time for coalescence is plotted against the distance traveled by the bubble for 220cP oil.
b) Time for coalescence is plotted against the distance traveled by the bubble for range of oil viscosities.

Relative Permeability in Heavy Oil Reservoirs

Yi Tak Leung

Introduction

Primary production in some heavy-oil reservoirs in Canada and Venezuela has been found to be higher than that estimated by conventional calculations. There have been studies done to determine the reason for this unexpected phenomenon and they will be discussed in the literature review. Conventionally, the main driving force behind primary recovery is pressure depletion through solution gas drive. Solution gas drive is the mechanism, whereby the lowering of reservoir pressure through production in an undersaturated reservoir will reach a point where gas starts to evolve from solution (bubble point pressure). Since gas is quite compressible, it acts as the primary driving force by keeping reservoir pressure high. The evolved gas does not begin to flow until the critical gas saturation has been reached. Once the critical gas saturation point is reached, there is an increase in rate of pressure drop due to the production of the gas-phase. It has been noted that the oil at the wellhead of these heavy-oil reservoirs resembles the form of foam, hence the term "foamy oil." This foamy appearance is due to its high content of bubbles dispersed in the oil, but is not directly the cause for high oil recovery.

There already have been studies performed demonstrating the positive effects of increasing flow rates on recovery. This corresponds to decreases in gas-phase mobility and thus gas relative permeability. A reduction in gas-phase relative permeability is the most likely cause for increased recovery. The motivation, through the process of experimentation, is to better understand the effects of high viscosity and differing depletion rates on relative permeability of the fluids in the system, particularly gas relative permeability.

Estimated recovery of oil and production forecasts are dependent upon knowledge of reservoir parameters. By having more knowledge of this heavy-oil mechanism, better predictions and more informed decisions can be made. Knowledge of optimal flow rates can then be used to obtain the best recovery and total cumulative production before other secondary or tertiary methods are implemented. Relative permeability plays an important role in determining optimal flow rates and should be researched further.

The objective of this work is to characterize fluid relative permeability with respect to flow rate and viscosity. This would further our understanding regarding fluid behavior during the solution gas drive mechanism of a heavy oil system.

Literature Review

Smith (1988) was the first to address this issue of anomalous behavior in heavy-oil reservoirs during primary production. He hypothesized that the oil and gas flowed together, where the gas is in the form of small bubbles interspersed throughout the oil. This simultaneous flow of oil and gas has a lower apparent viscosity as compared to oil alone, thereby increasing productivity. Smith also looked at the theory of sand production creating "wormholes", thereby increasing permeability in the neighborhood of the wellbore. It has been documented that initially, some new primary production wells produce oil at high sand cuts, which decreases as production continues until finally the sand cut stabilizes. This sand production is believed to increase the permeability near the wellbore, contributing to a negative skin. Smith

determined that this still would not account for the drastic increase in total recovery. He also theorized that the asphaltenes in the oil could act as nucleation sites for bubbles to form.

Claridge and Prats (1995) go one step further, basing an entire model on the process of asphaltene adsorption. They performed simulations but did not actually do laboratory experiments to confirm their theory where the asphaltenes coat the gas bubble preventing bubble growth and coalescence. Thus, the bubbles stay small enough to travel with the oil. This continual adsorption of asphaltenes onto the bubble's surface causes the oil viscosity to decrease.

Experiments were later done by Bora *et al.* (1997) using micromodels to test several theories. The main objective of their experiments were to determine the effects of asphaltenes, pressure depletion rates, and sand wettability on the process of solution gas drive. Their use of micromodels, though not as representationally accurate as the use of cores or sandpacks, permits them to examine pore-scale events. One concern about their apparatus design is the structure of their micromodels. They used a very symmetric and structured design probably not representative of the rough grains and tortuosity of the pores and throats encountered at the pore-scale. We should be cautious if we are to extrapolate their findings to processes that happen in the actual reservoir. They found that the asphaltenes tended to increase the supersaturation pressure and decrease the amount of bubble coalescence, but the asphaltenes did not increase the number of nucleation sites. They then found that higher depletion rates tended to keep bubbles dispersed as they flowed to the outlet and the effect of wettability on the depletion process was negligible.

Possibly from the same results as Bora *et al.* (1997), Maini (1999) presents a mechanistic model of foamy solution gas drive with possible explanations for the improved performance and recovery. In his mechanistic model, he compares the foamy flow and conventional solution gas drive. The main difference happens after nucleation and growth of bubbles up to pore size. The bubbles will continue to grow, staying immobile in the conventional solution gas drive process until it forms a continuous gas-phase by coalescing with other nearby bubbles. Once the continuous gas-phase is formed, it will then flow towards the producing end. But in the foamy flow situation, the bubbles will flow with the oil once it reaches a certain size. This bubble size is dictated by the equilibrium of capillary forces and viscous forces. As the bubbles flow, coalescence is offset by the breakup of bubbles keeping them dispersed. This results in a low gas oil ratio and high recovery. He then did experiments with micromodels and sandpacks to support his theories. Maini (1999) also notes the independence of wettability on the solution gas drive process. Since the solution gas drive process seems to be independent of wettability, we can extend and simplify our experiments by using an oil-gas wet system rather than go through the complicated process conducting three-phase (water-oil-gas) experiments. As to be expected, in Maini's sandpack experiments, the increase in flow rate corresponds to a higher pressure gradient, which leads to reduced coalescence, increased bubble dispersion and higher recoveries. Also, an increase in oil viscosity meant that these high recoveries could still be obtained at lower depletion rates, as compared to the lower viscosity oils.

A more representational experiment was done by Urgelli *et al.* (1999) using a sandstone core to investigate gravity and depletion rate effects. They found that recovery was lower when the core is in a horizontal position as compared to when it is in a vertical position. This is further compounded by the fact that there was higher gas saturation found at the top of the core. It was not determined whether this gas-phase was continuous or not. This indicates that there can be a gravity effect. These findings compete with the idea that the bubbles remain entrained in the oil. It should be noted that oil with viscosity 1500 cp was used. In their depletion rate tests, they found that higher depletion rates corresponded to higher oil recovery.

In contrast to the results of Urgelli *et al.* (1999), Pooladi-Darvish and Firoozabadi (1999) did similar experiments using a sandpack with light and heavy-oil and found that gas mobility in heavy-oil was much less than in light oil. Intuitively, this makes sense. The heavy-oil with higher viscosity will of course inhibit gas mobility. Other findings include, a lack of microbubble gas-phase flow with the oil and lack of increased liquid mobility upon nucleation of bubbles. Contrary to Claridge and Prats (1995), the evolution of the gas-phase, did not increase liquid mobility. But Claridge and Prats specifically indicated asphaltenes as the reason for increased liquid mobility. The presence of asphaltenes in the heavy-oil used by Pooladi-Darvish and Firoozabadi (1999) is not known. Pooladi-Darvish and Firoozabadi then did simulations,

varying relative permeability functions to fit experimental results. They found that there was a very large decrease in relative permeability to gas for the heavy-oil case as compared to the light-oil case.

Tang and Firoozabadi (1999) set out to disprove the idea of foamy oil as the reason for increased recovery. Their experiments compared recovery of mineral oil and crude oil. The mineral oil is taken to not have the ability to be in a foamy state. They found that the increased recovery was not due to the results of the oil's ability to be foamy, but rather the effect of low gas mobility. They then formulated a mathematical model to determine the relative permeability of gas and oil, but they cannot compare these relative permeability values to other independent measurements (to ensure that their mathematical model was accurate).

Kumar *et al.* (2000) takes the next step by changing depletion rates and observing its effect on gas mobility in an unconsolidated sandpack. They then match their experimental results using Eclipse-100 Black Oil Simulator to obtain gas relative permeability. They found that gas relative permeability decreases as depletion rate increases.

Apparatus Setup

The equipment will be setup as in Figure 1. The sandpack holder is 16 inches long, 2 inches in diameter, contains 11 pressure ports in the front (2001), and constructed out of aluminum. A circular water jacket surrounds the sandpack holder and allows for experiments to be conducted at a specified temperature. The pressure ports will be connected to a single pressure transducer which is connected to a multiplexing valve and a computer. The position of the pressure ports is such that it does not interfere with the scanning of the sandpack. The outlet end will lead to a viewing cell where a video recorder will be used to record flow of the oil and gas during experiments. The viewing cell will enable us to determine the size of bubbles and frequency of bubble flow. A back-pressure regulator and an accumulator will be connected to the outlet side of the viewing cell. Two ISCO pumps are connected to the accumulator acting as a continuous piston to control depletion rates. The CT scanner is a Picker 1200 SX X-ray scanner and will be used to scan the sandpack lengthwise.

Experimental Procedure

Mineral oil at different viscosity will be used as the oil phase. The sandpack is first saturated with dead oil and then CO_2 saturated mineral oil will be used to displace the dead oil. Once the CO_2 rich oil is injected into the sandpack and left to stabilize, the oil can then be produced at a constant rate. Saturation images of the sandpack will be obtained using the CT scanner at various intervals and pressure measurements from the pressure ports at the different locations of the sandpack will be recorded on computer. Once the sandpack is fully depleted, the sandpack will be cleaned out and new sand will be placed inside and the experiment can be redone using another oil with differing viscosity. Once saturation and pressure results are obtained for these experiments, a formal analysis can be done to determine the role that viscosity and depletion rates of the oil have on relative permeability.

Saturation Analysis

Preliminary experiments done are to determine the solubility of CO_2 in Kaydol, a white mineral oil, at varying pressures. Gas-free Kaydol has a viscosity of 220 cp at $20^{\circ}C$ and density of 0.878 gm/cm^3. We plan on using Kaydol as one of the oils produced from the sandpack. Results were obtained up to pressures of 700 psi, before tubing leading to the accumulator ruptured. The experiment will be done

again, this time using metal tubing rated at 8000 psi burst pressure. The initial results are displayed in Figure 2.

Conclusion and Future Work

Thus far, no one has tried to obtain a concrete analytical definition of how relative permeability is affected by viscosity and depletion rates of oil. The objective of the laboratory experiments will be to use the experimental results and try to formalize an analytical model relating flow rate of heavy-oil at their respective viscosity's with relative permeability curves, in particular the gas relative permeability curve. Hopefully, through these series of experiments, a model can be formed lending to better understanding of viscosity and flow rate, on relative permeability.

Also, very few experiments have been done using a means to visualize in-situ gas development in the context of gas formation in heavy oil

This understanding is important because gas and oil relative permeability have significant effects on the solution gas drive mechanism in heavy-oil reservoirs. We see this from Darcy's Law. By decreasing gas relative permeability, flow rate of gas decreases thereby enabling more gas to stay in the system prolonging the energy in the reservoir, and creating a solution gas drive mechanism that is more effective than expected.

References

1. Akin, S. and Kovscek, A., "Heavy Oil Solution Gas Drive Reservoirs: An Experimental Study," (to be published).

2. Arora, P. and Kovscek, A., "A Mechanistic Modeling and Experimental Study of Solution Gas Drive" (November 2000).

3. Bora, R., Maini, B.B., and Chakma, A., "Flow Visualization Studies of Solution Gas Drive Process in Heavy Oil Reservoirs Using a Glass Micromodel," SPE 37519, Presented at the SPE International Thermal Operations and Heavy Oil Symposium held in Bakersfield, California (February 10-12,1997).

4. Claridge, E.L. and Prats, M., "A Proposed Model and Mechanism For Anomalous Foamy Heavy oil Behavior," SPE 29243, Presented at the International Heavy Oil Symposium held in Calgary, Alberta, Canada (June 19-21, 1995).

5. Kumar, R., Pooladi-Darvish, M., and Okazawa, T., "An Investigation into Enhanced Recovery under Solution Gas Drive in Heavy Oil Reservoirs," SPE 59336, Presented at the SPE Improved Oil Recovery Symposium held in Tulsa, Oklahoma (April 3-5, 2000).

6. Maini, B.B., "Foamy Oil Flow in Primary Production of Heavy Oil under Solution Gas Drive," SPE 56541, Presented at the SPE Annual Technical Conference and Exhibition held in Houston, Texas (October 3-6, 1999).

7. Pooladi-Darvish, M. and Firoozabadi, A., "Solution-gas Drive in Heavy Oil Reservoirs," JCPT, pp. 54-61 (April 1999).

8. Sheng, J.J., Maini, B.B., Hayes, R.E., and Tortike, W.S., "Critical Review of Foamy Oil Flow," Transport in Porous Media, 1999, pp. 157-187.

9. Smith, G.E., "Fluid Flow and Sand Production in Heavy-Oil Reservoirs Under Solution Gas Drive," SPEPE, pp. 169-180 (May 1988).

10. Tang, G-Q. and Firoozabadi, A., "Gas and Liquid-Phase Relative Permeabilities for Cold Production from Heavy Oil Reservoirs," SPE 56540, Presented at the SPE Annual Technical Conference and Exhibition held in Houston, Texas, 3-6 October 1999.

11. Urgelli, D., Durandeau, M., Foucault, H., and Besnier, J-F., "Investigation of Foamy Oil Effect from Laboratory Experiments," SPE 54083, Presented at the SPE International Thermal Operations and Heavy Oil Symposium, held in Bakersfield, California (March 17-19, 1999).

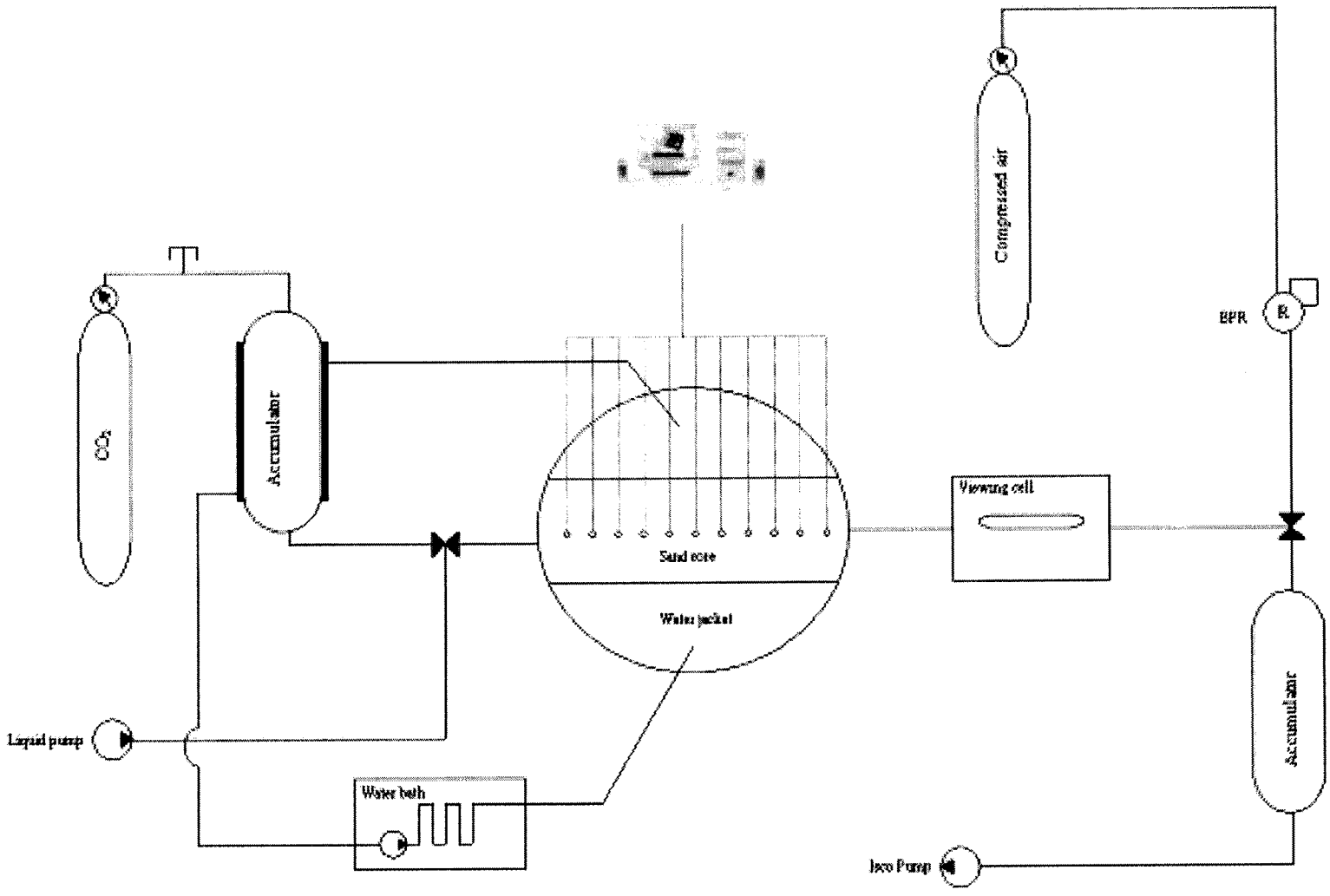

Figure 1 – Apparatus Setup.

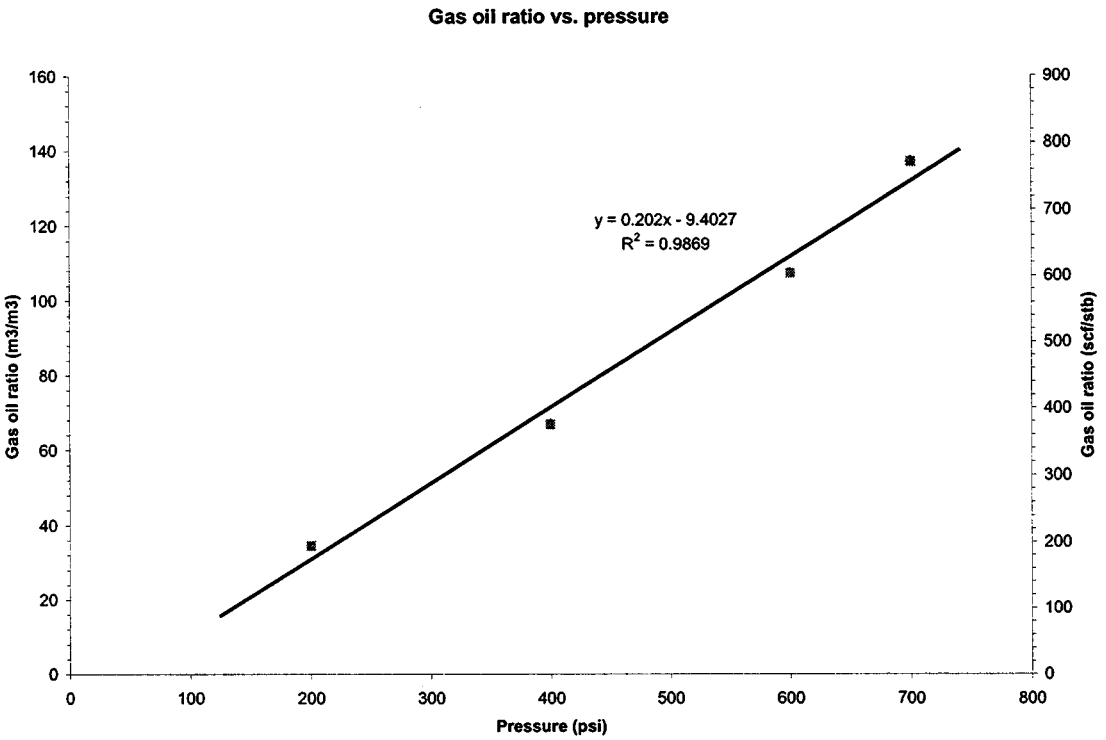

Figure 2 – Saturation test results for Kaydol.

INSITU COMBUSTION

Improving Performance Predictions of Field Projects

Louis Castanier

Introduction

Prediction of the performance of an in situ combustion field project is needed in order to assess its economic and technical potential. As numerical simulation of an in situ combustion field project is extremely difficult, we are proposing an alternative approach based on correlating the results of past in situ combustion projects. This should provide a tool to the engineer to at least roughly screen prospective fields and provide the basis for an estimate of the economic viability of a given prospect. Most of this work will be an extension and update of the work performed by Satman and Brigham (1981). We will endeavor to expand the database and include most of the results obtained since this work was first published.

Numerical Simulation

Numerical simulation of in situ combustion at the field scale is extremely difficult. There are two main reasons for these problems. First, it is difficult to properly include the kinetics of the reactions occurring during a combustion test because of the fact that literally hundreds of reactions occur and need to be described in the numerical model by only a few equations. Even when extensive preliminary laboratory testing is done, the distillation, cracking, pyrolysis, fuel depostion and oxidation are both matrix and oil dependent, and cannot at this stage be properly included in a numerical simulator. Despite much work in this direction, much remains to be done to improve the description of combustion reactions at field conditions.

The description of the temperature field is almost impossible to represent accurately for field cases. The very high temperature zone (combustion front) is usually only a few centimeters wide. When this front passes through large grid blocks, the model will give an average temperature for the grid block based on its total volume. This average temperature will be much lower than the front temperature. As the kinetics and types of reactions are highly temperature dependant, major errors will be introduced.

To our knowledge, in the industry there is no numerical simulator that completely solves those two problems. Simulation of experimental laboratory results is possible if enough grid blocks are used. In the field, grid blocks of a few feet are not realistic; and despite progress in numerical methods, such as variable grids or moving grid techniques, the problem of field simulation of in situ combustion is not solved and will not be solved in the near future.

Brigham-Satman Correlations

In 1980, Brigham and Satman gathered data on about forty different in situ combustion field pilots. Of these, twelve had enough detailed data to be analyzed. They were able to correlate the amount of air injected versus the oil produced with fairly good accuracy for these twelve cases, ending with two correlations; one valid for low viscosity oils, and the other applicable to higher viscosity crudes. These correlations were developed following careful examination of the parameters that could affect the

combustion process during a field project. The objective of this work was to predict the recovery as a function of the volume of air injected. Recovery and volume injected must be related with time, for most economic parameters vary as a function of time. Both of these predictions depend on reservoir parameters but must be handled separately. Recovery versus injection will depend mostly on the volume of oil in place, amount of fuel burnt and combustion efficiency while the volume versus time will depend on Darcy's law terms such as permeability, viscosity and pressure drops. Once injection volumes, production volumes and time correlations are known, economic calculations such as costs and income are fairly easy to make.

Brigham and Satman focused on the oil recovery versus volume of air injected part. Most of the work dealt with dry forward in situ combustion field projects. Figure 1 shows recovery of cumulative incremental oil produced (CIOP) versus cumulative air injected (CAI). The spread between the different fields is broad. If we normalize the data for field size by dividing the CIOP by the original oil in place (OOIP) and the air injected by the oil in place at the start of combustion (OIP) this spread was reduced (Fig.2). Notice that the curves have similar shapes. The abscisa was further modified to take into account the oxygen utilization $(O_2 Ut)$ and the rock volume to be heated expressed as $\mathrm{OIP}(1-\phi)/\phi S_o$. The ordinate is also modified to take into account the oil burnt as fuel (FB) and thus became (CIOP+FB)/OOIP. This result is shown in Fig. 3. Multiple linear regression analysis was performed to relate the ordinate with the oil saturation, S_o, viscosity, μ_o, and reservoir thickness, h. The relations were

$$x = (2.00 S_o - 0.001h - 0.00082\mu_o)\frac{(CAI)(O_2Ut)(\phi S_o)}{(OIP)(1-\phi)}$$

$$y = \left(\frac{CIOP + FB}{OOIP}\right)100$$

Using these parameters, we obtain Figure 4, where the scatter is reduced to 15%. The standard deviation is estimated at 17%. A smooth curve was drawn through those data to obtain the general recovery correlation curve. It is thus a simple procedure to predict combustion recovery as a function of air injected. Providing that S_o, h, μ_o, ϕ, $0_2 Ut$ and fuel content are known. The first four parameters are needed for any recovery process and the last two may be obtained from laboratory burns. The range of applicability of this correlation is for viscosities from 10 to 400cp. Viscosity was investigated as a variable in more detail. This led to a second correlation using $(1/\mu_o)^{0.25}$ as an independent variable. The resulting correlation is:

$$x = [0.427 S_o - 0.00135h + 2.196(1/\mu_o)^{0.25}]\frac{(CAI)(O_2Ut)(\phi S_o)}{(OIP)(1-\phi)}$$

$$y = \left(\frac{CIOP - FB}{OIP}\right)100$$

The standard deviation was only 9% and the scatter 14%, Figure 6 shows the results obtained. To use this correlation the oil viscosity must be above 10 cp , for most applications above this value it appears that the second correlation is the one to use.

Those correlations have been tested and were used by the 1994 National Petroleum Council study on Improved Oil Recovery.

Work In Progress

Considerable field work has been done during the twenty years since these correlations were first developed. Many field project results have become available. In addition, modern computers can help in the multi parameter regression. We propose to compile data on the recent projects and try to improve the correlations. A survey will be completed electronically to try to collect as much data as possible. A possible web page is shown below on the next two pages. As the work progresses, projects will be selected and more data may be needed, and in particular, parameters such as thickness, oil saturation, fuel burnt, and viscosity will be investigated. We will try to take advantage of the experience of the operators by interviewing engineers when possible. The general approach used by Satman and Brigham will be followed. We will , however try to expand the scope of the correlations. It is possible, wet in situ combustion projects will also be considered.

***In-Situ* Combustion Field Survey**

1. Field Miscellaneous

Operator	☐ _____	Geography	☐ _____
Years in commission	☐ _____		

2. Mode of Operation

History	☐ _____	Well Pattern	☐ _____
Injector BHP	☐ _____	Ignition Temperature	☐ _____
Injected Oxidant	☐ _____		

3. Reservoir Information (pls. check all that may be available)

GOR, OOIP and Pres.	☐ _____	Initial oil viscosity, API	☐ _____
Porosity (well-logs)	☐ _____	Permeability (well-tests)	☐ _____
Geological Setting	☐ _____	Seismic (fractures, dimensions, etc.)	☐ _____
Displacement Thickness	☐ _____	Reservoir Depth	☐ _____

4. Fluids: Oil and Gas

Cum. production to date	☐	Prod. rate	☐
Compositional analyses	☐	API and gas gravity	☐
Viscosity	☐	Density	☐

5. Fluids: Water

Water saturation	☐	Water cut/rate	☐

Submit When Ready

References

1. Brigham W.E. and Satman A: . "Recovery Correlation for In-Situ Combustion field Projects," J. Pet. Tech. (Dec 1980) 2132-2138.

2. Sarathi P.: "In-situ Combustion Handbook" DOE technical Report DOE/PC/91008-0374 (January 1999).

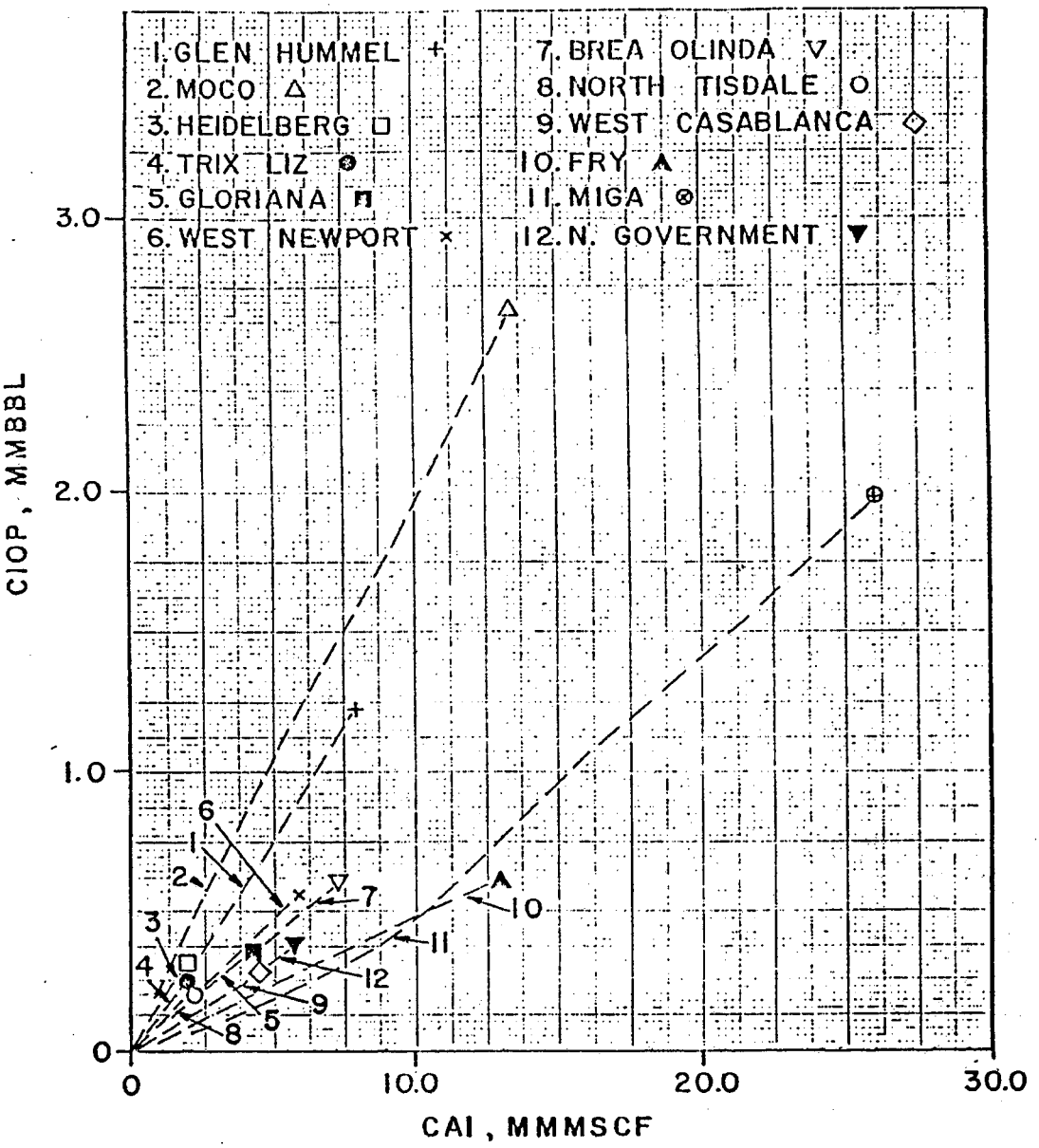

Figure 1. Cumulative incremental oil production vs. cumulative air injection for fieldwide combustion tests.

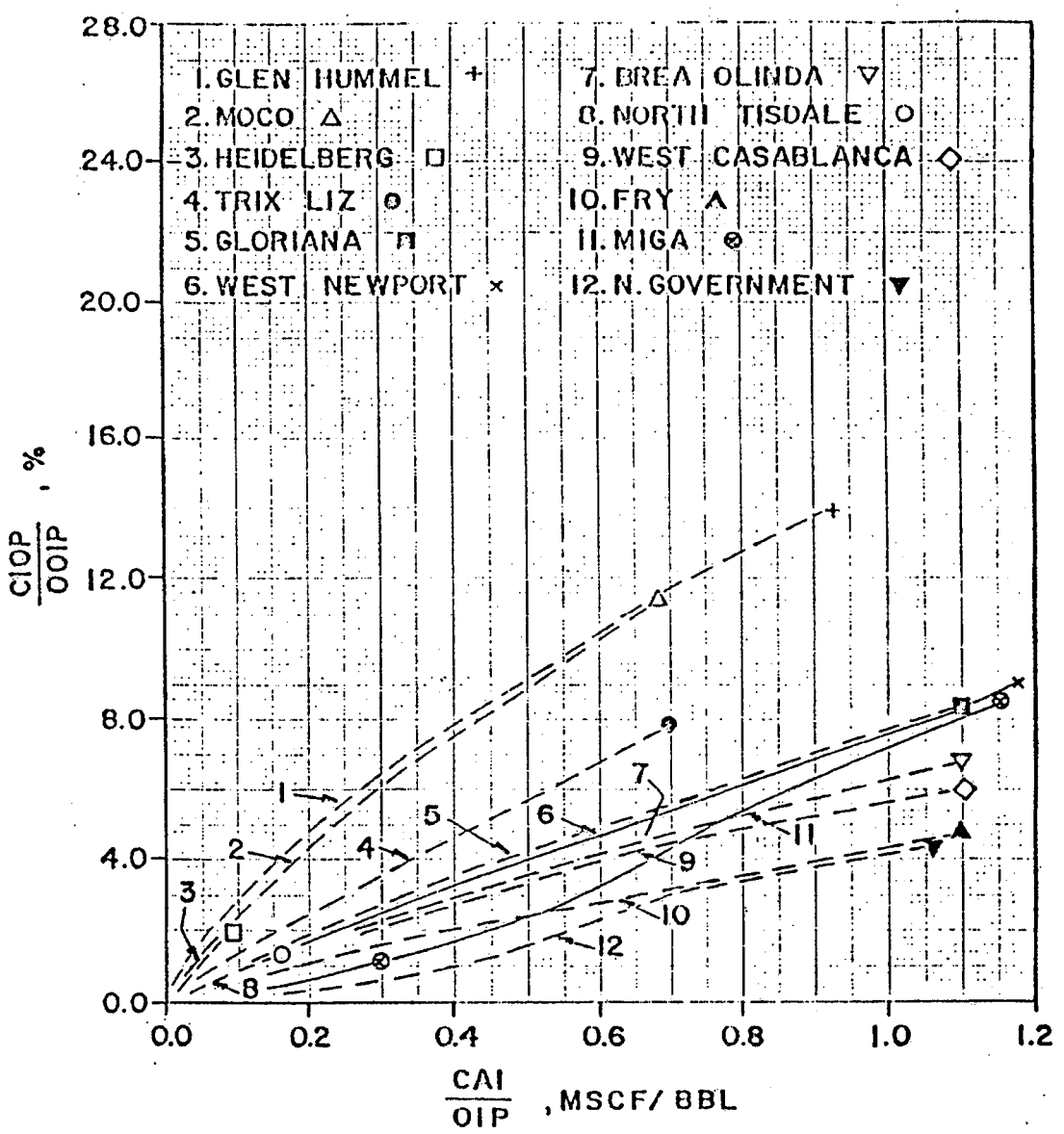

Figure 2. Dimensionless cumulative incremental oil vs. air injection for fieldwide combustion tests.

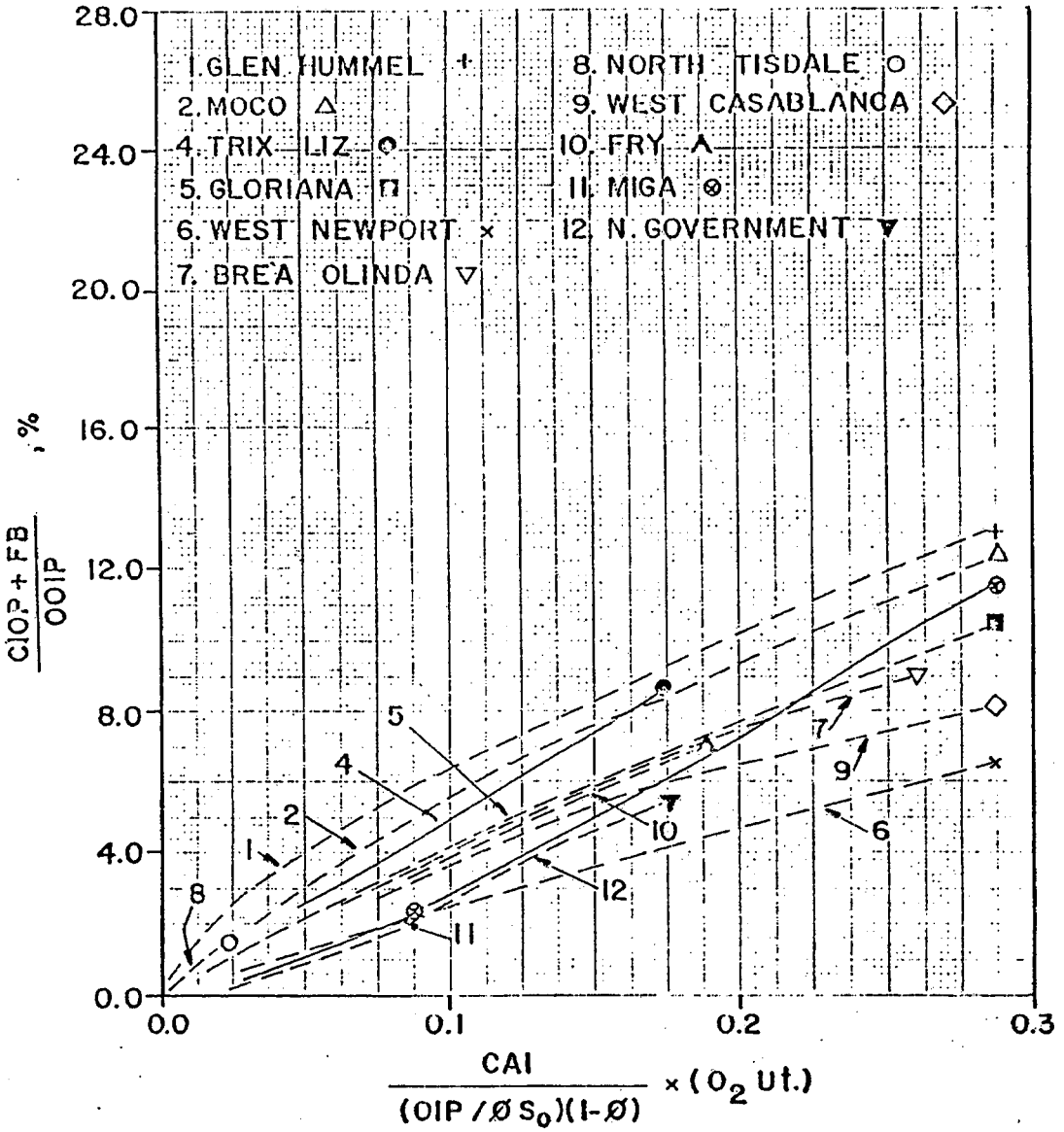

Figure 3. Effects of fuel burned, rock volume, and oxygen utilization on cumulative incremental oil vs. air injection for fieldwide combustion tests.

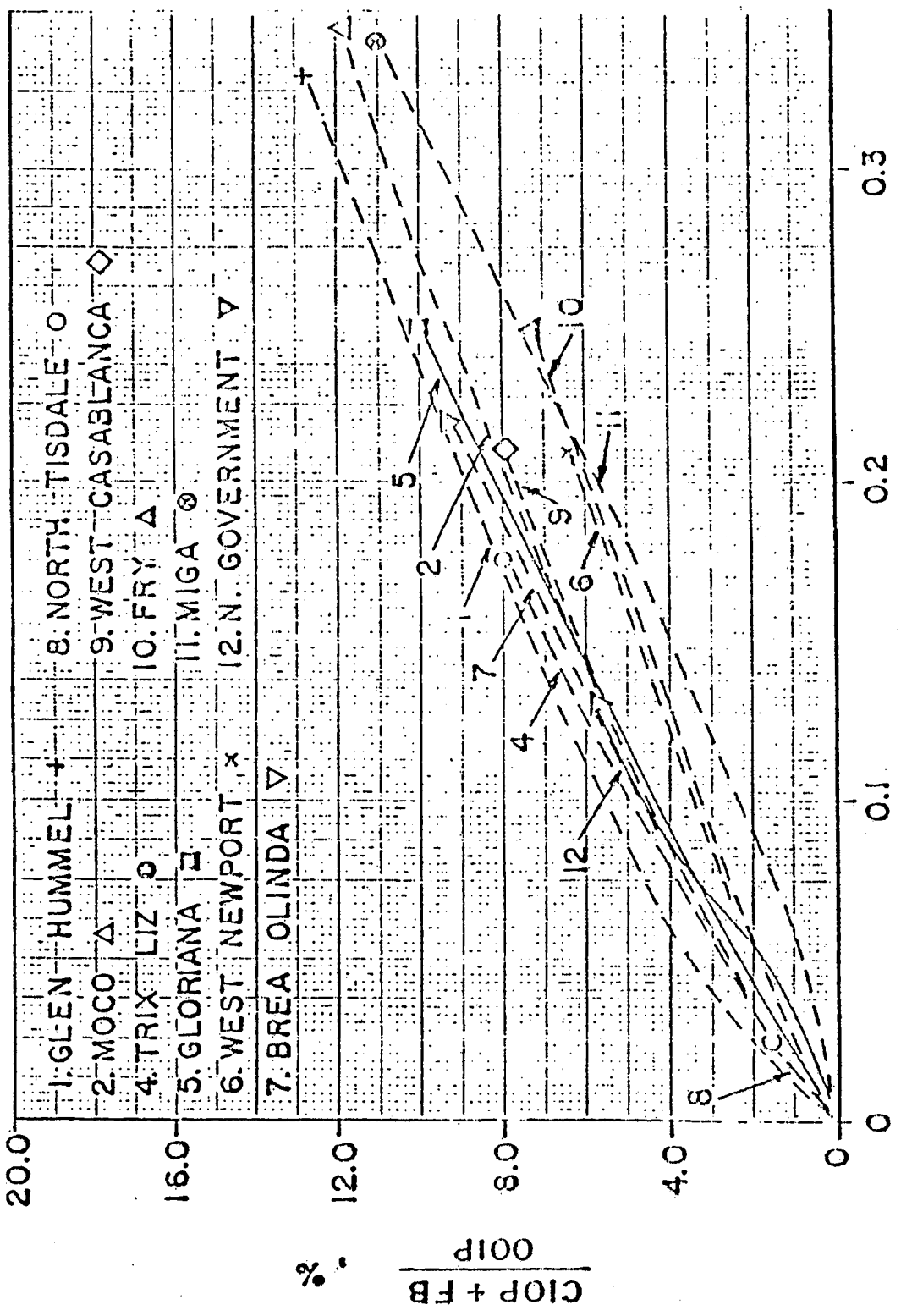

Figure 4. Effect of multiple linear regression analysis on data on Fig. 3.

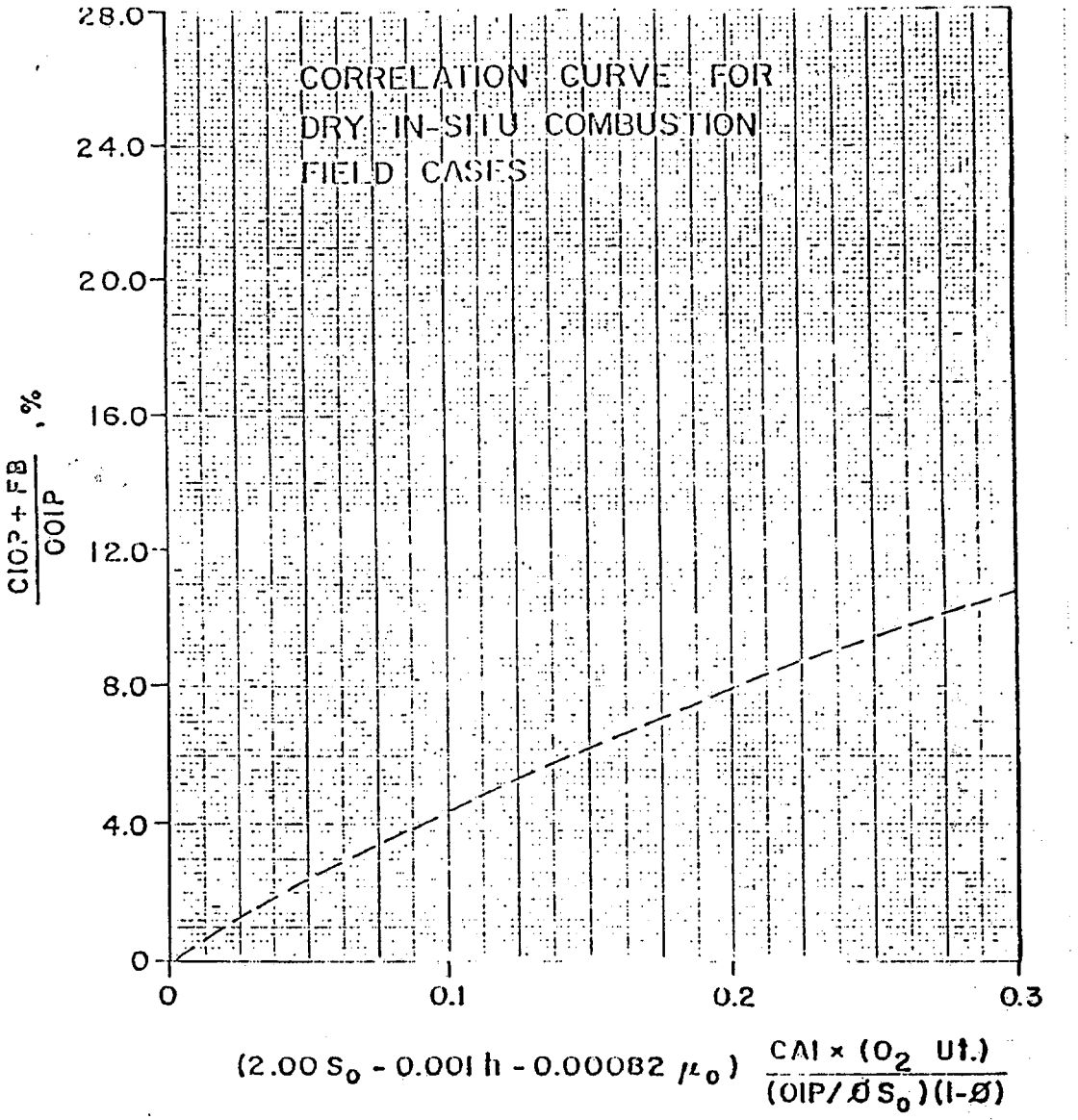

Figure 5. First correlation curve.

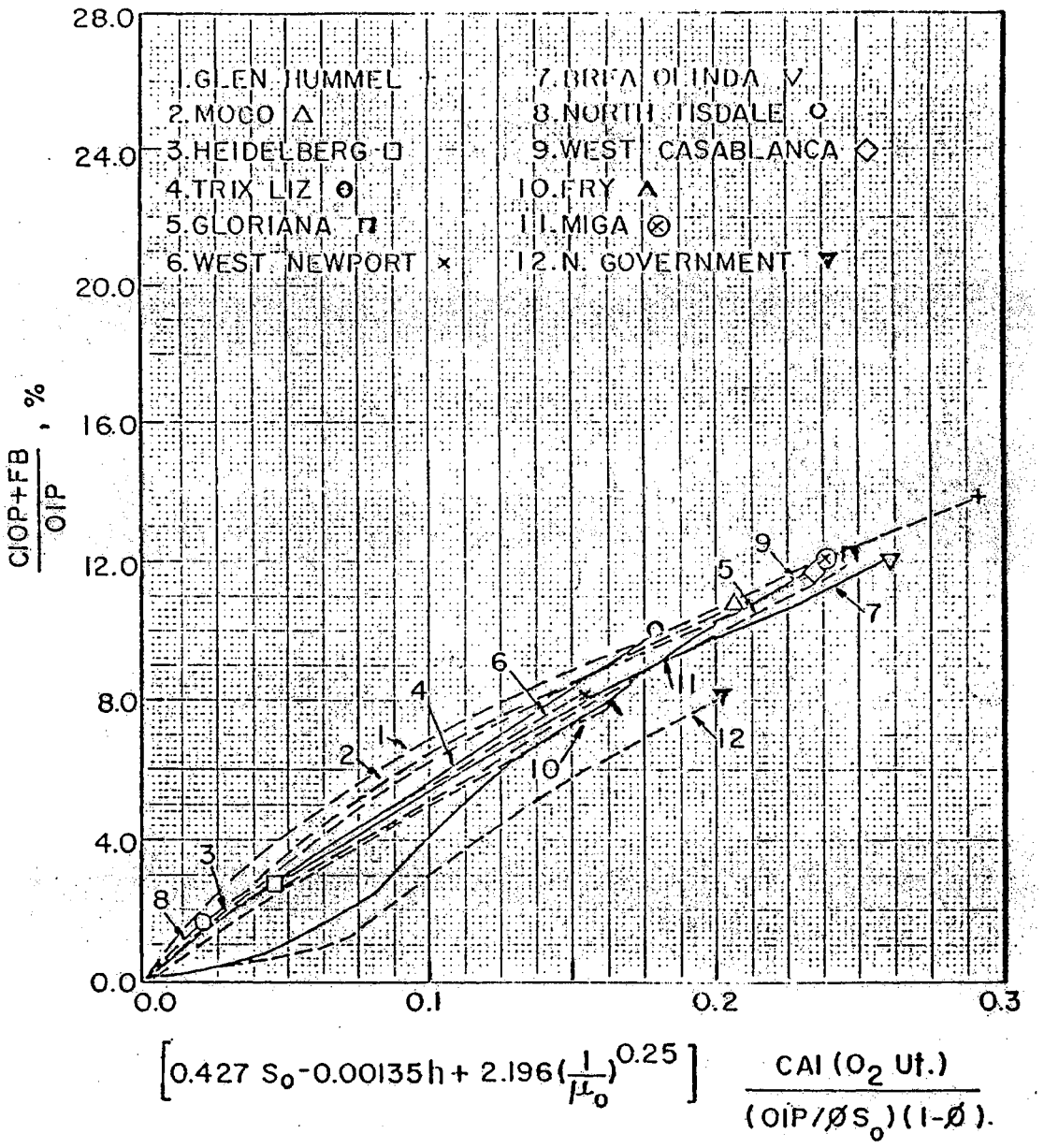

Figure 6. Data for the second correlation.

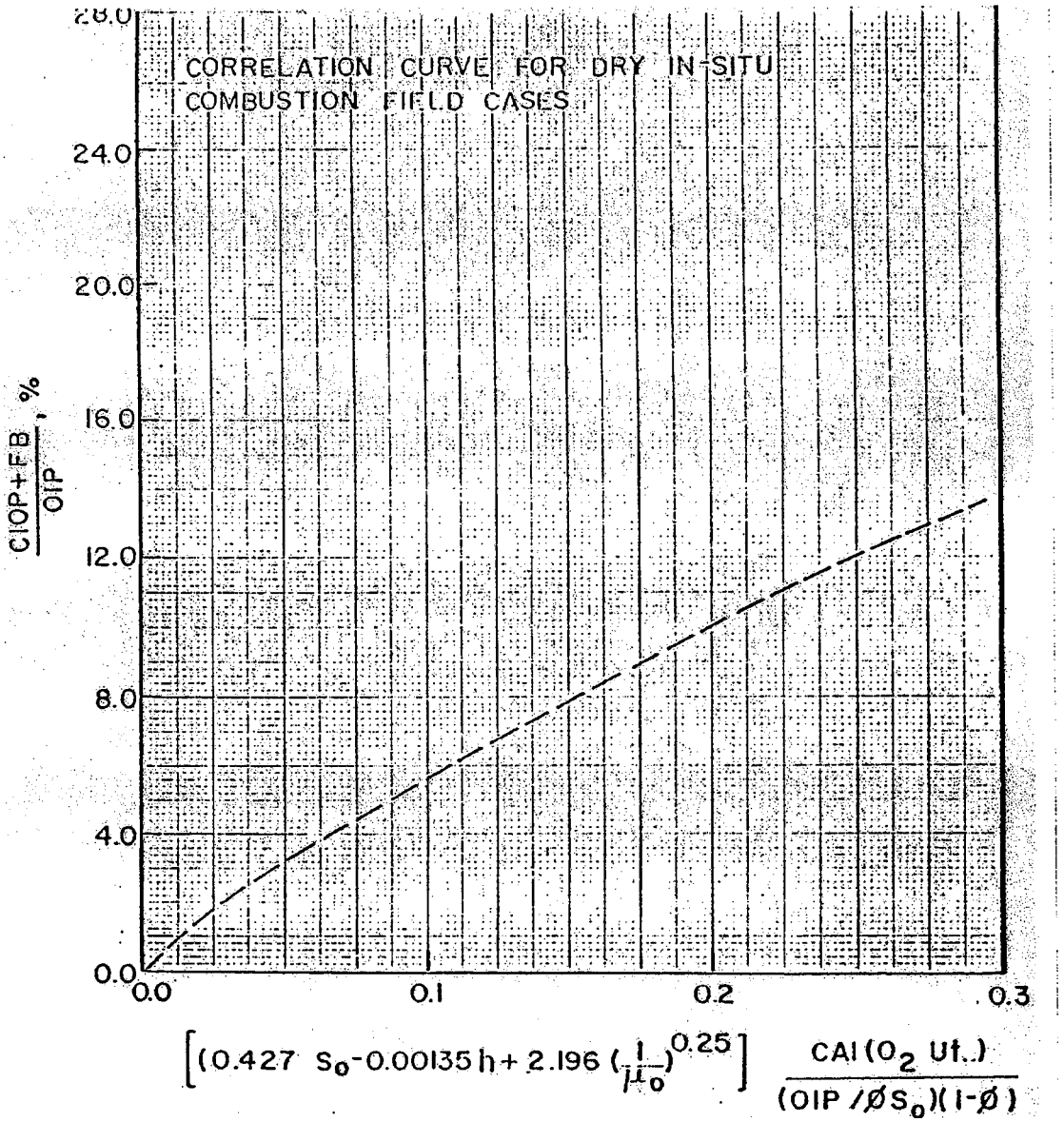

Figure 7. Second correlation curve.

RESERVOIR DEFINITION

Honoring Geological Data In Streamline Approaches For History-Matching

Yuandong Wang

Abstract

A streamline approach is proposed to infer field-scale effective permeability distributions based on dynamic production data including producer water-cut curve, well pressures, and rates. The basic idea is to relate the water-cut curve at a producer to the water breakthrough of individual streamlines. By adjusting the effective permeability along streamlines, the breakthrough time of each streamline is found that reproduces the reference producer fractional-flow curve. Then the permeability modification along each streamline is mapped onto grid-blocks of the simulation grid in a manner that honors observed geological data.

In this work, theories, formulations, and algorithms of the inverse process are developed. Formulations are given to (1) relate the error of production data to streamline TOF and construct the system of equations to solve; (2) simplify the inverse process by decoupling streamlines; (3) compute the sensitivity of streamline time of flight to streamline effective permeability; (4) compute sensitivity of streamline effective permeability to grid-block permeability. A Gauss-Markov random function technique is used to constrain the permeability to honor geological information. Preliminary results demonstrate robustness and computational efficiency. They indicate that a permeability field is inferred that can honor both the production data and geological information.

In summary, our method performs the inverse process sequentially. First, we relate the error of production data to streamline TOF, and then compute the desired modification of streamline permeability to minimize the error. Second, we compute the sensitivity of streamline effective permeability to grid-block permeability, and then compute the desired modification of grid-block permeability. By decoupling streamlines, we eliminate the necessity of solving a system of equations. This speeds up the inverse process while at the same time still allows an accurate match of production data. Some preliminary results indicate that this method is promising. Further effort is needed to complete this study.

1. Introduction

This study proposes a streamline approach for inferring field-scale effective permeability distributions based on dynamic production data including producer water-cut curve, well pressures, and rates. It is shown how the field-scale data can be used to constrain geostatistical models of the permeability field.

The basic idea is to relate the water-cut curve at a producer to the water breakthrough of individual streamlines. By adjusting the effective permeability along streamlines, the breakthrough time of each streamline is found that reproduces the reference producer fractional-flow curve. The permeability modification along each streamline is mapped onto grid-blocks of the conventional simulation grid. In this process, the sensitivity of streamline effective permeability to the change of permeability of each grid-block along the streamline is computed and used to compute the perturbation of the grid-block permeability to achieve the desired permeability of the streamline.

History-matching plays an important role in monitoring the progress of displacement processes and predicting future reservoir performance. Historical production data is routinely collected and it carries much information, although convoluted, that is useful for reservoir characterization and description of reservoir heterogeneity (Vasco and Datta-Gupta, 1997; Grinestaff, 1999). The cost of exhaustive direct measurement

of reservoir properties such as porosity and permeability is prohibitive. Therefore, inferring these properties by history-matching production data and constraining these matches with the available sparse data and geological information is desirable.

History matching has been a popular research topic since the advent of reservoir simulation. Many approaches have been introduced in literature. However, most of them are computationally intensive. Therefore, studies for developing a computationally efficient method are of great importance.

1.1 Previous Work

Most approaches to history-matching field data manipulate permeability at the grid-block level, and hence, demand a great amount of computational work because there are many grid-blocks in a typical simulation. Integration of production data with reservoir description remains an important issue because of the prevalence of production data and the information that it carries about the reservoir. In this brief review, we focus on work that is most similar to our method to follow. Other approaches to history matching are based upon simulated annealing (Gupta *et al.*, 1994), sensitivity coefficients (Wen *et al.*, 1998; Vasco *et al.*, 1998; Chu *et al.*, 1995), and parameter estimation approaches (Landa and Horne, 1997).

Sensitivity coefficient techniques compute the sensitivity of the objective function to the change of permeability of a cell or a set of cells and solve an inverse system that can be very large and somewhat difficult to construct (Chu *et al.*, 1995; Landa and Horne, 1997). Sensitivity coefficient methods might also be computationally expensive if the sensitivity coefficients are evaluated numerically by running multiple simulations. Chu *et al.* (1995) developed a generalized pulse spectrum technique to estimate efficiently the sensitivity of wellbore pressure to grid-block permeability and porosity. Other work employed sensitivity coefficients in the integration of well test information, production history, and time-lapse seismic data (Landa and Horne, 1997).

Vasco *et al* (1998) combined streamlines and a sensitivity coefficient approach while integrating dynamic production data. They employ streamlines to estimate sensitivity coefficients analytically thereby greatly speeding up the procedure. The streamline analysis allows them to "line up" the first arrival of injected fluid at production wells and then match the production history. This technique remains a grid-block-level optimization approach as all of the grid-blocks from the flow simulation are used to describe reservoir heterogeneity.

Sensitivity coefficients have also been employed in a scheme to identify the geometry of geological features such as faults and the dimensions of flow channels (Rahon *et al.*, 1998). In essence, the technique is to minimize an objective function incorporating single and/or two-phase production data. The parameters for minimization are the size and interfacial area of geological bodies rather than grid-block parameters.

Simulated annealing, as applied by Gupta *et al* (1994), perturbs permeability in a set of grid-blocks and evaluates energy objective functions or the degree of misfit between simulated and desired results. This process is stochastic and it is not guaranteed that a perturbation will decrease the energy level. The decision of whether or not to accept the perturbation is based on the change of energy caused by this perturbation. Perturbations that increase the degree of mismatch are accepted with a frequency that decreases with increase in the error. Many iterations are usually required to obtain an acceptable solution. In general, the computational costs of incorporating production data using simulated annealing become very large if a reservoir simulation must be conducted for each iteration.

Reservoir characterization approaches, such as geostatistics, do not explicitly account for field production data. Thus far, it has been a major task to determine the geostatistical realizations that are consistent with injection and production data. Generally, this involves conducting flow simulations for many different geostatistical simulation realizations. Efficient conditioning of permeability fields to both a geostatistical model and production data is discussed by Wu *et al.* (1994). In other work, Wen *et al.*

(1998a; 1998b) also present a geostatistical approach to the inverse problem of integrating well production data. They adapt the sequential self-calibration (SSC) inverse technique to single-phase, multi-well, transient pressure and production rate data. The SSC method is an iterative, geostatistically-based inverse method coupled with an optimization procedure that generates a series of coarse grid two-dimensional permeability realizations. In later work, they combine SSC with analytical computation of sensitivity coefficients using streamline distributions (Wen, 1998). The output realizations correctly reproduce the production data. In both instances, this approach is applied for single-phase flow.

Also in the area of geostatistics, Caers (2001) developed a Gauss-Markov random function technique (GMRF) to automatically constrain geostatistical realizations with some complicated data, such as production trends. Tran *et al.* (1999) developed a method for generating fine-scale three-dimensional reservoir models that are conditioned to multiphase production data by combining a streamline-based inversion technique with a geostatistical downscaling algorithm. Because production data reveals only the large scale trend of reservoir heterogeneity, they scaled up multiple geostatistical fine scale models to a coarse scale used in the inversion process. After inversion, the models are each geostatistically downscaled to multiple fine scale realizations. Those fine scale models are preconditioned to the production data and can be up-scaled to any scale for final flow simulation. In this method, performing up-scaling before inversion greatly reduces the size of the inverse problem and therefore can be computationally efficient, while the down-scaling may retain geological or geostatistical details. Seeking an efficient inversion process is not a topic in their method.

Emanuel *et al.* (1998) introduced a way to use three-dimensional streamlines to assist in history matching. They described the differences among three approaches for history matching in traditional, automated, and assisted modes. In their paper, streamlines are used to identify the flow path connecting injector/producer pairs. The permeability field is modified to match the Dykstra-Parson's coefficient. Then, the grid-blocks to be modified are identified and the multipliers are computed based on the heterogeneity match. This approach fixes the 3D streamlines to the traditional history matching method by simple computer program. It is different from our approach that belongs to automated history matching. However, the limitations and applicable conditions of the approach are very similar to those of our approach.

An interesting question that arises with any match to production data is the accuracy of the match. Lepine *et al.* 1998) combine error analysis with a gradient-based technique to compute the uncertainty in estimates of future performance based upon history-matched models. Their method helps to identify and select the parameters of a given reservoir model that most sensitively affect the match.

1.2 Outstanding Questions

History-matching has remained a research interest for decades. Every year, an increasingly greater number of papers are written on the topic. Streamline simulation has been a growing topic for many years, but the application of streamlines and their specific properties in the inverse process is limited in the literature. Notably, Vasco *et al.* (1998) applied streamlines to compute sensitivities of the mismatch of production data to grid-block properties. The first outstanding question is: "Can we use the specific properties of streamlines, such as time of flight, to develop a new inverse method for history-matching?" This study is an attempt of such a kind. In our method, streamlines and their properties are used in both computing sensitivities and in the inverse process. A second question is: "Can streamline properties be employed to speed up the inverse process?" In streamline simulators such as 3DSL (Batycky *et al.*, 1997; Batycky, 1997), solving the pressure field and updating saturation along streamlines are decoupled and the decoupling greatly speeds up the simulation. In our inverse method, we propose decoupling streamlines to eliminate the necessity of solving a system of equations. Also, sensitivity coefficients can be computed analytically through the use of streamlines. These are two possibilities that greatly speed up the inverse process. Another question is: "Does the approach provide new opportunities for constraining geologic

models with production data?" The combination of GMRF and streamline-based inversion appear to be well suited to this problem.

2. Theory, Algorithm and Formulations

A two-step method is proposed to match dynamic production data and infer reservoir heterogeneity. The first step is to compute corrections for the effective permeability of every streamline based on the difference between simulation results and field data for water cut, pressure drop, and flow rate. By matching the fractional-flow curve through manipulation of the permeability field, we try to capture information regarding reservoir heterogeneity. The second step is to map the streamline permeability modification onto the grid-blocks into a manner consistent with any measured geological information. Then flow simulation is performed to check the match. The above process is iterated until convergence. Below is the more detailed description of this relatively simple procedure.

Steps of the Method

1. Obtain an initial permeability field by guess or geostatistical realization;

2. Run a reservoir simulation on the initial permeability field (first iteration) or on a modified permeability field (after the first iteration).

3. Check whether the simulation results match the field data (reference data) including fractional-flow curve at the producers, flow rate, and pressure. If not, perform the inverse process below to modify the permeability to reduce the mismatch;

4. Iterate steps 2 to 3 until a satisfactory match is achieved.

Fig 1 illustrates the streamline inversion method. Displayed are reference and computed producer water-cut curves. In our approach, each streamline, as shown in Fig. 1b, carries the same amount of flow. When a streamline breaks through, its contribution to the water-cut is known. If we know the TOF order of streamlines, we know the breakthrough sequence. Therefore, we can also locate the portion of the water-cut curve that each streamline breakthrough contributes. As an example, twenty streamlines are launched in Fig. 1. Each streamline breakthrough contributes 0.05 to the water-cut at the producer. The eighth streamline breakthrough causes the water-cut to increase from 0.35 to 0.40. By discretizing in equal increments of water-cut, the error in the breakthrough time is related to the TOF, or effective (average) permeability of streamlines.

Steps for the Inversion Process

1. Compute streamlines. First, the flux at each interface between any two neighboring grid-blocks can be computed based on the pressure and saturation of each grid-block from the simulation result. Then streamline can be computed using the fluxes (Fig. 1 (b)).
2. Calculate the time of flight (TOF) for all streamlines. Sort the streamlines in ascending order of TOF. The TOF indicates the breakthrough time of the streamline;

3. Compute the difference in fractional flow, flow rate, and pressure between the simulation result and the reference. Relate differences in the fractional-flow curve to the corresponding streamline as is shown in Fig. 1.

4. Compute the required change of effective permeability for each streamline;

5. Compute the TOF-weighted sensitivities of streamline effective permeability to the permeability of each grid-block along the streamline. Compute the required modification of grid-blocks to achieve a desired permeability change of each streamline (Fig. 1 (b)).

Geological or geostatistical information can be employed here as constraints when computing the desired change of grid-block permeabilities. In this work, we use GMRF as described by Caers (2001).

The application of our method is quite general because the inputs that it takes are the normal output of a conventional simulator. A number of assumptions or simplifications were made in order to begin. Permeability is assumed to be isotropic and the fluids are incompressible. Gravity and capillary forces are taken as negligible. We assume no changes in well configuration, no infill wells, no conversion of producers to injectors, or vice versa. Also, we assume that other parameters such as porosity, relative permeability, and boundary conditions are known accurately. Once the method has been established to work under these conditions, it will be extended. Our method requires monotonic increasing fractional flow. Therefore, field production data for slug tracer injection must be processed by superposition before performing the inverse process. Likewise, noisy field production data must be filtered and pre-processed to obtain a good match.

The proposed inverse process makes use of streamline properties. In a multi-phase displacement, each streamline breakthrough contributes a small amount to the fractional-flow curve at a producer. The algorithms and formulations of streamline computation are not discussed here because the approach is similar to that of Batycky *et al.* (1997), Batycky (1997) and Pollock (1998).

Throughout, the terms water-cut and fractional flow are used interchangeably. The following pairs are also interchangeable: sensitivity and derivative, effective permeability and average permeability, mismatch and error. When computing streamlines in the inverse process, the equal flow rate property of streamlines is enforced. That is, every streamline breakthrough contributes the same amount to the fractional flow. Therefore, by ordering the streamlines with respect to their breakthrough time, we discretize the fractional-flow curve and relate various segments to the breakthrough of individual streamlines. When the fractional-flow curve of the forward simulation result for a given permeability does not match the field water-cut curve, we infer the streamlines responsible for the difference between the fractional flow curves. Then based on the relation between streamline breakthrough time and effective permeability, a modification of effective permeability along streamlines can be computed to match the production data. The objective function, as defined below, indicates the error of the simulation result compared to the field data:

$$E = \frac{1}{N_p} \sum_{n=1}^{N_p} (w_t E_{t,n} + w_p E_{p,n} + w_q E_{q,n}) \qquad (1)$$

In Equation (1), the subscript n is the index of the producer, N_p is the total number of producers of interest, $E_{t,n}$, $E_{p,n}$, and $E_{q,n}$ are errors in the dimensionless breakthrough time of individual streamlines, pressure, and flow rate at the producer, respectively. The terms w_t, w_p, w_q are weights for dimensionless breakthrough time of individual streamlines, pressure, and flow rate at producer i, respectively. For simplicity, we weight each term identically.

We decouple the computation of streamline permeability modification to match flow rate and/or pressure from that to match fractional flow. Heterogeneity of the reservoir is captured mainly by matching the fractional flow curve. Decoupling of streamlines is desired in order to eliminate the need for solving a large system of equations. This is the most important part of this study and is therefore discussed in detail in the next subsection.

2.1 Formulations for Matching Fractional Flow Curve

In the following development, the index of producer n is omitted because we decouple the producers and the inverse process is performed with respect to each individual producer. The degree of mismatch between reference and history-matched results is computed as

$$E_t = \frac{1}{N_{sl}} \sum_{i=1}^{N_{sl}} \left| E_{t_{BT},i} \right| \tag{2}$$

where N_{sl} is the number of streamlines connected to the producer. The error $E_{t_{BT},i}$ refers to breakthrough time of streamline i as defined below

$$E_{t_{BT},i} = t^C_{D,BT,i} - t^R_{D,BT,i} \tag{3}$$

where $t^C_{D,BT,i}$ and $t^R_{D,BT,i}$ are the computed, C, and reference, R, dimensionless breakthrough times (pore volume injected) for the i^{th} streamline, respectively.

Permeability modification of the i^{th} streamline alters the breakthrough time of not only the i^{th} streamline, but possibly the other streamlines. Therefore, for accuracy, all the streamlines must be considered, at least initially, and a system of equations has to be solved.

The system to solve is

$$\begin{bmatrix} a_{11} & a_{12} & a_{13} & \cdots & a_{1N} \\ a_{21} & a_{22} & a_{23} & \cdots & a_{2N} \\ a_{31} & a_{32} & a_{33} & \cdots & a_{3N} \\ \cdots & & & & \\ a_{N1} & a_{N2} & a_{N3} & \cdots & a_{NN} \end{bmatrix} \begin{bmatrix} \Delta k_1 \\ \Delta k_2 \\ \Delta k_3 \\ \cdots \\ \Delta k_N \end{bmatrix} = - \begin{bmatrix} E_{t,BT,1} \\ E_{t,BT,2} \\ E_{t,BT,3} \\ \cdots \\ E_{t,BT,N} \end{bmatrix} \tag{4}$$

where $E_{t,BT,i}$ is defined in Eq. (3), Δk_j is the modification of effective permeability along streamline j required to get a match, and a_{ij} is the sensitivity of breakthrough time (dimensionless) of the i^{th} streamline to the effective permeability of the j^{th} streamline. These derivatives are defined as

$$a_{ij} = \frac{\partial t_{D,BT,i}}{\partial k_j} \tag{5}$$

where $t_{D,BT,i}$ is the dimensionless breakthrough time of streamline i, and k_j is the effective permeability along streamline j. Because streamlines are non-communicating, the derivatives can be approximated by applying Dykstra and Parsons[27] method for non-communicating layers. The method relates the breakthrough time of different layers to the effective permeability of each layer. For unit mobility ratio and piston-like displacement, the approximation is exact. The generalization of Dykstra and Parsons method to streamlines is discussed elsewhere (Hewett and Yamada, 1997).

The breakthrough time for streamline i is calculated as

$$t_{D,BT,i} = \frac{\sum_{k=1}^{N_{sl}} (\bar{A}\bar{\phi}L)_k \, x_{D,k,i}}{\sum_{k=1}^{N_{sl}} (\bar{A}\bar{\phi}L)_k} \tag{6}$$

where L is the length of a streamline, $x_{D,k,i}$ is the the fraction of pore volume of streamline k swept when streamline i breaks through. Equivalently, $x_{D,k,i}$ is the dimensionless time of flight of the displacing front (Hewett and Yamada, 1997) along streamline k when the i^{th} streamline breaks through. Obviously, $x_{D,i,i} = 1$. For those streamlines that break through earlier than streamline i, $x_{D,k,i}$ can be greater than 1. The symbols $\overline{\phi}_k$ and $\overline{A}_k$ represent the average porosity and average cross-sectional area of streamline k respectively. They are defined as

$$\overline{A} = \int_0^1 A(x_D)dx_D \tag{7a}$$

$$\overline{\phi} = \int_0^1 \phi(x_D)dx_D \tag{7b}$$

Now, define the ratio of pore volume associated with streamline k over the total pore volume of all the streamlines connecting the producer as

$$V_{D,k} = \frac{(\overline{A}\,\overline{\phi}L)_k}{\sum_{i=1}^{N_{sl}} (\overline{A}\,\overline{\phi}L)_i} = \frac{V_{P,k}}{V_{P,T}} \tag{8}$$

where the subscript D denotes dimensionless, $V_{P,k}$ is the pore volume of streamline k, and $V_{P,T}$ is the total pore volume. The ratio $V_{D,k}$ is equivalent to the ratio of streamline TOF over the total TOF as defined below.

$$V_{D,k} = \tau_{D,k} = \frac{\tau_k}{\sum_{i=1}^{N_{sl}} \tau_i} \tag{9}$$

where τ denotes time of flight, subscripts D and k are the same as defined above. Equation (6) can be rewritten as

$$t_{D,BT,i} = \sum_{k=1}^{N_{sl}} V_{D,k} x_{D,k,i} = \sum_{k=1}^{N_{sl}} \tau_{D,k} x_{D,k,i} \tag{10}$$

Then by applying the chain rule, Eq. (5) is evaluated:

$$\frac{\partial t_{D,BT,i}}{\partial k_j} = \sum_{k=1}^{N_{sl}} \frac{\partial t_{D,BT,i}}{\partial x_{D,k,i}} \frac{\partial x_{D,k,i}}{\partial k_j} = \sum_{k=1}^{N_{sl}} \tau_{D,k} \frac{\partial x_{D,k,i}}{\partial k_j} \tag{11}$$

Dykstra and Parsons (1950) method provides $x_{D,k,i}$ in terms of the effective permeability of all the streamlines; hence, the summation above must be computed for all k streamlines. The formula for calculating $x_{D,k,i}$ for unit mobility ratio is slightly different from that for non-unit mobility ratio.

For unit mobility ratio, the pressure field as well as the streamline distribution remains unchanged throughout the displacement process for constant boundary conditions. When breakthrough happens at streamline i, the front position at streamline k is calculated by

$$x_{D,k,i} = c_{ik} \frac{k_k}{k_i} \tag{12}$$

where c_{ik} is a constant related to the length of the streamline i and k. It is computed from streamline geometry. Applying this definition and completing the partial derivative indicated in Eq. (7) yields

$$\frac{\partial t_{D,i}}{\partial k_j} = \sum_{k=1}^{N_{sl}} \tau_{D,k} \frac{\partial x_{D,k,i}}{\partial k_j} = \begin{cases} -\frac{1}{k_i^2} \sum_{k=1,k\neq i}^{N_{sl}} c_{ik} \tau_{D,k} k_k, & \text{if } i = j \\ c_{ij} \tau_{D,j} / k_i, & \text{if } i \neq j \end{cases} \tag{13}$$

This procedure can be repeated for non-unit mobility ratios given the standard Dykstra-Parsons result (Lake, 1989), where $x_{D,k,i}$ is a function of the permeability of streamlines i and k, and the end-point mobility ratio.

For non-unit mobility ratio cases, we approximate streamlines as non-evolving in inverse calculations. This assumption works well if the mobility ratio is unity or unfavorable and heterogeneity is a dominant factor during displacement. Therefore, it is most applicable to unfavorable mobility ratios and heterogeneous permeability fields. Although streamlines evolve during a non-unit mobility ratio displacement, for a heterogeneity dominant reservoir, the streamlines evolve little. An important fact is that the order of breakthrough of streamlines is preserved even though length and volume may change. That is, if a streamline passes through a high permeability channel at the start of the displacement process, that channel will remain a channel throughout the entire process. The streamlines with the smallest pore volume or time of flight always break through earliest, no matter how they evolve.

Simplifying the Inverse System

For unit mobility ratio, the inverse system can be simplified by defining relative or normalized parameters such as

$$\begin{bmatrix} b_{11} & b_{12} & b_{13} & \cdots & b_{1N} \\ b_{21} & b_{22} & b_{23} & \cdots & b_{2N} \\ b_{31} & b_{32} & b_{33} & \cdots & b_{3N} \\ \cdots & & & & \\ b_{N1} & b_{N2} & b_{N3} & \cdots & b_{NN} \end{bmatrix} \begin{bmatrix} \delta k_1 \\ \delta k_2 \\ \delta k_3 \\ \cdots \\ \delta k_N \end{bmatrix} = - \begin{bmatrix} e_{t,BT,1} \\ e_{t,BT,2} \\ e_{t,BT,3} \\ \cdots \\ e_{t,BT,N} \end{bmatrix} \tag{14}$$

where $e_{t,BT,i}$ is normalized error in breakthrough time of streamline i to be defined in Eq. (15), δk_j is the normalized modification of effective permeability along streamline j, and b_{ij} is the derivative of $e_{t_{BT},i}$ with respect to δk_j. For the purpose of discussing updates from one iteration to the next, let $k_j^{\lambda+1}$ be the new value of k_j, and likewise, k_j^{λ} be the previous value. In equation form, the normalized variables are

$$e_{t_{BT},i} = E_{t_{BT},i} / t_{D,BT,i}^R = (t_{D,BT,i}^C - t_{D,BT,i}^R) / t_{D,BT,i}^R \tag{15}$$

$$\delta k_j = \frac{k_j^{\lambda+1} - k_j^{\lambda}}{k_j^{\lambda}} = \frac{\Delta k_j}{k_j^{\lambda}} \tag{16}$$

$$b_{ij} = \frac{\partial e_{t_D,BT,i}}{\partial(\delta k_j)} = \frac{k_j^{\lambda}}{t_{D,BT,i}^R} \frac{\partial t_{D,BT,i}}{\partial k_j^{\lambda+1}} \tag{17}$$

Substitute Eq. (13) into (17),

$$b_{ij}=\begin{cases}\dfrac{k_i}{\sum_{k=1}^{N_{sl}} c_{ik}\tau_{D,k}k_k/k_i}\left(-\dfrac{1}{k_i^2}\sum_{k=1,k\neq i}^{N_{sl}} c_{ik}\tau_{D,k}k_k\right)\approx -1, & if\ i=j \\ \dfrac{k_i}{\sum_{k=1}^{N_{sl}} c_{ik}\tau_{D,k}k_k/k_i}\left(\dfrac{c_{ij}\tau_{D,j}}{k_i}\right)=\dfrac{c_{ij}\tau_{D,j}k_i}{\sum_{k=1}^{N_{sl}} c_{ik}\tau_{D,k}k_k}\approx\dfrac{1}{N_{sl}}, & if\ i\neq j\end{cases} \tag{18}$$

With the normalization above, the elements of the matrix are now functions of only matrix size N_{sl} for a given set of streamlines. Therefore, the inverse of the matrix is also solely a function of N_{sl}. As is shown in Equation (18), when the number of streamlines is large, the off-diagonal terms of the matrix are close to 0. Therefore, a unit matrix is a good approximation of this non-dimensionalized matrix ***[B]***, and therefore inversion of this matrix is also unit. This demonstrates that decoupling of the streamlines is possible. Decoupling of streamlines means that the contribution of a streamline to the error of the production data is mainly related to the average permeability of the streamline. Thus, all of the elements in the inverse of the matrix are calculated directly. This observation is verified by practice as discussed later.

The above simplification works well for unit mobility ratio, as will be demonstrated. For non-unit mobility ratios, it also works to some extent, especially for cases where the mobility ratio is close to unity or heterogeneity is the dominant factor.

In non-unit mobility ratio cases, the elements a_{ij} of matrix ***[A]*** are functions of mobility ratio M. If we repeat the above process, we do not get a matrix as simple as ***[B]*** in Eq. (18). An alternative for non-unit mobility ratio cases is to solve the system of equations in Eq. (4) by inverting the matrix ***[A]***. However, the streamlines evolve during the displacement process. To obtain a good history match with such a procedure, we may need to select several different streamline distributions over the time period of interest. Each of the distributions could be used to match a segment of the fractional flow curve. This is computationally intensive and so we have not implemented this alternative yet. The preliminary results indicate that it is appropriate to apply the simplification made for unit mobility ratio to non-unit mobility ratio cases and treat streamlines as non-evolving during inverse calculations (Wang and Kovscek, 2000).

2.2 Formulation for Matching Flow Rate and Pressure

As each streamline carries the same flow rate, we distribute evenly the error of flow rate of a producer to each streamline (or streamtube). The error in pressure drop of the injector-producer pair is exactly the same as that of each streamline connecting the pair.

We group flow rate and pressure as a single term

$$F = q/\Delta p \tag{19}$$

The contribution of each of the streamlines to the error of F for a producer is computed. The error in F for streamline i, denoted as ΔF_i is related to the average permeability of this streamline by Darcy's law. Therefore, the sensitivity of the ΔF_i to the average permeability can be computed analytically. Once the error of flow rate and pressure drop are known, we can readily compute the modification of average permeability of each streamline to minimize the error.

2.3 Modifying Permeability at the Streamline Level

The permeability modification for a streamline is the weighted geometric average of the two modifications: one for matching the fractional flow curve and the other for matching flow rate and pressure drop. Our preliminary results show that equal weighting is acceptable (Wang and Kovscek, 2000).

In the inverse process, we choose pressure and saturation distributions from the simulation results at the first time-step to compute the streamlines and then their properties such as TOF values. Permeability modification is computed on this streamline distribution. In the inverse process, parameters are non-dimensionalized, therefore, the modification of permeability is performed in a relative manner. That is, we compute a factor for each streamline that is used to multiply the original permeability value.

2.4 Modification of Permeability at Grid-block Level

The modification of streamline effective permeability needs to be mapped onto the grid-blocks because, at the end, what we need is the permeability value of each grid-block. Mapping the permeability modifications onto grid blocks is performed in the following way. First, we compute the TOF-weighted sensitivity of streamline effective permeability to the permeability change of grid-blocks along the streamline. Next, a scheme is developed to compute the modification of grid-block permeability based on the sensitivity and the desired change of streamline effective permeability. The algorithm and formulation for this purpose are discussed in detail below.

2.4.1 Compute the Sensitivity of Streamline Effective permeability to Grid-block Permeability

The effective permeability of a streamline can be expressed as a function of the permeability of all the grid-blocks along the streamline.

$$k_{SL_i} = \frac{\tau_i}{\sum_{j=1}^{n_b} \frac{\tau_{ij}}{k_j}} \tag{20}$$

where subscript i denotes streamline index, subscript j denotes grid-block index, n_b is the total number of grid-blocks, k_{SL_i} is the effective permeability of streamline I, τ_i is the total time of flight of streamline I, k_j is the permeability of grid-block j, and τ_{ij} is the time of flight that streamline i takes to travel through grid-block j. Obviously, if streamline i does not pass through grid-block j, then $\tau_{ij} = 0$.

The formulation for computing the sensitivity of effective permeability of streamline i to the permeability change of grid-block j can be derived from Eq. (20) as follows.

$$s_{ij} = \frac{\partial k_{SL_i}}{\partial k_j} = \frac{\tau_i}{\left(\sum_{j=1}^{n_b} \frac{\tau_{ij}}{k_j}\right)^2} \frac{\tau_{ij}}{k_j^2} = \frac{\tau_{ij} k_{SL_i}^2}{\tau_i k_j^2} \tag{21}$$

2.4.2 Compute the Weighted-Sensitivity

There are cases when more than one streamline passes through a particular grid-block. We should not treat the contribution of all the streamlines equally because that a streamline paths across a grid-block

are not necessarily equal. A streamline may only cut through a corner of a grid-block, while another streamline may traverse the grid-block diagonally. The larger distance a streamline travels through a grid-block, the greater contribution that streamline should have to the change of the grid-block's permeability. This can achieved by using the weighted-sensitivity instead of the sensitivity defined in Eq. (21). The weight can be computed in terms of TOF as follows.

$$w_{ij} = \frac{\tau_{ij}}{\tau_j} \tag{22}$$

where w_{ij} is the weight for sensitivity of permeability of streamline i to permeability of grid-block j. The TOF, τ_{ij}, is the same as in Eq. (20) and τ_j is the summation of the TOF of all the streamlines that travel through grid-block j. Obviously,

$$\tau_j = \sum_{i=1}^{n_{SL}} \tau_{ij} \tag{23}$$

Then the weighted sensitivity is

$$S_{ij} = w_{ij} s_{ij} \tag{24}$$

2.4.3 Algorithms for Modifying Grid-block Permeability

Assume $n_{b,i}$ is the number of grid-blocks that streamline i passes through. For each streamline, we choose a fraction c ($1 \geq c > 0$) of $n_{b,i}$ to modify in order to achieve the desired effective permeability of this streamline.

$$n_{m,i} = c n_{b,i} \tag{25}$$

The scheme for computing the modification of the grid-block permeability is as follows.

Start from the streamline with the smallest TOF and modify one streamline at a time in ascending order of streamline TOF. For each streamline i, first compute the modification of permeability that has already been made for streamlines with smaller TOF. Then, compute the new desired modification of effective permeability of this streamline. Next, choose $n_{m,i}$ grid-blocks with the greatest weighted sensitivity and modify their permeability based on the sensitivity and the desired modification of streamline effective permeability.

2.5 Apply Constraints to Honor Geological Data

Inverse solutions can be constrained in many different ways. At least two approaches, as described below, appear to be consistent with this method.

2.5.1 Post-Processing with the Gauss-Markov Technique

Perform the history-matching procedure as stated above to obtain the distribution of streamline TOF and the effective permeability of each streamline. This inversion result does not necessarily honor the distribution of permeability as expressed by the variogram, even though the production data is matched. We use a procedure that can take any initial reservoir model that matches any non-linear, multiple-point averaging constraint, and "add" the variogram on it using an iterative procedure (Caers, 2001). In this procedure, the effective permeability along each streamline is not changed. The distribution of permeability

values in the domain is made to honor the variogram. By doing so, we assume the streamline geometry does not evolve radically as a result of this post processing.

The procedure relies on what is called a Gauss-Markov random function (GMRF) technique that allows sampling, using a Markov chain Monte Carlo method. Multiple realizations are found that honor a specific variogram and histogram (Caers, 2001). The main difference between GMRF and sequential Gaussian Simulation (SGSIM) is that GMRF is iterative. SGSIM is a non-iterative technique. SGSIM starts with an empty grid and then simulates that grid sequentially node by node along a random path. The procedure finishes when every node is simulated. The problem with SGSIM is that it is difficult to constrain the realizations to complicated data. GMRF has the same goal as SGSIM, i.e., generate realizations with a specific variogram and histogram. The procedure operates grid node by node, changing the value at each node according to a probabilistic criterion. When it iterates long enough, the variogram will be honored, as will the histogram. The key is how to choose the probabilistic criterion, which is based on a new geostatistical idea that seems similar to the simulated annealing technique. The method is faster than simulated annealing, there is no objective function criterion, and we need not set any cooling schedule (Caers, 2001).

The fact that the grid is "full" while iterating, as opposed to SGSIM where the grid is filled gradually, allows us to condition to much richer data. Caers (2001) has extended this technique to include any type of non-linear averaging constraints. So, we can use this technique to post-process the inverse result that honors effective permeabilities along streamlines, but not the variogram, and turn it into a realization that honors the variogram, effective permeabilities, and the production data. To generate multiple geostatistical realizations, we just start over with a different random seed but there is no need for further flow simulation. We can also perform the inverse process with a different initial geostatistical model from which our final inverse result will most likely have different streamline geometry. By doing so, we may quantify the degree of uncertainty.

2.5.2 Sort Geostatistical Realizations

A simple, but probably inefficient, method is to generate a number of permeability fields by sequential Gaussian simulation, based on available geological information, and to check whether the effective permeability distribution from a particular realization matches that from the inversion. The check can be performed in the following way. Solve the pressure field for a single time-step and obtain pressure and saturation distributions for each permeability field from geostatistical simulation. A unit mobility ratio should suffice. Compute the streamline distribution and streamline properties such as time of flight and sort them in the order of breakthrough time or time of flight. Compute the effective permeability of each streamline, compare it with the effective permeability and time of flight from the inversion. In this manner, realizations are sorted. Those realizations within an acceptable value of the error in permeability are expected to generate a good match in production response, and therefore are accepted. It is easy to generate geostatistical realizations and solve the pressure field once to obtain streamline distribution. This approach requires much less computational work than running a full flow simulation on each realization.

2.6 Discussion of Sensitivity Computation and the Inverse Process

2.6.1 Minimize the Permeability Modification

As stated in section 2.2, we assume that the streamline with smallest TOF is responsible for the error of the displacing phase breakthrough at the producer and align the streamlines so that the breakthrough order of streamlines is preserved. This helps to minimize the changes of streamline permeability as well as of the grid-block permeability given the error in production data.

2.6.2 Pros and Cons of Decoupling of Streamlines

As stated previously, streamlines are decoupled to eliminate the need to solve a system of equations. By doing so, the interactions between streamlines are minimized. The interaction is physical. That is, modification of the permeability of one streamline will affect the breakthrough time of other streamlines. A large system of equations must be solved for an exact solution of streamline permeability modification to match the production data. Then, to map the streamline permeability modification to grid-block permeability modification, another system of equations needs to be solved for an exact solution. The first system requires sensitivity coefficients of error of production data to streamline effective permeability, and the size of the inverse system is the number of streamlines. The second system requires the sensitivity coefficients of streamline permeability to grid-block permeability, and the size of the system is proportional to the number of grid-blocks. The second system is a least-squares problem because the number of streamlines is usually smaller than the number of grid-blocks. Therefore, the solution of the second system, and consequently of the whole inverse process, is not unique. Different assumptions or constraints can result in different solutions.

Obviously, if we solve two systems, our method is similar to the conventional sensitivity method except that we compute the sensitivity coefficients analytically using streamlines. In that case, our method is basically the same as Vasco *et al*'s method and does not have great advantage over the conventional sensitivity approach.

Even though we solve the two systems of equations, our solution of grid-block permeability modifications may still not be accurate enough to produce a match to production data. The inaccuracy is due to the approximations and assumptions we made in the development of the method, such as treating streamlines as non-communicating layers and assuming that streamlines do not evolve. The inexactness introduced by these assumptions requires iteration. As discussed in Section 2.2, the permeability change of one streamline has little effect on the breakthrough time of other streamlines. Thus, non-communicating streamlines are a good approximation. The decoupling of streamlines introduces another source of small inaccuracy, thereby requiring iteration. However, the sources of inaccuracy appear to be independent. Therefore, the number of iterations may not necessarily be increased by decoupling the streamlines. The number of iterations required for a match is determined by the number of iterations to reduce each independent source of error to an acceptable level.

Decoupling may introduce a new source of error in the inverse process, but free us from solving the systems of equations. The error introduced by decoupling decreases as the system is iterated to convergence. Iteration is also needed due to the approximations and assumptions made about the inverse process. This approach is similar to using iterative methods to solve system of equations instead of solving the system directly. Decoupling of streamlines is the key to the switch from solving the system of equations directly to performing the iterative inverse process. Preliminary results indicate that our approach can generate good matches to the production history and is computationally efficient (Batycky, 1997). As stated in the previous section, constraints can be applied to honor geological information.

2.6.3 Comparison with Other Sensitivity Approaches--Advantages and Limitations

Our approach to computing sensitivity is similar to that developed by Vasco *et al.*(1998). The derivative of slowness to permeability is equivalent to the sensitivity of TOF to permeability. Both are applied to a streamline. In our approach, we compute the derivative of TOF to streamline effective permeability and then the sensitivity of streamline effective permeability to grid-block permeability. Essentially, it is the chain-rule expansion of the derivative of TOF to the permeability of all the grid-blocks along the streamline. The latter is equivalent to Eq. (7) in Vasco *et al.*(1998). Note that the derivative defined in Vasco *et al.* is in continuous form. The derivative of streamline permeability to grid-block permeability defined in Eq. (21) is the integral of Vasco's derivative with respect to the streamline coordinate (or TOF) over the range of a grid-block.

The way to use the sensitivities in our method is different from that of Vasco *et al.* In their method, derivatives are used as the coefficient matrix of the linear system. A system of equations, though sparse, needs to be solved in the inverse process. The size of the system depends on the number of grid-blocks and can be very large. In one sense, their method is the conventional sensitivity method with analytical computation of the sensitivities. In our method, mismatches of water-cut, pressure-drop and flow rate are linked to corresponding streamlines. By decoupling the streamlines, we can use weighted sensitivities to compute the desired modification of grid-block permeability directly without the necessity of solving a system. In their method, weighting is automatically incorporated when solving the system.

Our method is different from the conventional sensitivity approaches in the way in which sensitivity is computed and the way in which the sensitivity is used in the inverse process. We relate the mismatch to TOF of streamlines, and use streamlines and their properties to compute the sensitivity of the mismatch to the grid-block permeability. In some conventional sensitivity approaches, simulations need to be performed to compute the sensitivity and therefore they are extremely computationally intensive. We compute sensitivities analytically and, by decoupling streamlines, do not need to solve a system of equations. Therefore, our method is computationally efficient.

3. Preliminary Results

3DSL by Batycky *et a.* (1997) is used for forward simulation. Several cases have been tested with this approach. Some case studies have been presented in the 2000 SUPRI-A Annual Report and in our SPEJ paper (Wang and Kovscek, 2000). In this initial work, streamlines were constructed by reading coordinates of streamline points from streamline simulator output. Then, the pore volume associated with each streamline was computed from the coordinates of the points along the streamline. Reading streamline from the output of a streamline simulator makes our method rely on streamline simulators with streamline coordinate output. To improve generality, the scheme allows streamlines to be computed from grid-block pressure and saturation. Any finite difference or streamline simulator can be used for forward computation. The initial method for modifying grid-block permeability required that the permeability of all grid-blocks along the same streamline be modified by the same factor. This is unnecessarily restrictive. Lack of flexibility in modifying different grid-blocks along the same streamline by different factors makes it difficult to retrieve off-trend features and to apply geological constraints. It may reduce resolution of many permeability features. Without incorporating geological constraints, it is not wise to use the inferred permeability field to predict reservoir performance when infill wells are added or patterns are realigned.

Presented below are two cases incorporating geological constraints into the inversion process. In these two cases, streamlines are computed from pressure and saturation fields that are the usual output of conventional simulators. Additionally, sensitivity of streamline permeability to the grid-block permeability is computed and used to map the streamline permeability modification to grid-block permeability modification. We used the Gauss-Markov random function technique (Caers, 2001) to post-process the inverted permeability field. Thus, known geology is honored.

The procedure of the case studies is as follows. First, a reference permeability field is obtained, and then 3DSL run with constant injection rate to obtain the reference production data. Water cut and pressure drop are the data from the reference case that we try to match. An initial permeability field is guessed to start the procedure. The permeability field is either uniform or generated by a geostatistical sequential Gaussian simulation method (Deutsch and Journel, 1998) where the field is conditioned to sparsely distributed data. For simplicity, all the cases deal with a quarter of a five-spot pattern. Our formulation is not restricted to this pattern, nor is the method restricted to two-dimensional areal cases. For all of the cases, the injector is located at the lower-left corner, and the producer at the upper right corner of the pattern. The pressure at the producer is constant and the injection rate fixed. In both cases, we use a 50 by 50 grid.

3.1 Case 1

The mobility ratio is unity, the water injection rate is constant, and the initial guess for the permeability field is uniform. The relative permeability functions used for this case are described by the following expressions:

$$k_{rw} = S_w, \qquad k_{ro} = S_o \tag{26}$$

Viscosity is 1 *cp* for both phases. Thus, we obtain piston-like displacement along streamlines. The total simulation time is 500 days, or $t_D = 1.5$, i.e., 1.5 pore volume is injected.

The reference permeability field is generated using SGSIM with the parameter data shown in Appendix A. It contains a high permeability channel connecting the injector and producer as shown in Fig. 2(a). In Fig. 2, light gray indicates low permeability and dark gray high permeability. Starting from a uniform permeability field of 500 md, four iterations are required to match water-cut and pressure data. Each iteration includes running the flow simulation, computing errors, modifying the permeability of the streamlines, and mapping the modification onto the grid-blocks. The inferred unconstrained permeability field is shown in Fig. 2 (b). Gauss-Markov simulation is then run on the inferred permeability field to restore geology (histogram and variogram), while at the same time maintaining the effective permeability of the streamlines. We generated five such realizations of permeability fields using different initial seeds. The permeability distributions of these five realizations are shown in Fig. 2 (c)~(g). While visual inspection does reveal difference among the reference and post-processed permeability fields, Figs. 2(c)-2(g) do satisfy the variogram and histogram.

A key question is whether the match to water cut is maintained after the GMRF processing. Figure 3 shows the evaluation of the water-cut for the reference field and for all realizations. The match of water-cut curve between the reference permeability field and that of the permeability field inferred is satisfactory. The water-cut of the GMRF processed permeability fields is off from that of the reference and the inferred permeability fields by a small amount. The match is still good compared with that of the initial permeability field.

3.2 Case 2

The configuration of Case 2 is similar to that in Case 1. The total simulation time is 1000 days, or $t_D = 3$. We use the same reference permeability field as that in Case1. However, instead of starting from a uniform permeability field, we use an SGSIM realization conditioned to the same set of data as the reference permeability field. The reference permeability field and the initial permeability field are shown in Fig. 4(a) and 4(b), respectively. Though conditioned to the same set of data and geological information (variogram), the two permeability fields produce quite large difference in water-cut curve, as is shown in Fig. 5. Five iterations of the inverse process were performed to obtain the match with the production data. The inferred unconstrained permeability field is shown in Fig. 4(c) and the match of water-cut curve is shown in Fig. 5. The match is almost exact.

The Gauss-Markov technique is employed to impose geological constraints on the inferred permeability field and still honor the streamline permeability. Five such realizations of the permeability field were generated from different random seeds as shown in Fig. (d)~(h). We observe connected high permeability regions in the reference, the inferred, and the post-processed permeability fields, but not in the initial permeability field.

The water-cut curves of the five permeability fields are also shown in Fig. 5 for comparison. The match of the constrained permeability fields to the water-cut is not as good as that inferred by the inverse process, but the match is still acceptable. There are two possible reasons for the loss of match. One reason

is that streamline geometry may change during the post-processing procedure. The second reason is that some error in streamline effective permeability is allowed in the post-processing procedure as relaxation to avoid over-constraining the system.

Figure 6 shows the water-cut curves for 50 SGSIM realizations of permeability fields that are not constrained to the streamline effective permeability. The large spread of the curves is indicative of the large degree of uncertainty in the simulations. The water-cut curve of the reference, initial and inferred permeability fields are also plotted on Fig. 6 for a comparison. If we do not perform the history-matching process, there is small probability for a randomly chosen permeability field generated by SGSIM to match the production data.

Figure 7 shows the normalized error of fractional flow and pressure/flow-rate for initial, inferred and the five post-processed permeability fields. For water-cut, the error reduces from 17% with the initial permeability field to 0.7% with the inferred permeability field. This error goes up a small amount (2~4%) for the post-processed permeability fields, but the error is still much smaller than initially. For pressure/flow-rate, error drops from the initial 9% to 0.3% for the inferred permeability field. This error is 3% to 7% for the five post-processed permeability fields. The degree of mismatch is due to the above stated reasons.

Figure 8 shows the streamline distributions over the reference, initial, inferred permeability fields and one of the five permeability fields generated by Gauss-Markov technique. Dense streamlines indicate a high permeability channel. These channels are observed on the reference, inferred, and the post-processed permeability fields, but this channel is not obvious in the initial permeability field. This indicates that we have retrieved important flow information from production data.

Figure 9 (a)~(h) shows the histogram of streamline time of flight for the reference, the initial, the inferred, and the five post-processed permeability fields, respectively. We observe, as is expected, that a match of histogram of streamline TOF will result in a match of water-cut. In this figure, the inferred permeability field has the streamline TOF distribution that is closest to that of the reference permeability field. The streamline TOF distribution of the initial permeability is the one farthest from that of the reference permeability field. The smallest dimensionless time of flight for all the permeability fields is 0.5~0.6, except for the initial permeability field that has the smallest dimensionless time of flight of 0.7~0.9. That explains why the breakthrough time for the initial permeability field is much later than that for the other permeability fields shown.

Figures 10 and 11 show the histograms and variograms of the reference, initial, inferred, and five post-processed permeability fields. The histogram shows that all permeability fields except the inferred permeability field have a bi-normal distribution of permeability. The permeability field inferred by history-matching does not have such bi-normal feature. Instead, it fills out the valley between the two normal distribution peaks. That means that the unconstrained history-matching process has a tendency to smooth the distribution. After the post-processing, the bi-normal feature of the reference permeability field was restored, as is expected.

Based on these observations, the method is robust and converges very fast. The error reduces over each iteration. The computational time is spent mainly in running the forward flow simulation. For our 50 by 50 grid-block case, a forward flow simulation using 3DSL consumes about 10 seconds of CPU time of formery(600 MHz deck machine), whereas the inverse process consumes about 0.4 seconds. The inverse process is fast because no inversion of matrix equations is needed. Geostatistical post-processing takes another 10 to 15 seconds.

4. Future Work

It is necessary to extend the method to cases with multiple injectors and producers to make it general. Attempts have been made on this aspect and it seems to be straightforward. More effort is required to complete this task.

We used post-processing with the Gauss-Markov Technique to constrain our inversion result to honor geological information. To date, we have implemented geological constraints in just one pass. The post-processed permeability fields still yield some error, though much smaller than that of the initial permeability field, in the production data. We plan to construct a iterative scheme. An iteration includes the inverse process and geostatistical processing. After a few iterations, hopefully, the resulting permeability fields will honor geology and production data rigorously.

It is also desirable that some assumptions and simplifications be relaxed. For instance, we may extend our method to three dimensional cases where gravity might be an important factor, or incompressibility assumption can be removed so that this approach can be employed for well testing case where pressure change rather than water-cut is important information for inversion.

5. Summary

This approach relates producer water-cut curves to the breakthrough time of individual streamlines. The effective permeability along streamlines is modified directly to history-match the fractional flow curve, pressure drop, and flow rate information. No matrix inversion is involved in the inverse process, and therefore, it is quite fast. The forward flow simulation with 3DSL is also fast and so, for the examples examined, the entire process is computationally efficient. Our method belongs to category of sensitivity approaches, but it is drastically different from the conventional sensitivity approaches. We avoid solving the system of equations directly. Instead, we take an iterative approach by decoupling streamlines.

Constraints to honor geological information have been implemented. The example applications show that this approach is robust within the stated limitations and converges quickly. Each iteration significantly reduces the errors in fractional flow, pressure drop, and flow rate. In all of the examples, an acceptable match to the production data is obtained within a small number of iterations. Importantly, it appears to be expandable to integrate geostatistical data or to honor geological data.

The current work examined 2-D areal porous media, where the effect of gravity is not important, as well as incompressible two-phase flow. As with most history-matching approaches, high-quality, relatively noise-free data is needed for fast and accurate inversion. This approach works well for reservoirs where heterogeneity is a dominant factor. It also works well for unfavorable mobility ratios because the effects of heterogeneity are exacerbated by the unstable displacement. Although streamlines evolve for non-unit mobility ratio cases during the displacement process, we find it feasible to choose one streamline distribution and apply the simplified inverse system during the inversion. Further work and case studies are needed to extend the method to more general cases including multiple wells.

Nomenclature

A	cross-sectional area of a streamtube, L^2
c	constant
E	absolute error
e	relative error
f_w	fractional flow of water
k	permeability, L^2
k_{rw}	relative permeability of water
k_{ro}	relative permeability of oil
l	streamline length
M	mobility ratio
p	pressure, $M/(Lt^2)$
q	flow rate, L^3/t
t_D	dimensionless time
V	pore volume, L^3
V_P	pore volume
V_D	ratio of pore volume
x_D	dimensionless length
ϕ	porosity
τ	time of flight, t
τ_D	dimensionless time of flight

Subscripts:

n	producer index
i, j, k	streamline index
sl or SL	streamline
BT	breakthrough
D	dimensionless

Superscripts:

C	computed
R	reference
λ	iteration index

References

1. Batycky, R. P, "A Three Dimensional Two-phase Field Scale Streamline Simulator", Doctorial Dissertation, Stanford University, January 1997.

2. Batycky, R. P., Blunt, M. J., and Thiele, M. R.: "A 3D Field-Scale Streamline-Based Reservoir Simulator," *SPERE* (November 1997) 246-254.

3. Blunt, M.J., Liu, K., and Thiele, M.R.:"A Generalized Streamline Method to Predict Reservoir Flow," *Petroleum Geoscience* 2, (1996) 259-269.

4. Brigham, W.E. and Abbaszadeh-Dehghani, M., "Tracer Testing for Reservoir Description, JPT (May 1987) 519-527.

5. Caers, J., "Automatic Histogram and Variogram Reproduction in Simulated Annealing Simulation", Mathematical Geology, 33(2) (2001), 167-190

6. Chu, L., Reynolds, A. C. and Oliver, D. S.: "Computation of Sensitivity Coefficients for Conditioning the Permeability Field to Well-Test Pressure Data," *In Situ* , 19(2), (1995) 179-223.

7. Deutsch, C. V. and Journel, A. G., *GSLIB, Geostatistical Software Library and User's Guide*, Second Edition, Oxford University Press, New York (1998).

8. Dykstra, H. and Parsons, R.L., "The Prediction of Oil Recovery by Waterflood," Secondary Recovery of Oil in the United States, Principles and Practice, 2d ed., American Petroleum Institute (1950), 160-174.

9. Emanuel, A. S. and Milliken, W. J., "History Matching Finite Difference Models with 3D Streamlines", SPE 49000, proceedings of the SPE Annual Technical Conference, New Orleans (September 1998), 1-16.

10. Fay, C. H. and Prats, M.. "The Application of Numerical Methods to Cycling and Flooding Problems" Proceedings of the 3rd World Petroleum Congress (1951).

11. Grinestaff, G.H.: "Waterflood Pattern Allocations: Quantifying the Injector to Producer Relationship with Streamline Simulation," SPE 54616, paper presented at the 1999 Western Regional Meeting, Anchorage (May 26-28, 1999).

12. Gupta, A. D., Vasco, D. W. and Long J.C.S.: "Detailed Characterization of Fractured Limestone Formation Using Stochastic Inverse Approaches," *SPE Ninth Symposium* (1994).

13. Hewett, T.A. and Behrens, R.A.: "Scaling Laws in reservoir Simulation and Their Use in a Hybrid Finite Difference/Streamtube Approach to Simulation the Effects of Permeability Heterogeneity," in Reservoir Characterization, II, L. Lake and H.B.J. Carroll (eds.), Academic Press Inc., London (1991) 402-441.

14. Hewett, T. A., and Yamada, T.: "Theory of the Semi-Analytical Calculation of Oil Recovery and Effective Permeabilities Using Streamlines," *Advances in Water Resources* **20** (5-6), (1997) 279-295.

15. Higgins, R.V., Boley, D.W. and Leighton, A.J.: "Aids to Forecasting the Performance of Water Floods," *JPT* (September 1964) 1076-1082.

16. Higgins, R.V. and Leighton, A.J.: "A Computer Method to Calculate Two-Phase Flow in Any Irregularly Bounded Porous Medium," *JPT* (June 1962) 679-683.

17. King, M.J., and Datta-Gupta, A.: "Streamline Simulation: A Current Perspective," *In Situ*, **22**(1), (1998) 91-140.

18. Lake. L. W., *Enhanced Oil Recovery*, Prentice Hall, Englewood Cliffs, NJ (1989).

19. Landa, J. L. and Horne, R. N.: "A Procedure to Integrate Well Test Data, Reservoir Performance History and 4-D Seismic Information," SPE 38653, paper presented at 1997 Annual Technical Conference and Exhibition in San Antonio, (October 5-8, 1997).

20. Lepine, O. J., Bissell, R. C., Aanonsen, S. I., Pallister, I. and W Barker, J.: "Uncertainty Analysis in Predictive Reservoir Simulation Using Gradient Information," SPE 48997, proceedings of the SPE Annual Meeting, New Orleans (September 1998).

21. Martin, J.C. and Wegner, R.E.: "Numerical Solution of Multiphase, Two-Dimensional Incompressible Flow Using Streamtube Relationships," *SPEJ* (October 1979) 313-323.

22. Peddibhotla, S., Datta-Gupta, A., and Xue, G.: "Multiphase Streamline Modeling in Three Dimensions: Further Generalizations and a Field Application," SPE 38003, paper presented at 1997 Reservoir Simulation Symposium in Dallas, (June 8-11, 1997).

23. Pollock, D. W., "Semi-analytical Computation of Path Lines for Finite-difference Models", *Ground Water*, 26 (6), (1998), 743-750.

24. Portella, R. C. M. and Hewett, T. A.: "Fast 3-D Reservoir Simulation and Applications Using Streamlines," SPE 39061, paper presented at the Fifth Latin American and Caribbean Petroleum Engineering Conference and Exhibition in Rio de Janeiro (August 30 - September 3, 1997).

25. Rahon, D., Edoa, P. F. and Masmoudi, M.: "Identification of geological shapes in reservoir engineering by history matching production data," SPE 48969, proceedings of the SPE Annual Meeting, New Orleans (September 1998).

26. Thiele, M. R., Batycky, R. P., Blunt, M. J. and Orr Jr, F. M.Jr. "Simulating Flow in Heterogeneous Systems Using Streamtubes and Streamlines," *SPERE* (February 1996) 5-12.

27. Thiele, M.R., Blunt, M.J., and Orr, F.M. Jr.: "Modeling Flow in Heterogeneous Media Using Streamtubes--I. Miscible and Immiscible Displacements," *In Situ* **19**(3), (August 1995) 299-339.

28. Thiele, M.R., Blunt, M.J., and Orr, F.M. Jr.: "Modeling Flow in Heterogeneous Media Using Streamtubes--II. Compositional Displacements," *In Situ* **19**(4), (1995) 367-391.

29. Tran, T. T., Wen, X.H., and Behrens, R. A., "Efficient Conditioning of 3D Fine-Scale Reservoir Model to Multiple Production Data Using Streamline-Based Coarse-Scale Inversion and Geostatistical Downscaling", SPE 56518, proceedings of the SPE Annual Technical Conference, Houston (October 1999), 347-359.

30. Vasco, D.W. and Datta-Gupta, A.: "Integrating Multiphase Production History in Stochastic Reservoir Characterization," *SPEFE* (September 1997) 149-156.

31. Vasco, D.W., Yoon, S. and Datta-Gupta, A.: "Integrating Dynamic Data Into High- Resolution Reservoir Models Using Streamline-Based Analytic Sensitivity Coefficients," SPE 49002, paper presented at 1998 Annual Technical Conference and Exhibition in New Orleans, (September 27-30, 1998).

32. Wang, Y., "A Streamline Approach for History-Matching Production Data", 23rd Industrial Affiliates Meeting, Department of Petroleum Engineering, SUPRIA, Stanford University, April 7, 2000.

33. Wang, Y.D., Kovscek, A. R. and Brigham, W.E.: "Effect of Mobility Ratio on Pattern Behavior of a Homogeneous Porous Media", *In-Situ*, **23**(1) (1999) 1-20.

34. Wen, X.H., Clayton, D.V. and Cullick A.S.: "High Resolution Reservoir Models Integrating Multiple-Well Production Data," *SPEJ* (December 1998) 344-355.

35. Wen, X.H., Clayton, D.V. and Cullick A.S.: "Integrating Pressure and Fractional Flow Data in Reservoir Modeling with Fast Streamline-Based Inverse Method," paper SPE 48971 presented at 1998 Annual Technical Conference and Exhibition in New Orlean, (September 27-30, 1998).

36. Wu, Z., Reynolds, A. C. and Oliver, D. S.: "Conditioning Geostatistical Models to Two-Phase Production Data," *SPEJ* (June 1998) 142-155.

Appendix A

```
                  Parameters for SGSIM
                  ********************

START OF PARAMETERS:
../dATAFILES/cdata.dat          -file with data
1  2  0  3  0  0                -columns for X,Y,Z,vr,wt,sec.var.
-1.0       1.0e21               -trimming limits
1                               -transform the data (0=no, 1=yes)
../rESULTS/sgsim.trn            -file for output trans table
1                               -consider ref. dist (0=no, 1=yes)
../dATAFILES/refhist.dat        -file with ref. dist distribution
1  0                            -columns for vr and wt
0.0    1400                     -zmin,zmax(tail extrapolation)
1       0.0                     -lower tail option, parameter
4       3.0                             -upper tail option, parameter
0                               -debugging level: 0,1,2,3
../rESULTS/sgsim.dbg            -file for debugging output
../rESULTS/sgsim.out            -file for simulation output
1                               -number of realizations to generate
50     0.5     1.0              -nx,xmn,xsiz
50     0.5     1.0              -ny,ymn,ysiz
1      0.5     1.0              -nz,zmn,zsiz
111182                          -random number seed
0      8                        -min and max original data for sim
12                              -number of simulated nodes to use
1                               -assign data to nodes (0=no, 1=yes)
1      3                        -multiple grid search (0=no, 1=yes),num
0                               -maximum data per octant (0=not used)
20.0  20.0  20.0                -maximum search radii (hmax,hmin,vert)
 0.0   0.0   0.0                -angles for search ellipsoid
0      0.0                              -ktype:
0=SK,1=OK,2=LVM,3=EXDR,4=COLC
../data/ydata.dat               -file with LVM, EXDR, or COLC variable
4                               -column for secondary variable
1    0.0                        -nst, nugget effect
```

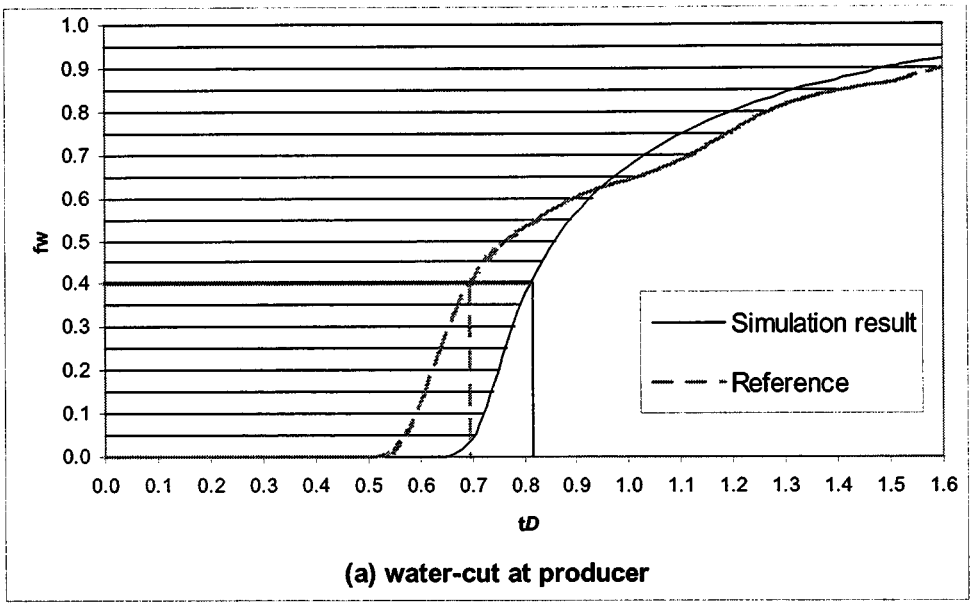

(a) water-cut at producer

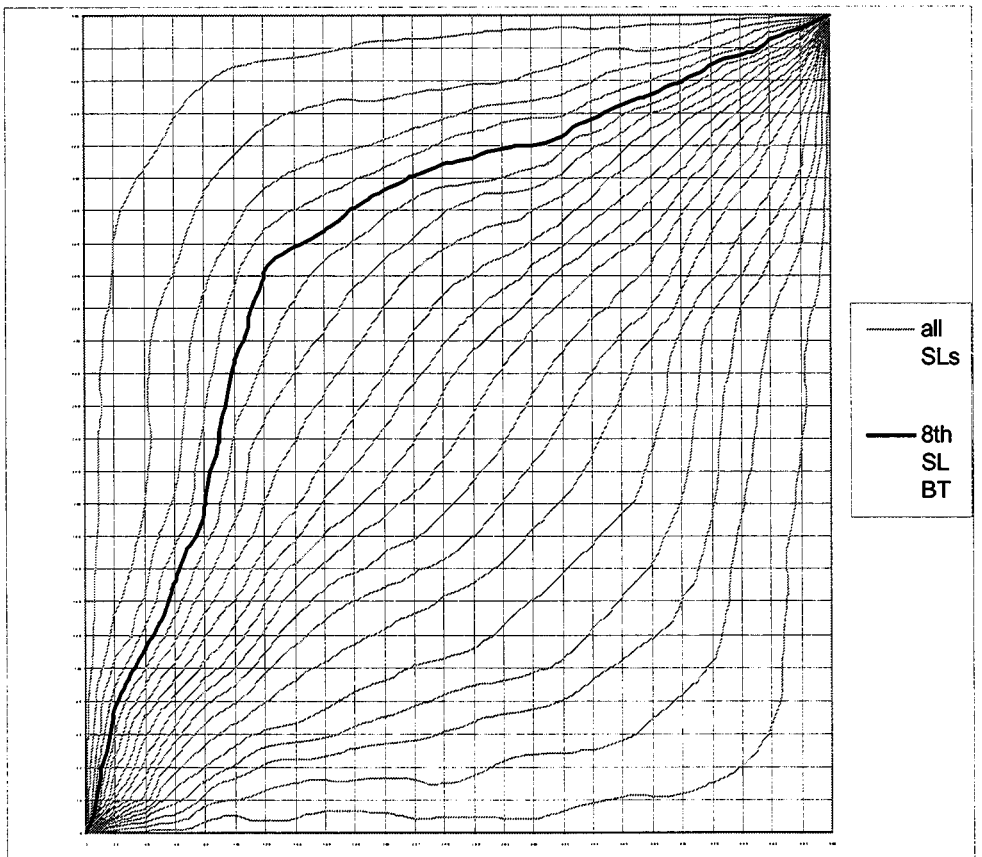

(b) Streamline distribution

Fig. 1 Illustration of streamline inversion method

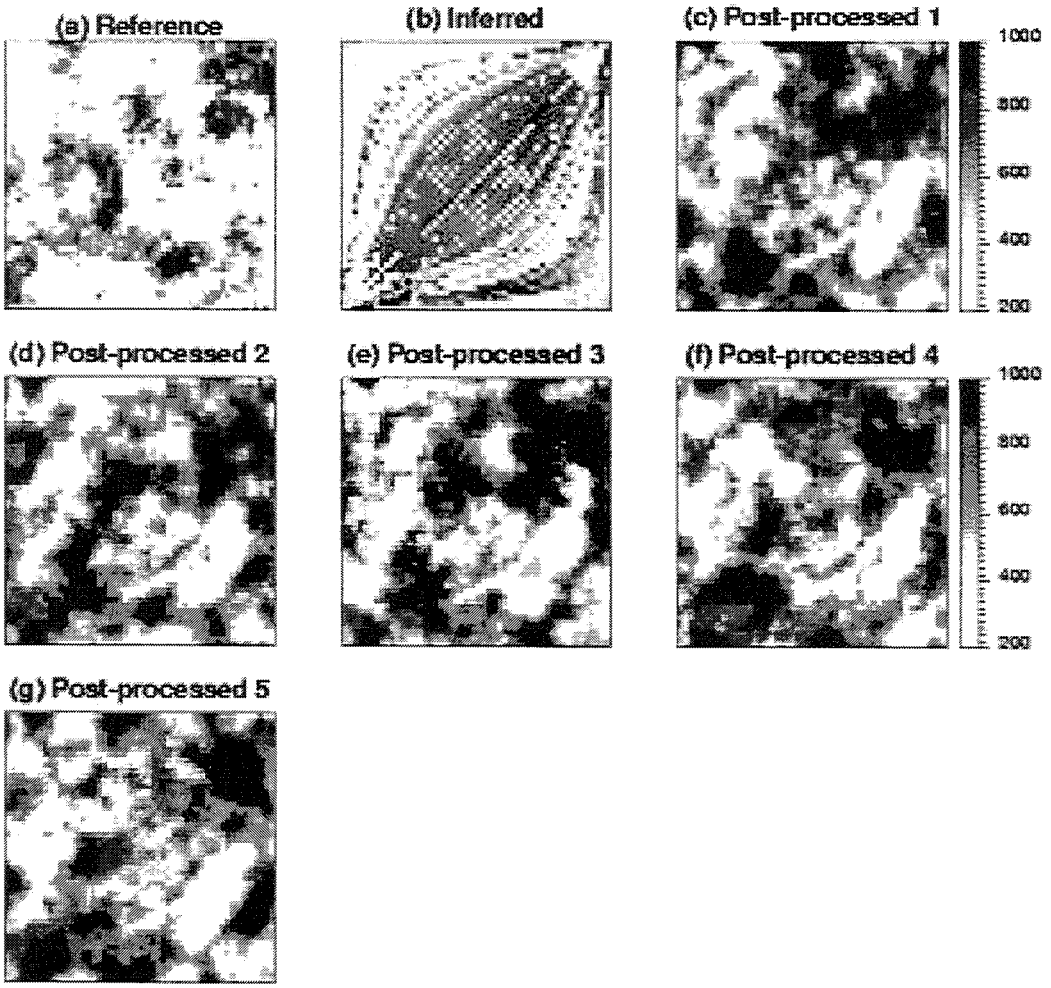

Fig. 2 Case 1, Comparison of permeability fields

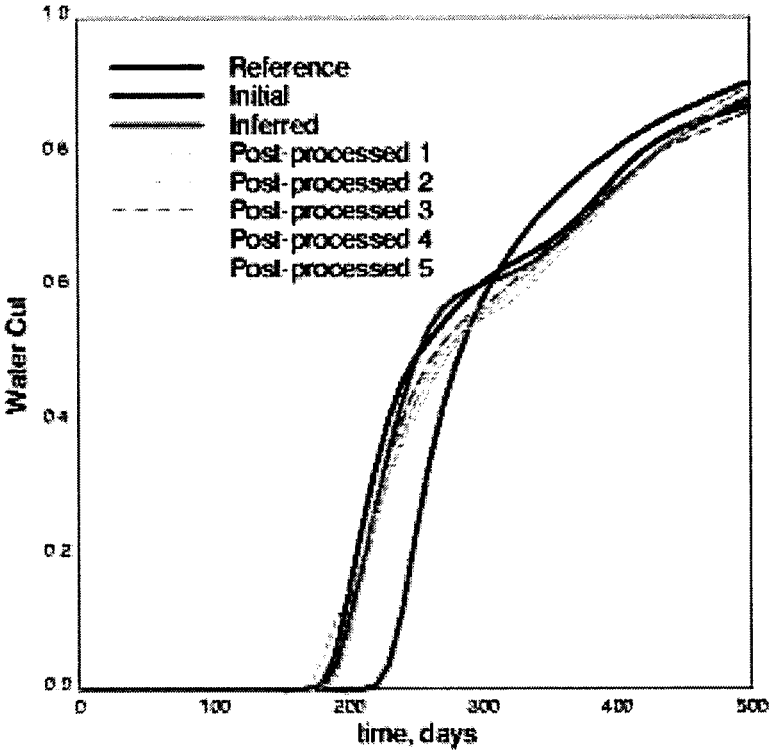

Fig. 3 Case 1. Comparison of water-cut

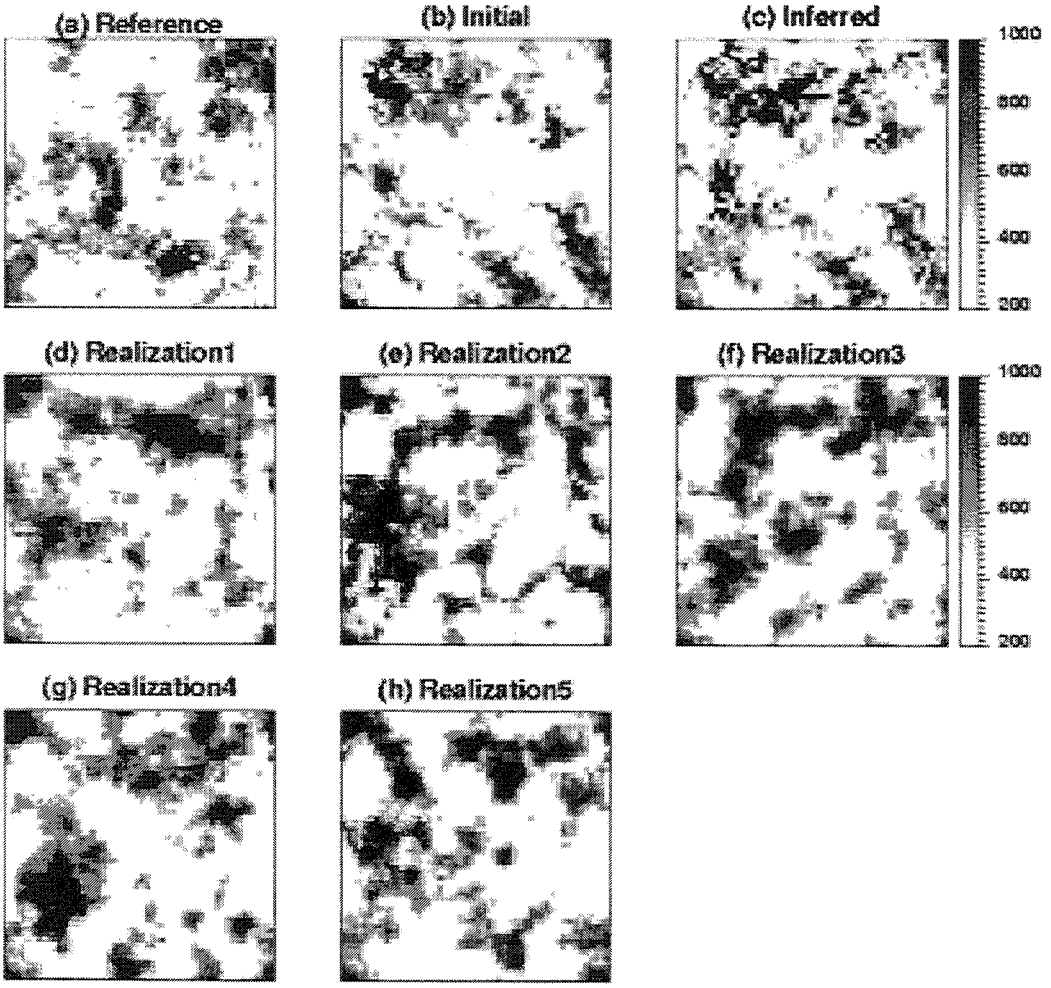

Fig. 4 Case 2, Comparison of permeability fields

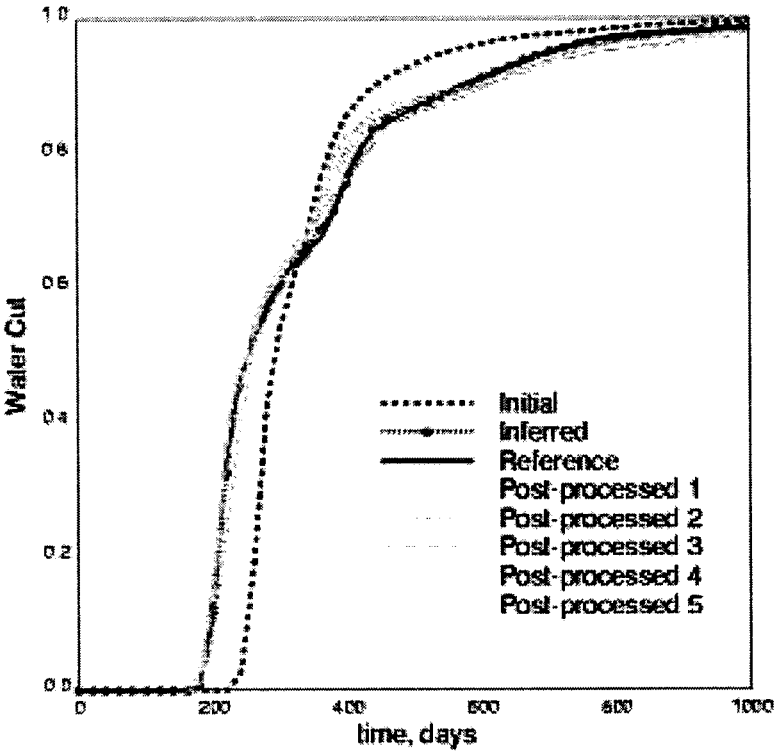

Fig. 5 Case 2. Comparison of water-cut

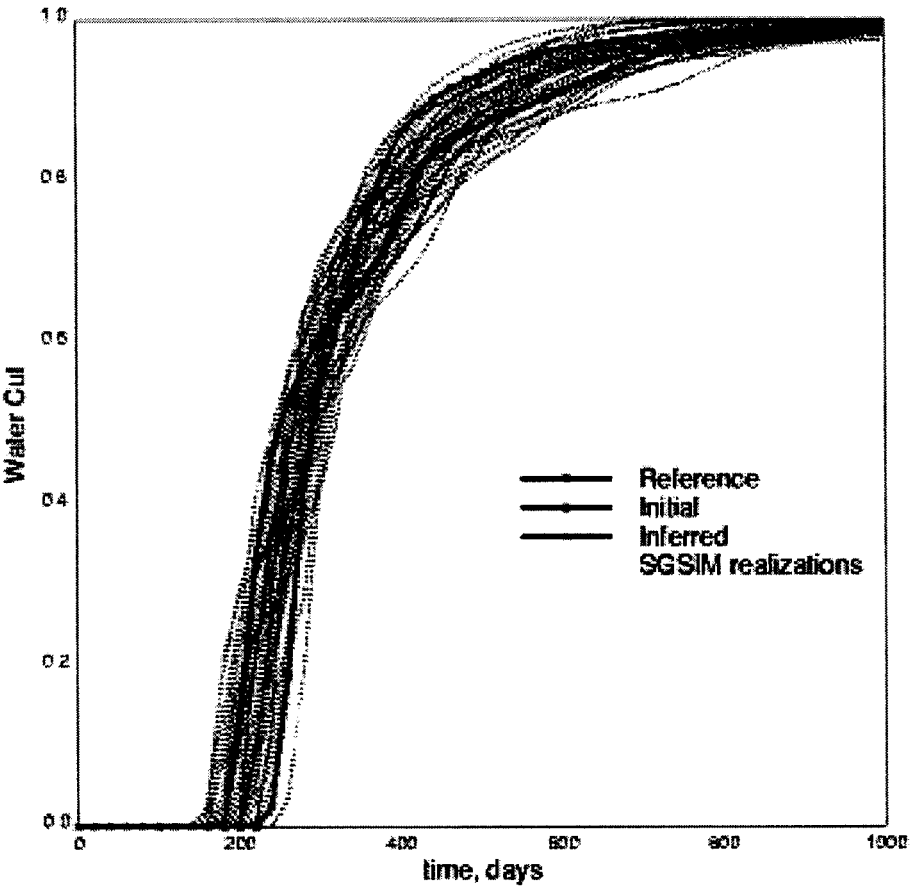

Fig. 6 Case 2, Comparison of water-cut over 50 SGSIM realizations

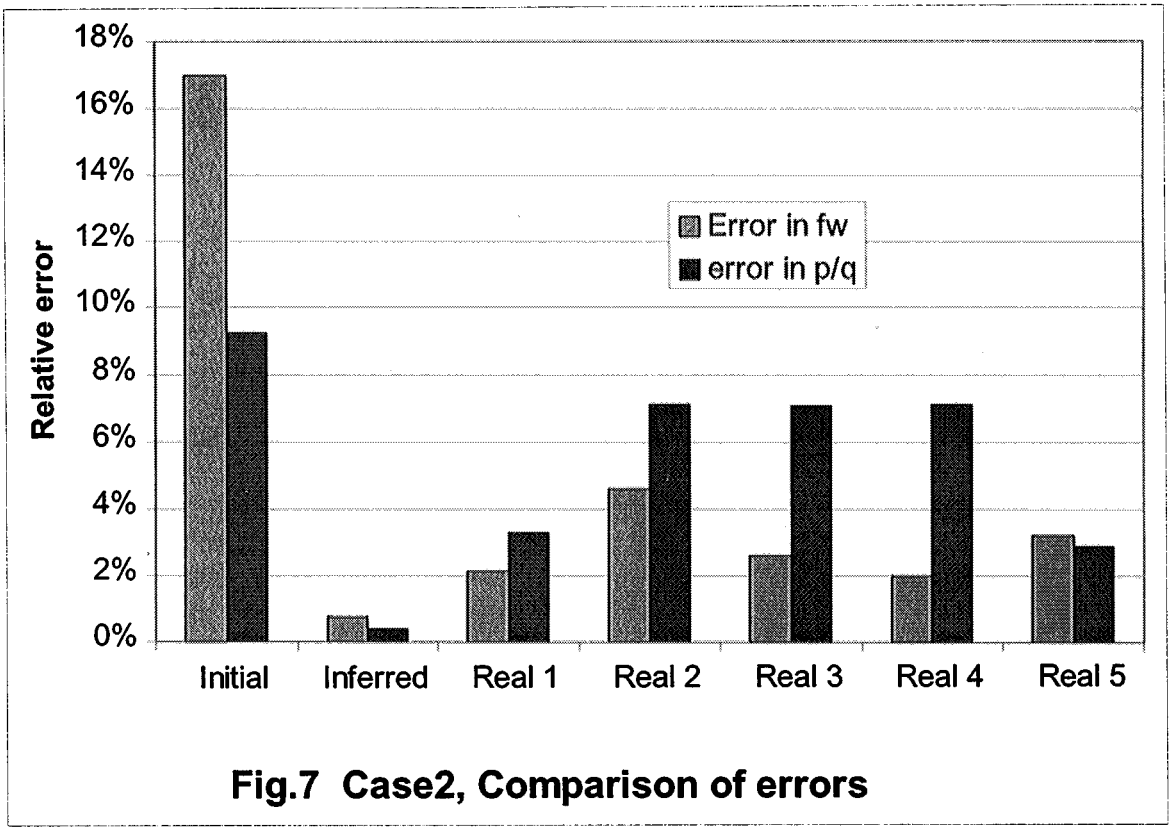

Fig.7 Case2, Comparison of errors

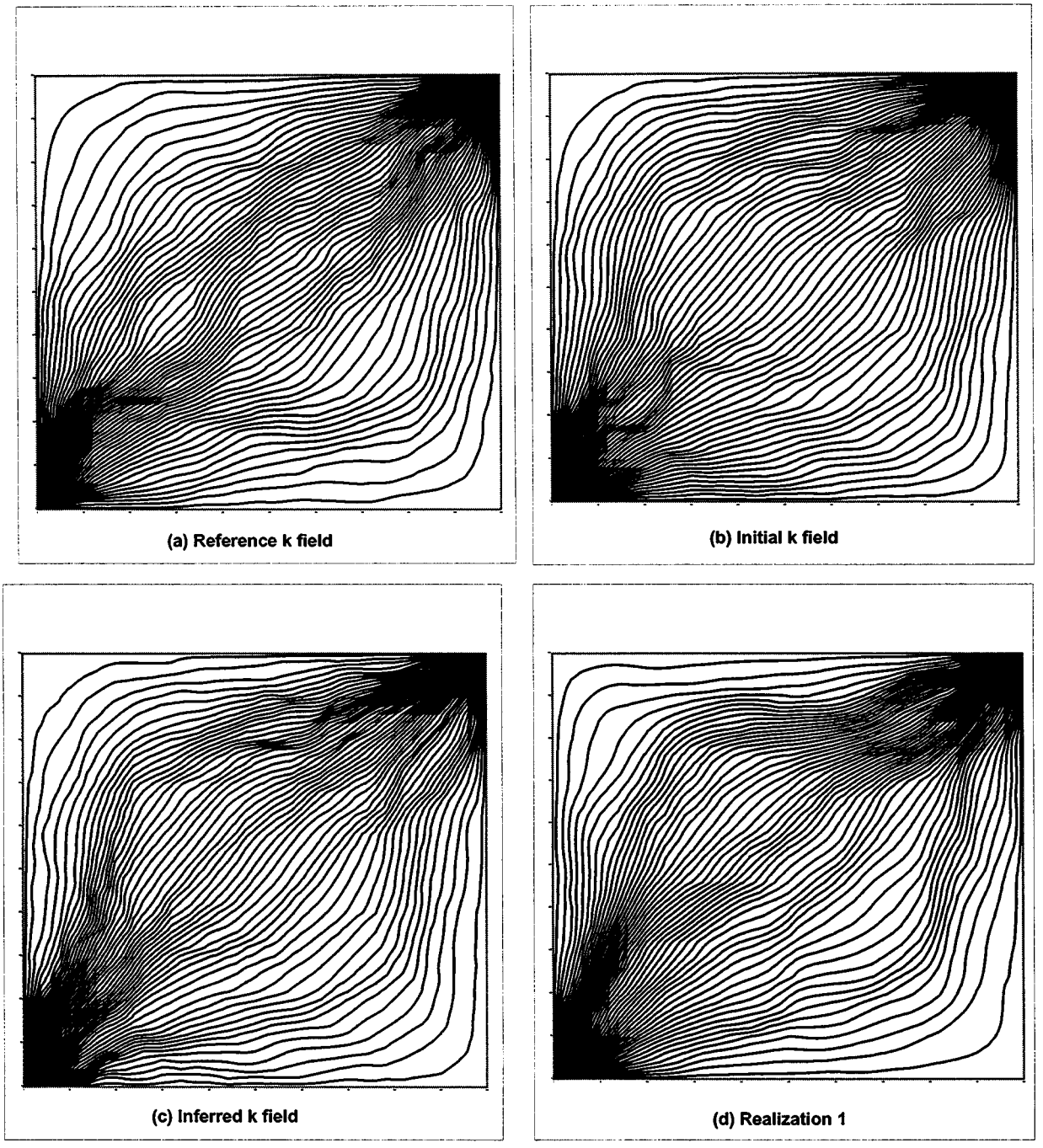

Fig. 8 Case2, Comparison on streamline distribution

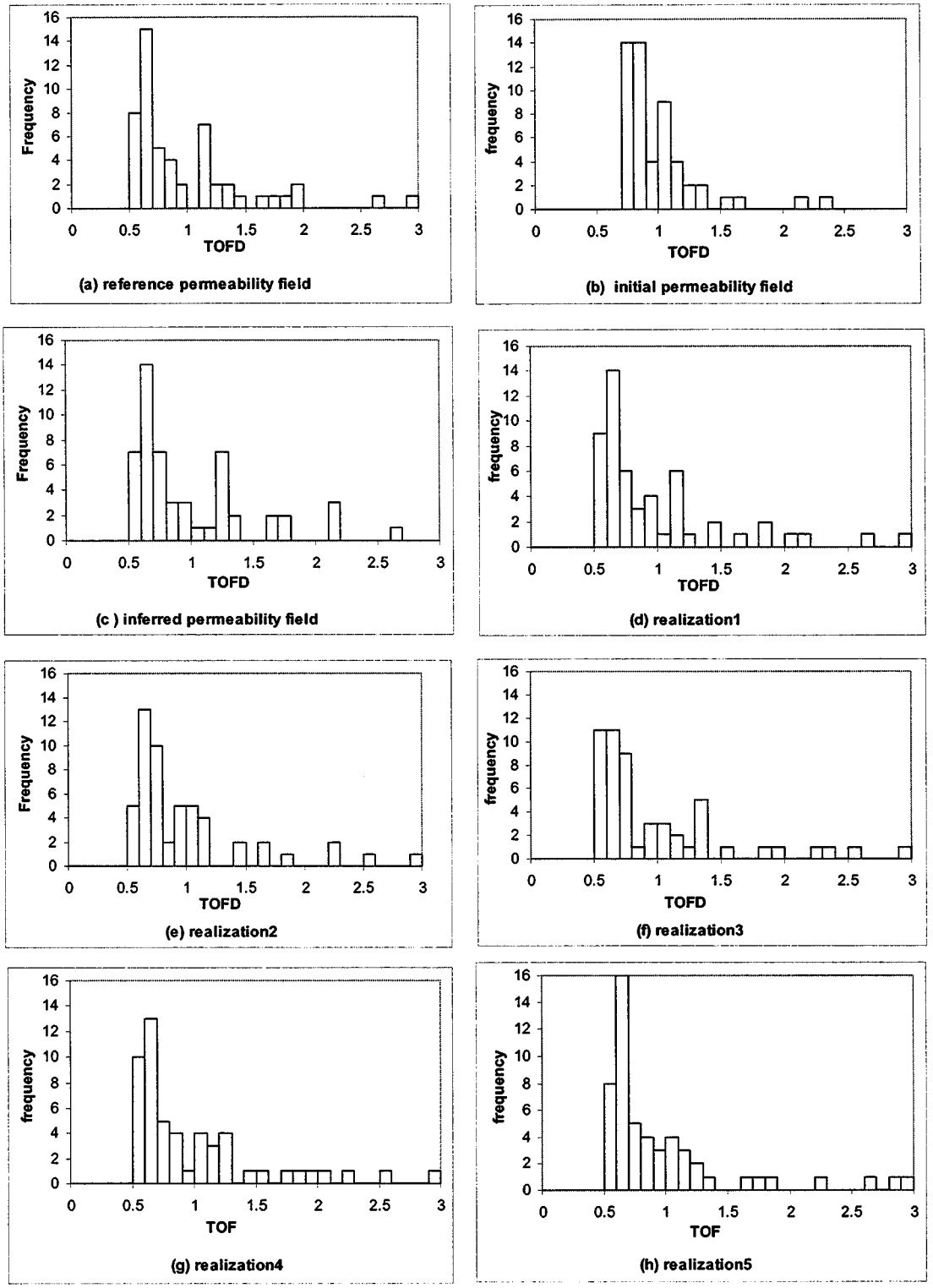

Fig.9 Case2, Comparison of streamline dimensionless TOF distributions

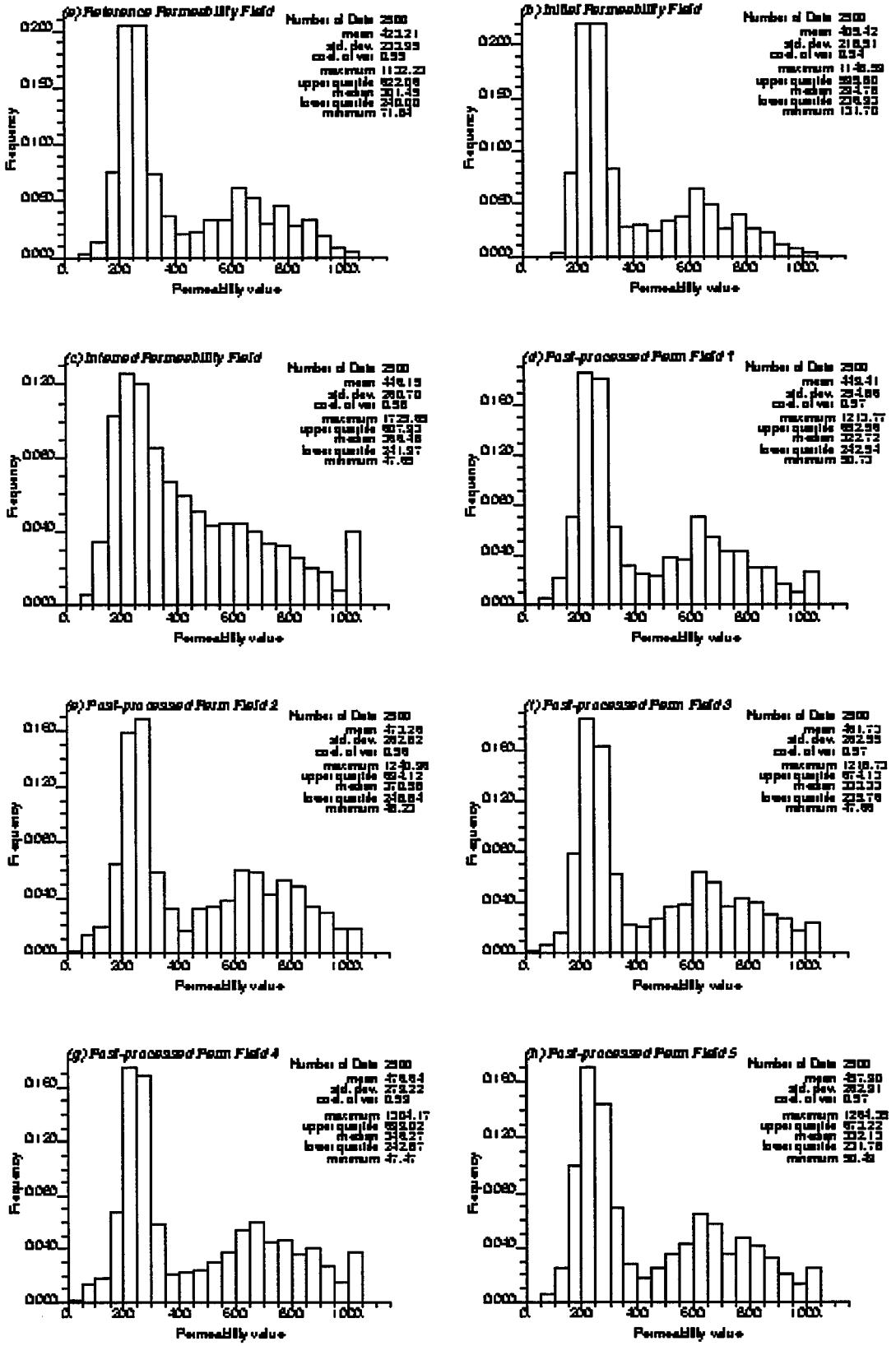

Fig. 10 Case 2, Comparison of histogram of permeability fields

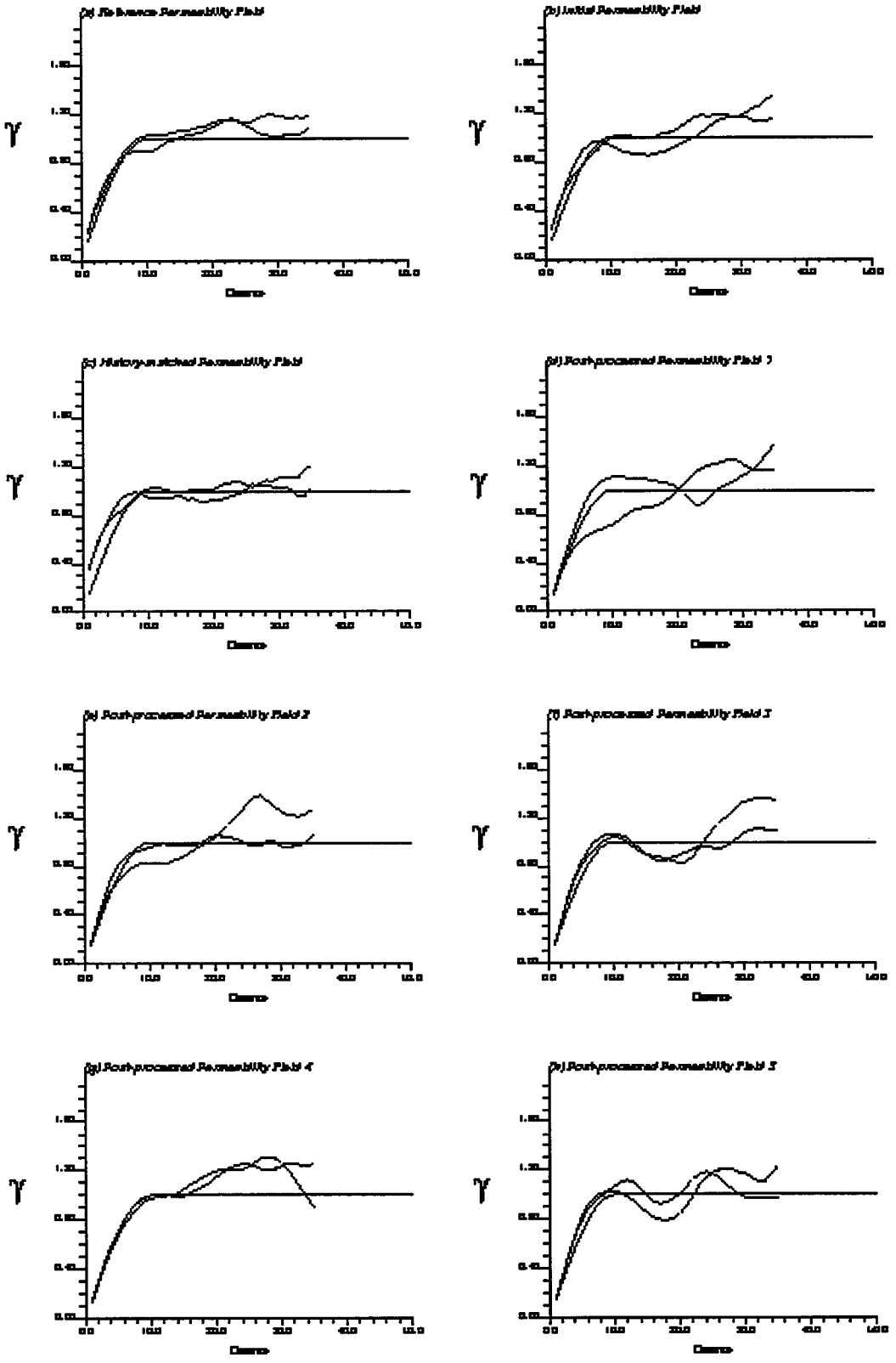

Fig. 11 Case 2, Comparison of variogram of permeability fields